Reconstruction of Electric Fields and Source Distributions in EEG Brain Imaging

Author: Alexandra Koulouri

A Thesis Submitted in Fulfilment of Requirements for the Degree of Doctor of Philosophy of Imperial College London

Communications & Signal Processing Group
Department of Electrical & Electronic Engineering
Imperial College London

Abstract

In this thesis, three different approaches are developed for the estimation of focal brain activity using EEG measurements. The proposed approaches have been tested and found feasible using simulated data.

First, we develop a robust solver for the recovery of focal dipole sources. The solver uses a weighted dipole strength penalty term (also called weighted $L_{1,2}$ norm) as prior information in order to ensure that the sources are sparse and focal, and that both the source orientation and depth bias are reduced. The solver is based on the truncated Newton interior point method combined with a logarithmic barrier method for the approximation of the penalty term. In addition, we use a Bayesian framework to derive the depth weights in the prior that are used to reduce the tendency of the solver to favor superficial sources.

In the second approach, vector field tomography (VFT) is used for the estimation of underlying electric fields inside the brain from external EEG measurements. The electric field is reconstructed using a set of line integrals. This is the first time that VFT has been used for the recovery of fields when the dipole source lies inside the domain of reconstruction. The benefit of this approach is that we do not need a mathematical model for the sources. The test cases indicated that the approach can accurately localize the source activity.

In the last part of the thesis, we show that, by using the Bayesian approximation error approach (AEA), precise knowledge of the tissue conductivities and head geometry are not always needed. We deliberately use a coarse head model and we take the typical variations in the head geometry and tissue conductivities into account statistically in the inverse model. We demonstrate that the AEA results are comparable to those obtained with an accurate head model.

Statement of Originality

I hereby declare that this thesis is the product of my own work under the supervision of my advisors, Mike Brookes and Maria Petrou. Any additional sources of information and ideas presented here from the published or unpublished work of others are fully acknowledged in accordance to the standard referencing practices of the discipline. The material of this work has not been submitted for any degree at any other academic or professional institution.

Copyright Declaration

Acknowledgements

My interest in brain activity imaging was triggered by Maria Petrou in 2010 when with great excitement she presented me her thoughts about how a different theoretical model (Vector Field Tomography) could be used for the tomographic imaging of the head without using expensive instrumentation. Her help and guidance was interrupted by her severe illness, and a bit later Mike Brookes filled our long discussions and mental excursions with vision and excellent comments.

In this challenging trip over the past five years, full of good and bad surprises, I would like to express my gratitude to the people who stood by me and supported me both scientifically and emotionally to complete this piece of work. Their shared thoughts have trickled into the following pages. I thank my supervisors, Mike Brookes and Maria Petrou, for their trust and constant support and the elaborate discussions we had about both research and other deeply philosophical questions. My sincere thanks also goes to Jari Kaipio for his time and effort to introduce me to Bayesian inverse problems. Lastly, I owe a debt of gratitude to Ville Rimpiläinen for embracing my attempts warmly and meticulously proof-reading my drafts.

Abbreviations

AEA	Approximation error approach
ADMM	Alternating Direction Method of Multipliers
ART	Algebraic reconstruction technique
BEM	Boundary element method
CM	Conditional mean
CSF	Cerebrospinal fluid
FST	Fourier slice theorem
CT	Computed tomography
DSM	Distributed source model
EEG	Electroencephalography
EIT	Electrical impedence tomography
EMD	Earth mover's distance
FEM	Finite element method
FT	Fourier transform
GM	Grey matter
LORETA	Low resolution electromagnetic tomography
MAP	Maximum a posteriori
MCE	Minimum current estimate
MEG	Magneto-encephalography
ML	Maximum likelihood
MNE	Minimum norm estimate
MRI	Magnetic resonance imaging
MUSIC	Multiple signal classification
NSD	Nearest source distance
ODT	Optical diffusion tomography
PCG	Pre-conditioned conjugate gradient
PEM	Positron emission tomography
REC	Average reconstruction error
SD	Strength difference
SNR	Signal-to-Noise ratio
SOCP	Second order cone program
tDCS	Trans-cranial direct current stimulation
TNIPM	Truncated Newton interior point method
VESTAL	Vector-based spatiotemporal analysis
VFT	Vector field tomography
WAD	Weighted angle difference
WM	White matter

Basic Notations

Γ, γ	covariance matrix and variance
$\delta(.)$	Dirac delta function
ε	approximation errors
$\mathcal{N}(,)$	Gaussian probability density function
ξ	additive measurement noise
σ	electric conductivity
$\pi(.)$	probability density
$\nabla\times$	curl operator
$\nabla\cdot$	divergence operator
A^{T}	transpose of a matrix A
$\Omega \subset \mathbb{R}^k$	domain of interest (k=2 in 2D and k=3 in 3D)
$\partial\Omega$	boundary of the domain
N	number of nodes of the discretized domain Ω
$\hat{n}$	unit normal vector
$\mathrm{x} \in \Omega$	position vector
$\mathrm{x}_i \in \Omega$	position vector at node i of a discrete domain
$u(\mathrm{x}) : \Omega \to \mathbb{R}$	potential function inside a domain
$u = (u_1, \ldots, u_N)^{\mathrm{T}} \in \mathbb{R}^N$	potential distribution
$v = (v_1, \ldots, v_m)^{\mathrm{T}} \in \mathbb{R}^m$	potential measurements on the m electrodes
$\mathrm{d}(\mathrm{x}) : \Omega \to \mathbb{R}^k$	dipole source
$\mathrm{d}_i \in \mathbb{R}^k$	dipole moment at node i of the discrete domain
n	number of dipole source location in a discretized domain
$d = (d_1, \ldots, d_{kn})^{\mathrm{T}} \in \mathbb{R}^{kn}$	dipole distribution
$\hat{d}$	estimated dipole distribution
$\|d\|_2 = \sum_{i=1}^{kn} d_i^2$	L_2 norm of the dipole distribution
$\|d\|_{1,2} = \sum_{i=1}^{n} \|\mathrm{d}_i\|_2$	$L_{1,2}$ norm or dipole strength norm
$\|d\|_1 = \sum_{i=1}^{kn} \|d_i\|$	L_1 norm of the dipole distribution
$K \in \mathbb{R}^{m \times kn}$	lead field matrix
w	depth weighting factors
$\mathrm{e}(\mathrm{x}) : \Omega \to \mathbb{R}^k$	electric field
$I^{\parallel}$	longitudinal line integral
$I^{\perp}$	transversal line integral
$\mathrm{j}(\mathrm{x})$	current density
$S^{\parallel}$	longitudinal ray transform matrix
$S^{\perp}$	transverse ray transform matrix

Contents

List of Figures

List of Tables

Chapter 1

Introduction

The development of intelligent systems for the analysis of bio-electric brain signals constitutes a springboard for the better understanding of brain structure, function and connectivity between different tissues. Therefore, these systems are crucial for both diagnosis and advanced surgical planning in case of brain dysfunction, and for the monitoring of cognitive processes.

The study of the structure and functional states of the human brain, mathematical modelling of nerve electrical behavior and experimental set-ups that resemble real conditions are very important for this development. For the study of the brain, specialized apparatus is required. The modalities on which brain studies rely are either signal processing-based, e.g. electroencephalography (EEG) and magneto-encephalography (MEG) [122, 13], or tomographic imaging-based, e.g. magnetic resonance imaging (MRI), positron emission tomography (PET), computer tomography (CT) [81, 147] and, more recently, functional near infra red (fNIR) spectroscopy [51]. For cognitive studies and temporal tracking of brain activity, mainly EEG, MEG and functional MRI have been used. Of these three modalities, the EEG devices have the advantage that real time recordings can be acquired and they do not require particularly bulky equipment, as MEG and MRI do. Moreover EEG devices are relatively inexpensive in comparison with the other modalities. For these reasons, in this thesis we focused on techniques for the analysis of EEG brain signals.

The activity measured with EEG electrodes is mainly the result of secondary ohmic current propagation within the tissues induced by primary intracellular currents. The computation of the scalp potentials when the brain activity generators are known, is referred to as the EEG forward problem. The inverse problem, EEG brain imaging, is based on the idea that by measuring the potentials on the head surface, the underlying brain electric activity can be inferred, and thus, the brain areas that are activated due to a stimulation or a pathological condition can be localized. For instance, an individual under examination may receive external sensory stimulation, execute a motor task or have a cognitive experience which results in the propagation of electric fields that can be observed with EEG. Consequently, the EEG inverse problem is referred to as the estimation of the location and properties of the underlying electric signal generators using the recorded data.

The standard methodologies for solving the EEG inverse problem rely on accurate and precise knowledge of the geometric and electrical properties of the head [55, 179]. In particular, for the brain activity an appropriate source model for the representation of the intracranial activity is required in addition to a computational model, the forward model, which describes how the electric current flow propagates in the different tissues and appears on the surface of the scalp. Moreover, a prior assumption on, for example, the types of sources or the extent of the activity is usually required [102, 36].

In this thesis, we consider only focal brain activity that arises, for examples, in cases related to an epileptic event or evoked potential responses to an external stimulus. For this purpose, a non linear convex optimization algorithm is proposed. In the algorithm, a dipole strength penalty term, also called a $L_{1,2}$ norm, is utilized in order to ensure sparsity of the estimated focal sources. The suggested optimization approach was proposed in [69] for the L_1 norm problem and in this thesis it has been further developed for $L_{1,2}$ norms and adapted for the sparse source reconstruction problem.

The accurate description of the electric flow propagation inside the brain is a challenging task because the head consists of several different types of tissue with different electric properties and complex intertwining shapes that differ from person to person. The previous methods use either crude models of the head which result in high estimation errors [143, 184] or expensive and time consuming methods, such as structural MRI (Diffusion tensor imaging/fMRI), to resolve the exact geometry and conductivity distributions of a specific subject's head which result in smaller estimation errors.

In this thesis, we present two new alternative approaches. The first approach lies in the application domain of vector field tomography (VFT) [155] and concerns the reconstruction of the electric fields produced by the electro-chemical activity of the neurons. The advantage of this approach is that a mathematical model for the sources is not required. The reconstructed electric field gives information related to the directions of the electric currents and the region of the brain activity.

In the second approach, we show that the conductivity and geometry modelling errors can be compensated by considering the Bayesian approximation error approach (AEA). The idea of AEA is to use an approximate computational model for the head and to estimate the statistics of the errors between the approximate and accurate head models. Finally, the error statistics are taken into account in the computation of the inverse solution. Thus, source localization errors can be alleviated when a standard head model with a probabilistic model for the uncertainties of the head features is employed. In other words, this means that with the AEA we can use the same generic head model for every patient in EEG source imaging by taking the individual variations into account with the help of approximation error statistics.

1.1 Outline

Chapter 2 describes the basics of the neural activity, and the EEG forward model and gives a review of the most common EEG inverse methods both from deterministic and probabilistic point of view. The EEG inverse problem is an ill posed problem and prior information needs to be included. Hence, the last section of this chapter is devoted to a qualitative explanation of the effects of the regularization used in the EEG inverse solution and the need to use weights in order to improve the reconstruction result. Specifically, when a prior without weighting factors is employed, the maximum values of the estimated brain activity are close to the cortex even when the actual activity is deeper in the brain. In EEG imaging, this intrinsic problem is referred to as depth bias [1, 175, 31].

In chapter 3, we describe the solver for the estimation of sparse/focal sources. The solver uses the dipole strength penalty (so called $L_{1,2}$ norm) which ensures that the solution is sparse and orientation unbiased. The problem is non linear and the solver is based on the truncated Newton interior point method (TNIPM) combined with a logarithmic barrier for the approximation of the penalty term. We estimate a robust stopping criterion for the algorithm and we derive an upper bound for the regularization parameter of the penalty term. All the theoretical and computational aspects of the methods are described analytically. Moreover, to make sure that the sources are not misplaced close to the surface, we present, in section 3.3, a probabilistic method for the selection of appropriate weights for the prior instead of using ad hoc selection methods. The accuracy of the solution is validated by performing reconstructions of deep and superficial sources and the solutions are also compared with the results obtained with the commonly used weighted L_2 and L_1 norms.

In chapter 4, we propose the recovery of the propagated electric fields using vector field tomography (VFT). The electric field is reconstructed using a set of longitudinal and traverse line integrals. The examined test cases include the recovery of harmonic fields, irrotational fields and electric fields caused by dipole sources inside a bounded domain using noisy measurements. The numerical implementation of the approach is studied and different regularization parameters are used depending on the properties of the field and the boundary conditions. In this chapter, we reconstruct electric fields generated by internal dipole sources and we show that the location of the activity can be found using VFT methods. These test cases correspond to EEG brain imaging

In chapter 5, we evaluate the feasibility of AEA to compensate for the errors introduced by the use of an approximated head model in EEG source imaging. We perform two sets of tests. In the first set of simulations we assess how the method can compensate source localization errors due to an approximated head geometry. In the second set, we consider additionally uncertainties and errors related to conductivity modelling and measurements. In all cases, we study reconstructions of sparse sources that arise for example in focal epilepsy. The results indicate that a coarse model accompanied with the approximation error statistics can give comparable results to those obtained using the accurate model.

Chapter 6 includes suggestions for the future. The chapter is divided into two sections. The first section concerns the future aspects of VFT and the second section, improvements in focal source estimation. Finally, in the same chapter we present a brief review of the thesis contributions.

1.2 Aims

The main objective of this thesis is twofold: first, to develop a robust solver for the EEG focal source imaging, and second, to introduce two alternative approaches for solving the EEG imaging problem. With the first, we aim to improve the performance of the existing dipole source solvers. With the second, our aim is to reformulate the EEG inverse problem in such way that we can exploit well-established techniques from other areas of inverse problems. The aims of this thesis as follows.

In the first part of the thesis,

- to develop a robust solver that utilizes the weighted $L_{1,2}$ norm for the recovery of focal dipole sources. To the best of our knowledge, the proposed solver has not been previously used for the $L_{1,2}$ norm based regularizations.
- to present a probabilistic way for the selection of appropriate weights for the regularization term in order to reduce the tendency of the solver to favor superficial sources, There has not been previously a rigorous presentation how to derive these weights; previously, the weights have mainly been considered as ad-hoc choices,
- to compare the dipole source solutions obtained using different prior models.

In the second part of the thesis, our aim was to utilize vector field tomography (VFT) in EEG brain imaging and specifically

- to present the theoretical aspects of the VFT for the EEG problem,
- to numerically approximate the line integrals,
- to use the line integral formulation with different regularization terms in order to reconstruct irrotational electric fields in unbounded and bounded domain,
- to reconstruct electric fields produced by dipole sources in a bounded domain which resembles the EEG imaging problem and to validate that the region of activity is detectable for different levels of measurement noise.

In the third part of the thesis, the approximation error approach (AEA) was used in EEG source imaging. Here, our aims were

- to develop the use of AEA in the context of EEG source imaging and to derive ways of estimating the approximation error statistics,

- to verify with simulations that accurate source results can be obtained for patients without requiring detailed knowledge of head geometry and the tissue conductivities.

1.3 Original Contributions

The following aspects of this thesis are believed to be original contributions:

Solver for focal sources: We developed a solver for the recovery of sparse focal sources that is based on the truncated Newton interior point method and utilizes $L_{1,2}$ norm and depth weights. We derived a probabilistic approach to estimate the depths weights that is based on setting appropriate variances in the posterior probability density. We developed a solver that can reconstruct accurately few or several focal sources and is superior compared to algorithms that utilize L_1 or L_2 norm penalty.

Vector field tomography for the recovery of EEG electric fields: We reformulated the EEG source localization problem and developed a VFT-based technique to reconstruct the electric field that corresponds to the source activity. VFT has not previously been used in cases in which the computational domain contains any kind of sources or sinks. The developed VFT approach can reconstruct electric fields that are generated by focal sources. Moreover, the location of the activity can be determined based on the reconstructed electric field.

Bayesian approximation error approach in EEG source imaging: We applied the approximation error approach in EEG source imaging to compensate geometry and tissue conductivity errors in the head model. We showed with numerical case studies corresponding to one, two and three focal sources that a simplified head model accompanied with AEA can give the same precision as the accurate head model. In other words, we developed an AEA-based approach in which it is not necessary to know neither the exact geometry nor the tissue conductivities of the head to get an accurate source reconstruction; it is enough to know the statistical variations in these features.

Chapter 2

Forward and Inverse Problem of Electroencephalography

Bioelectric measurements are manifestations of current densities inside the human body. The currents are generated when chemical energy is transformed to electrical form in living nerves, muscles cells and tissues. In the brain, the chemical energy is transformed into neural electric signal that induce bioelectric fields that can be detected with boundary measurements such as electroencephalography (EEG).

The electrical signals on the scalp are produced by macroscopic brain activity that can be mathematically described using the quasi-static Poisson equation with appropriate boundary conditions. The task of predicting the boundary signals when the sources are known is called the EEG forward problem.

In the bioelectric inverse problem, on the other hand, the properties of the sources are determined based on the boundary recordings and numerical algorithms. This problem is usually ill-posed i.e. the problem fails to satisfy one or more of the Hadamard's criteria for a well-posed problem [37]. These three criteria are (i) the existence of a solution, (ii) the uniqueness of the solution and (iii) the continuous dependence of the solution upon the data. Most of the computational models do not satisfy the second and third criterion and therefore additional assumptions are needed to obtain a good solution.

In this chapter, we describe the basics of human brain activity and the corresponding EEG forward modelling. Also, we review the most common approaches/techniques that are used to solve the EEG inverse problem.

2.1 Bioelectric Signal Generation

In this section, we briefly describe how bioelectric signal are generated. Detailed information can be found in [95, 122, 166]. The bioelectric signals recorded on the scalp are generated by synchronized neuronal activity in the brain. The skull encloses the brain which contains approximately one hundred billion interconnected neurons [122]. The nervous system is one of

the smallest and yet the most complex body systems. The main functions of the nervous system are (i) sensory, (ii) integrative (perception) and (iii) motor. A nerve is a bundle of hundreds or thousands of axons with associated connective tissues and blood vessels. Each nerve follows a specific path and serves a particular area of the body. Nervous tissue consists of two types of cells: neurons and neuroglia. Neuroglia support, nourish, and protect the neurons and neurons provide most of the functions of the nerve system e.g. controlling muscle activity, sensing and thinking [166].

A neuron consists of three main components: the cell body (soma), several short and highly branched protrusions called dendrites and a single nerve fiber called the axon (Fig. 2.1). The neurons are specialized to (i) conduct information i.e. they have a mechanism for conduction of internal communication between the neuron's soma and its own terminals via the axon and (ii) to transmit information between cells. The dendrites of a neuron receive impulses from other cells and transfer them to the soma. The axon propagates nerve impulses towards another neuron, muscle fiber or grand cell. In most neurons, nerve impulses arise at the junction point between the axon and the soma (the trigger zone), from which they travel along the axon to their destination. The site of communication between two neurons or a neuron and an effector

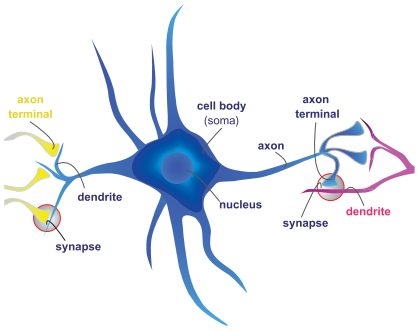

Figure 2.1: Schematic structure of a neuron.

cell is called a synapse. The communication between two neurons is called neuron-transmission. The signal transmission at the synapse is preformed by the release of chemical neurotransmitters from the first neuron (called presynaptic) and the activation of the receptor of the next neuron (postsynaptic cell).

To begin a conduction, a rapid change in the cross-membrane voltage occurs as a result of ion flows across the neuronal membrane in response to specific stimuli (depolarization phase). If this voltage (the membrane potential) exceeds a threshold value, a nerve action potential is initiated. Then the depolarization spreads through the axon to neighboring membrane of the postsynaptic cell causing an excitatory post-synaptic potential. The released neurotransmitter stimulates the neighboring neuron to form a post-synaptic potential in its dendrites and cell body. In response to the potential, the axon of this neuron forms a nerve action potential. The nerve action potential travels along the axon, which results in the release of neurotransmitter at the synaptic point with another neuron and this process is repeated over and over between neurons.

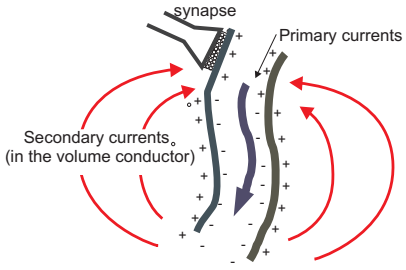

Figure 2.2: The intracellular and extracellular flow of ions causes the propagation of primary current inside the neurons and the induction of a secondary field outside of the cells.

The change of the electric potentials caused by the intracellular and extracellular flow of ions induces the propagation of electromagnetic fields within the tissues. The currents that are propagated within the neural trunk are called primary currents (intracellular). A secondary (Ohmic) current flow is induced in the opposite direction in the exterior of the neurons as a result of the electric charge conservation law (see Fig. 2.2).

The detectable electromagnetic signals arise as a result of simultaneous activation of a large population of neurons which are spatially oriented in a similar way. This kind of activity is mainly produced by pyramidal cells which are a type of neuron located mainly in the cortical areas, amygdala and hippocampus [122, 95]. The EEG signals are produced by the secondary (ohmic) current flow within the tissues and they are directly proportional to the potential differences on the scalp of the head. Therefore, EEG signals dependent strongly on tissue inhomogeneities and skull impedances. On the other hand, the Magnetoencephalography (MEG) signal is mainly induced by the primary currents and it is less affected by the volume conductivities. However, MEG only detects tangential currents and it is relatively insensitive to deep or radial currents which can by detected using EEG [110].

2.1.1 Electromagnetic Activity of the Brain

The electromagnetic activity of the brain is usually categorized into (a) spontaneous activity, (b) evoked potentials and (c) single neuron activity. The EEG devices can measure the spontaneous activity on the scalp or the dura. The frequencies of these signals are between $0 - 70\,\mathrm{Hz}$ and the voltage about $100\,\mu\mathrm{V}$ on the scalp [122]. Spontaneous brain activity can be related for instance to an epileptic condition, brain malignancies, head injury or brain death. The evoked potentials arise as a response to specific impulses, for example visual or auditory stimuli. The evoked potentials are typically one or two orders of magnitude below the noise level and multiple measurements are acquired to increase the signal to noise ratio. The recording and analysis of the evoked potentials have given a boost on the development of brain-computer interface (BCI) algorithms, mental monitoring and cognitive science [162]. The single-neuron recordings provide a way of measuring neural activity of a single spot by implanting a micro-electrode system into the cell. This signal can then be applied to BCI technologies for manipulating external devices using the brain signal. In this thesis, we are interested mainly in EEG recordings produced by

the spontaneous focal activity of the brain. The temporal behavior of the EEG waveforms is not analyzed here. An extensive description of the different rhythms of EEG signals and their interpretation can be found in [122].

2.2 EEG Measurement Devices

The EEG measurement system consists of (i) electrodes, (ii) a multichannel amplifier to strengthen the weak bio-signals and (iii) a data acquisition system in which the recordings are displayed and stored for further analysis. The most common EEG devices have been designed to record signals in the range from microvolt up to a few millivolts for frequencies up to 70 Hz [122].

EEG electrodes are small metal plates that are attached to the skin using a conducting electrode gel. The standard position scheme is the 10-20 system [123] to record spontaneous activity. In this system 21 electrodes are placed on the scalp. The 10 and 20 numbers refer to the relative distances between adjacent electrodes that are either 10% or 20% of the total front-back (nasion-inion) or right-left (ears) dimension of the skull [124]. The reference electrode is placed on the nose or the pre-auricular point (tip of the ear) (see Fig. 2.3). Frequently an

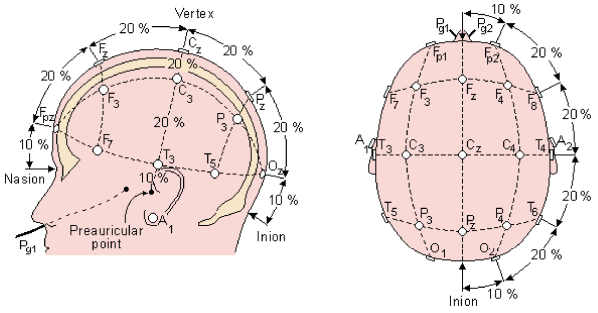

Figure 2.3: 10-20 standard system of electrodes positioning [148].

electrode cap is used to position the electrodes on the head. Electrode caps with, for example, 256 electrodes are available in multichannel configurations and provide a fast and easy way of placing the electrodes uniformly over a wide range of scalp sizes and shapes.

2.3 EEG Forward Problem

2.3.1 Physics of the Brain Sources

The electrical activity in the brain is induced by the flow of charged ions across membranes of the spatially aligned neural cells [122]. The collective interaction of the ion flow gives rise to potentials that can be measured using EEG. It has been shown that this activity can be modelled using the Poisson equation assuming that the geometric and conductivity properties of the head compartments are known [3].

An electrical signal in the brain is expressed as a primary current source which results from the transformation of the chemical energy inside the neuron cells to electric. This is a

nonconservative current which can be considered as the superposition of several electric current dipoles within individual active cells. The primary current source is zero everywhere outside the region of the active cells [14, 61].

The primary current induces an electric current of the form σe (secondary current flow), where σ is the bulk conductivity of the volume and e is the propagated electric field. The total current density is given by $\mathrm{j} = \mathrm{j}^p + \sigma\mathrm{e}$ where j^p are the primary currents and σe the secondary currents respectively and both are functions of spatial position and time. In general, the electric current density is time-varying. However, when using EEG to record bioelectric source behavior at low frequencies (below several kHz) and assuming conductive medium, the quasi-static approximation of the problem is justified [32, 62, 63] i.e. the currents and voltages can be considered static at any given instant. The static consideration of the field implies that the capacitance component of the tissue impendence can be assumed negligible and thus $\nabla\cdot\mathrm{j} = 0$ [95]. Additionally, the electromagnetic wave effects can be neglected at these frequencies [32] and therefore the electric field can be expressed as the gradient of a scalar potential u i.e. $\mathrm{e} = -\nabla u$. Therefore, under the quasi-static approximation the EEG problem can be mathematically described by

$$\nabla \cdot \mathrm{j} = 0 \Rightarrow \nabla \cdot \mathrm{j}^p = \nabla \cdot (-\sigma\mathrm{e}) \Rightarrow \nabla \cdot \mathrm{j}^p = \nabla \cdot \sigma\nabla u. \tag{2.1}$$

2.3.2 EEG Macroscopic Mathematical Model

The primary current source $\nabla \cdot \mathrm{j}^p$, produced by the electro-chemical activity of the neurons, gives rise to potentials u within the brain domain [95]. Under the quasi-static approximation of the Maxwell's equations, the relationship between the current sources and the potentials is described by the Poisson equation with a homogeneous Neumann condition on the head surface [14].

In particular, the computational domain is denoted by $\Omega \subset \mathbb{R}^k$ and its conductivity properties by $\sigma(\mathrm{x})$ where $\mathrm{x} \in \Omega$ is a position vector. For anisotropic media, the conductivity is direction dependent, and the conductivity is a rank-k tensor (i.e. a square matrix) [181, 122]. In this study, we assume isotropic conductivity within each of the head compartments and therefore the conductivity is a scalar quantity i.e. $\sigma(\mathrm{x}) : \Omega \to \mathbb{R}^+$.

The Poisson equation has the form

$$\nabla \cdot \sigma(\mathrm{x})\nabla u(\mathrm{x}) = \nabla \cdot \mathrm{j}^p(\mathrm{x}), \quad \mathrm{x} \in \Omega, \tag{2.2}$$

where $u(\mathrm{x}) : \Omega \to \mathbb{R}$ is the scalar potential function and $\nabla \cdot \mathrm{j}^p(\mathrm{x})$ is the current density with $\mathrm{j}^p(\mathrm{x}) : \Omega \to \mathbb{R}^k$. Here, k is equal to either 2 or 3 depending whether the analysis is carried out in 2D or 3D.

The boundary conditions are

$$u(\mathrm{x}) = 0, \quad \mathrm{x} \in \partial\Omega_0 \tag{2.3}$$

$$\sigma(\mathrm{x})\frac{\partial u(\mathrm{x})}{\partial \hat{n}} = 0, \quad \mathrm{x} \in \partial\Omega \setminus \partial\Omega_0, \tag{2.4}$$

where $\partial\Omega$ is the boundary of the domain, $\partial\Omega_0$ the subset of the boundary with Dirichlet boundary condition, typically a single reference electrode, and $\partial\Omega \setminus \partial\Omega_0$ with Neumann condition, and $\hat{n}$ the outward unit normal vector to the boundary of the domain. Thus, in the EEG formulation, the the Dirichlet (2.3) and the Neumann (2.4) boundary conditions are applied. The Neumann condition states that the current density is zero on the interface between the head and air and the Dirichlet condition ensures the uniqueness of the solution.

In the EEG forward problem the source $\mathrm{j}^p(\mathrm{x})$, the geometry and conductivity of the tissues are known and the potential distribution $u(\mathrm{x})$ is estimated[1]. A necessary condition for the existence of a solution $u(\mathrm{x})$ is that $\int_{\mathrm{x}\in\Omega} \nabla \cdot \mathrm{j}^p(\mathrm{x})\, d\mathrm{x} = 0$ which implies the conservation of the charge in Ω [30].

The general solution of the Poisson equation has the form

$$u(\mathrm{x}) = \int_{x'\in\Omega} g(\mathrm{x}, \mathrm{x}')\nabla \cdot \mathrm{j}^p(\mathrm{x}')\, \mathrm{dx}', \tag{2.5}$$

where $g(\mathrm{x}, \mathrm{x}')$ is a Green's function [3].

2.3.3 EEG Forward Model

In EEG source imaging, the observations are a scalar function defined as the voltage at a point $\mathrm{x} \in \partial\Omega \setminus \partial\Omega_0$ with respect to the reference electrode at location $\mathrm{x}_0 \in \partial\Omega_0$. In practice, there is a set of measurements $v = (v(\mathrm{x}_1), v(\mathrm{x}_2), \ldots, v(\mathrm{x}_m))^{\mathrm{T}} \in \mathbb{R}^m$ where $(\mathrm{x}_1, \ldots, \mathrm{x}_m) \in \partial\Omega \setminus \partial\Omega_0$ and m is the number of measurements. Furthermore, in EEG the primary current source is considered as an idealized electrical dipole source of very small spatial extent with vector moment, denoted by $\mathrm{d}(\mathrm{x}) : \Omega \to \mathbb{R}^k$.

Due to the quasi-static condition and the fact that all the underlying currents obey Ohm's law at low frequencies [146], the mapping from the source field to the i^{th} boundary measurements can be written as

$$v_i = \int_{\mathrm{x}\in\Omega} \mathrm{k}_i(\lambda, \sigma, \mathrm{x}) \cdot \mathrm{d}(\mathrm{x})\, d\mathrm{x}, \quad \text{for } i = 1, \ldots, m, \tag{2.6}$$

where $k_i(\lambda, \sigma, x)$ is a non-linear vector function that depends on the parameterizations of the geometry λ and material properties σ of the domain, and $\mathrm{d}(\mathrm{x})$ is the source configuration. Function $\mathrm{k}_i(\lambda, \sigma, \mathrm{x})$ is referred to as the lead field function [95].

Analytical expressions for the lead field function k_i in equation (2.6) and for the potentials, v_i, can be derived for certain types of volume conductor and geometries e.g. for concentric

[1] In this work, we denote continuous vector-valued functions by lower-case, non-italic letters (e.g. x is a position vector), scalars and discrete distributions by italic lower-case letters and matrices by italic upper-case letters. All vectors are column vectors unless explicitly stated otherwise.

spheres [183, 185]. For realistic head models, a numerical method based on the semi-analytic expansion of the lead field function was proposed in [118].

In practice, for realistic head geometries, the forward problem can solved in discrete domains. The integral (2.6) is approximated by a finite sum and the source distribution approximated by dipole moments at a finite set of points. For realistic head geometries with homogeneous and isotropic conductivities, the Boundary Element method (BEM) can be used. In the BEM [99, 28, 159], the surface of the domain is discretized and the solution is based on a set of surface integrals. BEM is better suited to MEG studies which are less sensitive to tissue conductivities whereas its use for EEG requires more accurate modelling of the different tissue thicknesses and conductivity distributions [21]. Alternatively, the Finite element method (FEM) can be applied to approximate the EEG observation model [62, 124, 182]. In this study, the FEM is used to calculate the EEG computational model since it can easily handle complex geometries and tissues with different, and possibly non-uniform, conductivities. In section 2.4, the estimation of the EEG observation model based on the FEM is presented.

2.3.4 Dipole Modelling

The mathematical dipole is a suitable model for the description of the source term, $\mathrm{j}^p(\mathrm{x})$, in (2.2) because it can adequately represent neural activity in the brain [109]. The brain activity can be considered to be generated by one or more dipoles. Thus, the primary current source density at location x_l can be described by two point current sources of opposite polarity (source/sink) with strength I_l and a vanishingly small separation vector h between the poles [152]. Also, the current source density at location x_l can be described by

$$\nabla \cdot \mathrm{j}^p(\mathrm{x}_l) = \lim_{\mathrm{h}\to 0} \left[I_l \delta(\mathrm{x} - \mathrm{x}_l + \frac{\mathrm{h}}{2}) - I_l \delta(\mathrm{x} - \mathrm{x}_l - \frac{\mathrm{h}}{2}) \right], \tag{2.7}$$

where $\delta(\cdot)$ is the Dirac delta function.

2.4 Finite Element Method in EEG and Construction of Lead field Matrices

In the forward solution, the potentials on the electrodes can be estimated given the current source configuration, Neumann boundary condition and a reference electrode [38]. The analytic solutions of the elliptic partial differential equations (2.2) can be derived for simple geometries such as spheres and cylinders, but not for the complex geometries associated with physiological structures. Therefore, the FEM is appropriate numerical method for the computation of the EEG forward solution [17]. In this section, we give a brief overview of the FEM modelling of the EEG forward problem. Moreover, we derive the lead field (2.6) employing the FEM approach and the mathematical dipole consideration (2.7).

The first step in FEM is the discretization of the domain Ω (head) into elements with different conductivities corresponding to specific tissues. In particular, the head consists of three main

compartment: the scalp, skull and brain. The brain can be further subdivided into white matter (WM), grey matter (GM) and cerebral spinal fluid (CSF). Within each compartment homogeneous electric conductivity is assumed. The shapes of the compartments can be acquired from Magnetic Resonance (MR) images and, based on these, a mesh can be constructed. This mesh defines the FEM space.

The continuous potential of (2.2) is projected into the FEM space considering a set of N piecewise basis functions ϕ_i with value 1 at node i of the mesh and zero at all other nodes (i.e. the basis function has support only on the elements where node i belongs) [171, 124]. The potential function is approximated, $u(\mathrm{x}) \approx u_h(\mathrm{x}) = \sum_{i=1}^{N} \phi_i(\mathrm{x}) u_i$ where u_i are the potential values on the N nodes of the mesh.

FEM solution is based on the weak formulation of the Poisson equation (2.2) with the Neumann condition (2.4) [86]. Briefly, to derive the weak formulation, Poisson equation (2.2) is multiplied with a test function, $g(\mathrm{x}) : \Omega \to \mathbb{R}$, and then is integrated over the domain Ω

$$\int_{\mathrm{x}\in\Omega} g(\mathrm{x}) \nabla \cdot \sigma \nabla u(\mathrm{x})\, d\mathrm{x} = -\int_{\mathrm{x}\in\Omega} g(\mathrm{x})\, \nabla \cdot \mathrm{j}^p(\mathrm{x})\, d\mathrm{x}. \tag{2.8}$$

Using Green's identity and Neumann condition,

$$\int_{\mathrm{x}\in\Omega} \sigma \nabla g(\mathrm{x}) \cdot \nabla u(\mathrm{x})\, d\mathrm{x} = -\int_{\mathrm{x}\in\Omega} g(\mathrm{x})\, \nabla \cdot \mathrm{j}^p(\mathrm{x})\, d\mathrm{x}. \tag{2.9}$$

With the Galerkin method, where the test functions $g(\mathrm{x})$ are chosen to be the basis functions ϕ_i, and by setting $u \approx u_h(\mathrm{x})$, the previous equation becomes

$$\sum_{i=1}^{N} u_i \int_{\mathrm{x}\in\Omega} \sigma \nabla \phi_i(\mathrm{x}) \cdot \nabla \phi_j(\mathrm{x})\, d\mathrm{x} = -\int_{\mathrm{x}\in\Omega} \phi_j(\mathrm{x})\, \nabla \cdot \mathrm{j}^p(\mathrm{x})\, d\mathrm{x}, \tag{2.10}$$

where $j = 1, \ldots, N$.

Finally, the above system is written in matrix form as

$$Au = b. \tag{2.11}$$

Matrix $A \in \mathbb{R}^{N\times N}$ is the conductance matrix (also referred as stiffness matrix [86]) and includes the geometry and conductivity properties of the domain with coefficients given by $a_{ij} = a_{ji} = \int_{\mathrm{x}\in\Omega} \sigma \nabla \phi_i(\mathrm{x}) \cdot \nabla \phi_j(\mathrm{x})\, d\mathrm{x}$.

The right hand side vector $b \in \mathbb{R}^N$ is the load vector and represents the contribution of the current sources to the potential values with coefficients $b_j = -\int_{\mathrm{x}\in\Omega} \phi_j(\mathrm{x})\, \nabla \cdot \mathrm{j}^p(\mathrm{x})\, d\mathrm{x}$. Vector $u \in \mathbb{R}^N$ denotes the potential values at the N mesh nodes. System (2.11) can be solved either using direct or iterative methods.

Before the solution, the right hand side (load vector) needs to be expressed in terms of FEM analysis. The activity inside the domain can be considered as the sum of multiple mathematical dipoles given by (2.7)

Let $(\mathrm{x}_1, \ldots, \mathrm{x}_n)$ denote the possible locations of the dipole sources and n the number of these locations ($n \leq N$ where N is the number of mesh nodes). Considering the dipole source modelling (2.7), the load vector becomes

$$\begin{aligned} b_j &= -\int_\Omega \sum_{l=1}^{n} \lim_{\mathrm{h}\to 0} \phi_j(\mathrm{x}) \left[I_l \delta(\mathrm{x} - \mathrm{x}_l + \frac{\mathrm{h}}{2}) - I_l \delta(\mathrm{x} - \mathrm{x}_l - \frac{\mathrm{h}}{2}) \right] d\mathrm{x} \\ &= \sum_{l=1}^{n} \lim_{\mathrm{h}\to 0} \left[I_l \phi_j(\mathrm{x}_l + \frac{\mathrm{h}}{2}) - I_l \phi_j(\mathrm{x}_l - \frac{\mathrm{h}}{2}) \right] \\ &\approx \sum_{l=1}^{n} I_l \mathrm{h} \cdot \nabla \phi_j(\mathrm{x}_l) = \sum_{l=1}^{n} \mathrm{d}_l \cdot \nabla \phi_j(\mathrm{x}_l), \end{aligned} \tag{2.12}$$

where $\mathrm{d}_l = I_l \mathrm{h}$ is the dipole moment at location x_l with strength I_l.

Alternative approaches to the simple mathematical dipole are the dipole formulation employing the potential subtraction approach [152] or the blurred dipole based on "St. Venant's" principle where a point dipole can by replaced by a distribution of electrical monopoles [15, 180]. In this study, only the mathematical dipole was used in the simulations.

2.4.1 Computation of the Lead Field Matrix

The lead field $\mathrm{k}_i(\lambda, \sigma, \mathrm{x})$ in equation (2.6) can be computed based on the knowledge of matrix A and load vector b (2.11). The dipole moment at location x_l, for the 3D case ($k = 3$), can be written as $\mathrm{d}_l = (d_x^{(l)}, d_y^{(l)}, d_z^{(l)})^{\mathrm{T}} \in \mathbb{R}^3$. Furthermore, for the source locations $(\mathrm{x}_1, \ldots, \mathrm{x}_n)$, the dipole moments can be expressed with a vector representation as $d = (d_x^{(1)}, d_x^{(2)}, \ldots, d_z^{(n)})^{\mathrm{T}} = (d_x, d_y, d_z)^{\mathrm{T}} \in \mathbb{R}^{3n}$. The load vector b (2.12) can be expressed as

$$b = \mathrm{B}d, \tag{2.13}$$

where matrix $\mathrm{B} \in \mathrm{R}^{N \times 3n}$ includes the values of the gradient of the basis functions $\phi_j(\mathrm{x}_l)$. From (2.11) and (2.13), we get

$$Au = \mathrm{Bd}. \tag{2.14}$$

Consequently, we solve (2.14) with respect to u. In order to do this, we need to invert matrix A. Matrix A is invertible if we include the Dirichlet boundary condition (2.3). The Dirichlet condition can be included as follows: If x_r is the node which corresponds to the reference electrode ($u(\mathrm{x}_r) = 0$), then we set $a_{rr} = 1$ in matrix A and all the other coefficients of the r^{th} row equal to zero. Then, we can write $u = K_u d$ where $K_u = A^{-1}\mathrm{B} \in \mathbb{R}^{N \times 3n}$ is the so-called lead field matrix [182].

Usually matrix A is sparse due to the small support of the basis functions, and many algorithms have been developed to enable fast inversion [82]. Also, an approach based on the reciprocity principle [122], was proposed in [182] in order to reduce the computational cost.

For the EEG observation model, only the rows of K_u which correspond to the measurement locations are required. For $v \in \mathbb{R}^m$ measurements around the domain, the lead field matrix is

$K \in \mathbb{R}^{m \times 3n}$ and the model which relates the measurements to the dipole distribution is

$$v = Kd. \tag{2.15}$$

2.5 EEG Inverse Problem

The EEG inverse source imaging problem concerns the estimation of the brain activity given the potentials along the scalp and the mapping operator which describes the propagation of the electric activity of brain to the EEG measurement on the electrodes.

2.5.1 Review on the Source Reconstruction Methods

The spatial resolution and quality of the EEG scalp recordings are often poor due to the noise and inhomogeneities of the skull conductivity which makes the analysis challenging. The current flows towards the scalp from the intracranial sources and follows a tangential trajectory within the skull which results in a significant voltage drop at the electrodes. To acquire an understanding of the brain activity, many source imaging techniques have been developed over the past 20 years for the accurate localization and visualization of the neural current sources (inside the brain) from the EEG measurements.

These source reconstruction methods can be divided into two main categories based on the assumptions about the sources and the utilized mathematical tools. The first methods concern the estimation of dipoles which fit best with the observations solving the problem in the least squares (Dipole fit model) [128, 151, 7]. These methods attempt to explain the measurement with a small number of dipole sources. The single or few dipole assumption has proven to be useful in cases where the underlying brain activity is concentrated in a relatively small volume (most of the brain is electrically silent). Additionally, the dipole term of a multi-pole source expansion is the principle factor affecting the potential measurements. The main disadvantages of the approach are that the number of dipole source needs to be predefined and that the approach is non linear. There are also studies in which the number of sources is predefined using temporal information [104]. However, in case the number of sources is incorrect, the approach fails to localize the activity. The approach often works well for up to 2 dipoles, especially for sources which are spatially separated.

When there are simultaneously several active regions, then the actual source configuration is modelled using the so-called Distributed Source Modelling (DSM) [27]. In this approach, a large number of sources is distributed in an relatively extended area. Methods using the DSM attempt to compute a distribution of dipole moments at every point in a specified reconstruction space, e.g gray matter. These methods are sometimes called tomographic reconstruction techniques. The source locations are fixed while the amplitude and orientation are unknown. These methods have the advantage that the computational model is linear, there is no need for prior estimation of the number of sources and it can be used for extended source configuration. The solution space consists of all the possible source locations in this area and therefore a significant problem

is that the computational model (linear system) is severely under-determined. The distributed source EEG problem is an ill-posed inverse problem and relatively strong assumptions are needed for regularization. Additionally, noisy and incomplete data impose the need for additional constraints related also to the physiological and anatomical information, for example recovering only radial cortical sources [22].

In the following sections, commonly used time-invariant source reconstruction methods based on the dipole fit modelling and the DSM employing different priors are reviewed. There are also other modelling methods which are not included in this overview. For example the spatial filtering method [172, 142] in which a set of spatial filters is designed in such a way that the filter passes signals originating from a specified location within the brain while eliminates signals from other locations and the Multiple Signal Classification (MUSIC) and (RAP)MUSIC [104, 88]. MUSIC separates the measured data into signal and noise subspaces and the best orthogonal projection operator of the signal onto the data-noise space is estimated. Subsequently, the orthogonal projection operator can be used to guide a recursive parametric dipole fitting algorithm. For an extended review of the inverse modelling methods, we suggest [61, 102, 36, 140]. Additionally, when spatio-temporal methods the interested reader is referred to [101, 131, 104, 88] where the temporal information in the signal is used. Furthermore, in spatio-temporal approaches, different dipole models [158] are used, for example the moving dipole model where all the dipole parameters change over time, the rotation dipole model in which the source location is constant during the EEG measurement acquisition [150, 105] or the fixed dipole mode, widely used in evoked response studies with both the orientation and the location constant.

2.5.2 Dipole Fit Model

In the dipole fit modelling, the neural activity in the brain is considered to be restricted to a relatively small volume allowing it to be well approximated by an equivalent single source or a small number of sources. The method tries to estimate a small number of dipoles which fit best with the observed potential measurements.

The sources are mathematically assumed to be dipoles with unknown positions and moments (magnitude and orientation) [62, 14]. In this approach, the observation (2.6) equals to

$$v_i = \sum_{l=1}^{n} \mathrm{k}_i(\mathrm{x}_l) \cdot \mathrm{d}_l, \tag{2.16}$$

where n is the number of the candidate dipole locations, $\mathrm{d}_l \in \mathbb{R}^k$ is the l^{th} dipole moment at location $\mathrm{x}_l \in \Omega$ and $k_i : \Omega \to \mathbb{R}^k$. The associated minimization problem is

$$\min_{(l,\mathrm{x}_l,\mathrm{d}_l)} \sum_{i=1}^{m} \left[v_i - \sum_{l=1}^{n} \mathrm{k}_i(\mathrm{x}_l) \cdot \mathrm{d}_l \right]^2, \tag{2.17}$$

where m the number of observations. The minimization problem is neither convex or linear. Direct search, non linear fitting methods or global optimization techniques can be used for the

solution (e.g. the Levenberg-Marquardt algorithm). For several dipoles (i.e. $n > 2$) the problem (2.17) due to non-convexity does not have a global minimum. Additionally, when the number of unknown parameters exceeds the observations, the problem becomes under-determined. In these cases, the DSM approach is used or temporal information is integrated in the model, i.e. use measurements recorded over a time interval [131].

The simplest problem uses the assumption that there is only a single dipole source characterized by three parameters corresponding to magnitude, position and orientation (six degrees of freedom). These parameters are adjusted in such way that the resulting electrostatic potential matches the best with the given data [62]. The dipole moments are linear parameters and the three location parameters are non linear. This problem can be solved recursively by a sequence of linear and non linear solutions [128]. Specifically, if we consider a fixed source location then the problem becomes linear and over determined and it can be easily solved using linear least square method [43]. The least square estimate gives the optimal dipole for a given location. The non linear part of the problem is to find the best of all optimal dipoles by changing the location parameters.

The single dipole assumption can be used to estimate a distinctive spatial source. For multiple sources with overlapping fields the dipole fit approach breaks down.

2.5.3 Distributed Source Model

In the DSM approach, the electrical activity is considered in the entire brain (or in an extended region). The domain is divided into elements (voxels) and a dipole moment is placed at the centre of the element. The mesh with the dipole locations is the source space. If these fixed locations are denoted with $\mathrm{x}_1, \mathrm{x}_2, \ldots, \mathrm{x}_n$, then (2.6) becomes $v_i = \sum_{l=1}^{n} \mathrm{k}_i(l) \cdot \mathrm{d}_l$

$$v = Kd, \tag{2.18}$$

where $v \in \mathbb{R}^m$, $K \in \mathbb{R}^{m \times kn}$ is the lead field matrix and $d \in \mathbb{R}^{kn}$ is the dipole distribution. With the distributed source model the problem becomes linear, however in most cases the linear system is severely under-determined ($m \ll kn$). To solve the inverse problem, different prior assumptions and constraints have been proposed such as the (weighted) minimum norm [39, 58] and smoothness properties [134] to ensure consistency. Also, anatomical and physiological priors have been proposed [83, 70] which reflect the nature and the properties of the brain activity. Additionally, for better performance, the number of unknowns can be reduced by restricting the region of interest, e.g. by considering sources only in the cortical surface. In the following paragraphs we review the most representative methods using the distributed source model (2.18).

The first distributed source model is the minimum norm estimate (MNE) introduced in [39]. The solution is based on the estimation of the dipole distribution with the lowest overall power which also satisfies the potential measurements. The problem can be expressed as

$$\min_d \|d\|_2^2 \quad \text{subject to } v = Kd, \tag{2.19}$$

where $\|.\|_2$ is the L_2 norm [100]. The solution is given by

$$\hat{d}_{\text{MNE}} = K^{\text{T}}(KK^{\text{T}})^{-1}d. \tag{2.20}$$

The MNE was first introduced for the MEG problem however it can be similarly applied for the EEG inverse problem. Usually, to improve the result a particular brain area is selected.

In practice, instead of the unconstraint MNE, the Tikhonov regularization (L_2 norm regularization) is used [40] and problem becomes

$$\hat{d}_{\text{Tikh}} := \min_d \|Kd - v\|_2^2 + \alpha\|d\|_2^2, \tag{2.21}$$

where α is a regularization parameter. However, MNE and (2.21) give solutions with maxima close to the boundary. This is a consequence of the intrinsic depth bias of this lead field matrix which results in shifting the dipole sources near the surface [1, 175, 31]. For the compensation of the lead field matrix depth effect, the use of a weighted minimum norm estimate (WMNE) was suggested in [58, 29]. This problem was formulated as

$$\min_d \|Wd\|_2^2, \quad \text{subject to } v = Kd, \tag{2.22}$$

where matrix W is diagonal and has elements $w_{ii} = (\|K_i\|_2)^{-1}$ with K_i denoting the column of the lead field matrix. The corresponding solution is $\hat{d}_{\text{WMNE}} = WW^{\text{T}}K^{\text{T}}(KWW^{\text{T}}K^{\text{T}})^{-1}v$.

An commonly used approach is also the Low Resolution Electromagnetic Tomography (LORETA) [134]. LORETA is a generalized minimum norm estimate in which the distributed (smooth) electric activity is computed under the assumption that the neighboring neurons are simultaneously and synchronously active. A discrete Laplace operator denoted by B is used as a smoothness regularization and the problem is formulated as

$$\min_d \|BWd\|_2^2, \quad \text{subject to } v = Kd, \tag{2.23}$$

where W is a depth compensation diagonal matrix with $w_i = \|K_i\|_2$. Matrix B is constructed to be a full rank and symmetric matrix employing a vanishing boundary condition. Consequently, with the LORETA approach, the superficial sources are forced to be close to zero, which is a drawback for the case of superficial brain activity. The solution is $\hat{d}_{\text{LORETA}} = (WB^{\text{T}}BW)^{-1}K^{\text{T}}[K(WB^{\text{T}}BW)^{-1}K^2]^{\dagger}v$ where $\dagger$ denotes the Moore-Penrose pseudo-inverse [100].

The standardized low resolution tomography (sLORETA) [133] is another approach for the unbiased localization of a single underlying dipole source detection assuming no noise. The location of the source is designated by the maximum value of the standardized power given by $P_i = \hat{d}_i^{\text{T}}(R_{ii})^{-1}\hat{d}_i$ for $i = 1, \ldots, kn$ where R_{ii} are the diagonal elements of the resolution matrix defined as $R = K^T(KK^{\text{T}})^{\dagger}K$.

The previous described methods are linear and therefore the dipole distribution can be solved directly. However, the solution usually has many small dipoles and only a few dipoles

with larger magnitude, and the reconstructed images have low spatial resolution. In the best cases, the L_2 norm regularization results in a blurred version of the actual dipole distribution [23] while sometimes imagining artefacts are introduced [97].

For better source resolution, the first proposed approach was the FOcal Under-determined System Solver (FOCUSS) where focal sources were estimated using a recursive WMNE [35, 34]. In every iteration the weighting matrix is updated using the previous step values until most of the elements of the solution become nearly zero. The algorithm terminates when the rank of the weighting matrix drops below the number of the observations. The final solution of FOCUSS depends highly on the initial source distribution and is sensitive to noise. In [87], the authors discussed the integration of FOCUSS with the LORETA in a similar fashion as in [35] with the WMNE.

For the detection of single dipoles, methods employing the sparse L_1 norm [97, 98] or mixed norms [168, 42, 41, 26] have also been suggested. All these approaches are non linear and non linear optimization techniques need to be used for the solution. The first sparse inverse method is the minimum current estimate (MCE) that was introduced in [97] and was formulated as

$$\min_d \|d\|_1, \quad \text{subject to } v = Kd. \tag{2.24}$$

In [97], feasible solutions were obtained by selecting as many dipole moments as the the number of the observations. The L_1 norm imposes sparsity on the individual components of the dipole moments, and therefore the solution is axes-parallel. In [168], a two step algorithm was suggested such as to avoid the orientation bias i.e the orientation was solved using MNE and the amplitude via L_1 norm minimization scheme.

Mixed norms, e.g. the dipole strength norm were suggested in [131, 42, 26] in order to eliminate the axes-parallel dipole distribution and the scattering result. In [42], the Focal Vector Field Reconstruction approach was proposed. In this approach, the cost function was penalized with the L_1 norm of the dipoles strengths augmented by the L_1 norm of the weighted Laplacian. Particularly, the weighted Laplacian adjusts the spatial size of the focal sources and the L_1 norm maintains the high spatial resolution, and thus the ability to discern multiple sources. The estimation was based on

$$\min_d \sum_{i=1}^{n} \|\mathrm{w}_i \cdot \mathrm{d}_i\|_2 + \alpha \sum_{i=1}^{n} \|\mathrm{w}_i \cdot \mathrm{t}_i\|_2, \text{ subject to } v = Kd, \tag{2.25}$$

where $\mathrm{d}_i \in \mathbb{R}^k$ is the dipole moment and t_i the Laplace operator evaluated in the components of d. The weights $\mathrm{w}_i \in \mathbb{R}^k$ are the corresponding diagonal elements of the sLoreta resolution matrix [133]. According to the authors, with this approach imaging artefacts were reduced because the L_1 norm of the weighted dipole strength ensures sparsity in the coupled dipole components and not in individual components which can cause spikes. Additionally, the L_1 norm of the Laplace operator term imposes local smoothness and thus defines the extent of focal sources. However the complexity of the algorithm and the tuning of the extra regularization parameter α does not

make this approach very preferable.

2.5.4 EEG Inverse Problem using Bayesian Framework

The need to use prior information for the reconstruction of dipole sources and the availability of only a limited number of noise-corrupted potential measurements makes the use of probabilistic approaches appropriate. In this section, the basis of the probabilistic theory [66] and the Gaussian assumptions for the solution of EEG inverse problem are discussed. Under certain assumptions, the results of this section coincide with the results of the deterministic approaches of the previous section.

Let us assume that the general observation model for the EEG source imaging problem can be written in the form

$$v = Kd + \xi, \tag{2.26}$$

where $v \in \mathbb{R}^m$ are the potentials around the scalp, $K \in \mathbb{R}^{m \times kn}$ is a mapping between sources $d \in \mathbb{R}^{kn}$ and the measurements, and $\xi \in \mathbb{R}^m$ is the measurement noise.

In the Bayesian framework, all model variables are considered as random and the stochastic nature of the problem is described by means of probability density functions[2]. In this section, all the random variables are denoted with capital letters and their realizations with lowercase letters. Thus, the model is

$$V = KD + \Xi, \tag{2.27}$$

where the observable random variable V is called the measurement, and its realization $V = v$ is called the observation. The random variable D, that is of primary interest, is called the unknown and Ξ is the random noise.

The joint probability of D, V and Ξ, $\pi(d, v, \xi)$, can be decomposed as

$$\pi(d, v, \xi) = \pi(d, \xi)\pi(v|d, \xi), \tag{2.28}$$

where $\pi(d, \xi)$ is the prior probability density of D and Ξ and expresses the information we have about these parameters without taking into account the observations. The likelihood density, $\pi(v|d, \xi)$, denotes the likelihood of different outcomes of the variable V for given dipole distribution $D = d$ and noise $\Xi = \xi$.

From the Bayes' rule, we can estimate the joint posterior

$$\pi(d, \xi|v) = \frac{\pi(v|d, \xi)\pi(d, \xi)}{\pi(v)}, \tag{2.29}$$

which expresses the information we can infer after the realized observation $V = v$.

For the statistical inference of the sources D based on given observations $V = v$, we estimate

[2]for a random variable Y with realization y, instead of writing the probability $\pi(Y = y)$ we write $\pi(y)$.

the posterior density, i.e. the marginalization of $\pi(d, n|\xi)$ over ξ given by

$$\pi_{post}(d) = \pi(d|v) = \int_{\mathbb{R}^m} \pi(d, \xi|v)\ d\xi. \tag{2.30}$$

The integral (2.30) usually cannot be solved analytically. Instead point estimates can be used for the interpretation and visualization of the result. The most common estimate is the maximum a posterior (MAP) estimate which is the solution of the optimization problem

$$\hat{d}_{\text{MAP}} := \arg\max_{d \in \mathbb{R}^{kn}} \pi(d|v). \tag{2.31}$$

Another commonly used point estimate is the conditional mean (CM) given by

$$\hat{d}_{\text{CM}} = \int_{\mathbb{R}^{kn}} d\ \pi(d|v)\ dd = E\{d|v\}. \tag{2.32}$$

If no prior information is considered then the maximum likelihood (ML) can be used as a point estimate,

$$\hat{d}_{\text{ML}} := \arg\max_{d \in \mathbb{R}^{kn}} \pi(v|d), \tag{2.33}$$

expressing our belief in the observed data.

Likelihood Estimation

In order to estimate the likelihood $\pi(v|d)$, we use the Bayes' formula and chain rule [132]. The joint density

$$\pi(v, \xi|d) = \pi(v|\xi, d)\pi_{noise}(\xi|d), \tag{2.34}$$

where the subscript, *noise*, is used to clarify that $\pi_{noise}(.)$ is the probability density of the noise Ξ. Subsequently, the likelihood density is estimated with the marginalization of (2.34) over ξ, i.e.

$$\pi(v|d) = \int_{\mathbb{R}^m} \pi(v, \xi|d)\ d\xi = \int_{\mathbb{R}^m} \pi(v|\xi, d)\pi_{noise}(\xi|d)\ d\xi. \tag{2.35}$$

The conditional probability of the measurements is $\pi(v|d, \xi) = \delta(v - Kd - \xi)$ where $\delta(\cdot)$ is the Dirac delta function. Thus, (2.35) becomes

$$\pi(v|d) = \int_{\mathbb{R}^m} \delta(v - Kd - \xi)\pi_{noise}(\xi|d)d\xi = \pi_{noise}(v - Kd|d). \tag{2.36}$$

Gaussian Assumptions

Assuming that the additive noise Ξ (2.26) is Gaussian with distribution $\Xi \sim \mathcal{N}(\xi_*, \Gamma_\xi)$, where ξ_* is the mean values and Γ_ξ is the covariance matrix and is independent of D then the likelihood (2.36) becomes

$$\pi(v|d) = \pi_{noise}(v - Kd) \tag{2.37}$$

and

$$\pi(v|d) \propto \exp\left(-\frac{1}{2}(v - Kd - \xi_*)^{\mathrm{T}}\Gamma_{\xi}^{-1}(v - Kd - \xi_*)\right) = \exp\left(-\frac{1}{2}\|L_{\xi}(v - Kd - \xi_*)\|_2^2\right) \quad (2.38)$$

where L_{ξ} comes from the Cholesky decomposition of Γ_{ξ}^{-1} (where $\Gamma_{\xi}^{-1} = L_{\xi}^{\mathrm{T}}L_{\xi}$) [100]. The maximization of (2.38) gives the ML estimate. If prior information is considered, by Bayes' rule we have

$$\pi(d|v) \propto \pi(v|d)\pi(d). \quad (2.39)$$

The statistical inference is based on the posterior probability density

$$\pi(d|v) \propto \pi(d)\exp\left(-\frac{1}{2}\|L_{\xi}(v - Kd - \xi_*)\|_2^2\right). \quad (2.40)$$

For Gaussian prior $D \sim N(d_*, \Gamma_d)$ with mean d_* and covariance Γ_d, the MAP estimate is

$$d_{\mathrm{MAP}} := \arg\max_{d\in\mathbb{R}^{kn}} \pi(d|v) = \min_{d} \|L_{\xi}(v - Kd - \xi_*)\|_2^2 + \|L_d(d - d_*)\|_2^2, \quad (2.41)$$

where $L_d^{\mathrm{T}}L_d$ is the Cholesky decomposition of Γ_d^{-1}. The minimization problem can be also written as

$$d_{\mathrm{MAP}} := \min_{d} \left\| \begin{pmatrix} L_{\xi}(v - \xi_*) \\ L_d d_* \end{pmatrix} - \begin{pmatrix} L_{\xi}K \\ L_d \end{pmatrix} d \right\|_2^2. \quad (2.42)$$

According to the previous analysis, we see that the deterministic L_2 norm minimization problem (2.21) corresponds to the MAP estimate with Gaussian prior dipole distribution [58, 92] and the minimization problem MCE corresponds to the MAP estimate when the prior is the Laplace distribution [97, 168].

Alternatively, instead of a prior distribution with parameters (i.e. covariance and mean), a Bayesian learning (SBL) can be employed for the adaptive computation of these prior parameters (which are called hyper-parameters) based on the measured data [93]. Once the optimal hyper-parameters have been learned (e.g. by using Markov Chain Monte Carlo (MCMC) strategies), the estimation of the dipole distribution is performed. Also, the parametrization of the prior covariance matrix can vary depending on the features of the problem e.g. sparse or dense source modelling [121, 177, 178, 91].

One important advantage of the statistical approaches is that the noise model is integrated in the computational model and thus the selection of the prior coefficients (regularization parameters) is performed implicity through the probabilistic modelling. For instance, equation (2.21) is equivalent to the MAP formulation assuming Gaussian noise with zero mean and Gaussian prior [67]. The numerical computation of the statistical parameters of the noise and prior (through for example MCMC) can automatically define the values of the regularization parameters, and thus there is no need to use heuristic or other deterministic techniques (e.g. L-curve) [40].

2.5.5 Regularization and Depth Bias

Usually, the EEG inverse solution is based on the assumption that a large number of candidate sources is distributed inside the gray matter of the brain. The solution space consists of all the possible source locations in this area while the number of potential measurements is very restricted. In practice, this means that the derived linear system used for the inversion is severely under-determined and different source configurations can give rise to the same scalp recordings. Therefore, prior information needs to be incorporated in the computational model.

In this section, we present a qualitative explanation of the effects of the different regularization terms in the EEG inverse solution. Also, we explain why it is important the use of depth weights in the penalty term in order to reduce the tendency of the solver to favour superficial source. Here, we revisit the analysis presented in [16].

Assuming the simplified case where the domain Ω is homogeneous with boundary $\partial\Omega$ and $\mathrm{x} \in \Omega$, we consider the constrained EEG inverse problem

$$\begin{aligned} &\min_{\rho} \; R(\rho) \\ &\text{subject to: } \nabla^2 u(\mathrm{x}) = \rho(\mathrm{x}), \;\; u(\mathrm{x}) = v|_{\partial\Omega} \;\text{ and }\; \nabla u(\mathrm{x}) \cdot \hat{n}|_{\partial\Omega} = 0, \end{aligned} \tag{2.43}$$

where $R(\rho)$ is the regularization term, $\rho(\mathrm{x})$ the source current density, v the voltages along the scalp are known and $\hat{n}$ the unit normal vector to the boundary. This problem can be formulated as a constrained minimization problem with the Lagrangian [11]

$$\begin{aligned} L(\rho, u, \nu, \lambda) =& R(\rho) + \int_{\partial\Omega} \nu(u(\mathrm{x}) - v)\, ds + \int_{\Omega} \lambda(-\nabla^2 u(\mathrm{x}) - \rho(\mathrm{x}))\, d\mathrm{x} \\ =& R(\rho) + \int_{\partial\Omega} \nu(u(\mathrm{x}) - v)\, ds + \int_{\Omega} (\nabla\lambda\nabla u(\mathrm{x}) - \lambda\rho(\mathrm{x}))\, d\mathrm{x}, \end{aligned} \tag{2.44}$$

where ν and λ are the Lagrange multipliers. According to the Saddle Point Theorem [11], if there exist ν and λ such that (ρ, u, ν, λ) define a saddle point for the Lagrangian $L(\rho, u, \nu, \lambda)$, then this ρ is a solution of the constrained problem (2.43). Solving the equation $\partial L = 0$ with respect to ρ, u and λ, we get

$$\partial R(\rho) + \{\lambda\} \;\in\; 0, \tag{2.45}$$

$$\nu + \nabla\lambda \cdot n \;=\; 0 \text{ on } \partial\Omega, \tag{2.46}$$

$$\nabla^2 \lambda \;=\; 0 \text{ in } \Omega. \tag{2.47}$$

From (2.47), we have that λ is harmonic and consequently attains its maximum on $\partial\Omega$ (maximum principle for harmonic functions [103]).

If the regularization term is $R(\rho) = \frac{1}{2}\int_{\Omega} \rho(\mathrm{x})^2\, d\mathrm{x}$ (Tikhonov) then the conditions (2.45)-(2.47) imply that the source distribution is also harmonic ($\rho = \lambda$) and thus the solution yields source maxima close to the boundaries.

One way to shift the energy from the boundary to deeper in the domain is by using ap-

propriately selected weights $w(\mathrm{x})$ (e.g. [58, 29]). In this case, the WMNE with $R(\rho) = \frac{1}{2}\int_\Omega w(\mathrm{x})\rho(\mathrm{x})^2\,d\mathrm{x}$ results in $\lambda = w\rho$.

For the case where the source is sparse, the regularization $R(\rho) = \int_\Omega |\rho(\mathrm{x})|\,d\mathrm{x}$ and condition (2.45) gives

$$\lambda \in \begin{cases} -1 & \text{if } \rho < 0 \\ 1 & \text{if } \rho > 0 \\ (-1, 1) & \text{if } \rho = 0 \end{cases} \tag{2.48}$$

Because λ is harmonic, from (2.48) we conclude that λ attains the values ± 1 on the boundaries, and therefore the solution ρ will also have its maximum strictly on the boundary of the domain and zero inside the domain, except for the case in which λ is constant and equal to either 1 or -1. In this case, the source distribution is zero everywhere. Similarly with the MNE, when using weights the solution is a source distribution with minimum and maximum deeper in the domain. The selection of the weights is further discussed in section 3.3.

2.6 Summary

The major objective of this chapter was to introduce the brain imaging using the EEG as one of the most prominent biomedical application for monitoring the brain activity.

The analysis began by describing the basics of human brain activity and the mechanisms of the electrical signal generations. Subsequently, we defined the EEG forward modelling and we reviewed the most common approaches that are used to localize the brain activity both from deterministic and probabilistic point of view. Finally, we explained the role of the weights in the regularization terms in order to reduce the selective source placement closer to the boundaries of the brain.

Chapter 3

Reconstruction of Focal Sources in the EEG Imaging

The potentials measured on the scalp surface using Electroencephalography (EEG) do not directly designate the location and the strength of neuron activity inside the brain since many different source configurations can give rise to the same measurements [95, 63]. The way to localize the presumed sources inside the brain is through the solution of the so called inverse problem. Due to the ill-posed nature of the inverse problem further assumptions and prior information need to be imposed. Many approaches have been proposed for the instantaneous localization of the neural activity [36]. These approaches can be categorized into three main classes, the dipole fitting techniques [102, 150, 149, 167], the distributed source models (DSM) [39, 35, 58, 134, 97, 106, 23, 182] and the scanning techniques in which alogorithms from the field of radar are used to recover the dipole field (e.g. MUSIC [104], beam-former [172]). In every approach the selection of the preconditions and assumptions are crucial and need to be chosen according to the neurophysiological information that we want to extract from the observed measurements [102].

In the current study, we consider the DSM [7] which relates the dipole source distributions linearly to the measured potentials on the scalp without requiring the number of sources to be defined. The DSM was described in section 2.5.3. The solution space consists of all possible source locations which are far more than the number of the sensors and therefore the linear system is severely under-determined. In order to get a unique solution to the problem, prior information (a penalty term) needs to be incorporated into the model. Our principle assumptions are that the sources are sparse and that there is only a small number of active regions within the brain. Our assumption is justified since focal brain activity can arise in such cases as in pathological epileptic syndrome [122].

The minimum L_2 norm estimate (MNE), weighted or not [39, 134], recovers source distributions which are consistent with the observed data, however the solution is often too blurred and thus does not reflect the actual focal activity. Focal source images are usually obtained by imposing a sparsity-enforcing L_1 norm penalty on the sources. However, the results tend to be

unstable and spatially scattered [168]. An additional drawback is that the L_1 norm forces sparsity on the individual components of the dipole moments and thus the solver favors axes-parallel dipole solutions which do not correspond to realistic physiological behaviour [42, 26].

In order to overcome this problem, the minimum current estimate (MCE), proposed by Uutela *et al.* [168], suggested the prior estimation of the source orientations. The MCE algorithm consisted of two step. In the first step, the MNE was employed for the estimation of the source orientations. Subsequently, the dipole amplitudes were estimated by minimizing the weighted L_1 norm. The final result depended on the accuracy of the first step. The vector-based spatiotemporal analysis (VESTAL) [54] applied the L_1 norm to each source component via an orientation bias-reduction scheme i.e. weighting factors were added in order to penalize the dipole vector when it was close to the coordinates axes. In the cortically-constrained L_2 minimum-norm problem ([83, 70]), the orientation was determined prior to L_1 norm minimization using both MNE and cortical anatomical information. The main difficulty arising in this approach was that the precise knowledge of the subject's cortical structure was essential.

Instead of applying an L_1 norm penalty to the individual components, we employ the dipoles strength penalty that is also referred as $L_{1,2}$ norm [42, 131]. The idea of using the L_1 norm of the dipoles strengths has been previously stated (e.g. there is a first reference in [168]), as it guarantees unbiased estimation of the dipole orientations and the solution is independent of the rotation of the coordination system (see the rotationally invariant reconstruction proof in [42]). Additionally, there is no requirement for intermediate steps. However, at that time, there were technical difficulties and gaps in the knowledge related to the optimization methods for general convex problems. Nowadays, the development of generic methods for the formulation and modification of general minimization problems to convex optimization forms can enable direct, accurate and fast reconstruction of sparse focal sources in the inverse EEG problem [11].

In particular, the sparse source reconstruction problem can be transformed to a second order cone programming (SOCP) problem [89] which can be solved reliably and efficiently using one of the state of the art optimization methods such as the interior point method, the active set method or the dual augmented Lagrangian method [11]. Although these methods can potentially provide accurate and fast solutions, their direct utilization is not always straightforward, practical or even possible. Available software implementations are usually explicitly tailored to a specific convex problem formulation. This limitation arise from the complexity and the variability of the constraints, parameters and the formulation of the non-linear convex problem. In some cases, the convex problem can be reformulated in such a way that it is compatible with an existing software package, however, usually researchers face difficulties in specifying hidden parameters and sometimes the solver is not thoroughly analyzed.

To the best of our knowledge, the previous publications related to the sparse source EEG problem do not include explicit formulae or details either on the way that the algorithm was implemented or the use of heuristic/empirical threshold or bounds (e.g. no details are given in [131, 26, 42]). In this chapter, we rigorously describe, derive and analyze a solver for the sparse source problem which employs robust stopping criteria. The proposed solver estimates the time-

invariant source localization problem, solving the quadratic loss norm problem regularized by the $L_{1,2}$ norm. The solver uses the truncated Newton interior point method (TNIPM) [69]. The generic method in which our solver is based on, was developed by Boyd *et al.* [69] for the solution of large scale L_1 norm convex problem.

TNIPM was selected for the solution of the EEG sparse source problem because (i) this algorithm can very efficiently deal with dense matrices (like the lead field matrix) [69], (ii) it is faster compared to other interior-point methods that use direct or standard conjugate gradient methods [72, 11] which have used previously in the EEG problem [138, 94, 131]. Furthermore, the TNIPM performs comparably to the dual augmented Lagrange (DAL) and is simpler to be applied [165]. Also, higher accuracy can be attained in a reasonable amount of time using the TNIPM in contrast to the alternating direction method of multipliers (ADMM) which usually converges slowly and has only modest accuracy [10].

Additionally, the TNIPM can solve efficiently large scale problems [69]. In previous approaches, dimensionality reduction was performed prior to the estimation in order to increase the computation efficiency of the algorithms [94, 131]. Alternatively, the indirect estimation of the source distribution by first approximating each weighted dipole with a linear combination of spatial basis functions (called "dictionary") and subsequently estimating the corresponding coefficients of this basis expansion was proposed in [41]. This approach possibly can simplify the problem, however the main challenge is the selection of the basis functions that recover meaningful source distributions and balance smoothness and sparsity. So in conclusion, TNIPM is more preferable for the solution of problems in 2D and 3D domains.

The structure of this chapter is as follows. First we give a general overview and the main steps of the interior point method (IPM) and the truncated Newton version of it. Subsequently, in section 3.2, we solve the problem of the quadratic loss function penalized with the weighted $L_{1,2}$ norm (dipole strengths penalty). We reformulate the problem to a convex second order cone program (SOCP) and we employ the truncated Newton interior point method (TNIPM)[89, 2]. In particular, we approximate the SOCP using logarithmic Barrier Method [11] and we solve the derived augmented logarithmic barrier cost function iteratively, applying the truncated Newton method [43]. In addition, we define a dual problem and suggest the duality gap as a robust stopping criterion of the IPM. We derive an upper bound for the useful range of the regularization parameter of the penalty term [11]. Section 3.3 includes the description of the effect of the absence of depth weighting factor in the penalty term and the selection of appropriate weights for the reduction the tendency of the solver to misplace the sources in the superficial layers of the domain [73, 134, 168]. Finally, we compare the reconstruction results using the weighted $L_{1,2}$, L_1 and L_2 norms. We show that the solution based on the $L_{1,2}$ norm (dipole strength penalty) can recover focal sources with gopd accuracy.

3.1 An Interior Point Method for Convex Problems

We consider the general form of a non-linear convex problem

$$\underset{d}{\text{minimize}} \quad f(d) = f_0(d) + \sum_{i=1}^{n} f_i(d) \tag{3.1}$$

where $f_0 : D \to \mathbb{R}$ is considered differentiable and convex while $f_i : D \to \mathbb{R}$ are considered convex but not differentiable in a D real vector space. For this problem an optimal $d^* \in D$ exists. A non-linear differentiable functional can be minimized using iterative methods [43]. For instance, at each iteration we can approximate the minimizer of (3.1), $d_{k+1} = d_k + \Delta d_k$ by solving the Newton system $H_f(d_k)\Delta d_k = -\nabla f(d_k)$ where $H_f(d_k) = \nabla^2 f(d_k)$ is the Hessian matrix at d_k and Δd_k the search direction, until it converges to a fixed point [43].

The solution of (3.1) by solving the Newton system is possible when f_i are twice differentiable. However, as we will see in section 3.2, f_i function which corresponds to the dipole strength is not a continuous differentiable function. Therefore, the Hessian and gradients cannot be estimated, and the direct application of the iterative method is impossible. To overcome this, we employ the interior point methodology [11]. First we approximate the functional with a new one which is continuous and differentiable. Then, we can use an iterative method to estimate the minimizer of the new functional which is an approximation to the actual solution.

3.1.1 Overview of the Logarithmic Barrier Method

The unconstrained non-differentiable convex problem (3.1) can be approximated by a convex constrained problem using the variable-splitting method [11]. Therefore, a new variable r_i is defined, such as $r_i \geq f_i(d)$, and the problem becomes

$$\begin{aligned} &\underset{(d,r)\in C}{\text{minimize}} \; f_0(d) + \sum_{i=1}^{n} r_i \\ &\text{subject to } \; r_i \geq f_i(d), \quad i = 1 \dots n, \end{aligned} \tag{3.2}$$

where the feasible set C is defined as $C = \{d \in D, r \in \mathbb{R}^n \; : \; r_i - f_i(d) \geq 0 \text{ for } i = 1, \cdots, n\}$. For the solution of (3.2) with the IPM we implicitly express the inequality constraint in the objective, i.e.

$$\underset{(d,r)\in C}{\text{minimize}} \quad f_0(d) + \sum_{i=1}^{n} r_i + \sum_{i=1}^{n} I(f_i(d) - r_i), \tag{3.3}$$

where $I : \mathbb{R} \to \mathbb{R}$ is the indicator function defined as

$$I(f_i(d) - r_i) = \begin{cases} 0, & \text{when } r_i - f_i(d) \geq 0 \\ \infty, & \text{otherwise} \end{cases} \tag{3.4}$$

The indicator function is not differentiable. However, it can be approximated by a logarithmic function

$$\hat{I}(f_i(d) - r_i) = -(1/t)\log(-(f_i(d) - r_i)), \tag{3.5}$$

where $t > 0$ is a parameter which tunes the accuracy of the approximation [11]. Function $\hat{I}$ is convex, differentiable for $r_i - f_i(d) > 0$ and approximates the indicator function I for increasing values of t.

Hence, problem (3.3) is approximated with the minimization problem

$$\underset{(d,r)}{\text{minimize}} \quad f_0(d) + \sum_{i=1}^{n} r_i - (1/t)\Phi(d, r) \tag{3.6}$$

where

$$\Phi(d, r) = \sum_{i=1}^{n} \log(r_i - f_i(d)) \tag{3.7}$$

is called logarithmic barrier function. Term $\Phi(d, r)$ acts as a barrier which ensures that the minimizer (d^*, r^*) of (3.6) is in the interior of the feasible set C. For $t \to \infty$, term $\Phi(d, r)$ affects the minimization only if $r_i \simeq f_i(d)$ due to the singularity of the logarithm. Instead of having $1/t$, the objective function can be multiplied by t without affecting the solution. Thus, the IPM for the constrained convex problem (3.2) is the solution of a sequence of the unconstrained problems

$$\underset{(d,r)}{\text{minimize}} \quad \Phi_t(d, r) = t f_0(d) + t \sum_{i=1}^{n} r_i - \Phi(d, r) \tag{3.8}$$

for various $t > 0$.

For given $t > 0$, the objective function (3.8) is convex and differentiable in the interior of the feasible set C of (3.2). Thus, any local minimum is also a global minimum. With the IPM, we solve a sequence of minimization problems (3.8) for increasing value of t. In particular, the interior point algorithm based on the barrier function method consists of the two loops called inner and outer loop, respectively. In the inner loop, the value of $t > 0$ is constant and we estimate the solution of (3.8) denoted by $(d^*(t), r^*(t))$. The solution $(d^*(t), r^*(t))$ is usually computed solving a Newton system. In the outer loop, the value of t is updated and problem (3.8) can be solved again using as a starting point the previous estimated solution. The sequence of the solutions $(d^*(t), r^*(t))$ for $t > 0$ is usually referred as the central path of the method [11].

Problem (3.8) is an approximation of the original problem (3.1). For large values of t, the approximation improves and the optimal value of (3.8) converges to the minimum of (3.1). The proof of this convergence can been found in appendix C. However, in IPM the value of t increases progressively as the number of outer iterations increases. This is happening because the choice of large initial t can cause numerical instabilities.

The algorithm terminates when a stopping criterion ϵ_{tol} (in Alg. 1) is satisfied. As a robust stopping criterion, we can employ the so-called duality gap η between the primal problem (3.1) and its dual problem [11]. The duality gap η is defined as the difference between the primal and

the dual objective values at each iteration. The derivation of the dual problem will be rigorously analyzed in section 3.2.2. As an example, (Fig. 3.1.a) shows how the duality gap progressively decreases as the IPM converges. In Figure (3.1.b), we can see the corresponding values of the primal and dual problems at each iteration. In Alg. 1, we show the basic steps of the IPM with logarithmic barrier function.

Algorithm 1 Interior Point Method with Logarithmic Barrier

Initialization: t, (d, r) and ϵ_{tol}.
Repeat (Outer Loop):

1. **Inner Loop**: Minimize objective function Φ_t (3.8) and estimate $(d^*(t), r^*(t))$.
2. Update (d, r).
3. Estimate dual problem and the duality gap η.
   Quit if $\eta < \epsilon_{tol}$
4. Update t.

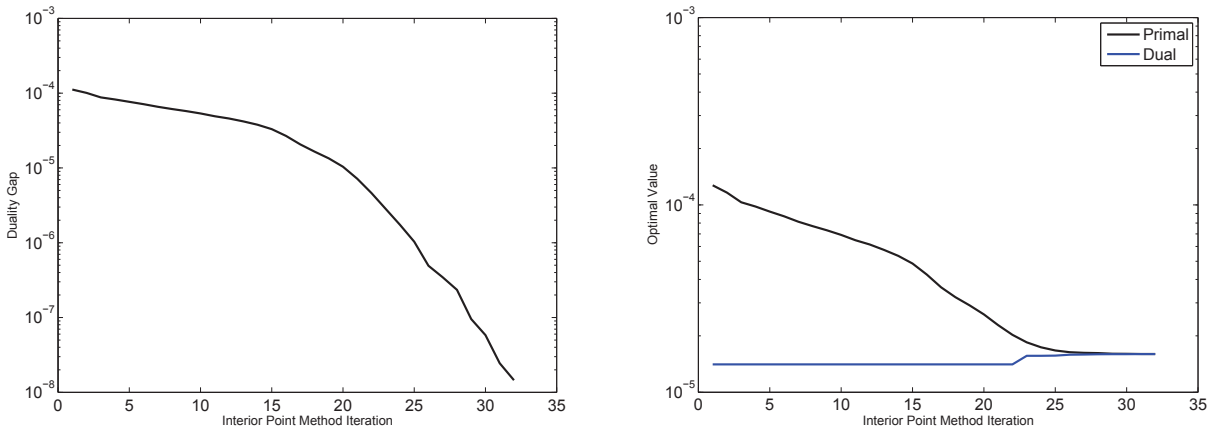

(a) Duality gap (b) Optimal values of Primal and Dual Problems

Figure 3.1: (a) Duality Gap and (a) optimal values of the Primal and Dual problem at each iteration of the IPM for the EEG sparse focal source problem.

3.1.2 Inner Loop of IPM

The minimization of the objective (3.8) at step 1 of the Alg. 1 is the most computationally expensive process, especially when we deal with large scale problems. Hence, a method which balances the computational complexity and the convergence rate is preferable. For the solution of (3.8) we use an iterative method which is more efficient than the direct method for medium and large scale problems [43].

In the current implementation, we estimate the solution of (3.8) in two steps. First, we compute the search direction denoted by $(\Delta d, \Delta r)$, by approximately solving the Newton system

$H_{\Phi_t}(\Delta d, \Delta r) = -\nabla\Phi_t$ where H_{Φ_t} is the Hessian matrix of (3.8) at (d, r). The search direction is approximately solved using the Preconditioned Conjugate Gradient (PCG) method with adjustable stopping criterion [72, 11].

Specifically, the PCG converges faster compared to other iterative methods (e.g steepest descent [43]) and it is efficient to compute because at each iteration it requires only two matrix vector multiplications and a small number of inner products [43]. The storage needs are very modest as most of the variables are overwritten and no explicit representation of the Hessian is required [43]. Moreover, the adjustable tolerance leads to an approximate solution of Newton system by truncating the number of iterations while keeping an acceptable convergence rate [72]. The term Truncated Newton in IPM refers to the estimation of an approximate solution of the Newton system using PCG which is terminated earlier than the convergence point.

In the second step, a line search is performed along the search direction $(\Delta d, \Delta r)$ (damped Newton method [43]) and we estimate a scalar s. The new solution becomes $(d, r) := (d, r) + s(\Delta d, \Delta r)$. The second step is important because the Newton system usually returns an unreliable search direction unless it is started close enough to the actual solution.

3.2 Focal Sources Reconstruction using TNIPM

In the EEG focal source imaging, we want to minimize the quadratic $\|Kd - v\|_2^2$ term regularized by the $L_{1,2}$ norm, i.e.

$$f(d) = \|Kd - v\|_2^2 + \|d\|_{1,2}, \tag{3.9}$$

where $d \in \mathbb{R}^{kn}$ is the component-wise representation of the dipole distribution, k is the number of components ($k = 2$ or 3 depending on the dimension of the problem), n is the number of discretization points in the dipole distribution, $K \in \mathbb{R}^{m \times kn}$ is the lead field matrix, m is the number of measurements and $v \in \mathbb{R}^m$ the measured potentials ($m < kn$). With d_i, we denote the dipole moment at location i. The $L_{1,2}$ norm (also called dipole strength penalty) is defined as

$$\|d\|_{1,2} = \alpha \sum_{i=1}^{n} w_i \|\mathrm{d}_i\|_2 = \sum_{i=1}^{n} w_i \sqrt{\sum_{j=1}^{k} d_{i+(j-1)n}^2}, \tag{3.10}$$

where $\alpha > 0$ is a scaling parameter and $w_i > 0$ are weighing factors. The $L_{1,2}$ norm in (3.9) restricts the solution to have only a small number of non zero amplitudes.

The functional in (3.9) is convex and thus an optimal minimizer d^* exists, however it is not differentiable. For the solution of problem (3.9) we transform it to one which has differentiable objective and constraint functions, and subsequently we solve it using TNIPM described in section 3.1.

Problem (3.9) can be transformed to the convex Second Order Cone program (SOCP) [89],

$$\begin{aligned} \underset{(d,r)}{\text{minimize}} \quad & \|Kd - v\|_2^2 + \alpha \sum_{i=1}^{n} r_i \\ \text{subject to} \quad & r_i > w_i \|\mathrm{d}_i\|_2, \quad i = 1, \ldots, n \end{aligned} \tag{3.11}$$

where $r \in \mathbb{R}_+^n$. Then, SOCP is reformulated to an unconstrained problem using a barrier method [11].

Let's define the logarithmic barrier function for the constraints $r_i \geq w_i \|\mathrm{d}_i\|_2$ of (3.11)

$$\Phi(d, r) = -\sum_{i=1}^{n} \log(r_i^2 - w_i^2 \|\mathrm{d}_i\|_2^2) \tag{3.12}$$

where $r_i > 0$ and $r_i^2 - w_i^2 \|\mathrm{d}_i\|_2^2 > 0$ for $i = 1, \ldots, n$.

The associated interior point problem is the minimization of the weighted objective function (3.11) augmented by the logarithmic barrier for the constraints, i.e.

$$\underset{(d,r)}{\text{minimize}} \ \Phi_t(d, r) = t\|Kd - v\|_2^2 + t\alpha \sum_{i=1}^{n} r_i - \sum_{i=1}^{n} \log(r_i^2 - w_i^2 \|\mathrm{d}_{i*}\|_2^2), \tag{3.13}$$

where t varies from 0 to ∞.

Function Φ_t is smooth and strictly convex and it has a unique minimizer $(d^*(t), r^*(t))$ for each given value of t. For $t > 0$, the set of points $(d^*(t), r^*(t))$ which minimize (3.13) defines the so-called central path of the IPM associated with problem (3.11). In IPMs, we compute a sequence of $(d^*(t), r^*(t))$ for increasing values of t using the previously computed central points [11]. The method is terminated when a stopping criterion is satisfied. In Appendix C.1, we show that as t increases the minimum of Φ_t converges to the optimal value of (3.11) and consequently to the optimum of (3.9). In the following section, we focus first on the solution of problem (3.13) for given t (inner loop of the method).

3.2.1 Inner Loop of the TNIPM

Search Direction using Precondition Conjugate Gradient

For given $t > 0$, we solve (3.13) following two steps. First we compute the search direction using the preconditioned conjugate gradient method (PCG). The search direction is defined as $\Delta p = [\Delta d^{\mathrm{T}}, \Delta r^{\mathrm{T}}]^{\mathrm{T}} \in \mathbb{R}^{(k+1)n}$ with $\Delta d \in \mathbb{R}^{kn}$, $\Delta r \in \mathbb{R}^n$ and T denoting the transpose. Then, we update the solution, given in column vector, $p = [d^{\mathrm{T}}, r^{\mathrm{T}}]^{\mathrm{T}} \in \mathbb{R}^{(k+1)n}$ using the backtracking line search [11].

In particular, we use the truncated Newton method [43] to estimate the search direction Δp as an approximate solution to Newton system

$$H_{\Phi_t}(p)\Delta p = -g_{\Phi_t}(p), \tag{3.14}$$

where $H_{\Phi_t}(p) = \nabla^2\Phi_t(d,r) \in \mathbb{R}^{(k+1)n\times(k+1)n}$ is the Hessian and $g_{\Phi_t}(p) = \nabla\Phi_t(d,r) \in \mathbb{R}^{(k+1)n}$ the gradient of Φ_t. The truncated Newton method employs the PCG solver with pre-conditioner $P_{\text{PCG}} \in \mathbb{R}^{(k+1)n\times(k+1)n}$ and adjustable tolerance ϵ_{PCG} to balance the trade off between the convergence rate and the computational effort. In other words, it estimates an approximate solution of (3.14) by truncating the number of iterations while keeping an acceptable convergence tolerance. In the current algorithmic implementation, the PCG terminates when the maximum number of iterations N_{max}^{PCG} is exceeded or the relative tolerance of the residual is less than ϵ_{PCG}. Details about the selection of ϵ_{PCG} are given in section 3.2.4.

We employ a pre-conditioner to accelerate the convergence. Even though the pre-conditioner requires an extra matrix-vector multiplication per iteration, it can accelerate the conjugate gradient method because the new transformed linear system $P_{\text{PCG}}^{-1}H_{\Phi_t}\Delta p = -P_{\text{PCG}}^{-1}g_{\Phi_t}(p)$ has more clustered eigenvalue distribution (i.e. lower condition number and more stable system) and thus the algorithm converges with fewer iterations [43].

The pre-conditioner we employ here is given by $P_{\text{PCG}} = 2t\,\text{diag}(K^{\text{T}}K) + \nabla^2\Phi_t(d,r)$ which is similar to the pre-conditioner proposed in [69]. The pre-conditioner improves the condition of the Hessian matrix H_{Φ_t}. For instance, in a test case we saw that the condition number of H_{Φ_t} was $k_H \approx 10^3$ and the preconditioned Hessian $P_{\text{PCG}}^{-1}H_{\Phi_t}$ had condition number $k_{PH} = 643$ at the 16^{th} outer loop iteration of the IPM (Alg. 3). Details about the PCG algorithm and the explicit formulae of the pre-conditioner and Hessian of (3.14) can be found in Appendix C.2.2.

Backtracking Line Search

We can make the truncated Newton method more robust by performing a line search along the estimated direction of the Newton step $\Delta p = [\Delta d^{\text{T}}, \Delta r^{\text{T}}]^{\text{T}}$. The new solution is $p := p + s\Delta p$ where $s \in \mathbb{R}^+$ is the step size estimated by the Backtracking line search [69].
In backtracking line search (BLS) $s = \beta^\rho$, where $\rho \geq 0$ is the smallest integer that satisfies

$$\Phi_t(p + \beta^\rho\Delta p) \leq \phi_t(p) + \alpha\beta^\rho\nabla\Phi_t(p)\Delta p \tag{3.15}$$

where $\alpha \in (0, 0.5)$ and $\beta \in (0, 1)$. The backtracking line search algorithm is the following:

Algorithm 2 Backtracking Line Search (BLS)-Estimate the step size s

Initialize: $\rho = 0$, $(\alpha, \beta) = (0.01, 0.5)$, $s = 1$.

Set: estimated search direction Δp and p (PCG results).

Repeat:

Check if condition (3.15) is satisfied. If Yes then **Quit**.

Else: update $p := p + s\Delta p$, $\rho := \rho + 1$, $s := \beta^\rho$.

3.2.2 Outer Loop Stopping Criterion: Duality Gap

The convex problem (3.9) is called the primal problem. For the estimation of a robust stopping criterion, we need to derive a Lagrange dual of the primal functional (3.9) [11]. The Lagrange dual function is always concave and yields lower bounds on the optimal value of the primal problem (3.9) which can be used as non-heuristic criterion for the termination of the algorithm [50, 11]. Here, we derive a Lagrange dual function of the primal problem (3.9). Subsequently, we use the difference between the values of functional (3.9) and its dual function as a stopping criterion. This difference is the so called duality gap. The algorithm terminates when the duality gap is less than a given tolerance.

In order to estimate the dual function, we elect to reformulate the problem (3.9) as an equality constrained problem. In particular, we introduce a new variable $z \in \mathbb{R}^m$ and the equality constraint $z = Kd - v$. The functional in (3.9) can be written with the equal expression

$$\begin{aligned} &\tilde{f}(d,z) = z^{\mathrm{T}} z + \alpha \sum_{i=1}^{n} w_i \|\mathrm{d}_i\|_2 \\ &\text{subject to } \; z = Kd - v \end{aligned} \tag{3.16}$$

where $\tilde{f} : \mathbb{R}^{kn} \times \mathbb{R}^m \to \mathbb{R}$.

Let us redefine the primal problem as

$$\begin{aligned} &p^* := \min_{d \in \mathbb{R}^{kn}} \min_{z \in \mathbb{R}^m} \tilde{f}(d,z) \\ &\text{subject to } z = Kd - v \end{aligned} \tag{3.17}$$

where p^* denotes the optimal value.

The Lagrangian of (3.17) is

$$L(d,z,\nu) = z^{\mathrm{T}} z + \alpha \sum_{i=1}^{n} w_i \|\mathrm{d}_i\|_2 + \nu^{\mathrm{T}}(Kd - v - z), \tag{3.18}$$

where $\nu \in \Re^m$ is the Lagrange multiplier.

If C is the feasible set of (3.17) i.e. $C = \{(d,z) \in \mathbb{R}^{kn} \times \mathbb{R}^m \; : \; z = Kd - v\}$ then by construction

$$\tilde{f}(d,z) = L(d,z,\nu) \quad \forall \; (d,z) \in C. \tag{3.19}$$

We obtain the Lagrange dual function $\tilde{g} : \mathbb{R}^m \to \mathbb{R}$ by minimizing the Lagrangian over $(d,z) \in \mathbb{R}^{kn} \times \mathbb{R}^m$

$$\tilde{g}(\nu) = \inf_{(d,z)} \left(z^{\mathrm{T}} z + \alpha \sum_{i=1}^{n} w_i \|\mathrm{d}_i\|_2 + \nu^{\mathrm{T}}(Kd - v - z) \right) \tag{3.20}$$

From (3.17) and (3.19) we have

$$p^* = \min_{(d,z) \in C} \tilde{f}(d,z) = \min_{(d,z) \in C} L(d,z,\nu) \geq \tilde{g}(\nu) \tag{3.21}$$

which shows that the dual function (3.20) yields lower bounds on the optimal values of problem (3.16) for feasible points (d, z). This bound has a practical meaning if we can make sure that the dual problem is feasible, i.e $\tilde{g}(\nu) > -\infty$ for some ν. We define as *dual* feasible points ν, the values of ν which ensure that $\tilde{g}(\nu) > -\infty$. If we can construct a *dual* feasible point then we can ensure a finite lower bound on the optimal value of (3.16) and thus an accurate stopping criterion for the TNIPM (Alg. 3). Next, we derive an explicit formula for the dual problem and subsequently we construct *dual* points ν, which give us finite bounds $\tilde{g}(\nu)$. Additionally, we shall see that the *dual* points are explicitly associated with the primal feasible points $(d, z) \in C$, hence when we have an estimate for the values of (d, z) then we can directly estimate the value of ν [11].

We re-write the Lagrange dual function (3.20) as

$$\tilde{g}(\nu) = \inf_{z} \left(z^{\mathrm{T}} z - \nu^{\mathrm{T}} z\right) + \inf_{d} \left(\alpha \sum_{i=1}^{n} w_i \|\mathrm{d}_i\|_2 + \nu^{\mathrm{T}} (Kd) \right) - \nu^{\mathrm{T}} v. \tag{3.22}$$

The first term of (3.22) can be denoted as $L(z) = z^{\mathrm{T}} z - \nu^{\mathrm{T}} z$ and it is quadratic with respect to z. Thus, it has minimum for $\frac{dL(z)}{dz} = 0 \Rightarrow z = 0.5\nu$.
By substituting $z = 0.5\nu$ in (3.22) we obtain

$$\tilde{g}(\nu) = \inf_{d} \left(\alpha \sum_{i=1}^{n} w_i \|\mathrm{d}_i\|_2 + \nu^{\mathrm{T}} (Kd) \right) - 0.25\nu^{\mathrm{T}}\nu - \nu^{\mathrm{T}} v. \tag{3.23}$$

Next, we find such a condition that

$$\min_{d} \left(\alpha \sum_{i=1}^{n} w_i \|\mathrm{d}_i\|_2 + \nu^{\mathrm{T}} (Kd) \right) > -\infty \tag{3.24}$$

We set $Kd = \sum_{i=1}^{n} \sum_{j=1}^{k} K^{(i+(j-1)n)} d_{i+(j-1)n}$ where $K^{(i+(j-1)n)} \in \mathbb{R}^{m \times 1}$ is the $(i + (j-1)n)^{th}$ column of the lead field matrix and the dipole strength term equals to $\|\mathrm{d}_i\|_2 = \sqrt{\sum_{j=1}^{k} d_{i+(j-1)n}^2}$. So, the left-hand side of (3.24) becomes

$$\min_{d} \left(\sum_{i=1}^{n} [\alpha\, w_i \sqrt{\sum_{j=1}^{k} d_{i+(j-1)n}^2} + \sum_{j=1}^{k} \nu^{\mathrm{T}} K^{(i+(j-1)n)} d_{i+(j-1)n}] \right). \tag{3.25}$$

Using the following linear transform

$$p_i = \sum_{j=1}^{k} \nu^{\mathrm{T}} K^{(i+(j-1)n)} d_{i+(j-1)n} \tag{3.26a}$$

$$q_i^{(ul)} = \nu^{\mathrm{T}} K^{(i+(u-1)n)} d_{i+(l-1)n} - \nu^{\mathrm{T}} K^{(i+(l-1)n)} d_{i+(u-1)n}, \tag{3.26b}$$

where $l = 1, \ldots, k-1$ and $l < u \leq k$, expression (3.25) is transformed into a form that enables

the estimation of the minimum[1]. Particularly, by applying the linear equations, (3.25) becomes

$$\min_{p,q}\left(\sum_{i=1}^{n}\alpha\, w_i\frac{\sqrt{p_i^2+\sum_{l<u}^{k} q_i^{2(ul)}}}{\sqrt{\sum_{j=1}^{k}(\nu^{\mathrm{T}}K^{(i+(j-1)n)})^2}}+p_i\right). \tag{3.27}$$

The minimum of (3.27) is finite iff

$$\frac{\alpha\, w_i}{\sqrt{\sum_{j=1}^{k}(\nu^{\mathrm{T}}K^{(i+(j-1)n)})^2}}>1 \ \text{ for all } \ i=1,\ldots,n \tag{3.28}$$

Therefore, the minimum of (3.24) is finite and equals zero when

$$\alpha>\left(\frac{\sqrt{\sum_{j=1}^{k}(\nu^{\mathrm{T}}K^{(i+(j-1)n)})^2}}{w_i}\right)_{i=1:n}. \tag{3.29}$$

The dual problem is defined as

$$\begin{aligned}&\text{maximize } \ \tilde{g}(\nu)=-0.25\nu^{\mathrm{T}}\nu-\nu^{\mathrm{T}}v\\&\text{subject to } \alpha>\left(\frac{\sqrt{\sum_{j=1}^{k}(\nu^{\mathrm{T}}K^{(i+(j-1)n)})^2}}{w_i}\right)_{i=1:n}.\end{aligned} \tag{3.30}$$

A *dual* feasible point ν needs to satisfy the constraints of (3.30). We construct the following *dual* point

$$\begin{aligned}&\nu=\lambda z\\&\text{where } \lambda=\min\left\{\alpha\frac{w_i}{\sqrt{\sum_{j=1}^{k}(z^{\mathrm{T}}K^{(i+(j-1)n)})^2}} \text{ for } i=1,\cdots,n\right\}\end{aligned} \tag{3.31}$$

and $z=2(Kd-v)$. Parameter λ ensures that the constraints of (3.30) are applied and therefore ν is a *dual* feasible point.

[1]Let assume that instead of (3.25), we have the simplified 2D equivalent expression $\sqrt{x^2+y^2}+ax+by$. Then, in this case (3.26a) becomes $p=ax+by$ and (3.26b) $q=bx-ay$ and the expression can be linearly transformed to $\sqrt{\frac{p^2+q^2}{a^2+b^2}}+p$. From the transformed equation, we can see that the minimum of the equation is finite and equal to 0 when $\frac{1}{\sqrt{a^2+b^2}}>1$ otherwise it is minus infinity.

We define the duality gap between (3.17) and (3.30) as

$$\eta = \|Kd - v\|_2^2 + \alpha \sum_{i=1}^{n} w_i \|\mathrm{d}_i\|_2 - \tilde{g}(\nu) \geq 0 \tag{3.32}$$

The duality gap η ensures that the estimated minimizer of (3.16) cannot be more than η-suboptimal (see appendix C.1 for further details). Also frequently, the relative duality gap defined as the fraction $\eta/\tilde{g}(\nu)$ is used and the algorithm terminates when $\eta/\tilde{g}(\nu) \leq \epsilon_{\text{tol}}$ where ϵ_{tol} is selected sufficiently small.

3.2.3 Optimality Condition

In Tikhonov regularization, the penalty parameter varies over $[0, +\infty)$, the solution converges to zero for $\alpha \to +\infty$ and the solution equals to $(K^{\mathrm{T}}K)^{\dagger}K^{\mathrm{T}}v$ when α is zero [40]. However, in problem (3.9), the range of the parameter α is different and it shows different limiting behaviour. In particular, for $\alpha \to 0$ the solution satisfies the minimum sum of the dipole strengths among all the possible solutions of $K^{\mathrm{T}}(Kd - v) = 0$, and the solution is $d = 0$ when α is greater than a finite upper limit [69].

In this section, we derive the upper bound of the parameter α for problem (3.9). This upper bound is also referred to as the optimality condition of the convex problem because it guarantees that the convex functional (3.9) has an optimal solution at zero for the values of α equal or greater than this upper bound [11].

In the following paragraphs, we show that the upper bound for the scaling parameter is

$$\alpha_{max} = \left\| \frac{\sqrt{\sum_{j=1}^{k} \left[2v^{\mathrm{T}} K^{(i+(j-1)n)}\right]^2}}{w_i} \right\|_{\infty}, \tag{3.33}$$

where $K^{(i+(j-1)n)}$ is a column of the lead field matrix $K \in \mathbb{R}^{m \times kn}$, v the observations and norm $\|\cdot\|_{\infty} = \max_i |\cdot|$, for $i = 1, \ldots, n$ [100].

For the derivation of (3.33), we use the first order optimality condition for convex functionals [11]. The functional in (3.9) is not differentiable at zero and thus we estimate the sub-differential[2] of (3.9).

The necessary and sufficient condition for optimality is that

$$0 \in \quad \nabla_d \left(\|Kd - v\|_2^2\right) + \alpha \partial_d \left(\sum_{i=1}^{n} w_i \sqrt{\sum_{j=1}^{k} d_{i+(j-1)n}^2} \right) \tag{3.34}$$

First we compute the sub-differential[3] $\partial_d \left(\sqrt{\sum_{j=1}^{k} d_{i+(j-1)n}^2} \right)$.

[2]Sub-differentials generalize the derivative to functions which are not differentiable everywhere in their domain of definition. The sub-differential of a function is set-valued. For the definition see appendix C.1.1.

[3]We estimate to sub-differential because the dipole strength $\|\mathrm{d}_i\|_2$ is not continuously differentiable (i.e at

The sub-differential with respect to the dipole component $d_{i+(l-1)n}$ for $l = 1, \ldots, k$ is

$$\frac{\partial \sqrt{d_{i+(l-1)n}^2 + \sum_{j \neq l} d_{i+(j-1)n}^2}}{\partial d_{i+(l-1)n}} = \begin{cases} U_i^{(l)} & d_{i+(l-1)n} > 0 \\ -U_i^{(l)} & d_{i+(l-1)n} < 0 \\ (-U_i^{(l)}, U_i^{(l)}) & \mathrm{d}_i = 0 \end{cases} \tag{3.35}$$

where $U_i^{(l)} = \frac{|d_{i+(l-1)n}|}{\sqrt{\sum_{j=1}^{k} d_{i+(j-1)n}^2}}$ and $(\cdot, \cdot)$ denotes the open interval.

From (3.35) and (3.34) the differential of $\nabla_d \left(\|Kd - b\|_2^2 \right)$ with respect to the dipole component $d_{i+(l-1)n}$ equals to

$$\left[2(K^{(i+(l-1)n)})^{\mathrm{T}} (Kd - v) \right]_i \in \begin{cases} \alpha\, w_i\, U_i^{(l)} & d_{i+(l-1)n} > 0 \\ -\alpha\, w_i\, U_i^{(l)} & d_{i+(l-1)n} < 0 \\ \alpha\, w_i (-U_i^{(l)}, U_i^{(l)}) & \mathrm{d}_i = 0 \end{cases} \tag{3.36}$$

where $K^{(i+(j-1)n)}$ is the $(i + (j-1)n)^{th}$ column of K.

From the previous equation we have that $d = 0$ iff

$$|2v^{\mathrm{T}} K^{(i+(l-1)n)}| \leq \alpha\, w_i\, U_i^{(l)} \tag{3.37}$$

for $l = 1, \ldots, k$ and $i = 1, \ldots, n$. The sum

$$\sum_{l=1}^{k} U_i^{(l)2} = \frac{1}{\sum_{j=1}^{k} d_{i+(j-1)n}^2} \sum_{l=1}^{k} |d_{i+(l-1)n}|^2 = 1. \tag{3.38}$$

So, term $U_i^{(l)}$ can be eliminated from the previous inequalities i.e

$$\sum_{l=1}^{k} \left[2v^{\mathrm{T}} K^{i+(l-1)n} \right]^2 \leq \alpha^2\, w_i^2 \sum_{l=1}^{k} U_i^{(l)2} = \alpha^2\, w_i^2. \tag{3.39}$$

Finally, we obtain

$$\frac{\sqrt{\sum_{l=1}^{k} \left[2v^{\mathrm{T}} K^{i+(l-1)n} \right]^2}}{w_i} \leq \alpha, \tag{3.40}$$

for $i = 1, \ldots, n$. Hence, for values of α equal or greater than the left hand side of the inequality (3.40) the solution of (3.9) is zero.

zero, the partial derivatives do not exist).

3.2.4 TNIPM Algorithm for Sparse Sources

In this section, we give an overview of the TNIPM algorithm for the solution of (3.9) We describe the details concerning about the initial values of (d, r), the updating rule t, the initial values of t and the stopping criteria. The TNIPM algorithm is described in Alg. 3. The algorithm consists of two loops, the outer and inner loop. In the inner loop, the value of $t > 0$ is constant and we estimate the solution $(d^*(t), r^*(t))$ of (3.13) using the PCG and line search. In the outer loop, the solution and the value of t are updated.

Algorithm 3 TNIPM for Sparse Source Reconstruction

Initialization: $d := 0$, $r := 1$, relative tolerance $\epsilon_{\text{tol}} = 10^{-4}$,
scaling parameter $\alpha < \alpha_{max}$ where α_{max} is defined in (3.33) and $t := \min\{1/\alpha, n/\eta\}$.
Stopping criteria for:
Outer loop: ϵ_{tol}
Inner (PCG) loop: Maximum number of iterations $N_{max}^{\text{PCG}} = 600$ or ϵ_{PCG} defined in (3.42)
Outer loop:

1. **Inner loop**

   a. PCG: Compute search direction $[\Delta d, \Delta r]$ by solving (3.14).

   b. BLS: Estimate the step size s using (Alg.2) where $(\alpha, \beta) = (0.01, 0.5)$

2. Update $[d, r] := [d, r] + s[\Delta d, \Delta r]$ and estimate $z := Kd - v$.

3. Estimate the *dual* feasible point ν (3.31) and the dual problem $\tilde{g}(\nu)$ (3.30) and the duality gap η (3.32).
   Quit if $\eta/\tilde{g}(\nu) \leq \epsilon_{\text{tol}}$

4. Update t (3.41)

t-Update Rule

The most frequently used updating rule is $t := \mu t$ where μ is a constant number greater than 1 [11]. However, the main drawback of this rule is that the value of μ influences the performance of the algorithm in such way that when μ is large the value of t changes rapidly which increases both the number of the PCG and line search iterations. On the other hand, for μ close to 1, we have a very slow convergence of the algorithm to the optimal value [11]. To balance the trade off between the PCG cost and overall convergence, the update rule can be designed in a more sophisticated way [72]. Better performance can be achieved if we keep t constant, until Φ_t (3.13) is nearly minimized, i.e. $\|\nabla\Phi_t\|_2 \simeq 0$ and then increase the value of t by a factor $\mu > 1$ ([72, 69]).

Therefore, we use the the following rule

$$t := \begin{cases} \max\{\mu \min\{n/\eta, t\}, t\}, & s \geq s_{\min} \\ t & s < s_{\min}, \end{cases} \tag{3.41}$$

where $s \in (0, 1]$ is the line search step and μ a constant between 2 and 50 [11]. In the current application we found good performance when $s_{\min} = 0.5$ and $\mu = 4$. Further explanation about the selection of the rule (3.41) can be found in appendix (C.2.4).

Initial Values

We select the starting value $d = 0$ which is close to the desired solution as we want most of the dipole sources to be equal to zero. The choice of $r = \mathbf{1}$ guarantees the constraints of (3.11) and that the logarithmic barrier (3.12) exists. The initial values do not affect the performance significantly, however they need to be selected in such a way that the constraints are satisfied.

The initial value of t is $t_0 = \min\{1/\alpha, n/\eta\}$ where α is the scaling parameter of (3.9), n the number of the dipoles and η the initial value of the duality gap (3.32) for $[d, r] = [0, 1]$. The value $1/\alpha$ is estimated by minimizing $\|1/t\nabla\Phi_t(0, 1)\|_2$ However, when α is selected to be very small, t_0 is very large and this results in an increase in the condition number of (3.14). For that reason, we select the initial value of $t_0 = \min\{1/\alpha, n/\eta\}$.

Stopping Criteria

The performance of the algorithm depends on the selection of the tolerance rate ϵ_{PCG} of PCG. Low precision may cause failure in convergence and a very low duality gap reduction at each iteration. On the other hand, demanding too fine precision makes the computation too slow and, in effect, eliminates the truncation rule. A good overall performance can be achieved with the adjustable tolerance [69],

$$\epsilon_{\text{PCG}} = \min\left\{0.1, \frac{0.5\eta}{\min\{1, \|g_{\Phi_t}\|_2\}}\right\}, \tag{3.42}$$

where η is the duality gap (3.32) and g_{Φ_t} is the gradient of (3.13) at the current iteration. Tolerance ϵ_{PCG} ensures that the precision is not worse than 10% at the early stages of the algorithm where η is large and gives more accurate solution as the duality gap decreases.

The algorithm terminates when the the fraction of the duality gap over the value of the dual functions falls below ϵ_{tol}. We selected $\epsilon_{\text{tol}} = 10^{-4}$ which gives a good precision.

Selection of Parameter α

The value of parameter α can change significantly the performance of Alg. 3 (see details in [69, 72]). The number of PCG iterations (step 1.a of Alg. 3) varies with α. When α is near α_{max} then the solution is strictly sparse i.e. only a very small number of dipoles are non-zero, the algorithm converges fast and only a small number of PCG iterations is required. When the scaling parameter is too low, the solution includes many non-zero amplitudes. In this case, PCG can work slower.

Intuitively we can understand this behavior of the PCG algorithm from Fig. 3.2. For large values of α, the PCG algorithm slides down directly to the minimum of the functional in (3.9)

which is shaped like paraboloid bowl. On the other hand, when α is small, the shape of functional is more flat, which results in rocking back and forth along the valley of the bowl before eventually settling at the lowest point. In addition, for low α, the conditioning of the problem (3.9) worsens as a result of the high condition number of the lead field matrix and the low influence of the penalty term. Ill-conditioning is inherited by the Hessian matrix (3.14). Consequently, for small values of α, the Hessian has a high condition number and a non-clustered eigenvalue spectrum which leads to a slower convergence of the PCG algorithm. The pre-conditioner can accelerate the converge of PCG, however for very low α this improvement is not significant [11]. In the current implementation we selected values in the range $[0.1\alpha_{max}, 0.001\alpha_{max}]$. This particular range seemed to work well for the reconstruction of single or few focal sources as will see later.

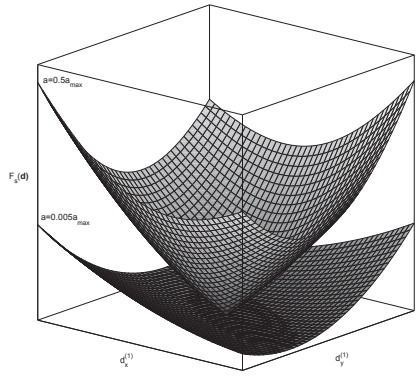

Figure 3.2: Shapes of $f(d)$ for large and small scaling parameter.

3.3 Weights for Depth Compensation

In this section, we define the weighting factors w_i of the penalty term in (3.9). The weights are important for the accurate localization of sources. In particular, in the absence of any prior, the solution of the under-determined system $Kd = v$ results in a dipole distribution with the lowest overall power and an exact fit to the measured observations, also referred to as minimum norm estimate (MNE). The MNE is prone to misplace deep sources close to the surface. This happens because less power is required for a superficial source distribution than for deep sources to give rise to the same surface potential values since the electric potentials fall quadratically with respect to the distance between the source and the sensors. Additionally, when we employ the $L_{1,2}$ norm and $w_i = 1$, the solution is focal but there is no restriction related to the depth of the source. Hence, for instance, instead of an actual deep source, the solver may result in several scattered superficial sources.

There are several authors who have suggested different weights in order to reduce the source misplacement. The first approach was to weight the dipole activity in the penalty term with the inverse of the Euclidean norm of the columns of the lead field matrix [73, 134, 168]. The reason

for this selection is because, by construction, the columns of the lead field matrix express the potential contribution of the dipole locations to the measured observation. Unfortunately, this approach did not seem to work very well.

In sLORETA [133], the depth compensation was treated by the post hoc normalization of the minimum norm solution $\hat{d}$. Specifically, the standardized power distribution was estimated as $\hat{d}_i^{\mathrm{T}}(R_{ii})^{-1}\hat{d}_i$ for $i = 1, \ldots, kn$ where R_{ii} were the diagonal elements of the resolution matrix defined as

$$R = K^{\mathrm{T}}(KK^{\mathrm{T}})^{\dagger}K, \tag{3.43}$$

where K is the lead field matrix and $\dagger$ is the Moore-Penrose pseudo-inverse [100]. From the probabilistic point of view, it can been shown that R coincides with the covariance of the maximum likelihood (ML) (or equivalently the MNE) estimate [133]. The diagonal elements of R are variances which correspond to each dipole component. We can see that the variances differ depending on the depth i.e. we have higher variances closer to the surface and very low variances deeper in the domain and thus the MNE estimate favours more intense superficial sources (Fig. 3.3). The standardization of the estimate with the variances reduces the depth biased effect. However, the sLORETA gives a power distribution and not dipole distribution and works well only for a single blurred source. In [42], it was suggested using the sLORETA variances, R_{ii}, in the penalty term. The source activity at locations with high variance were penalized with higher weighting factors than locations with low variance. However, it was not stated clear how or why these precise weights were selected.

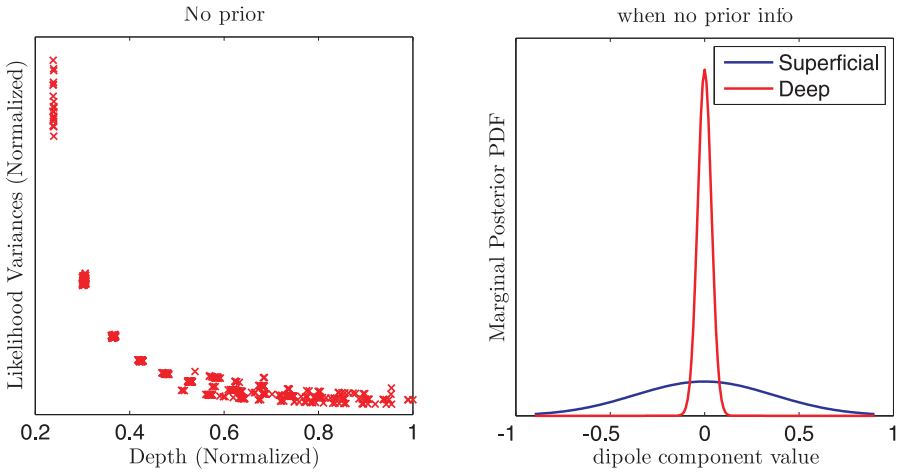

Figure 3.3: (Left image) The normalized variances of the dipole locations with respect to depth for the ML estimate (equivalent to MNE). (Right image) The marginal posterior density of a dipole which is located deep (in red) in the domain and the marginal posterior of a dipole of a superficial location (in blue). Without any prior information, the ML estimate favours superficial sources. This can be explained with the marginal distributions. More precisely, if the same measurements are produced by either a small superficial dipole or a large dipole deeper in the domain, then from the marginal distributions we can see that the probability of the small superficial source is much higher than the probability of the big deep source.

3.3.1 Weight Estimation using Bayesian Analysis

In the following text, we use Bayesian analysis to estimate the weights w_i in the penalty term (3.9). Our aim is to reduce the high variances in the superficial locations and to increase the variances in deeper locations, and therefore to reduce the tendency of the solver to give solutions mainly close to the boundaries. The problem is solved indirectly by estimating first the variances of the prior that is considered as Gaussian given the posterior variances. The posterior variances were selected to be equal to the inverse of the variances of the maximum likelihood (ML) estimate in order to allow the dipole strength to increase with respect to the depth. Subsequently, the estimated Gaussian prior variances are used to derive the weights of the $L_{1,2}$ prior model given by $\pi(d) \propto \exp\left(-\alpha \sum_{i=1}^{n} w_i \|\mathrm{d}_i\|_2\right)$.

Selection of Posterior Variances

Let us assume that the EEG observation model is

$$v = Kd + \xi, \quad \xi \sim \mathcal{N}(0, \Gamma_\xi) \tag{3.44}$$

where $K \in \mathbb{R}^{m \times kn}$, $d \in \mathbb{R}^{kn}$ and $\xi \in \mathbb{R}^m$ is the additive measurement noise with covariance $\Gamma_\xi = \gamma_\xi I^{m \times m}$ (where $I^{m \times m}$ is the identity matrix).

The posterior of the dipole distribution d is

$$\pi(d|v) \propto \pi(v|d)\pi(d) \tag{3.45}$$

where

$$\pi(v|d) \propto \exp\left(-\frac{1}{2}(Kd - v)^{\mathrm{T}} \Gamma_\xi^{-1} (Kd - v)\right) \tag{3.46}$$

is the likelihood density and $\pi(d)$ the prior.

We begin our analysis with the case where we do not have any prior information. This case coincides with the MNE and, in probabilistic terms, is the ML estimate. The solution in this case is given by

$$\hat{d}_{\mathrm{ML}} = K^{\mathrm{T}}(KK^{\mathrm{T}})^{-1} v. \tag{3.47}$$

From (3.45) and (3.46) the corresponding covariance matrix is

$$\Gamma_{\mathrm{ML}} = (K^{\mathrm{T}} \Gamma_\xi^{-1} K)^{\dagger} \tag{3.48}$$

By construction ML favors shallow sources even though the same observed measurements can be explained by strong dipoles deeper in the domain. Intuitively, we can understand this by observing the variances of the dipole locations with respect to depth in Fig. 3.3. A deep source has a very low variance compared to a superficial source. However, a deep source must be much more intense than a superficial to give rise to the same measurements, as the strength of the dipole is reduced quadratically with the distance. This means that the low variance restricts

the power range of a deep source making a deep source very unlikely.

We can compensate this if the variances of the posterior are selected in such a way that they allow the dipole strength to increase quadratically with respect to the depth. There are different ways to achieve this. One of these is to choose the inverse of the ML variances as the posterior variances (see Fig. 3.4). This choice takes into account apart from the depth, the conductivities and all the properties that are included in the lead field matrix. For the estimation of the ML

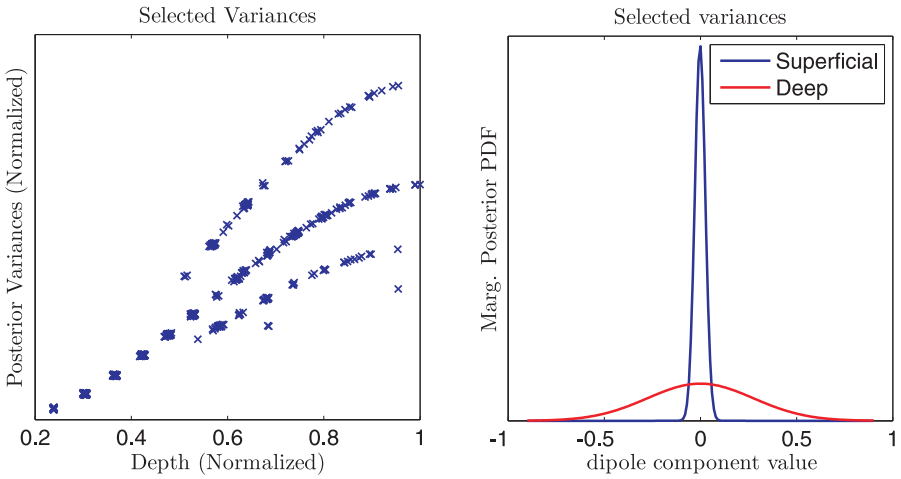

Figure 3.4: (Left image) The selected variances (normalized) for each dipole location with respect to depth. The selected variances are the inverse variances of the ML estimate. (Right image) Marginal posterior densities for a dipole component in a deep and superficial location considering Gaussian approximation. Our aim is to reduce the depth bias. This can be achieved if the probability of a source distribution with maxima deeper in the domain to be as equal as possible to the source distribution with maxima in superficial layers for given measurements. Accordingly, the type of the prior model e.g. sparce/focal or blurred property can define which distribution will be selected.

variances, $\mathrm{diag}(\Gamma_{\mathrm{ML}}) = \gamma_{\mathrm{ML}}^{(i)}$, we select to run simulations (Alg. 4) that require the solution of a smaller linear system instead of estimating (3.48 which requires the inversion of a large ill-conditioned matrix.

Algorithm 4 Estimate Variances of the ML estimate

Repeat $l = 1 : N_s$ **times**:

1. Draw dipole sample $d^{(l)} \sim \mathcal{N}(0, \alpha I^{kn \times kn})$ and noise sample $\xi^{(l)} \sim \mathcal{N}(0, \gamma_\xi I^{m \times m})$
2. Estimate: $v^{(l)} = K d^{(l)} + \xi^{(l)}$
3. Solve: $\hat{d}^{(l)} = K^{\mathrm{T}}(KK^{\mathrm{T}})^{-1} v^{(l)}$

Estimate covariance matrix: $\Gamma_{\mathrm{ML}} = \frac{1}{N_s - 1} \sum_{l=1}^{N_s} (d^{(l)} - d_*)(d^{(l)} - d_*)^{\mathrm{T}}$ where $d_* = \frac{\sum_{l=1}^{N_s} d^{(l)}}{N_s}$.

Estimation of the Depth Weights

The depth weights of the $L_{1,2}$ norm are derived based on the posterior variances derived in the previous section. For the estimation of the weights (variances) of the prior model, an analytical equation which relates the weights (variances) of the prior model with the posterior variances is usually required. However, in the case of the $L_{1,2}$ norm prior, the posterior covariance matrix cannot be written in a closed form (expression). In this case the problem can be solved indirectly. First, we consider a Gaussian prior that gives us an analytical expression for the posterior covariance matrix that includes the prior parameters. In practice, considering Gaussian distributions, the posterior and prior variances lead to a set of non-linear equations. Therefore, the Gaussian prior variances can be estimated based on the posterior variances. Finally, the Gaussian prior variances are used to estimate the weights of the $L_{1,2}$ norm prior model.

We assume that the prior in (3.45) is Gaussian $\pi(d) \propto \exp\left(-\frac{1}{2}d^{\mathrm{T}}\Gamma_d^{-1}d\right)$ with zero mean and Γ_d covariance matrix. The covariance matrix has non-zero entries only on the diagonal i.e. $\Gamma_d = \alpha^{-2}\mathrm{diag}(\gamma_d^{(i)})$ for $i = 1, \ldots, kn$ where α is a scaling factor. The posterior density (3.45) becomes

$$\pi(d|v) \propto \exp\left(-\frac{1}{2}(Kd - v)^{\mathrm{T}}\Gamma_\xi^{-1}(Kd - v)\right)\exp\left(-\frac{1}{2}d^{\mathrm{T}}\Gamma_d^{-1}d\right). \tag{3.49}$$

By multiplying the exponential terms of the likelihood and prior and completing squares we obtain

$$\pi(d|v) \propto \exp\left(-\frac{1}{2}(d - d_{*|v})^{\mathrm{T}}\Gamma_{d|v}^{-1}(d - d_{*|v})^{\mathrm{T}}\right), \tag{3.50}$$

where the posterior mean $d_{*|v}$ and covariance $\Gamma_{d|v}$ are

$$\begin{aligned} d_{*|v} &= (K^{\mathrm{T}}\Gamma_\xi^{-1}K + \Gamma_d^{-1})^{-1}K^{\mathrm{T}}\Gamma_\xi^{-1}v \\ \Gamma_{d|v} &= (K^{\mathrm{T}}\Gamma_\xi^{-1}K + \Gamma_d^{-1})^{-1}. \end{aligned} \tag{3.51}$$

The posterior variances depend on the lead field matrix K, the covariance matrix Γ_ξ and the prior variances $\gamma_d^{(i)}$.

The diagonal entries of the posterior covariance (3.51) were selected to be equal to the inverse of the diagonal entries of the estimated ML covariance, i.e.

$$\mathrm{diag}((K^{\mathrm{T}}\Gamma_\xi^{-1}K + \Gamma_d^{-1})^{-1}) = \mathrm{diag}(\gamma_{\mathrm{ML}}^{(i)})^{-1}. \tag{3.52}$$

The prior variances $\gamma_d^{(i)}$ are estimated solving the system (3.52). By employing the matrix inversion lemma [100] the covariance matrix $\Gamma_{d|v}$ can be rewritten as

$$(K^{\mathrm{T}}\Gamma_\xi^{-1}K + \Gamma_d^{-1})^{-1} = \Gamma_d - \Gamma_d K^{\mathrm{T}}(\Gamma_\xi + K\Gamma_d^{-1}K^{\mathrm{T}})^{-1}K\Gamma_d. \tag{3.53}$$

From (3.52) and (3.53)

$$\mathrm{diag}(\Gamma_d - \Gamma_d K^{\mathrm{T}}(\Gamma_\xi + K\Gamma_d^{-1}K^{\mathrm{T}})^{-1}K\Gamma_d) = \mathrm{diag}(\gamma_{\mathrm{ML}}^{(i)})^{-1}. \tag{3.54}$$

So, from (3.54) a set of non linear equations for $i = 1, \ldots, kn$ can be obtained, given by

$$\frac{\alpha^2}{\gamma_{\mathrm{ML}}^{(i)}} = \gamma_d^{(i)} - \gamma_d^{2(i)} K^{(i)\mathrm{T}} M K^{(i)} \tag{3.55}$$

where $M = \alpha^{-2}(\Gamma_\xi + K\Gamma_d K^{\mathrm{T}})^{-1}$ and $K^{(i)}$ is the i^{th} column of K.
The variances $\gamma_d^{(i)}$ are estimated by minimizing

$$G(\gamma_d) = \frac{1}{2}\sum_{i=1}^{kn}(rs^{(i)})^2 \tag{3.56}$$

where $rs^{(i)} = \frac{\alpha^2}{\gamma_{\mathrm{ML}}^{(i)}} - \gamma_d^{(i)} + \gamma_d^{2(i)} K^{(i)T} M K^{(i)}$. We estimated $\gamma_d^{(i)}$ using Levenberg-Marquardt (LMA) algorithm (see Alg.6 in appendix C.3). The next step is the estimation of the weights in

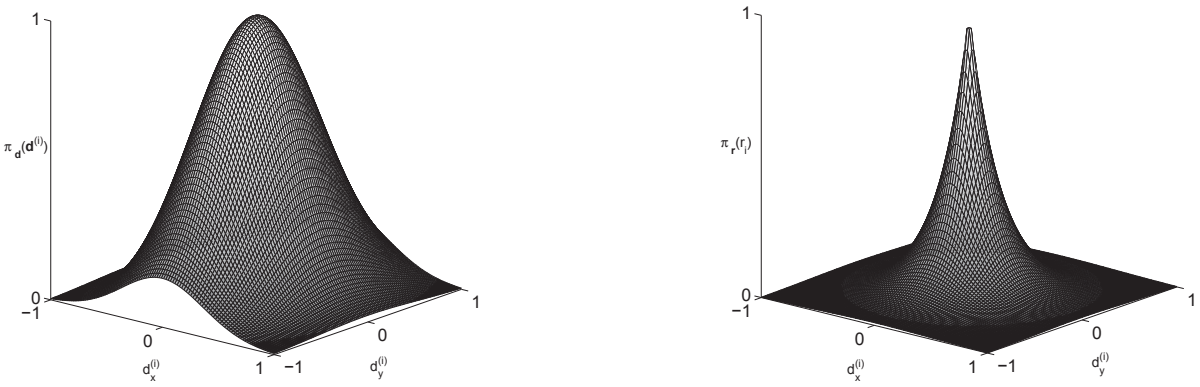

(a) (b)

Figure 3.5: (a) 2D Gaussian prior, (b) $L_{1,2}$ norm prior .

the $L_{1,2}$ norm prior. The $L_{1,2}$ norm prior is given by

$$\pi(d) \propto \exp\left(-\alpha \sum_{i=1}^{n} w_i \|\mathrm{d}_i\|_2\right). \tag{3.57}$$

We can set $\|\mathrm{d}_i\|_2 = r_i$ and the prior for the dipole strength at location i using r_i can be written as

$$\pi(r_i) \propto \exp\left(-\alpha w_i r_i\right). \tag{3.58}$$

We approximate the standard deviation $\sqrt{\gamma_{r_i}}$ of the prior $\pi(r_i)$ at location i with the corresponding Gaussian prior standard deviations of the dipole components $\sqrt{\gamma_d^{(i+(j-1)n)}}$ at the same

location according to

$$\gamma_{r_i} = 2\alpha^{-2} \frac{\prod_{j=1}^{k} \gamma_d^{(i+(j-1)n)}}{\sum_{j=1}^{k} \gamma_d^{(i+(j-1)n)}}, \tag{3.59}$$

where $j = 1, \ldots, k$. In Fig 3.5, we see the Gaussian and the corresponding $L_{1,2}$ prior densities at location i when the relationship (3.59) holds.

The variances of the prior $\pi(r_i)$ at location i is

$$\begin{aligned} \gamma_{r_i} &= c \int_0^\infty (r_i - r_{*i})^2 \exp\left(-\alpha w_i r_i\right) \, dr_i \\ &= 2c\frac{1}{\alpha^3 w_i^3} - 2c\frac{r_{*i}}{\alpha^2 w_i^2} + c\frac{r_{*i}^2}{\alpha w_i} = \frac{1}{\alpha^2 w_i^2} \end{aligned} \tag{3.60}$$

where $r_{*i} = c\int_0^\infty r_i \exp\left(-\alpha w_i r_i\right) \, dr_i = \frac{c}{\alpha^2 w_i^2}$ and from $\int_0^\infty c \exp\left(-w_i r_i\right) \, dr_i = 1 \Rightarrow c = \alpha w_i$.

From (3.60) and (3.59) the weights are

$$w_i = \sqrt{\frac{\sum_{j=1}^{k} \gamma_d^{(i+(j-1)n)}}{2\prod_{j=1}^{k} \gamma_d^{(i+(j-1)n)}}} \tag{3.61}$$

The estimated variances and the corresponding weights of the $L_{1,2}$ prior with respect to the depth are shown in Fig. 3.6. The estimated weights force the sparse source solver to be less

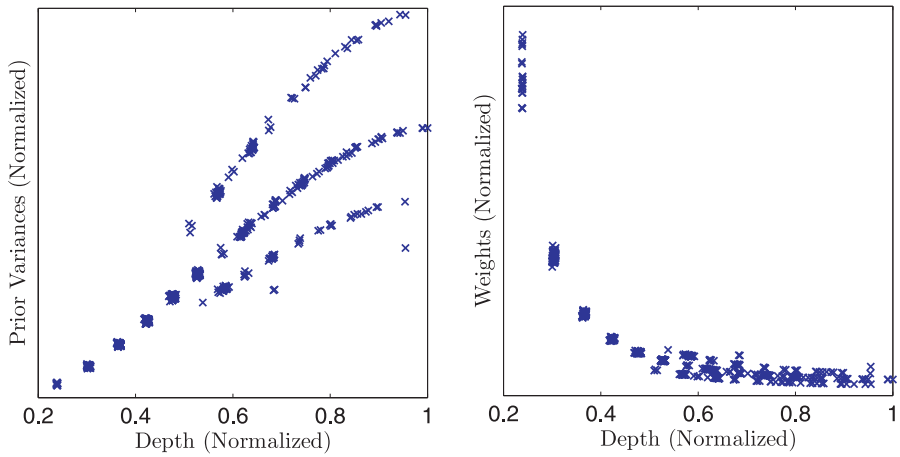

Figure 3.6: Variances of candidate source locations and the corresponding weights with respect to depth for the $L_{1,2}$ norm prior.

prone to favor superficial sources. In particular, with these weights the variances are higher for deep source locations and lower for shallow locations. In this analysis, there was only one weight factor for every candidate source location and the suggested approach works well when the estimated variances of the dipole components at a location i are in the same range. It would

be worth studying whether the use of different weights for x- and y- components improve the result.

3.4 Results and Discussion

3.4.1 Comparisons and Evaluation

In this section we describe the set up of the simulations that evaluate the efficiency of the TNIPM algorithm with $L_{1,2}$ norm penalty to recover focal sources. We compare the obtained results with the solutions of the quadratic loss function $\|Kd - v\|_2$ augmented with the L_2 and L_1 norm priors respectively.

The potential measurements v were obtained from 32 point sensors equally spaced around the boundary of a $2D$ domain

$$v = \bar{K}\bar{d} \tag{3.62}$$

where lead field matrix $\bar{K} \in \mathbb{R}^{m\times 2\bar{n}}$ and $\bar{d} \in \mathbb{R}^{2\bar{n}}$ is the simulated dipole vector with only few non-zero peaks. For the forward and the inverse model we use meshes with different number of nodes, i.e. the forward mesh is finer than the inverse one in order to decrease the dimensionality of the inverse problem and to avoid inverse crimes[4].

Then, we compare the solution from the following three functionals for given v. First, we estimate the solution given by the minimization of the so called L_2 norm model, i.e.

$$\hat{d}_{L_2} := \min_d \|(v - Kd)\|_2^2 + \alpha_{L_2} \sum_{i=1}^{n_0} w_i^2 \|\mathrm{d}_i\|_2^2, \tag{3.63}$$

where $K \in \mathbb{R}^{m\times 2n_0}$ with $n_0 < \bar{n}$ and $d = P\bar{d} \in \mathbb{R}^{2n_0}$ where P is the projection operator from the fine forward mesh to the inverse mesh. The penalty term is $\|\mathrm{d}_i\|_2^2 = \sum_{j=0}^{1} d_{i+jn_0}^2$.

Next, we compute the solution of the L_1 model

$$\hat{d}_{L_1} := \min_d \|(v - Kd)\|_2^2 + \alpha_{L_1} \sum_{i=1}^{N_0} w_i \|\mathrm{d}_i\|_1, \tag{3.64}$$

where $\|\mathrm{d}_i\|_1 = \sum_{j=0}^{1} |d_{i+jn_0}|$.

The solution of the $L_{1,2}$ model is given by

$$\hat{d}_{L_{1,2}} := \min_d \|(v - Kd)\|_2^2 + \alpha_{L_{1,2}} \sum_{i=1}^{n_0} w_i \|\mathrm{d}_i\|_2, \tag{3.65}$$

where $\|\mathrm{d}_i\|_2 = \sqrt{\sum_{j=0}^{1} d_{i+jn_0}^2}$.

[4]The term "inverse crimes" is used in [66] and it is referred to the numerical method contain features that "effectively" lead to a "less ill-posed" inverse problem than it actually is and consequently yielding optimistic results. In practice, an "inverse crime" is committed in cases where the discretization and lead field matrix of the forward model are the same as the ones used in the inverse problem.

For the solution of the L_2 and L_1 models we used the CVX toolbox [52]. The solution of the $L_{1,2}$ model is estimated using the TNIPM (Alg. 3). The weights w_i were the same for the three models and estimated as was described in section 3.3. The scaling parameter α_{L_1} in (3.64) is was equal to $\alpha_{L_1} = c\alpha_{max_{L_1}}$ where $\alpha_{max_{L_1}} = \max_i \left\{ \frac{(2K^{\mathrm{T}}v)_i}{w_i} \right\}$ for $i = 1, \ldots, 2n_0$ [69]. The scaling parameter in (3.65) is $\alpha_{L_{1,2}} = c\alpha_{max_{L_{1,2}}}$ and it is lower than the bound (3.33). For the 2D case, we can rewrite the upper bound (3.33) as

$$\alpha_{max_{L_{1,2}}} = \max \left\{ \frac{\left[\sqrt{(2K_x^{\mathrm{T}}v)^2 + (2K_y^{\mathrm{T}}v)^2} \right]_i}{w_i} \quad \text{for } i = 1, \ldots, n_0 \right\} \tag{3.66}$$

where $(K_x, K_y) = K$ and index i denotes the i^{th} element of the vector $(\cdot)$. The constant c is selected to be in the interval $[0.01, 0.001]$. The scaling parameter α_{L_2} of the L_2 model was selected after visual inspection. We noticed that the L_2 models gives the best possible results when parameter α_{L_2} is close to the value of $\alpha_{L_{1,2}}$.

For the evaluation of the results we employ the earth mover's distance (EMD) metric [145]. The EMD can be used as a measure of disagreement between the simulated and the estimated dipole distribution when there are only few non-zero values. Also, it can be used when the actual distribution has only few non-zero values but the inverse solution is highly dispersed. Thus, the EMD is a good metric both for the L_1 and $L_{1,2}$ models (sparsity constraints) as well as the L_2 model which recovers more blurred sources. The EMD is defined in detail in section 5.3.5.

3.4.2 Circular model

In this section we show the results for one, two, three focal source reconstructions and a case with ten focal sources. We use the three layer circle model both for the forward and inverse model with lead field matrices having conductivity values equal to 0.33/0.015/0.33 (S/m) for the scalp/skull/brain respectively. In these simulations there was no additive noise.

In the following figures, the small images on the left hand side show the test case with the actual dipole distribution. The location of the simulated dipole is marked with a blue circle and the orientation with a small blue line. The remaining images, starting from left, show the reconstruction solution using L_2 prior model (3.63), L_1 model (3.64) solved using CVX toolbox [52] and $L_{1,2}$ prior model by employing the TNIPM (Alg. 3). The blue marker x shows the locations of actual focal sources.

For the test cases, the scaling parameters were $\alpha_{L_1} = 0.005\alpha_{maxL_1}$, $\alpha_{L_{1,2}} = 0.005\alpha_{maxL_{1,2}}$ and $\alpha_{L_2} = 1.2\alpha_{L_{1,2}}$. In the multiple source cases, the dipoles have equal strengths and randomly chosen orientation.

By comparing the reconstruction results in Fig. 3.7 and the corresponding EMD values we can see that the $L_{1,2}$ norm model works the best. The solver with the L_2 norm penalty gives a blurred source distribution as was expected and the L_1 norm mode yields a sparse solution but the result is more scattered compared to the $L_{1,2}$ norm based prior model. This is mainly

because L_1 norm forces sparsity on the individual components of the dipole. A multiple source

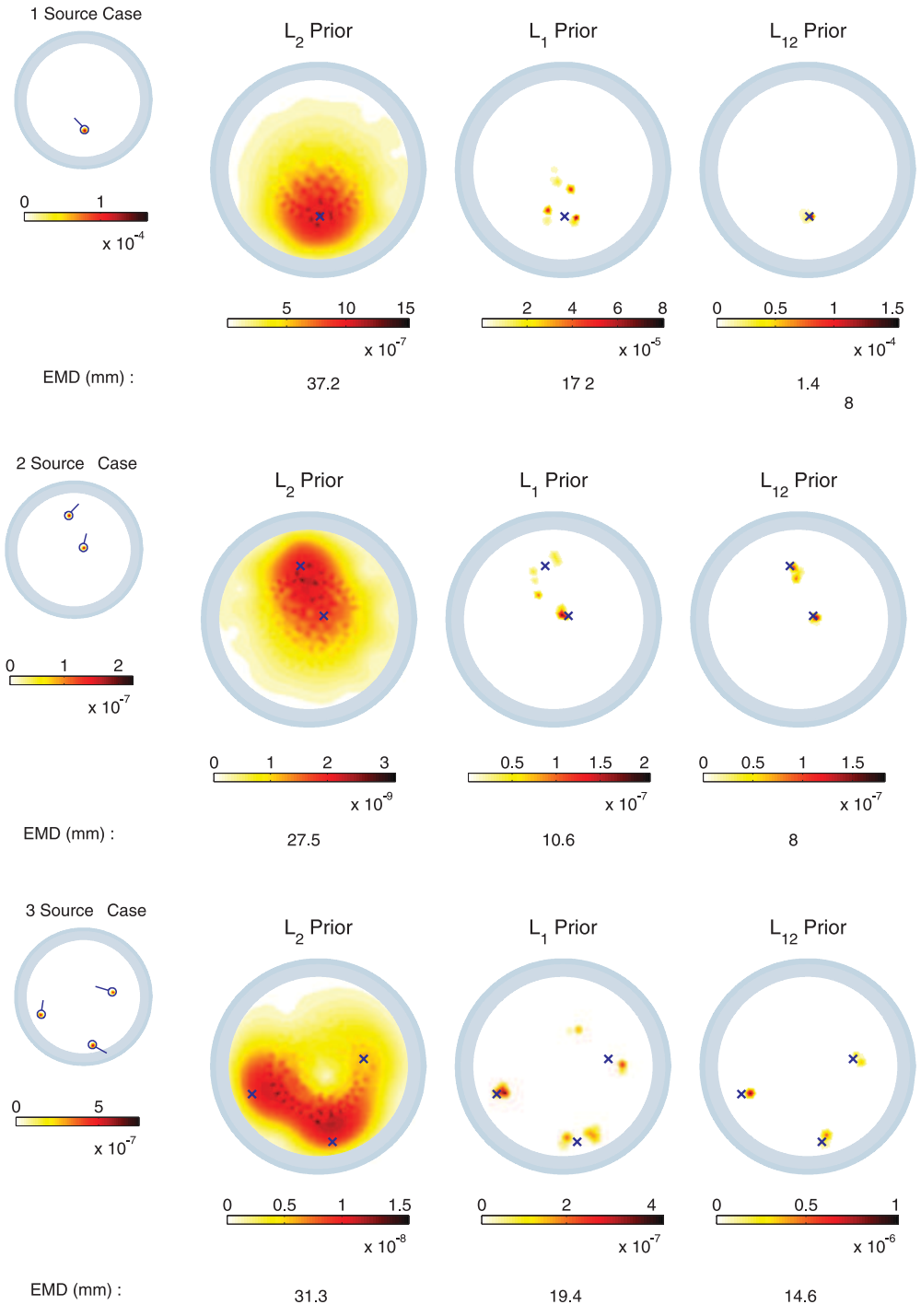

Figure 3.7: Reconstruction of source distribution using 32 electrodes around the circular domain. The rightmost images present the actual source configurations (one, two and three source cases) and the rest of the images, the reconstructions based on different penalty terms.

case may fall in a different brain activity category e.g. generalized epilepsy. However, a test case with multiple dipole source is presented here to show the feasibility and the limitations of the reconstruction algorithms for more scattered focal sources. In this case all the models face difficulties to recover the source distribution (Fig. 3.8). The EMD indicates that there are no gross differences between the solutions but it seems that the $L_{1,2}$ prior gives slightly better results than the other two prior models.

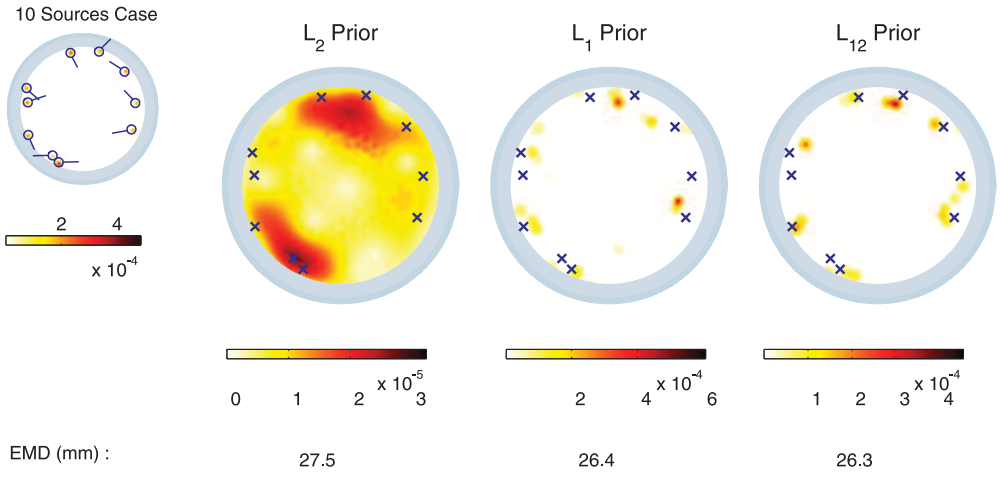

Figure 3.8: Reconstruction of ten focal points. This test does not correspond to a sparse source case and thus the reconstruction results using the $L_{1,2}$ norm penalty deteriorates.

3.4.3 MRI cross section model

In this section, we illustrate the reconstruction results when the lead field matrix is constructed considering the five layer model with conductivities equal to 0.33 and 0.015 (S/m) for scalp and skull, respectively, and 1.76/0.016/0.33 for the cerebral spinal fluid (CSF), grey matter (GM) and white matter (WM). The results show that the $L_{1,2}$ norm model gives the least scattered results and it works the best for single focal sparse sources (Fig. 3.9). For the two source case, the L_1 and $L_{1,2}$ norm results are similar (i.e. equal EMD values) and the L_2 norm result is blurred.

Also, we can see that the results for two and three sources are slightly scattered when the 5 layer MRI model is used. This is possibly related to the discontinuity of the conductivity values within the brain in the 5 layer model. Also, the different discretization (between the forward and inverse MRI mesh) close to the boundaries can cause some numerical errors. However, it is worth noting that the localization of the brain activity is accurate which implies that the applied weights reduce the source localization error (the depth bias).

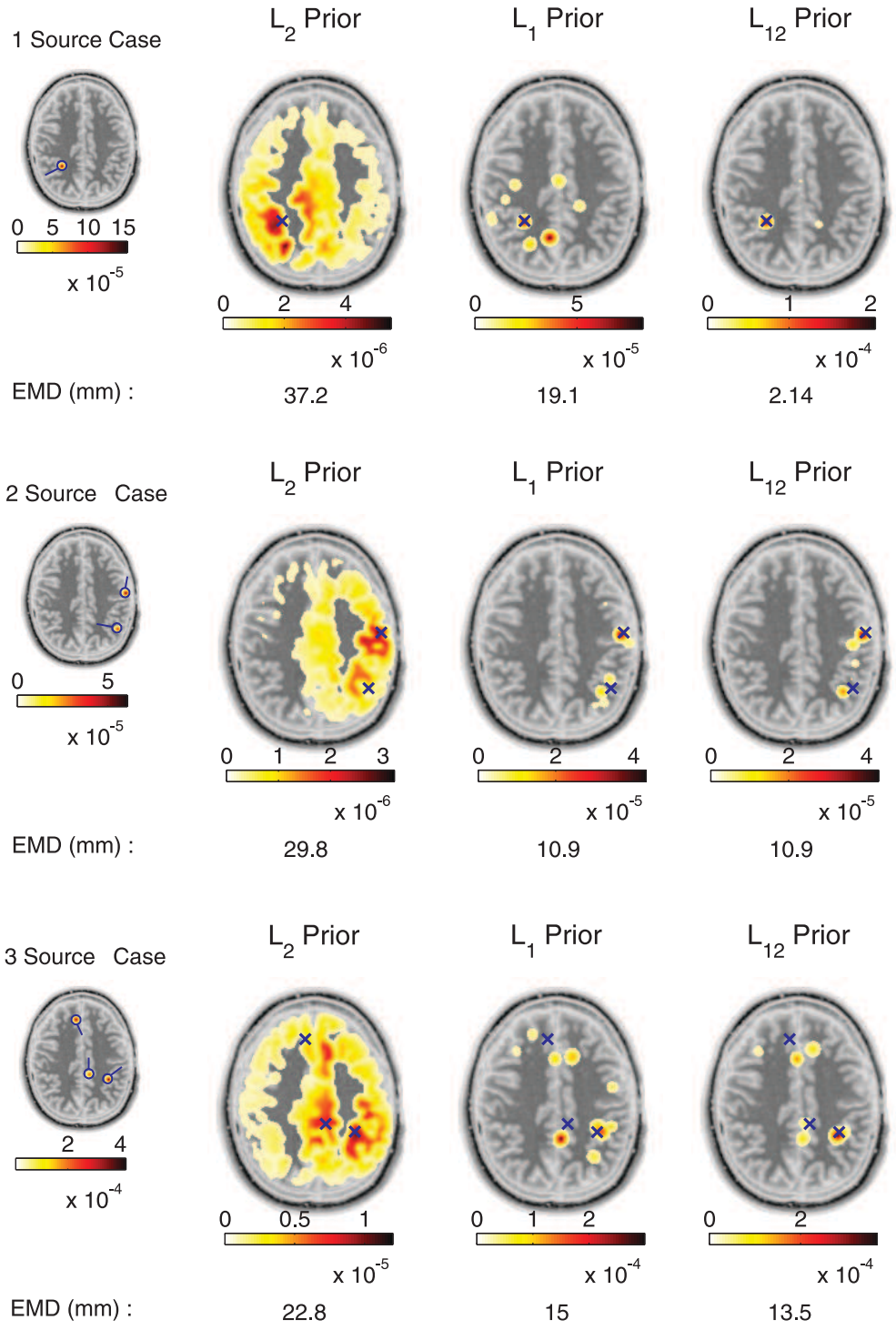

Figure 3.9: Reconstruction of source distributions using different prior models. The right most images show the actual source configuration and the reconstruction results (starting from left to right) using the solvers: (3.63), (3.64) and (3.65) respectively.

Finally, a 3D case of a single dipole source was studied and preliminary results are shown in Fig. 3.10. In this figure the blue cone denotes the actual dipole source and the red cones show

the reconstructed dipole distributions. According to these results, we can say that the weighted $L_{1,2}$ norm based prior performs better that the other two models as it achieves to reconstruct a sparse and focal source even though the recovered source is slightly in the wrong location. The L_2 norm model reconstructs a blurred source while the L_1 norm model recovers a scattered dipole distribution.

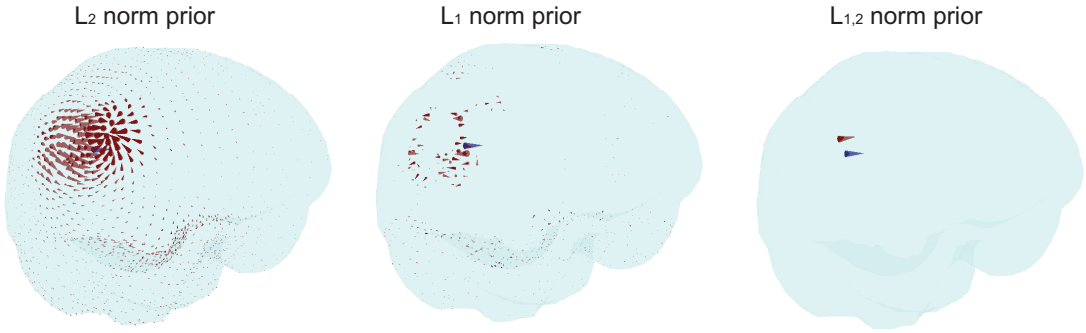

Figure 3.10: Reconstruction results of a single focal source using different prior models in a 3D domain. The blue cone denotes the actual dipole source and the red one, the reconstructed source distribution.

3.5 Summary

In this chapter we developed a solver that uses the TNIPM for the reconstruction of focal sources in the inverse EEG problem. We analyzed the algorithmic details and derived all the essential formulae for the design of a software directly applicable to the sparse-focal EEG problem.

Moreover, we employed a Bayesian analysis to derive the weights in the prior that reduce the tendency of the solver to favor superficial sources.

Finally, we verified the ability of the solver to recover sparse sources by performing simulations and we compared the results of different prior models. The reconstructions indicated that the best localization results were obtained especially for single focal source cases with the weighted $L_{1,2}$ prior. We can point out here that the TNIPM can be used also for larger scale problems. For the interested readers the computational advantage of TNIPM method compared to other relevant methods can be found in [69].

Chapter 4

Electric Field Imaging using Vector Field Tomography

Vector field tomography (VFT) concerns the reconstruction of a vector field in a bounded domain by using integral data over projections of this vector field [155, 161]. In this chapter, we introduce an approach in which VFT is used in EEG source imaging. In particular, we propose recovering the electric field evoked by bio-electric activity of the brain with a finite set of line integrals. The proposed modeling obeys the same physical principles as the EEG source imaging problem i.e. (i) the quasi-static approximation and (ii) the field is the negative gradient of the scalar potential [95]. In the literature, this kind of field is called irrotational [103].

In the proposed approach, the line integrals along lines which "trace" the brain are approximated linearly and result in a linear system of equations. The recovery of vector fields using VFT is an ill posed and shares the same features as many other inverse problems [78, 71]. Therefore, prior information and boundary constraints are required for a good solution. The final minimization problem is solved using convex optimization techniques [11]. In the presented test cases, the field was reconstructed using simulated data. The simulations presented in this chapter suggest that the VFT solution can give information comparable to a solution of the dipole source reconstructions (problem) and the active area of the brain can be localized based on the estimated field. It is worth noting that the electric field reconstruction requires neither an estimate of the lead field matrix nor any knowledge of the underlying source model.

The chapter is organized as follows. In section 4.1, we give a brief overview of the mathematical foundation of VFT. Section 4.2 reviews the theoretical approaches for the recovery of 2D and 3D vector fields in boundless domains using different types of Radon integral data. Subsequently in section 4.3, we present the reconstruction of a continuous 2D field in a bounded domain using line integrals. Details about the approximation of the line integrals and the numerical formulation of the proposed approach are described in section 4.4. In sections 4.6 and 4.7, we evaluate the use of the line integrals in the recovery of different types of fields beginning first with simple irrotational vector fields that also have analytical expressions, and we conclude with electric fields produced by focal sources in a bounded domain. To best of our knowledge,

VFT has not previously been used in cases in which internal sources are present for example in electric field imaging using EEG data.

4.1 Introduction to VFT problem

The reconstruction of a scalar function from its line integrals in a bounded domain is a well known problem. Today there are many practical applications in different fields such as in biomedicine (e.g. MRI, CT), acoustic and seismic tomography which employ this method with great success and accuracy [111]. However, there are other applications, such as the blood flow tracking in vessels and the diffusion tensor MRI problem, in which we are interested in the estimation and visualization of a vector field. In these cases, tomographic vector methods can be used to reconstruct these fields from integrals in a similar way as in the scalar tomographic methods [24, 161].

Let's denote a computational domain $\Omega \subset \mathbb{R}^k$ and a position vector $\mathrm{x} \in \Omega$. For a general vector $\mathrm{f(x)} : \Omega \to \mathbb{R}^k$, the vector field tomographic problem is defined as the reconstruction of the field from integral data over projections of the field in different directions (e.g. orthogonal, tangential with respect to the line of integration).

The general form of the problem is given by a line integral (along a line L) that "traces" the domain Ω, i.e.

$$I_L(\mathrm{f}) = \int_L \mathrm{f(x)} \cdot \hat{\mathrm{s}}_L \; d\ell(\mathrm{x}), \tag{4.1}$$

where $\hat{\mathrm{s}}_L$ is the unit vector in a predefined direction and $d\ell(\mathrm{x})$ is a "vanishingly" small segment of the line.

The integrals used most in VFT approaches are the longitudinal line integral given by

$$I_L^{\parallel} = \int_L \mathrm{f(x)} \cdot \hat{\mathrm{s}} \; d\ell(\mathrm{x}), \tag{4.2}$$

where $\hat{\mathrm{s}}$ is the unit vector in the direction of line L and the transverse line integral

$$I_L^{\perp} = \int_L \mathrm{f(x)} \cdot \hat{\mathrm{s}}_{\perp} \;\; d\ell(\mathrm{x}), \tag{4.3}$$

where $\hat{\mathrm{s}}_{\perp}$ is the unit vector orthogonal to the line.

The line integral data (4.2) over projections of the field in the direction of the line is the so-called longitudinal ray transform and the transverse line integral (4.3) is also referred to as transverse ray transform [155]. The longitudinal transform is closely related to the Radon transform and coincides with it in two dimensions ($k = 2$). However, in higher dimensions ($k = 3$), the Radon transform is defined as the integral data over projections of the field along hyper-planes instead of lines [47].

As we shall see in the next section, the VFT methods focus usually on the reconstruction of different types of fields depending on the physical properties of the problem. Here, we give brief definitions of these fields. If field $\mathrm{f(x)}$ satisfies the condition $\nabla \cdot \mathrm{f(x)} = 0$, then it is

called solenoidal (divergence-free or incompressible) field. For a field in a bounded domain, the solenoidal condition implies that there are no sources or sinks in this domain but there may be vortices. If the solenoidal condition holds then there exists a vector a(x) (potential vector) such as $\mathrm{f(x)} = \nabla \times \mathrm{a(x)}$. Alternatively, for the irrotational fields, the curl vanishes i.e. $\nabla \times \mathrm{f(x)} = 0$. The irrotational field property implies that the field can be expressed as the gradient of a scalar function. If both conditions are satisfied then the field is both irrotational and solenoidal and it is called a harmonic field.

4.2 Theoretical Aspects for the Recovery of 2D and 3D Continuous Vector Fields

The theoretical analysis for the recovery of an unknown vector field in the continuous domain using line integrals [119, 120, 12, 161], is mainly based on (i) the decomposition of the vector field into an irrotational and solenoidal component (Helmholtz Decomposition) and (ii) the use of the Fourier slice theorem (FST) [111] (defined in appendix B.2).

According to Helmholtz Decomposition, a continuous vector field f(x) in an infinite space ($\mathrm{x} \in \mathbb{R}^k$) that vanishes at infinity and is twice differentiable, can be expressed as the sum of an irrotational component $-\nabla u_0(\mathrm{x})$ and a solenoidal component $\nabla \times \mathrm{a(x)}$, i.e.

$$\mathrm{f(x)} = -\nabla u_0(\mathrm{x}) + \nabla \times \mathrm{a(x)}. \tag{4.4}$$

The decomposition holds for infinite spaces or for bounded domains if the vector flow on the boundary is zero [9].

The first application of longitudinal line integrals for the reconstruction of vector fields was presented in [119]. In [119], it was shown that, in a 2D domain Ω, the Fourier transform (FT) of the longitudinal line integral of field f(x) (4.2) is equal to the FT of its solenoidal component a(x), considering vanishing boundary values of the irrotational part[1]. If the longitudinal line integral (4.2) is re-written as a surface integral

$$I_L^{\parallel} = \int_{\mathrm{x}\in\Omega} \mathrm{f(x)} \cdot \hat{\mathrm{s}}\, \delta(\mathrm{x} \cdot \hat{\mathrm{s}}_{\perp} - p)\, d\mathrm{x}, \tag{4.5}$$

where p is the distance of the line L from the origin and $\delta(.)$ is the Dirac delta function.

Then, the FT of this line integral is

$$\widetilde{I}_L^{\parallel} = \int_{p\in\mathbb{R}^+} I_L e^{-i(\kappa p)} dp = (2i\pi\kappa)\widetilde{a}, \tag{4.6}$$

where $\widetilde{\cdot}$ denotes the FT of the corresponding functions, $2i\pi\kappa$ comes from the exponent of the FT and $\widetilde{a}$ is the FT of the solenoidal part $\nabla \times \mathrm{a(x)} = (\frac{\partial a}{\partial y}, -\frac{\partial a}{\partial x})$, when $\mathrm{x} = (x, y)$. For the numerical computation of the solenoidal part, classical methods of the scalar tomography have

[1]For the interested reader, the derivation of this proof, for the 3D case, can be found in appendix B.4

been suggested based on either transformed oriented methods (e.g. filtered back-projection) [153, 120, 77, 111] or algebraic methods (e.g. algebraic reconstruction techniques (ART)) [176, 65, 25].

Regarding the recovery of the irrotational component $u_0(\mathrm{x})$ of the field, different methods have been proposed, using either prior information [119] or integral based approaches [12, 77, 139]. More precisely, in [119] it was shown that the full reconstruction of a 2D field is feasible under the assumption that the unknown field is divergence-free ($\nabla \cdot \mathrm{f}(\mathrm{x}) = 0$) which implies that there are no sources or sinks inside the domain. In this approach, the solenoidal component was estimated using the longitudinal line integral while the irrotational component was computing solving the Laplace's equation. In particular, the divergence of the field decomposition (4.4) yields Laplace's equation,

$$\nabla \cdot \mathrm{f}(\mathrm{x}) = -\nabla \cdot \nabla u_0(\mathrm{x}) + \nabla \cdot \nabla \times \mathrm{a}(\mathrm{x}) \;\Rightarrow\; \nabla^2 u_0(\mathrm{x}) = 0. \tag{4.7}$$

The Laplacian (4.7) can be solved using either finite difference methods [186, 8], finite elements methods (FEM) [61, 174] or boundary element methods (BEM) [159, 154].

The integral based approaches suggested the estimation of integrals over projections of the field in directions other than the longitudinal direction [77, 12, 139]. In [12], the recovery of 2D fields using both the longitudinal and transverse line integrals was described. Furthermore, the reconstruction in domains with non homogeneous boundary condition was examined. In the latter case, the decomposition of the field into a solenoidal and irrotational part was not unique and therefore an extra term in the vector decomposition was added to ensure that the boundary conditions hold. This extra term is called a harmonic component. It was proved that the combination of the longitudinal and transverse integrals can fully recover a field in a circular domain. The approach was verified by carrying out reconstructions of simulated fluid flows (also called incompressible vector fields). Later in [77], a 3D incompressible field was full reconstructed using a similar concept. A more general approach for the full recovery of a 3D arbitrary field in a 3D domain Ω using inner product formulation was described in [139, 130]. The so-called Radon probe transform was defined as the integral data over the projection of a field on planes and is given by

$$I^{\mathrm{b}}(\hat{n}, \mathrm{p}) = \int_{\mathrm{x} \in \Omega} \mathrm{f}(\mathrm{x}) \cdot \mathrm{b}\, \delta(\mathrm{x} \cdot \hat{n} - \mathrm{p})\; d\mathrm{x}, \tag{4.8}$$

where b is the so-called probe vector, p the distance between the projection plane $\delta(\mathrm{x} \cdot \hat{n} - \mathrm{p})$ and the origin and $\hat{n}$ the unit normal vector to the plane. Particularly, with the help of the field decomposition (4.4) and by applying the FST, the FT of the previous integral (4.8) results in

$$\widetilde{I}^{\mathrm{b}}(\hat{n}, \kappa) = (i 2\pi\kappa)\, \mathrm{b} \cdot [\widetilde{u}_0(\kappa\hat{n})\hat{n} + \hat{n} \times \widetilde{\mathrm{a}}(\kappa\hat{n})], \tag{4.9}$$

where $\widetilde{.}$ denotes the FT of the corresponding function, κ the FT variable and i the imaginary unit. Therefore, if the probe vector b is selected orthogonal to $\hat{n}$ then the irrotational component

is eliminated. On the other hand when b is parallel to $\hat{n}$ then the solenoidal component vanishes. However, in practice measuring the transverse line integrals of the Radon probe transform is difficult or even impossible in most cases, for instance in Doppler techniques [25] or in geophysics [120]. That means that the full recovery of a field using solely integrals is a challenging task in practical applications.

Until now, the majority of the existing literature in VFT methods has been directed towards the imaging of fluid velocity fields from actively acquired measurements [119, 120, 156, 64, 12, 90, 144, 176, 76, 59, 155]. In these problems, the fluid is assumed incompressible [119, 176] which in mathematical terms ensures a divergence-free field and there are no sources/sinks in the domain which results in a solenoidal field that can be estimated following the FT based methods [153, 77]. These applications include the use of ultrasound measurements (acoustic rays) to reconstruct the velocity field of blood veins [64, 60], estimation of a field in Kerr materials in optical polarization tomography [48] and oceanographic tomography [144]. In [76] the vector field approach was used for the estimation of the magnetic field of the corona of the sun.

As far as we know, VFT has been previously used only in applications for the reconstruction of incompressible fluid flows which are solenoidal fields. In this work however, we are interested in applying similar methods to reconstruct electric fields produced by source/sinks in bounded domains. These fields are irrotational and arise in applications such as in electroencephalography (EEG) [95]. Our aim is to recover fields which resemble the bioelectric field induced by the neural activity using the potential measurements on the scalp. For this purpose, we follow the numerical concepts suggested in [137, 176], i.e. we use the discretized longitudinal line integral for the reconstruction of electric fields from potential measurements. In particular, we show that the numerical solution of the linear system that is derived from the numerical approximation of the line integrals can be used for the reconstruction smooth irrotational fields and more complex electric fields which resemble bioelectric fields. The main advantage of this approach is that there is no need for the incorporation of the source model in the equations unlike, for example, in the EEG source imaging problem [62, 61, 55].

4.3 Reconstruction of 2D Continuous Vector Field in Domains with non-Homogeneous Boundary

In this section, we employ the FST to derive relationships between the irrotational, solenoidal and harmonic components of a 2D field with its longitudinal and transverse line integrals by assuming non homogeneous boundary conditions. The analysis is based on [12] where theoretical aspects of the recovery of fluid velocity fields using ultrasonic measurements was presented. However, here we deal with a more general case. We show that the FT of the longitudinal line integral equals to the harmonic component when the solenoidal part of the field is zero. Additionally, when the field is both irrotational and divergence-free then only the longitudinal and transverse line integrals are needed for the reconstruction of the field. This section was

added in order to clarify the vector components which can be retrieved from the integral data when the analysis is carried out in a continuous and bounded domain. Most of the previously published theoretical analysis deals with fields with zero values on the boundaries or infinite domains.

In a 2D domain $\Omega \subset \mathbb{R}^2$, let us denote $\mathrm{f(x)} = (f_x(\mathrm{x}), f_y(\mathrm{x})) : \Omega \to \mathbb{R}^2$ as the unknown vector field. The field is non-zero on the boundary $\partial\Omega$, $\mathrm{f(x)}|_{\partial\Omega} \neq 0$. The line L of integration is defined by the parametric expression

$$L(\phi, p) := \{\mathrm{x} = (x, y) \in \Omega : x\cos\phi + y\sin\phi = p\} \tag{4.10}$$

where p is the signed distance of the line from the origin and ϕ the angle as shown in Fig. 4.1.

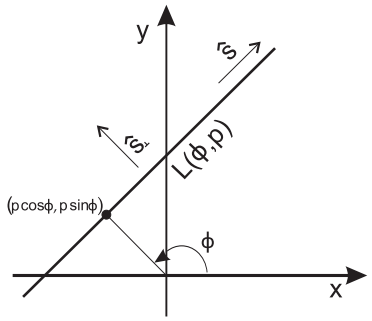

Figure 4.1: 2D Line L on z plane with parameters (ϕ, p) where $0° \leq \phi \leq 180°$ and $p \in \mathbb{R}$.

The longitudinal line integral (4.2) can be expressed as a surface integral using the $1D$ Dirac delta function $\delta(\cdot)$ and $\hat{\mathrm{s}} = (\sin\phi, -\cos\phi)$, i.e.

$$I_L^{\parallel} = \int\int_{(x,y)\in\Omega} (f_x \sin\phi - f_y \cos\phi)\delta(x\cos\phi + y\sin\phi - p)\, dxdy. \tag{4.11}$$

Similarly, the transverse line integral is

$$I_L^{\perp} = \int\int_{(x,y)\in\Omega} (f_x \cos\phi + f_y \sin\phi)\delta(x\cos\phi + y\sin\phi - p)\, dxdy, \tag{4.12}$$

as $\hat{\mathrm{s}}_{\perp} = (\cos\phi, \sin\phi)$. The FTs of (4.11) and (4.12) are

$$\widetilde{I}_{\phi}^{\parallel}(\kappa) = \int I_L^{\parallel} e^{-i(\kappa p)}\, dp = \widetilde{f}_x \sin\phi - \widetilde{f}_y \cos\phi \tag{4.13}$$

$$\widetilde{I}_{\phi}^{\perp}(\kappa) = \int I_L^{\perp} e^{-i(\kappa p)}\, dp = \widetilde{f}_x \cos\phi + \widetilde{f}_y \sin\phi, \tag{4.14}$$

where $\widetilde{f}_x = \int\int_{(x,y)\in\Omega} f_x(x,y) e^{-i\kappa(x\cos\phi + y\sin\phi)}\, dxdy$ and $\widetilde{f}_y = \int\int_{(x,y)\in\Omega} f_y(x,y) e^{-i\kappa(x\cos\phi + y\sin\phi)}\, dxdy$ are the FTs of the f_x and f_y components and $\widetilde{\cdot}$ refers to the FT of the components.

Furthermore, according to the Helmholtz-Hodge decomposition theorem [9], a smooth vector field f(x), defined in a bounded domain, can be uniquely decomposed into three components: 1) an irrotational component $\nabla u_0(\mathrm{x})$, which is normal to the boundary; 2) an incompressible com-

ponent $\nabla \times \mathrm{a(x)} = (\frac{\partial a}{\partial y}, -\frac{\partial a}{\partial x})$, which is parallel to the boundary; and 3) a harmonic component $\mathrm{h(x)} = (h_x, h_y)$, i.e.

$$\mathrm{f(x)} = -\nabla u_0(\mathrm{x}) + \nabla \times \mathrm{a(x)} + \mathrm{h(x)}. \tag{4.15}$$

The harmonic component h(x) satisfies the conditions $\nabla \cdot \mathrm{h(x)} = 0$ and $\nabla \times \mathrm{h(x)} = 0$.

From (4.15), we have that the derivatives of f(x) are

$$\begin{aligned} f_x(\mathrm{x}) &= \frac{\partial a}{\partial y} - \frac{\partial u_0}{\partial x} + h_x, \\ f_y(\mathrm{x}) &= -\frac{\partial a}{\partial x} - \frac{\partial u_0}{\partial y} + h_y \end{aligned} \tag{4.16}$$

and the FTs of the f_x and f_y components are

$$\begin{aligned} \widetilde{f}_x(\kappa) &= (i\kappa)\widetilde{a}\, \sin\phi - (i\kappa)\widetilde{u}_0\, \cos\phi + \widetilde{h}_x \\ \widetilde{f}_y(\kappa) &= -(i\kappa)\widetilde{a}\, \cos\phi - (i\kappa)\widetilde{u}_0\, \sin\phi + \widetilde{h}_y. \end{aligned} \tag{4.17}$$

From (4.13) and (4.17), the FT of the longitudinal ray transform becomes

$$\widetilde{I}^{\parallel}_{\phi}(k) = (i\kappa)\, \widetilde{a} + \widetilde{h}_x\, \sin\phi - \widetilde{h}_y\, \cos\phi. \tag{4.18}$$

And equations (4.14) and (4.17) results in the FT of the transverse integral

$$\widetilde{I}^{\perp}_{\phi}(\kappa) = -(i\kappa)\, u_0 + \widetilde{h}_x\, \cos\phi + \widetilde{h}_y \sin\phi. \tag{4.19}$$

When the field f(x) is irrotational ($\nabla \times \mathrm{f(x)} = 0$) then $\nabla \times \mathrm{a(x)} = 0$. The field is $\mathrm{f(x)} = -\nabla u_0(\mathrm{x}) + \mathrm{h(x)}$ and the FT of the longitudinal line integral becomes

$$\widetilde{I}_{\phi}(\kappa) = \widetilde{h}_x\, \sin\phi - \widetilde{h}_y\, \cos\phi. \tag{4.20}$$

In this case, the longitudinal integral gives information related to the harmonic component. However, (4.20) and (4.19) measurements are not sufficient for the full reconstruction of a 2D irrotational field, since we have two integral measurements and three unknowns and an extra condition is required. Now, when the field is also irrotational ($\nabla \times \mathrm{f(x)} = 0$) then $\mathrm{f(x)} = \mathrm{h(x)}$ and the FT of the traversal ray transform becomes

$$\widetilde{I}^{\perp}_{\phi}(\kappa) = \widetilde{h}_x\, \cos\phi + \widetilde{h}_y\, \sin\phi. \tag{4.21}$$

Therefore, the longitudinal and the transverse integrals can recover a harmonic field in an area. However, in practice the transverse integral is difficult to be measured. Thus, instead of the transverse line integrals for the reconstruction of a harmonic field we can use alternative prior knowledge. In section 4.6, we show that the numerical computation of harmonic fields is feasible in a discrete domain using the longitudinal line integral and the prior knowledge that the field is divergence-free.

4.4 Estimation of Electric Fields in Discrete Domains

In this section, we describe the numerical estimation of a 2D electric field using the line integral measurements. We formulate the discrete VFT problem for the reconstruction of irrotational field and we describe the line integral approximations used in the computations.

Let us assume that in a convex domain $\Omega \subset \mathbb{R}^k$, where k is equal to either 2 or 3 depending whether the analysis is carried out in 2D or 3D (in the following simulations $k = 2$), the field $\mathrm{e}(\mathrm{x}) : \Omega \to \mathbb{R}^k$, where $\mathrm{x} \in \Omega$, satisfies the curl-free condition

$$\nabla \times \mathrm{e}(\mathrm{x}) = 0. \tag{4.22}$$

This condition implies that $\mathrm{e}(\mathrm{x})$ can be expressed as the gradient of a scalar function $u(\mathrm{x}) : \Omega \to \mathbb{R}$ [3], i.e.

$$\mathrm{e}(\mathrm{x}) = -\nabla u(\mathrm{x}). \tag{4.23}$$

Therefore, the longitudinal line integral (4.2) of $\mathrm{e}(\mathrm{x})$ along a ray L with end points x_a and x_b on the domain boundary $\partial\Omega$ equals to

$$I_L^{\parallel} = \int_L \mathrm{e}(\mathrm{x}) \cdot \hat{\mathrm{s}} \; d\ell(\mathrm{x}) = \int_{L(\mathrm{x}_a, \mathrm{x}_b)} -\nabla u(\mathrm{x}) \cdot \hat{\mathrm{s}} \; d\ell(\mathrm{x}) = u(\mathrm{x}_a) - u(\mathrm{x}_b). \tag{4.24}$$

In this inverse problem, the potential differences between boundary measurements, which equal to the longitudinal integral data, will be used for the numerical estimation of the field in the domain Ω (see Fig. 4.2).

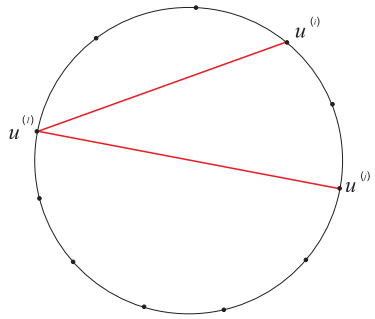

Figure 4.2: Tracing lines between the measurements. The difference between $u^{(1)}$ and $u^{(j)}$ gives the value of the line integral along the line which connects measurement points (1) and (j). In this problem, the observation vector comprises the potential differences between all possible pairs of electrodes.

For the solution of the problem, the concept of the numerical methods, described in [137, 176, 111], was followed. The domain Ω is divided into elements Ω_i and N nodes. The approximate longitudinal line integral along a line L_j which "traces" Ω and intersects Ω at two points equals to

$$\Delta u_j = I_{L_j}^{\parallel}(\mathrm{e}) = \int_{L_j} \mathrm{e}(\mathrm{x}) \cdot \hat{\mathrm{s}} \; d\ell(\mathrm{x}) = \sum_{L_j \in \Omega_i} \mathrm{s}_i^{\parallel} \cdot \mathrm{e}_i, \tag{4.25}$$

where Δu_j is the potential difference between these two electrodes, $\mathrm{e}_i \in \mathbb{R}^k$ is the electric field at node $\mathrm{x}_i \in \Omega_i$ and $\mathrm{s}_i^{\parallel} \in \mathbb{R}^k$ are the corresponding approximated line integral coefficients. If line L_j does not intersect the discrete element which includes the node x_i then the respective $\mathrm{s}_i^{\parallel} = 0$. Analytical description of the estimation of the coefficients $\mathrm{s}_i^{\parallel}$ is given in section 4.4.3.

In practice, the number of the electrodes is finite and thus a finite set of boundary potential measurements can be obtained. The set of potential measurements is $u = (u(\mathrm{x}_1), u(\mathrm{x}_2), \ldots, u(\mathrm{x}_m))$ where $(\mathrm{x}_1, \ldots, \mathrm{x}_m) \in \partial\Omega$ and m is the number of electrodes. For the potential differences between all possible pair of electrodes, equation (4.25) can be expressed in matrix form as

$$Du = S^{\parallel} e, \tag{4.26}$$

where $e \in \mathbb{R}^{kN}$ is the electric field distribution, $S^{\parallel} \in \mathbb{R}^{l \times kN}$ is the so-called longitudinal ray matrix with $l = \frac{m(m-1)}{2}$ and $D \in \mathbb{R}^{l \times m}$ is the difference matrix to calculate the differences between the potential measurements $u \in \mathbb{R}^m$. So, the longitudinal integral data vector comprises the potential differences between all possible pairs of electrodes and is given by $I^{\parallel} = Du \in \mathbb{R}^l$.

Similarly, a set of transverse line integrals

$$I_L^{\perp} = \int_L \mathrm{e}(\mathrm{x}) \cdot \hat{\mathrm{s}}_{\perp} \, d\ell(\mathrm{x}) \tag{4.27}$$

yields the linear system

$$I^{\perp} = S^{\perp} e, \tag{4.28}$$

where $I^{\perp} \in \mathbb{R}^l$ is the transverse integral data and $S^{\perp} \in \mathbb{R}^{l \times kN}$ is the transverse ray matrix.

4.4.1 Ill-posedness and ill-conditioning of the Problem

The line integrals of the vector field are compact operators between appropriately defined spaces and therefore, they are not continuously invertible [111]. Thus, the continuous VFT problem is ill-posed, as the third Hadamard's condition is not satisfied [37]. Generally speaking, the ill-posedness term technically applies only to continuous problems. The ill-posedness of the continuous problems is inherited as ill-conditioning of the discrete version of the problem. Even though, the discretization of the problem is an implicit regularization (this, in literature, is referred to as regularization by discretization [40]), usually some kind of extra regularization is required in order to obtain a good solution.

Furthermore, in practical applications, usually the line integral measurements are an incomplete sampling of information. Therefore, the ill-posedness, in addition to the instability, is also related to the non-uniqueness of the solution (second Hadamard's condition) and therefore prior information needs to be incorporated in the modeling.

In the discrete electric field reconstruction, the ill-conditioning of the ray matrix (4.26) is related to the invertibility of the integral operator as well as to the fact that the number of observed measurements is normally far less than the number of unknowns. Thus, in the test cases examined in sections 4.6 and 4.7, penalties and prior information are used to ensure an

accurate reconstruction.

4.4.2 Implicit Regularization using Line Integrals

The fact that the number of the integral data ($l = \frac{m(m-1)}{2}$) is larger than the number of potential measurements m in equation (4.26) can be used as an implicit regularization to the problem. In this section, we give a brief explanation how the integral data redundancy can act as an implicit regularization.

In particular, using the QR decomposition [100], the difference matrix D in equation (4.26) can be decomposed as

$$D = Q[R^{\mathrm{T}}, 0^{\mathrm{T}}]^{\mathrm{T}} \tag{4.29}$$

where $Q \in \mathbb{R}^{l\times l}$, $R \in \mathbb{R}^{m\times m}$ is an upper triangle matrix, $0 \in \mathbb{R}^{(l-m)\times m}$ is a zero matrix and T denotes the transpose of a matrix. Thus, the linear system (4.26) can be re-written as

$$Q[R^{\mathrm{T}}, 0^{\mathrm{T}}]^{\mathrm{T}} u = S^{\|} e. \tag{4.30}$$

Because $Q^{-1} = Q^{\mathrm{T}}$,

$$[R^{T}, 0^{T}]^{\mathrm{T}} u = Q^{\mathrm{T}} S^{\|} e. \tag{4.31}$$

If $Q = [Q_1, Q_2]^{\mathrm{T}}$ where $Q_1 \in \mathbb{R}^{m\times l}$ and $Q_2 \in \mathbb{R}^{(l-m)\times l}$ then from (4.31) we obtain

$$R^{\mathrm{T}} u = Q_1 S^{\|} e \quad \text{and} \quad Q_2 S^{\|} e = 0. \tag{4.32}$$

So, the solution of (4.26) is equivalent to the solution of $(R^{\mathrm{T}})u = Q_1 S^{\|} e$ with constraint $Q_2 S^{\|} e = 0$.

However, due to the (intrinsic) instability of the integral operator as well as to the fact that the number of observed measurements is usually less than the number of unknowns ($l \ll kN$), further regularization is required for a good solution.

4.4.3 Computation of the Longitudinal Line Integrals

For the numerical formulation of the problem, the 2D domain Ω was discretized using triangular elements Ω_i i.e. $\Omega = \bigcup_{i=1}^{\mathrm{K}} \Omega_i$ where K is the number of triangles. The longitudinal ray transform (4.25) was defined by

$$I^{\|}_{L_j} = \sum_i I^{(i)\|}_{\Delta L}, \tag{4.33}$$

where $I^{(i)\|}_{\Delta L}$ is the longitudinal line integral along the line segment of line L_j in the triangle i (e.g. Fig. 4.3).

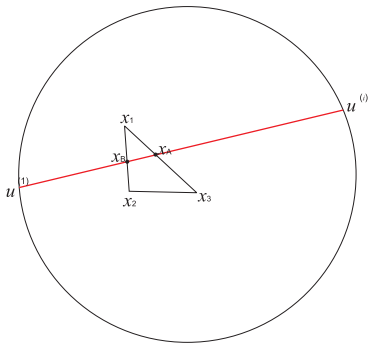

Figure 4.3: In a discrete domain, the ray transform can be expressed as the sum of the line integrals along the line segments of the ray L which intersect the discrete elements.

In the following analysis, we estimate the line integral in one triangle with corner point x_1, x_2 and x_3. The estimated integral coefficients are assigned to the corresponding elements of the ray matrix $S^{\parallel}$ in (4.26).

The line integral along the segment ΔL defined by the intersection of the line L_j with the triangle at points x_A and x_B (Fig. 4.3) is

$$I_{\Delta L}^{(i)\parallel} = \int_{\Delta L} \mathrm{e}(\mathrm{x}) \cdot \hat{\mathrm{s}}\; d\ell(\mathrm{x}) = \int_{\Delta L} \mathrm{e}(\mathrm{s}) \cdot d\mathrm{s}, \tag{4.34}$$

where $\hat{\mathrm{s}}\; d\ell(\mathrm{x}) = d\mathrm{s}$ and the position vector along the line segment $\Delta L = \|\mathrm{x}_A\mathrm{x}_B\|_2$ is given by

$$s = \mathrm{x}_A + (\mathrm{x}_B - \mathrm{x}_A)t \tag{4.35}$$

for $t \in [0, 1]$.

Also,

$$d\mathrm{s} = (\mathrm{x}_B - \mathrm{x}_A)dt. \tag{4.36}$$

Thus, the line integral (4.34) can be rewritten as

$$I_{\Delta L}^{(i)\parallel} = \int_{\Delta L} \mathrm{e}(\mathrm{s}) \cdot d\mathrm{s} = \int_0^1 \mathrm{e}(t) \cdot (\mathrm{x}_B - \mathrm{x}_A)\; dt = (\mathrm{x}_B - \mathrm{x}_A) \cdot \int_0^1 \mathrm{e}(t)\; dt. \tag{4.37}$$

The next step is to approximate the field $\mathrm{e}(t)$ and solve the integral (4.37). We approximate the field using a linear interpolation. In particular, the field inside the triangle is approximated by

$$\mathrm{e}(\mathrm{x}) = \mathrm{e}_1 + \begin{bmatrix} \mathrm{e}_2 - \mathrm{e}_1 & \mathrm{e}_3 - \mathrm{e}_1 \end{bmatrix} \lambda = \mathrm{e}_1 + P\lambda\mathrm{x}, \tag{4.38}$$

where e_1, e_2 and $\mathrm{e}_3 \in \mathbb{R}^2$ are the field values at the nodes of the triangle, $P = \begin{bmatrix} \mathrm{e}_2 - \mathrm{e}_1 & \mathrm{e}_3 - \mathrm{e}_1 \end{bmatrix} \in \mathbb{R}^{2\times 2}$ and $\lambda(\mathrm{x}) = [\lambda_1\, \lambda_2]^{\mathrm{T}}$ are the interpolation coefficients.

For the estimation of the coefficients λ we use an iso-parametric mapping in which the element geometry and the field are represented by the same interpolation polynomial [171]. The

position vector inside the triangle is given by

$$\mathrm{x} = \mathrm{x}_1 + \begin{bmatrix} \mathrm{x}_2 - \mathrm{x}_1 & \mathrm{x}_3 - \mathrm{x}_1 \end{bmatrix} \mathrm{d} = \mathrm{x}_1 + J\lambda, \tag{4.39}$$

where

$$J = \begin{bmatrix} \mathrm{x}_2 - \mathrm{x}_1 & \mathrm{x}_3 - \mathrm{x}_1 \end{bmatrix} \tag{4.40}$$

and $\lambda = [\lambda_1\ \lambda_2]^{\mathrm{T}}$ are the coefficients defined in (4.38) that satisfy $\lambda_1 \geq 0$, $\lambda_2 \geq 0$ and $\lambda_1 + \lambda_2 \leq 1$. We estimate λ by solving (4.39), i.e.

$$\lambda = J^{-1}(\mathrm{x} - \mathrm{x}_1). \tag{4.41}$$

Substituting (4.41) into (4.38) we get

$$\mathrm{e}(\mathrm{x}) = \mathrm{e}_1 + PJ^{-1}(\mathrm{x} - \mathrm{x}_1). \tag{4.42}$$

Finally, the field $\mathrm{e}(t)$ along the line segment is given by setting $\mathrm{x} = \mathrm{s} = \mathrm{x}_A + (\mathrm{x}_B - \mathrm{x}_A)t$, i.e.

$$\mathrm{e}(t) = \mathrm{e}_1 + PJ^{-1}(\mathrm{x}_A - \mathrm{x}_1 + (\mathrm{x}_B - \mathrm{x}_A)t) \tag{4.43}$$

Substituting (4.43) into (4.37), we obtain the linear approximated line integral

$$\begin{aligned} I_{\Delta L}^{(i)\parallel} &= (\mathrm{x}_B - \mathrm{x}_A)^{\mathrm{T}} \cdot \mathrm{e}_1 + (\mathrm{x}_B - \mathrm{x}_A)^{\mathrm{T}} \cdot \int (PJ^{-1}(\mathrm{x}_A - \mathrm{x}_1 + (\mathrm{x}_B - \mathrm{x}_A)t)dt \\ &= (\mathrm{x}_B - \mathrm{x}_A)^{\mathrm{T}} \cdot \left(\mathrm{e}_1 + PJ^{-1}(\mathrm{x}_A - \mathrm{x}_1 + (\mathrm{x}_B - \mathrm{x}_A) \int_0^1 tdt \right) \\ &= (\mathrm{x}_B - \mathrm{x}_A)^{\mathrm{T}} \cdot \left(\mathrm{e}_1 + PJ^{-1}(\mathrm{x}_A - \mathrm{x}_1 + \frac{1}{2}(\mathrm{x}_B - \mathrm{x}_A) \right) \\ &= (\mathrm{x}_B - \mathrm{x}_A)^{\mathrm{T}} \cdot \left(\mathrm{e}_1 + PJ^{-1}(\frac{1}{2}(\mathrm{x}_B + \mathrm{x}_A) - \mathrm{x}_1) \right). \end{aligned} \tag{4.44}$$

If we set $J^{-1} = \begin{bmatrix} \mathrm{B}_1 & \mathrm{B}_2 \end{bmatrix}$ and $\mathrm{y} = \frac{1}{2}(\mathrm{x}_B + \mathrm{x}_A) - \mathrm{x}_1$, then

$$I_{\Delta L}^{(i)\parallel} = \left((\mathrm{x}_B - \mathrm{x}_A)^{\mathrm{T}} \cdot \begin{bmatrix} e_1 & e_2 & e_3 \end{bmatrix} \right) \mathrm{T}, \tag{4.45}$$

where $\mathrm{T} = \begin{bmatrix} 1 - (\mathrm{B}_1 + \mathrm{B}_2) \cdot \mathrm{y} & \mathrm{B}_1 \cdot \mathrm{y} & \mathrm{B}_2 \cdot \mathrm{y} \end{bmatrix}$.

The coefficients of the transverse ray matrix (4.28) can be estimated in a similar way by replacing the vector $(\mathrm{x}_B - \mathrm{x}_A)$ with its normal. In the following sections, we use this numerical approach for the estimation of the coefficients in the ray matrices.

4.5 Simulation Set-up and Evaluation Metric

In the following sections, irrotational fields satisfying different properties are reconstructed. In particular, two different sets of tests are performed. In the first one, the approach is evaluated for the reconstruction of smooth harmonic and irrotation fields using the proposed approach. In the second set of tests, we deal with the reconstruction of electric fields produced by dipole sources inside a bounded domain. In this latter case, we use prior information related to the structure of the field and penalty terms which satisfy the boundary conditions.

In all cases, the electric field minimization problem has the general form

$$\min_{e} \|Du_{\xi} - S^{\|}e\|_2^2 + \text{ regularization term}, \tag{4.46}$$

where $e \in \mathbb{R}^{2N}$ is the electric field, N the number of discretization points, $Du_{\xi} \in \mathbb{R}^{l}$ the potential differences in the presence of additive noise ξ and $S^{\|} \in \mathbb{R}^{l \times 2N}$ is longitudinal ray matrix.

The observation vector, Du_{ξ}, which is the multiplication of matrix D with the potential measurements u_{ξ}, comprises the potential differences between all possible pairs of electrodes, i.e. for m electrodes, the integral data is of size $l = \frac{m(m-1)}{2}$. The potential measurements are given by $u_{\xi} = u + \xi$ where $u \in \mathbb{R}^m$ and $\xi \in \mathbb{R}^m$ is the noise vector with distribution $\xi \sim \mathcal{N}(0, \gamma_{\xi} I^{m \times m})$.

We quantified the reconstruction accuracy of the approach using the point-wise reconstruction criterion, called reconstruction error (REC) [42], given by

$$\text{REC} = \left\| \frac{e}{\|e\|_2} - \frac{\hat{e}}{\|\hat{e}\|_2} \right\|_2, \tag{4.47}$$

where e denotes the correct (forward) field and $\hat{e}$ the estimated one.

The Signal-to-Noise ratio of the input data (SNR_{in}) was defined as $\text{SNR}_{in} = 20 \log \frac{\|u\|_2}{\sqrt{\gamma_{\xi}}}$. In the following simulations, for each value of $\sqrt{\gamma_{\xi}}$ (noise level), we performed 40 reconstructions using different noise vectors which were drawn from the Gaussian distribution. The average and standard deviation of the REC were estimated based on the corresponding reconstructed fields.

In the following test cases, the vector fields were reconstructed in a 2D homogeneous circular domain Ω with radius 0.1m and center at the origin $(0, 0)$. The potential measurements u were obtained from $m = 32$ point electrodes equally distributed around the domain.

4.6 Smooth Field Reconstructions

In this section, we reconstruct vector fields at a set of N discrete nodes inside a 2D region of interest from integral data under the assumption that $\nabla \times \mathrm{e} = 0$. We reconstruct two simple fields in order to assess the potential of the numerical approach to recover fields without any singularities or very high frequency components.

4.6.1 Divergence-free Electrostatic Field

The first experiment concerned the reconstruction of a field which is both irrotational and divergence-free. The divergence-free property (i.e. $\nabla \cdot \mathrm{e} = 0$) implies that there are neither sources nor sinks in this region and thus the field does not have singularities.

The field was estimated using the linear system (4.26). To improve the stability of the system and to obtain a good solution, the divergence of the field was used as a penalty term. The estimation of the field was based on the minimization

$$\hat{e} := \min_{e} \|Du_{\xi} - S^{\|}e\|_2^2 + \lambda\|\nabla \cdot e\|_2^2, \tag{4.48}$$

where $e \in \mathbb{R}^{2N}$, $Du_{\xi} \in \mathbb{R}^{l}$ the potential differences in the presence of noise ξ, $S^{\|} \in \mathbb{R}^{l\times 2N}$ is longitudinal ray matrix and λ the regularization parameter selected by visual inspection ($\lambda = 0.001$). The number of mesh node was $N = 480$. The divergence operator was numerically approximated using the Graph toolbox (Matlab) [79].

In this section, we solved the minimization problem (4.48) for the case of a smooth electrostatic field. The integral data was obtained from the potential differences between pairs of electrodes. The potential value at each electrode was estimated from the Columb's law i.e. $u(\mathrm{x}_i) = -k_e \sum_{j=1}^{k} \frac{q_j}{\|\mathrm{x}_i - \mathrm{x}_{q_j}\|_2}$ for $i = 1, \ldots, m$. The constant k_e is the Coulomb's constant [3] (for the simulation we set $k_e = 1$), x_i are the locations of the electrodes (sensors), x_{q_j} are the locations of the electric charges (monopoles) with q_j the values of the charges. The source locations x_{q_j} were outside the domain of interest in order to ensure that the field inside the domain does not have singularities.

In the test case (Fig. 4.4), the potential measurements were computed considering two monopoles located at $(0.0373, -0.1684)$ and $(-0.0224, 0.1711)$ with respective charges q_j equal to 1 and -1. The potential measurements were taken from $m = 32$ points around the circular domain and the input integral data had size $l = 496$. The field $\hat{e}$ was estimated by solving

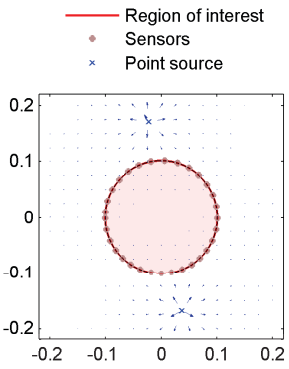

Figure 4.4: Test Set-up: The circular domain (coloured in red) designates the area of interest. The sensors (electrodes) are placed around the domain. The blue x show the locations of the charges and the arrows the correct electrostatic field. In this experiment, we are interested in estimating the electrostatic field inside the circle.

		Average REC ± std		
	SNR_{in}(dB)	60	40	30
# point sources	2	0.35 ± 0.002	0.67 ± 0.055	1.01 ± 0.065

Table 4.1: Average Reconstruction Error (REC) and standard deviation (std) of the electrostatic field of two monopoles. 40 different noise vectors where used for each noise level.

(4.48) (inverse solution) and it was compared with the correct electrostatic field computed using the analytical expression (Coulomb's law) for the electrostatic field (forward solution) $e(\mathrm{x}_l) = \sum_{j=1}^{k} \frac{q_j(\mathrm{x}_l - \mathrm{x}_{q_j})}{\|\mathrm{x}_l - \mathrm{x}_{q_j}\|_2^3}$, for $l = 1, \ldots, N$ and where x_l denotes the coordinates of the l^{th} node. Figure 4.4 shows the test set-up and the forward solution. The arrows and the blue markers indicate the correct field and the location of the sources. The light red circle designates the region where the field $\hat{e}$ is estimated.

In Fig. 4.5, we see the results for different levels of noise, the first row corresponds to the amplitude of the field and the second row to the normalized field orientation lines. We visualized the normalized vector field lines instead of the actual ones in order to improve the clarity of the figure. Additionally, the leftmost pictures, titled "Test case", designate the magnitude and the unit length field lines of the correct field, and the rest of the pictures, the reconstructions for decreasing value of SNR_{in}.

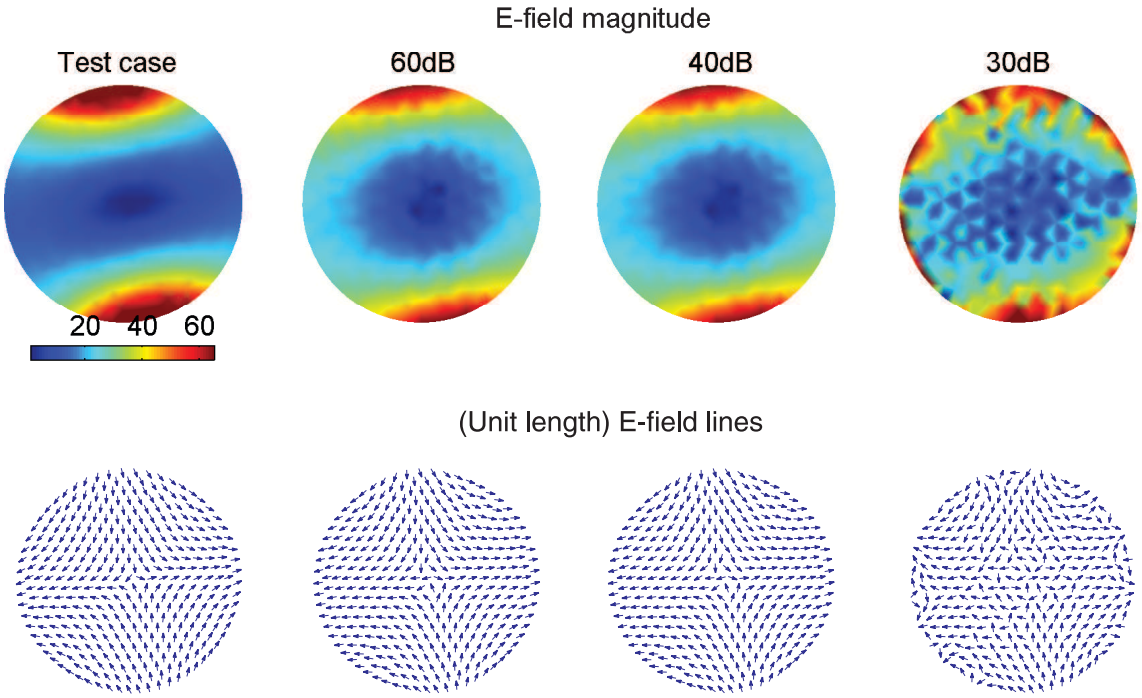

Figure 4.5: Left column depicts the magnitude and vector lines of the reference vector field (analytically estimated field using Coulumb's law) and the remaining pictures, the reconstructions for decreasing SNR_{in} ($\lambda = 10^{-3}$).

For each noise level, minimization problem was solved 40 times using different noisy data.

The average values of the reconstruction error metric REC and the corresponding standard deviations are shown in Table 4.1. According to Fig. 4.5 and Table 4.1, the pattern of the reconstructed field follows the correct vector field for low noise level. The orientation of the recovered field is similar to the correct field with very few small deviations and the same can be said about the magnitude when the additive measurement noise is not prominent. However, there seems to appear some artefact and small discontinuities in the reconstruction. These may be related to the discretization of the domain, the linear approximation of the field and the linear approximation of the penalty term.

4.6.2 Irrotational Vector Fields

In the second experiment, two smooth fields with non-zero divergence were studied. These fields were estimated by minimizing

$$\hat{e} := \min_{e} \|Du_{\xi} - S^{\|}e\|_2^2 + \lambda\|\nabla^2 \cdot e\|_2^2, \tag{4.49}$$

where $e \in \mathbb{R}^{2N}$, $Du_{\xi} \in \mathbb{R}^{l}$ is the vector with the differences between the noisy potential measurements, $S^{\|} \in \mathbb{R}^{l\times 2N}$ is longitudinal ray matrix, $\nabla^2 = (\frac{\partial^2}{\partial x^2}, \frac{\partial^2}{\partial y^2})$ is the Laplace operator and λ the regularization parameter. The vectorial Laplace operator was used as a smoothness penalty term and it was approximated numerically using the Graph toolbox [79].

The domain of reconstruction was a circle with radius 0.1 and centered at $(0, 0)$. The $m = 32$ potential measurements at the electrodes were computed analytically, according to

$$u(x_i, y_i) = -\sum_{j=1}^{k} \tan^{-1} \frac{y_i - b_j}{x_i - a_j}, \quad \text{for } i = 1, \ldots, m, \tag{4.50}$$

where (x_i, y_i) are the coordinates of the electrodes and (a_j, b_j) are constants and indicate the locations of the field vortices. The integral data Du_{ξ} was estimated by taking the differences between pairs of potential measurements. Subsequently, the field $\hat{e}$ was estimated by minimizing (4.49). The regularization parameter in (4.49) was equal to 0.005.

In the following test cases, we compared the estimated solutions $\hat{e}$ (inverse solution) with the field (forward solution) given by the analytical expression

$$\mathrm{e}(x_l, y_l) = \left(-\sum_{j=1}^{k} \frac{y_l - b_j}{(x_l - a_j)^2 + (y_l - b_j)^2}, \sum_{j=1}^{k} \frac{x_l - a_j}{(x_l - a_j)^2 + (y_l - b_j)^2} \right), \quad \text{for } l = 1, \ldots, N, \tag{4.51}$$

where (x_l, y_l) are the coordinates of the N mesh nodes and k indicates the number of vortices of the field. The vector fields (4.51) satisfy the irrotational property if we exclude the vortex point (a_j, b_j). Thus, we selected $\sqrt{a_j^2 + b_j^2} > 0.1$ in order to ensure that the vortices at points (a_j, b_j) are outside of the circular domain (region of interest) and thus the estimated potential data corresponds to an irrotational field.

In this section, we present the reconstruction of two vector fields with different number of vortices k. For the test case A, the boundary data (4.50) was estimated for $k = 1$ and $(a_1, b_1) = (0.12, 0)$. In test case B, the potentials were computed for $k = 3$ and $(a_1, b_1) = (0.12, 0)$, $(a_2, b_2) = (0, -0.12)$ and $(a_3, b_3) = (-0.101, 0.101)$. The second field B is less smooth compared to the first one. The correct field A and B and the reconstruction area for the two test cases are shown in Fig. 4.6. The area of interest was the circle coloured in light red.

In Table 4.2 and Fig 4.7 are summarized the estimated average REC for the two cases. In both cases, we can see that the reconstruction results are good when the level of measurement noise is low and the estimates deteriorate when the level of noise increases. Additionally, for

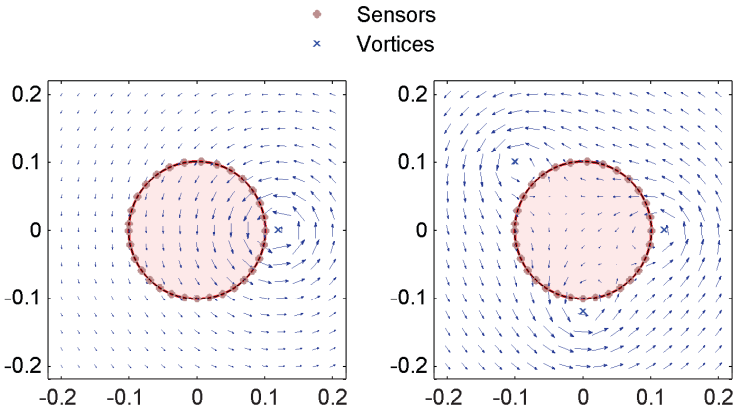

Figure 4.6: Test Set-up: the reconstruction area is the circle (in light red)(A) Test case A (left image) correct field A with vortex at point $(a_1, b_1) = (0.12, 0)$. (B) Test case B (right image) correct field B with $k = 3$ and $(a_1, b_1) = (0.12, 0)$, $(a_2, b_2) = (0, -0.12)$, $(a_3, b_3) = (-0.101, 0.101)$.

all the noise levels, according to the REC, the reconstruction result is slightly better for the test case A, where the actual field is simpler, compared to test case B where the field is more complicated with 3 vortices close to the region of interest.

		Average REC $\pm$ std		
	SNR_{in}	60	40	30
# vortices	$k = 1$	0.18 ± 0.003	0.36 ± 0.049	0.72 ± 0.09
	$k = 3$	0.26 ± 0.008	0.71 ± 0.095	1.10 ± 0.13

Table 4.2: Average reconstruction error (REC) and standard deviation (std) for the irrotational fields. 40 simulated noise vectors were used for each noise level for the estimation of the statistics.

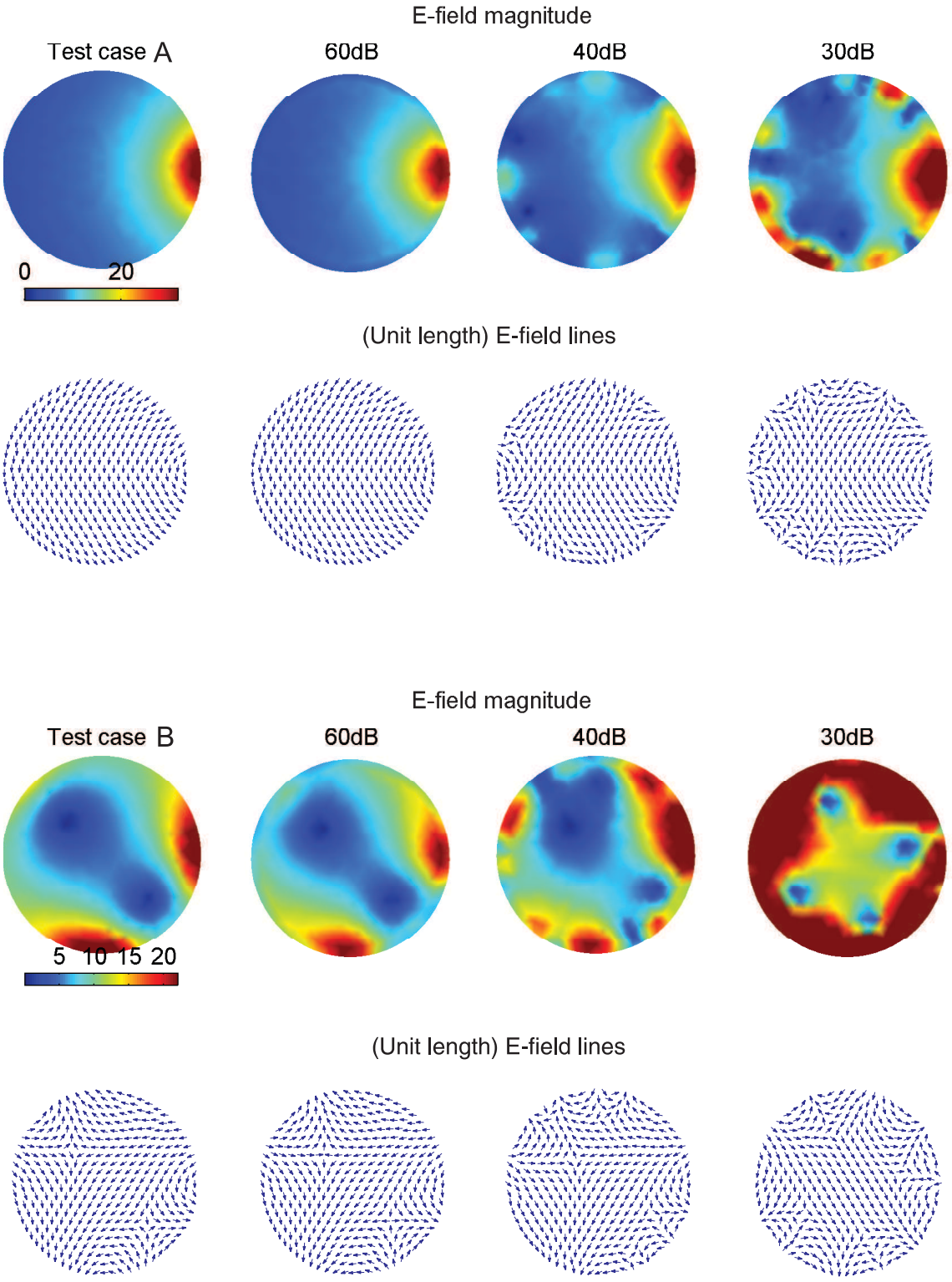

Figure 4.7: Left column shows the magnitude and the vector lines of the correct field (Test case) and the remaining pictures staring from left to right, the reconstruction results for SNR_{in} equals to 60dB, 40dB and 30dB. Test case A (first two rows): reconstruction of a field with $k = 1$ vortex at location $(a_1, b_1) = (0.12, 0)$. Test case B (the last two rows) reconstruction of a field which has $k = 3$ vortices at locations $(a_1, b_1) = (0.12, 0)$, $(a_2, b_2) = (0, -0.12)$ and $(a_3, b_3) = (-0.101, 0.101)$.

Figure 4.8 shows the average REC and the corresponding standard deviation intervals as a functions of the SNR_{in}. As it was expected, when the SNR_{in} is high, i.e. the additive noise is low, the REC decreases and the reconstruction result improves. We can notice that for high values of the SNR_{in} (above 40dB) the variation of the REC is very low. Additionally, we can observe that the reconstruction error is higher for the test case B because the vector field B is more complex compared to the vector field in test case A.

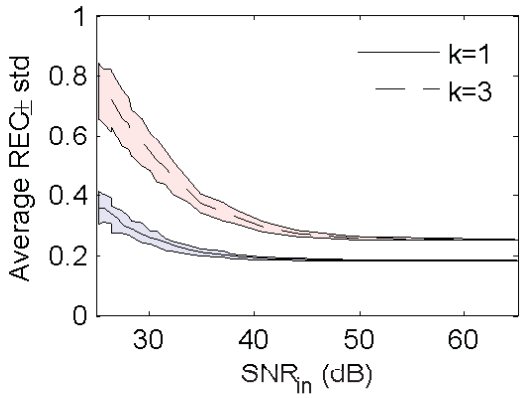

Figure 4.8: Average REC ± std (standard deviation) with respect to the SNR_{in}.

4.7 Electric Field Reconstructions produced by Dipole Sources

In this section, we test the approach for the reconstruction of an electric field produced by a focal source inside the domain. Such vector field is of great interest because it resembles the bio-electric field generated by brain activity. In addition, we examine the reconstruction performance in the case of additive boundary noise. For the evaluation of the reconstructions we used the REC metric defined in (4.47).

In particular, we reconstruct electric fields $\mathrm{e}(\mathrm{x}) = (e_x(\mathrm{x}), e_y(\mathrm{x})) : \mathrm{x} \in \Omega \to \mathbb{R}^2$ caused by a focal (dipole) source inside a homogeneous bounded circle Ω. Considering that the quasi-static approximation holds, the Maxwell's equations for the electric field are $\nabla \times \mathrm{e}(\mathrm{x}) = 0$ and $\nabla \cdot \mathrm{e}(\mathrm{x}) = \rho(\mathrm{x})$ where $\rho(\mathrm{x})$ is the current source density inside the domain. The boundary condition is $\mathrm{e}(\mathrm{x}) \cdot \hat{n}|_{\partial\Omega} = 0$, where $\hat{n}$ is the unit normal vector of the boundary $\partial\Omega$ of the domain.

The electric field is estimated by minimizing the functional

$$\begin{aligned} \min_{\mathrm{e}} \sum_j [\Delta u_j - I^{\parallel}_{L_j}(\mathrm{e})]^2 + \lambda \Big| \int_{\mathrm{x}\in\partial\Omega} \mathrm{e}(\mathrm{x}) \cdot \hat{n} \; d\ell(\mathrm{x}) \Big|^2 \\ + \nu \int_{\mathrm{x}\in\Omega} |w(\mathrm{x})(\nabla^2 \cdot \mathrm{e}(\mathrm{x}))| \; d\mathrm{x} + \kappa \sum_j |I^{\perp}_{L_j}(\mathrm{e})|, \end{aligned} \tag{4.52}$$

where the first term is called fidelity term and is defined as the difference between the potential measurement difference on the boundary and the longitudinal line integrals $I^{\parallel}_{L_j}$ (4.25). The second term is the boundary condition which ensures that there is no outwards flux. The third penalty term is the L_1 norm of the Laplacian, $\nabla^2 = (\frac{\partial^2}{\partial x^2}, \frac{\partial^2}{\partial y})$, which imposes connectivity and sparsity in the field. In particular, the electric field is almost everywhere smooth and close to zero apart from a small area around the dipole source. Hence, we employ the Laplace operator in order to smooth the solution; however, because there is a source inside the domain, we relax the strict smoothing effect by using the Laplace with the L_1 norm. Additionally, the weights w ensure that the solution is not a harmonic field and it attains its maximum only on the boundary (see section 2.5.5). Thus, using the weights it is possible to reconstruct also fields with maximum amplitude deeper inside the domain.

The last penalty term corresponds to the transverse line integral (4.27). A transverse line integral $I^{\perp}_{L_j}(\mathrm{e})$ can be interpreted as the vector flux across the line of integration. Numerically, the transverse line integral is equal to the sum of the inner products between the field along the line and the unit normal vector of the line. For an electric field in a domain with sources/sinks (dipole source), the total flux across most of the lines is zero because either the field values are very low far from the source or the field is parallel to the line (see for example the red line in Fig. 4.9). However, the transverse integral is non-zero only for few lines (e.g. blue line in Fig. 4.9) which trace the domain close to the source location and are normal (or nearly normal) to the dipole direction. Hence, sparsity was imposed on the transverse line integral term. This sparsity constraint forces the source and sink to be close to each other in order to resemble a neural source. Finally (λ, ν, κ) denote the corresponding regularization parameters. For the

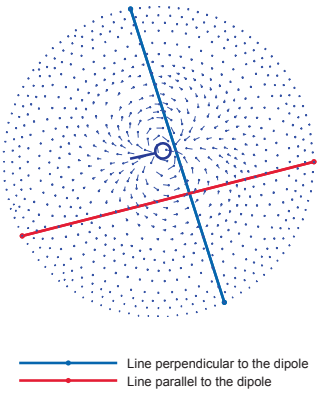

Figure 4.9: Two tracing lines and the vector field. The red line is parallel to direction of the dipole moment and the blue line is normal to the dipole moment. The total flux across the red line which corresponds to the tangential integral along this line is equal to zero. On the other hand, we see that the blue line divides the circle into two regions and there is flux from the left hand side region to the right hand side.

numerical estimation of the field, the above minimization problem is written in matrix form as

$$\min_{e} \|Du - \mathrm{S}^{\|}e\|_2^2 + \lambda\|Te\|_2^2 + \nu\|\mathrm{B}e\|_1 + \kappa\|S^{\perp}e\|_1 \tag{4.53}$$

where $e \in \mathbb{R}^{2N}$ is the discrete electric field (E-field), $Du \in \mathbb{R}^{l}$ are the differences of the potential measurements, $S^{\|} \in \mathbb{R}^{l\times 2N}$ is the longitudinal ray matrix and l the number of line integrals. Furthermore, the L_2 norm of Te corresponds to the boundary condition with $T \in \mathbb{R}^{b\times 2N}$ and b is the number of boundary nodes. Matrix $\mathrm{B} = (WB \otimes I^{2\times 2})$ is the weighted discrete Laplace operator (see appendix B.5 for further details), $\otimes$ denotes the Kronecker product and matrix W is a diagonal matrix, $W = \mathrm{diag}(w_1, \ldots, w_N)$. In the current implementation, we selected the weight w_i to be the normalized distance of the i^{th} node from the center of the circle. Finally, matrix $S^{\perp} \in \mathbb{R}^{lN}$ includes the coefficients of the transversal ray matrix. Problem (4.53) is a non-linear optimization problem. For the estimation of the field, the CVX toolbox was used [11, 52].

Forward Model and Measurements

In this paragraph we describe the model that was used to derive the observations. Moreover, the same model was used to compute the forward field (forward solution) in order to compare and evaluate the reconstruction results (4.53). For the forward estimation we used finer mesh compared to the mesh used for the inverse solution (4.53). The nodes of the forward mesh are denoted ny $\bar{N}$ and of the inverse mesh by N (Table 4.3). In particular, the potential values $\bar{u}_+ \in \mathbb{R}^{\bar{N}}$ in a circular domain were estimated from the the linear system

$$\bar{u}_+ = \bar{K}_+\bar{d}_+, \tag{4.54}$$

Mesh	Forward	Inverse
# Nodes	3045	760

Table 4.3: Number of node for the forward and inverse mesh.

where $\bar{K}_+ \in \mathbb{R}^{\bar{N}\times 2\bar{n}}$ is the lead field matrix of the forward model (assuming constant conductivity equals to 1). The number of possible source location is denoted by $\bar{n}$ and the number of mesh nodes by $\bar{N}$ ($\bar{n} \leq \bar{N}$). The simulated dipole source is $\bar{d}_+ \in \mathbb{R}^{2\bar{n}}$. For a single source, vector $\bar{d}_+$ has only two non-zero values, one for the x- and y- component respectively.

The potential measurements $v_+ = (\bar{u}_+(\mathrm{x}_1), \ldots, \bar{u}_+(\mathrm{x}_m))^{\mathrm{T}} + \xi$ were obtained from 32 points at locations x_i equally placed around the circular domain. The noise vector ξ was drawn from a Gaussian distribution, $\xi \sim \mathcal{N}(0, \gamma_\xi I^{m\times m})$. The integral data was estimated by taking the potential differences Dv_+ between the m electrodes.

Also, the forward field, given by $\bar{e}_+ = -\nabla\bar{u}_+ \in \mathbb{R}^{2\bar{N}}$, was computed numerically by applying the linear gradient reconstruction approach [19]. The results, estimated solving (4.53), were compared with projected forward field, $e_+ = P\bar{e}_+$ where $P \in \mathbb{R}^{N\times\bar{N}}$ is a linear reduction mapping operator, using the REC (4.47).

Inverse Solutions

The field was estimated solving

$$\hat{e} := \min_e \|Dv_+ - S^{\|}e\|_2^2 + \lambda\|Te\|_2^2 + \nu\|\mathrm{B}e\|_1 + \kappa\|S^{\perp}e\|_1 \tag{4.55}$$

The following figures show the reconstruction results of the E-Fields produced by a single dipole source which was (i) deep in the domain, (ii) superficial-normal (iii) superficial-tangential to the boundaries. The results are summarized in Fig. 4.10, Fig. 4.11 and Table 4.4.

		Average REC ± std		
	SNR_{in}(dB)	60	40	30
Deep Dipole		1.4 ± 0.0	1.5 ± 0.011	1.5 ± 0.031
Superficial Dipole	Normal	1.22 ± 0.0	1.223 ± 0.017	1.26 ± 0.043
	Tangential	1.23 ± 0.0	1.25 ± 0.08	1.2 ± 0.012

Table 4.4: Average Reconstruction Error (REC) and standard deviation (std) for the E-Field of a single dipole source. For each noise level, 40 reconstruction were performed using different noise vectors.

About the E-field results we can say that the maximum strength of the electric field is in the correct location in all the test cases. However, the reconstructed electric field strengths are lower than the correct strengths. In addition, the reconstruction accuracy decreases with increasing noise as it was expected.

Moreover, the dipole, by definition, consists of a source and a sink that are separated by a (very) short distance. This can be seen in the leftmost pictures with the unit length E-field

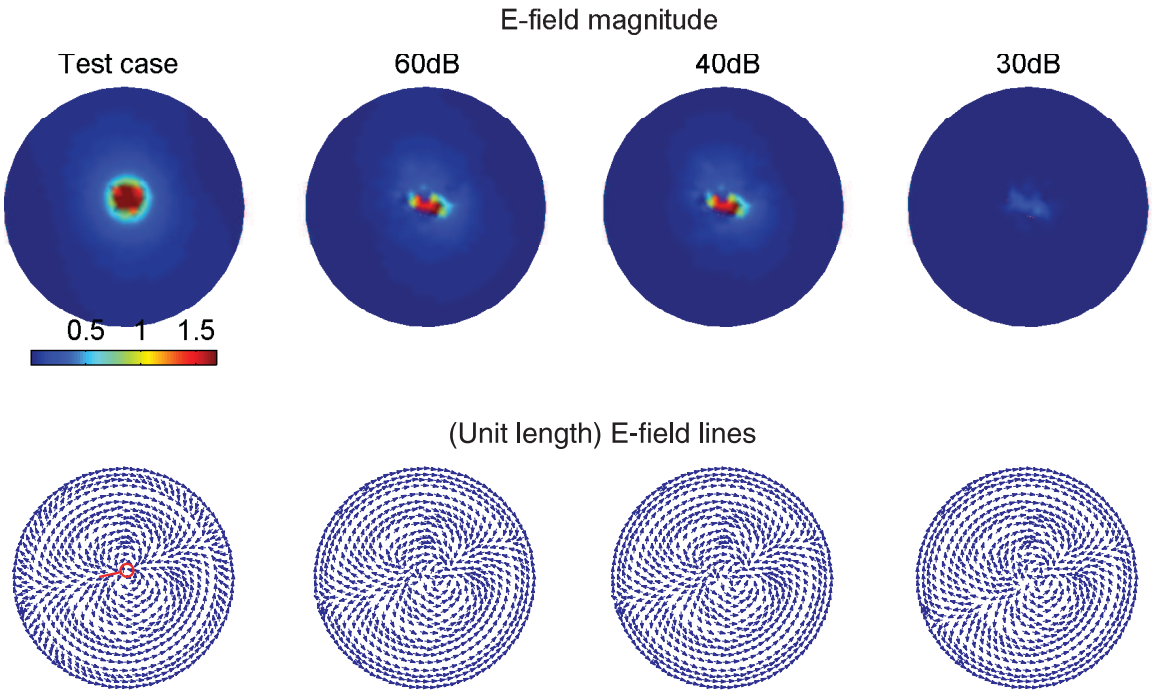

Figure 4.10: A test case of an E-field produced by a deep source. Left column shows the magnitude and the vector lines of the forward field (Test case) and the remaining pictures staring from left, show the reconstruction results for SNR_{in} equals to 60dB, 40dB and 30dB.

arrows in Fig. 4.11, the arrows point inwards and outwards at the ends of the dipole. In the reconstructions of field produced by superficial sources, it can be seen that the source and the sink are separated by slightly larger distance than what should. The mentioned reconstruction errors both in the magnitude and the orientation may be partly due to the linear approximation of the line integrals and partly due to the coarse discretization of the domain.

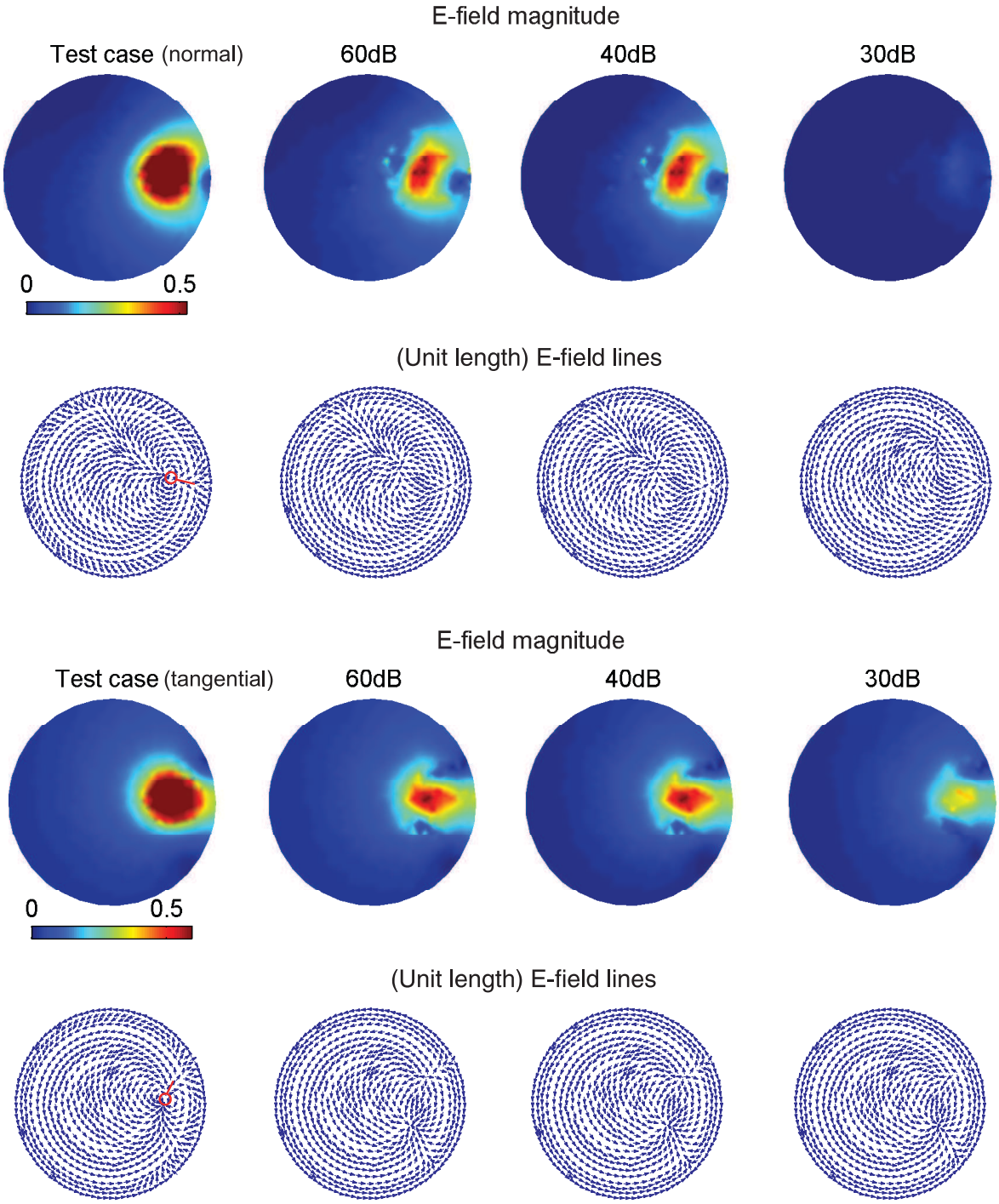

Figure 4.11: This figure shows two different test cases. Left column shows the magnitude and the vector lines of the forward field (for each test case) and the remaining pictures staring from left, show the reconstruction results for SNR_{in} equals to 60dB, 40dB and 30dB. The two top rows correspond to the test case where the E-field was produced by a superficial source which is normal to the boundary. The last two rows correspond to the reconstruction case where the field was produced by dipole source (almost) tangential to the closest boundary point.

4.8 Summary

In this chapter, vector field tomography was employed to reconstruct electric fields based on known boundary data. The test cases included the reconstruction of harmonic fields, irrotational fields and non-zero divergence electric fields caused by dipole sources inside the domain. Spesifically, the last case which is the most challenging has practical importance because it corresponds to EEG imaging in which brain activity (caused by dipole-like sources) is localized based on potential measurements around the scalp.

It was shown that the pattern of the electric field strength distribution could be reconstructed correctly using vector field tomography, even though the absolute values were not always correct. Due to the linear approximation of the line integrals also the arrow figures that depict the E-field lines had sometimes errors near the dipole source. Nevertheless, it is noteworthy that based on the form of the electric field strength, correct active areas could still be localized even in the case of dipole source imaging.

Chapter 5

Compensation of Approximation and Modeling Errors in EEG Imaging

The goal of EEG source imaging is to reconstruct the source activity inside the brain from potential measurements on the scalp. The main factor that limits the current accuracy and applicability of the approach is the complexity and the variability of the brain anatomy. In particular, because the EEG source imaging is an ill-posed inverse problem [122], the solution is highly sensitive to measurement and modeling errors. Specifically, the accuracy of the inverse solution can be affected by errors in the shape of the head model [55] and in the conductivity distribution within the brain [169].

The geometry of the skull and the conductivities of the different tissues within the brain vary among individuals. For instance, in Fig. 5.1 we see the variation in the geometries and the thicknesses of the main head compartments for three different individuals. Typical values for the conductivities of different brain tissue types can be obtained from the literature [122], but the imaging results can be incorrect if the variation of the conductivities and the anatomical complexity and lesions of the individual under examination are significant [170].

The effect of the head geometry and the induced errors in the inverse solution have been studied by several authors. The differences in the solutions between a simplified geometry, such as a spherical head with concentric layers and a realistic head were studied in [21, 143, 184, 7]. Also, the discrepancies in the shape and thicknesses of skulls are significant factors resulting in source misplacement [5, 184]. The evaluation of the skull inhomogeneities (i.e. holes, lesions) was presented in [125] and the effect of the variation of the skull thickness was studies in [20, 5]. All these studies indicated the need of an accurate computational implementation of the underlying model while only very small scale details, e.g. sulci and fissures on the cortical layer, may be neglected from the EEG modeling [173]. Furthermore, the effects of variations in the conductivities and anisotropic properties of the brain tissues and the resulting imaging errors caused by poor conductivity modeling have been investigated in [6, 170, 179, 181].

The inverse solution should ideally be based on an exact head model for each particular individual. However, the extraction of the real geometry for each individual is a multidisciplinary,

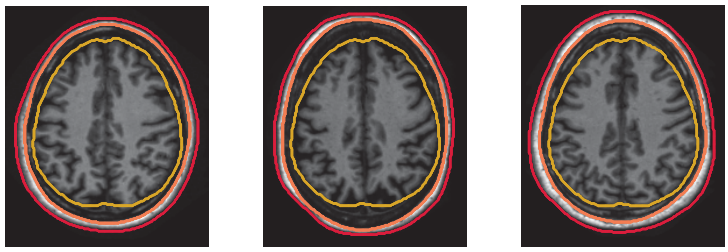

Figure 5.1: Head geometries for different individuals. The three different lines show the three main head compartments [96].

time consuming, expensive and challenging task. Strong clinical expertise is required while the development of fast and robust segmentation, registration and post-processing algorithms for the extraction of the conductivities and the construction a head with the conjunction of multi-modalities (CT/D-MRI) are still open fields of research [160]. Therefore, the use of exact head models is not feasible if we wish to use the EEG as a fast and low cost modality for monitoring of the electrical activity.

In this chapter, we apply the so-called Bayesian approximation error approach (AEA) [67] to the EEG imaging problem to take into account modeling errors due to unknown head geometry and uncertainty in the conductivities of the different tissues. The AEA has been developed specifically to cope with both modeling and numerical discretization errors [66, 4, 112]. Hence, instead of an accurate head model which is too complex and time consuming to be extracted, an approximative computational model is employed in the inversion. The statistical discrepancy between the accurate model and the approximate model is pre-computed and considered in the inverse modeling. This discrepancy is called the approximation error and is incorporated in the model as an additional term. The approach is Bayesian in the sense that the computation of the approximation error statistics is performed over the modeled priors of the unknowns. The likelihood model includes the statistical models of both the approximate error and the measurement noise. By incorporating an appropriate prior, it is possible to construct the posterior density. A Bayesian point estimate, e.g. maximum a posterior (MAP), can be used to visualize the brain activity [66]. To summarize the main idea, the AEA allows the use of a simple head model for every patient by taking the individual variations into account by means of a statistical model.

In this work, we evaluate the feasibility of the AEA to reduce the errors caused due to the use of a coarsely discretized, three-layer, concentric circle geometry in the EEG source imaging instead of a realistic head model. In the simulations, we consider only the reconstruction of sparse sources arising in cases like focal epilepsy. In particular, we examine two different cases; in the first case we assess how the method can compensate for the source localization errors arising from the discrepancies in the head geometry and the model reduction. In this first case, we consider fixed conductivity values and noiseless measurements. In the second case, we consider the combination of unknown geometry, unknown conductivities and additive measurement noise. With the second set of experiments, our intention is to test the method with more realistic examples. The conductivities are isotropic in both cases. The tests were performed only in 2D

domain. However, the extension of the method in 3D cases is straightforward and is left as a future work. Our simulations show that the incorporation of the approximation error statistics in the inverse model improve the estimation of the location of the focal sources.

The remainder of the chapter is organized as follows. In section 5.1, we give a brief overview of the application domains where the AEA has previously been applied. The theoretical background of the AEA is presented in section 5.2. In section 5.3, we describe the details about the the simulation configurations, the test cases we examine and the computation of the approximation error statistics. The results using simulated data are shown in section 5.4 which discusses the feasibility of the AEA approach to reconstructing focal sources.

5.1 Review on Approximation Error Studies

The AEA has been successfully utilized in several applications, mainly in tomography-related inverse problems, for example optical diffusion tomography (ODT) was studied in [4, 75, 164, 163], electrical impedance tomography (EIT) in [114, 85, 115], and several cases were studied in [66] including dental X-ray imaging and image de-blurring. The extension of the AEA to non-stationary linear and non-linear inverse problems was considered in [56], with application in the time dependent tracking of the distributed thermal conductivity and perfusion coefficients of human tissue [57]. The source of the approximation and modelling errors includes dimensionality reduction (coarse mesh) of the model [4, 74, 85], unknown boundary shape [115], using isotropic model for an anisotropic medium [45], truncation of the computational domain [75], unknown contact impedances or sensors locations [114, 107], domain mismodelling [44] and approximative mathematical model [164].

In ODT, the reduction of modelling errors caused by coarse discretization was studied in [4]. The method was tested with simulated data for two dimensional examples. It was shown that the AEA allows significant reduction in the dimensionality of the FEM model while maintaining accurate reconstruction compared with the conventional model when denser discretization is employed. The feasibility of the AEA for the three-dimensional ODT problem with real data in a cylindrical structure was presented in [75]. The method was able to compensate errors caused both by coarse meshing and by truncation of the computational domain. The approach appears to be especially attractive for low noise levels. In [44], the effects of the body shape discrepancy on the computational model was studied. The difference between the actual geometry and the standard model caused modelling anisotropy even though the actual medium was considered isotropic. The optical absorption coefficients were estimated taking into consideration these uncertainties when employing the AEA.

The anisotropic property of different tissues was considered in [45]. The uncertainties in the background anisotropy values were treated as approximation errors. Specifically, the tissues anisotropy parameters (i.e. the strengths and the direction) were considered as random variables, with Gaussian prior distribution and the approximation error statistics were carried out. In [163], the AEA was applied in order to reduce errors due to the approximate mathematical modelling

of the light propagation in a low scattering body and the model dimensionality reduction. More precisely, the computationally demanding radiative transfer equation was approximated with the approximate diffusion model. However, the diffusion model describes light propagation in strongly scattering media. Therefore, the AEA was used to balance the low accuracy of modelling when a medium with weakly scattering property is examined. In [164], the approximation error caused by the linear formulation of the problem was reduced applying AEA. In particular, the linear model was derived from the first order Born approximation with an infinite space Green's function. Usually, the modelling errors can be corrected when reference measurements with known background optical properties are available. However, frequently the background properties are mismodeled and the reference measurement is not available. In those cases, it was shown that the AEA allowed the reconstruction of good images. In addition, AEA was applied to reduce the spurious artifacts caused by the scalp blood flow which can mask the underlaying cortical activity [46]. Other errors related to optical sensors coupling, position inaccuracies of the electrodes, unknown domain boundary and the feasibility of the AEA to reduced these errors was studied in [107, 108].

Moreover, the approximation error approach has been utilized extensively in the electrical impedance tomography (EIT). In particular, the AEA was applied for compensation of the errors due to coarse discretization and restriction of the domain of interest in geophysical application of EIT [80]. In process tomography, the model reduction and partially unknown level of the liquid inside a cylindrical tank causing erroneous conductivity estimation, was treated with the AEA [113]. Moreover, the extension of the previous study taking into account the errors due to the unknown contact impedances of the electrodes was tested in [114]. In medical applications, EIT has been proposed for the reconstruction of the conductivity distributions in the chest region. The use of a generic geometry (in this case a cylinder) instead of the actual thorax geometry and the reduced discretization introduced errors which were handled with AEA [115]. A further step for the approximate reconstruction of the chest cross sections was proposed in [116]. Particulary, in addition to the conductivity estimation, a low rank approximation of the modelling error was computed. An estimate of the modelling error was then used to compute an approximation for the actual domain boundary shape which had been parameterized with low number of parameters. Finally, other applications using EIT modality in process tomography for the time-dependent tracking of the velocity flows in pipelines employed AEA for the reduction of the model uncertainties [84, 85, 80].

5.2 Approximation Error Approach in EEG Imaging

In this section, we describe the theoretical background of the AEA for the generic EEG imaging problem based on the analysis presented in [67]. The observation model for the EEG imaging problem can be written in the form

$$v = A(\lambda, \sigma, x) + \xi \tag{5.1}$$

where $v \in \mathbb{R}^m$ contains the measured potentials around the scalp, A is a mapping between the quantity of interest x and the measurements. The variable x can be for example the source distribution or the cortical potentials. The parametrization of the head geometry is denoted by λ, σ are the electric conductivity of the tissues and $\xi \in \mathbb{R}^m$ is the measurement noise which is modeled as Gaussian $\xi \sim \mathcal{N}(\xi_*, \Gamma_\xi)$ with mean ξ_* and covariance $\Gamma_\xi \in \mathbb{R}^{m \times m}$.

In practice, for the estimation of x, the problem is represented in discrete form, i.e.

$$A_h(\lambda, \sigma, x) \to A(\lambda, \sigma, x) \quad \text{as} \quad h \to 0, \tag{5.2}$$

where h denotes the discretization level of the domain and $A_h \in \mathbb{R}^{m \times n}$ is the numerical approximation of A.

Let's now define a sufficiently accurate numerical model

$$v = A_\delta(\lambda, \sigma, \bar{x}) + \xi, \tag{5.3}$$

where $A_\delta \in \mathbb{R}^{m \times \bar{n}}$ is the operator between $\bar{x} \in \mathbb{R}^{\bar{n}}$ and the measurements $v \in \mathbb{R}^m$. The index δ in the operator implies that the discretization level and geometry description is such that the numerical approximation errors are lower that the observation errors ξ.

In the AEA, the accurate model is replaced by an approximate computational model $A_0(\lambda_0, \sigma_0, x) \in \mathbb{R}^{m \times n_0}$ with $x \in \mathbb{R}^{n_0}$ in the following way:

$$\begin{aligned} v =& A_0(\lambda_0, \sigma_0, x) + (A_\delta(\lambda, \sigma, \bar{x}) - A_0(\lambda_0, \sigma_0, x)) + \xi \\ =& A_0(\lambda_0, \sigma_0, x) + \varepsilon(\lambda, \sigma, \bar{x}) + \xi \\ =& A_0(\lambda_0, \sigma_0, x) + \nu, \end{aligned} \tag{5.4}$$

where

$$\nu = \varepsilon(\lambda, \sigma, \bar{x}) + \xi \tag{5.5}$$

includes all the model uncertainties and the measurement noise. The error term $\varepsilon(\lambda, \sigma, \bar{x})$ includes all the modeling/approximation errors caused by the discretization, the geometry distortion and the unknown conductivities. In probabilistic terms, the approximation error is the discrepancy of the predictions of the measurements when using the the accurate and approximate model.

The variables $\bar{x}$ and x in (5.4) are related according to

$$x = P\bar{x}, \tag{5.6}$$

where $P : \mathbb{R}^{\bar{n}} \to \mathbb{R}^{n_0}$ is a linear model reduction map from the fine domain to the coarse approximative domain.

The objective in AEA is to solve of the problem from Bayesian point of view, by deriving an computationally efficient approximation $\tilde{\pi}(x|v)$ for the posterior density $\pi(x|v)$ based on the model (5.4). In particular, in the Bayesian framework, all the variables including the measure-

ments are considered as random and the stochastic nature of the problems is described with the help of the probability distributions. The joint density of parameters x, ν and v is

$$\pi(x, \nu, v) = \pi(v|x, \nu)\pi(x, \nu), \tag{5.7}$$

where $\pi(v|x, \nu)$ is the likelihood and $\pi(x, \nu)$ the prior model of x and ν.

The joint posterior density using Bayes' formula, is

$$\pi(x, \nu|v) = \frac{\pi(x, \nu)\pi(v|x, \nu)}{\pi(v)}. \tag{5.8}$$

The joint posterior density model encodes all the uncertainties of the unknowns given the measurements. In practice, our interest is the primary unknown x which is obtained from the marginal conditional distribution

$$\pi(x|v) = \int \pi(x, \nu|v)\, d\nu. \tag{5.9}$$

In general cases, integral (5.9) does not have an analytical solution. However, it can be numerically approximated with algorithms that are computationally highly demanding (e.g. MCMC [66]). As we shall see in then next section, an alternative is to obtain a computationally efficient approximation of the posterior density (5.9), by considering the Gaussian approximation $\tilde{\pi}(x, \nu)$ of the joint density $\pi(x, \nu)$.

5.2.1 Construction of the posterior density

In this section, our objective is to derive a computationally efficient approximation to the posterior density (5.9) using the model (5.4). From Bayes' rule, the posterior is given by

$$\pi(x|v) = \frac{\pi(v|x)\pi(x)}{\pi(v)} \propto \pi(v|x)\pi(x), \tag{5.10}$$

where $\pi(v|x)$ is the likelihood and $\pi(x)$ is the prior density. The probability $\pi(v) > 0$ is a constant and can be neglected. The first step for the estimation of the posterior is the derivation of the likelihood. In particular, from (5.4) we have that the likelihood for given x and ν is

$$\pi(v|x, \nu) = \delta(v - A_0(\lambda_0, \sigma_0, x) - \nu), \tag{5.11}$$

where $\delta(\cdot)$ is the Dirac-delta function. The marginal likelihood over ν is

$$\pi(v|x) = \int \pi(v, \nu|x)\, d\nu. \tag{5.12}$$

From chain rule $\pi(x, v, \nu) = \pi(v|x, \nu)\pi(x, \nu) = \pi(v|\nu, x)\pi(\nu|x)\pi(x)$ [132] and Bayes' theorem, we can derive the density $\pi(v, \nu|x)$, i.e.

$$\pi(v, \nu|x) = \pi(v|\nu, x)\pi(\nu|x). \tag{5.13}$$

From (5.12), (5.13) and (5.11) the likelihood is

$$\pi(v|x) = \int \pi(v|\nu, x)\pi(\nu|x)\, d\nu = \int \delta(v - A_0(\lambda_0, \sigma_0, x) - \nu)\pi(\nu|x)\, d\nu. \tag{5.14}$$

Thus,

$$\pi(v|x) = \pi_{\nu|x}(v - A_0(\lambda_0, \sigma_0, x)|x). \tag{5.15}$$

The subscript $\nu|x$ is used to clarify that $\pi_{\nu|x}(.)$ is the conditional probability density of the random variable ν given x.

From (5.10) and (5.15), the posterior density becomes

$$\pi(x|v) \propto \pi(v|x)\pi(x) = \pi_{\nu|x}(v - A_0(\lambda_0, \sigma_0, x)|x))\pi(x). \tag{5.16}$$

In the AEA, the additive noise is consider Gaussian with $\xi \sim \mathcal{N}(\xi_*, \Gamma_\xi)$ and independent of x and the modelling parameters. Furthermore, before the inference, the joint density $\pi(x, \varepsilon)$ is approximated by a Gaussian distribution $\tilde{\pi}(x, \varepsilon)$. Therefore, the conditional $\pi_{\nu|x}$ (5.15) is approximated by

$$\tilde{\pi}_{\nu|x}(v - A_0(\lambda_0, \sigma_0, x)|x) \propto \exp\left(-\frac{1}{2}(v - A_0(\lambda_0, \sigma_0, x) - \nu_{*|x})^{\mathrm{T}}\Gamma_{\nu|x}^{-1}(v - A_{h_0}(\lambda_0, \sigma_0, x) - \nu_{*|x})\right) \tag{5.17}$$

where

$$\begin{aligned} \nu_{*|x} =& \varepsilon_{*|x} + \xi_* \\ \Gamma_{\nu|x} =& \Gamma_{\varepsilon|x} + \Gamma_\xi \end{aligned} \tag{5.18}$$

The approximate posterior model (5.16) becomes

$$\tilde{\pi}(x|v) \propto \tilde{\pi}_{\nu|x}(v - A_0(\lambda_0, \sigma_0, x)|x))\pi(x). \tag{5.19}$$

In the next section, we derive the formulae of the conditional mean $\varepsilon_{*|x}$ and covariance matrix $\Gamma_{\varepsilon|x}$.

Approximation Error Statistics

Let's z denote the stacked variables

$$z = \begin{pmatrix} x \\ \varepsilon \end{pmatrix}. \tag{5.20}$$

The joint distribution of z is

$$\tilde{\pi}(x,\varepsilon) = \pi(z) \propto \exp\left(-\frac{1}{2}(z-z_*)^{\mathrm{T}}\Gamma_z^{-1}(z-z_*)\right) \tag{5.21}$$

where

$$\Gamma_z = \begin{bmatrix} \Gamma_x & \Gamma_{x\varepsilon} \\ \Gamma_{\varepsilon x} & \Gamma_\varepsilon \end{bmatrix} \tag{5.22}$$

is the joint covariance matrix with the following inverse

$$\Gamma_z^{-1} = B = \begin{bmatrix} B_{11} & B_{12} \\ B_{21} & B_{22} \end{bmatrix} \tag{5.23}$$

and mean $z_* = (x_*, \varepsilon_*)^{\mathrm{T}}$.

From (5.20) and (5.23), the expansion of the exponent in (5.21) yields

$$\tilde{\pi}(x,\varepsilon) \propto \exp -\frac{1}{2}\left((x-x_*)^{\mathrm{T}}B_{11}(x-x_*) + (\varepsilon-\varepsilon_*)^{\mathrm{T}}B_{22}(\varepsilon-\varepsilon_*) + 2(x-x*)^{\mathrm{T}}B_{12}(\varepsilon-\varepsilon_*)\right) \tag{5.24}$$

as $B_{12} = B_{21}^{\mathrm{T}}$.

The conditional $\tilde{\pi}(\varepsilon|x)$ is estimated from (5.24) by completing the quadratic form in the exponential into squares

$$\tilde{\pi}(\varepsilon|x) \propto \exp\left(-\frac{1}{2}(\varepsilon-\varepsilon_{*|x})^{\mathrm{T}}B_{22}(\varepsilon-\varepsilon_{*|x})\right) \tag{5.25}$$

where the conditional mean is

$$\varepsilon_{*|x} = \varepsilon_* - B_{22}^{-1}B_{21}(x-x_*) \tag{5.26}$$

and the covariance matrix

$$\Gamma_{\varepsilon|x} = B_{22}^{-1} \tag{5.27}$$

Using the matrix inversion Lemma [66], we have that $B_{22}^{-1} = \Gamma_\varepsilon - \Gamma_{\varepsilon x}\Gamma_x^{-1}\Gamma_{x\varepsilon}$ and $B_{22}^{-1}B_{21} = -\Gamma_{\varepsilon x}\Gamma_x^{-1}$. Substituting these identities into (5.26) and (5.27)

$$\begin{aligned} \varepsilon_{*|x} =& \varepsilon_* + \Gamma_{\varepsilon x}\Gamma_x^{-1}(x-x_*) \\ \Gamma_{\varepsilon|x} =& \Gamma_\varepsilon - \Gamma_{\varepsilon x}\Gamma_x^{-1}\Gamma_{x\varepsilon}. \end{aligned} \tag{5.28}$$

5.2.2 Maximum A Posteriori Estimate

The statistical inference from the posterior density in a high-dimensional parameter space is conceptually and computationally inconvenient. Instead, Bayesian point estimates such as the maximum a posteriori (MAP) estimate enables visualization and ease interpretation of the so-

lution. The MAP estimate of x is

$$\hat{x} = \arg \max_x \tilde{\pi}(x|v) \tag{5.29}$$

where $\tilde{\pi}(x|v)$ was defined in (5.19).

Thus, variable x is estimated according to

$$\hat{x} := \min_x \|L_\nu(v - A_0(\lambda_0, \sigma_0, x) - \nu_{*|x})\|_2^2 - 2\ln \pi(x), \tag{5.30}$$

where $\Gamma_{\nu|x}^{-1} = L_\nu^{\mathrm{T}} L_\nu$ is the Cholesky factorization of $\Gamma_{\nu|x}^{-1}$ [100] and $\pi(x)$ is chosen prior model.

There are also other Bayesian point and spread estimates e.g. conditional mean (CM) $x_{\mathrm{CM}} = \int x\tilde{\pi}(x|v)\,dx$ and conditional covariance estimate given by $\mathrm{cov}(x|v) = \int (x - x_{\mathrm{CM}})(x - x_{\mathrm{CM}})^{\mathrm{T}}\tilde{\pi}(x|v)\,dx$. In this thesis, we use only the MAP estimate and we compute x by solving problem (5.30).

5.3 Computations and Simulated Data

5.3.1 EEG focal Source Imaging using AEA

For the EEG inverse computations, we employ the distributed source modeling(DSM) which relates linearly the dipole source vector with the measured potentials, $v \in \mathbb{R}^m$ [7]. The finite element method (FEM) is used for the numerical formulation of the problem.

Briefly, the EEG observation source model in a 2D domain is

$$v = \bar{K}_{\bar{\lambda}}(\bar{\sigma})\bar{d} + \xi, \quad \xi \sim \mathcal{N}(0, \Gamma_\xi), \tag{5.31}$$

where $\bar{K}_{\bar{\lambda}}(\bar{\sigma}) \in \mathbb{R}^{m\times 2\bar{n}}$ is the lead field matrix of the accurate geometry, $\bar{d} = [\bar{d}_x^{\mathrm{T}}, \bar{d}_y^{\mathrm{T}}]^{\mathrm{T}} \in \mathbb{R}^{2\bar{n}}$ is the accurate representation of the dipole components in column form, index $\bar{\lambda}$ denotes the domain (i.e. geometry parameter) and $\bar{\sigma} \in \mathbb{R}^{\bar{n}}$ is the conductivity distribution. For the additive noise ξ we assume that has covariance matrix $\Gamma_\xi = \gamma_\xi^2 I^{m\times m}$ where $I^{m\times m}$ is the identity matrix.

In practical clinical measurements, the exact knowledge of the geometry and electrical properties of the head are not always available and therefore the reconstruction is carried out using an approximate model λ_0.

The accurate model is replaced by an approximate model and the approximation error is incorporated in the previous equation according to

$$\begin{aligned} v =& K_{\lambda_0}(\sigma_0)d + (\bar{K}_{\bar{\lambda}}(\bar{\sigma})\bar{d} - K_{\lambda_0}(\sigma_0)d) + \xi \\ =& K_{\lambda_0}(\sigma_0)d + \varepsilon(\bar{d}, \bar{\lambda}, \bar{\sigma}) + \xi \\ =& K_{\lambda_0}(\sigma)d + \nu \end{aligned} \tag{5.32}$$

where $d = [d_x^{\mathrm{T}}, d_y^{\mathrm{T}}]^{\mathrm{T}} \in \mathbb{R}^{2n_0}$, $K_{\lambda_0}(\sigma_0) \in \mathbb{R}^{m\times 2n_0}$ $(m < n_0)$ is the lead field matrix of the standard geometry λ_0 and $\sigma_0 \in \mathbb{R}^{n_0}$. The total noise is $\nu = \varepsilon(\bar{d}, \bar{\lambda}, \bar{\sigma}) + \xi$, where $\varepsilon(\bar{d}, \bar{\lambda}, \bar{\sigma})$ is the

approximation error term due to the geometry and conductivity uncertainty. The additive noise ξ is statistically independent of the dipole distribution d.

The dipole source distribution in the standard geometry can be represented by a linear transformation

$$d = P\bar{d}, \tag{5.33}$$

where $P \in \mathbb{R}^{n\times\bar{n}}$ is a matrix that interpolates nodal dipoles from geometry $\bar{\lambda}$ to λ_0 according to a deformation scheme. The geometry deformation model is defined as

$$\mathrm{x} = T(\bar{\mathrm{x}}), \tag{5.34}$$

where $\bar{\mathrm{x}} \in \Omega_{\bar{\lambda}}$ is a position vector in the MRI domain $\Omega_{\bar{\lambda}}$ and $\mathrm{x} \in \Omega_0$ a position vector in the standard circular domain Ω_0 and $T : \Omega_{\bar{\lambda}} \to \Omega_{\lambda_0}$ is the domain deformation operator.

Analogous to the analysis in section 5.2, the posterior distribution is

$$\tilde{\pi}(d|v) \propto \tilde{\pi}_{\nu|d}(v - K_{\lambda_0}(\sigma_0)d|d))\pi(d). \tag{5.35}$$

For the reconstruction of sparse focal sources, the prior distribution $\pi(d)$ is

$$\pi(d) \propto \exp\left(-\frac{\alpha}{2}\sum_{i=1}^{n_0} w_i\|\mathrm{d}_i\|_2\right), \tag{5.36}$$

where d_i is the dipole vector at location i, α a scaling factor and w_i the depth weighting factors defined in section 3.3. The approximate posterior is

$$\tilde{\pi}(d|v) \propto \exp\left(-\frac{1}{2}\|L_\nu(v - K_{\lambda_0}(\sigma_0)d - \nu_{*|d})\|_2^2 - \frac{\alpha}{2}\sum_{i=1}^{n_0} w_i\|\mathrm{d}_i\|_2,\right) \tag{5.37}$$

where $L_\nu^{\mathrm{T}}L_\nu$ is the Cholesky factorization of $\Gamma_{\nu|d}^{-1}$. The joint covariance matrix is

$$\Gamma_{\nu|d} = \Gamma_{\varepsilon|d} + \gamma_\xi \mathrm{I}^{m\times m} \tag{5.38}$$

and the mean is $\nu_{*|d} = \varepsilon_{*|d}$. The approximation error statistics are

$$\begin{aligned}\varepsilon_{*|d} =& \varepsilon_* + \Gamma_{\varepsilon d}\Gamma_d^{-1}(d - d_*)\\ \Gamma_{\varepsilon|d} =& \Gamma_\varepsilon - \Gamma_{\varepsilon d}\Gamma_d^{-1}\Gamma_{d\varepsilon}\end{aligned} \tag{5.39}$$

The dipole mean is considered $d_* \simeq 0$. As in section 3.2.3, we have that the scaling parameter α is $\alpha = c\alpha_{max}$ where $c \in (0, 1)$ and

$$\alpha_{max} = \max\left\{\frac{\sqrt{\sum_{j=1}^{2} b^{\mathrm{T}}U^{(i+(j-1)n_0)}}}{w_i} \text{ for } i = 1, \ldots, n_0\right\} \tag{5.40}$$

where $U^{(i+(j-1)n_0)}$ is the corresponding column of the matrix $U = L_\nu(K_{\lambda_0} + \Gamma_{\varepsilon d}\Gamma_d^{-1})$ and $b = L_\nu(v - \varepsilon_*)$.

5.3.2 Computation of the Error Statistics

The approximation error statistics can be enclosed in the the analytical expression of the conditional mean (CM) or MAP estimate in the case of linear Gaussian observation model, Gaussian prior and simple modelling errors e.g. model reduction errors. However, the computation of the estimate requires the solution of a system which still includes the complexity of the accurate modeling (see for instance equation (5.26) in [66]). Additionally, for general cases where the prior is not Gaussian, for example, in the EEG sparse imaging problem where $L_{1,2}$ norm prior is employed or for a non linear problem, these estimates do not have analytical expressions. Thus, the mean and covariance of the approximation error (5.39) need to be computed through simulations.

For the estimation of the mean and covariance matrix of the approximation error, we employed K different (training) geometries denoted $\{\bar{\lambda}^{(i)};\ i = 1, \ldots, \mathrm{K}\}$. The dipole moments were drawn from a Gaussian distribution given by $\pi(\bar{d}) \propto \exp\left(-\frac{1}{2\gamma_{\bar{d}}}\bar{d}^{\mathrm{T}}\bar{d}\right)$. We note that this distribution is a function of $\bar{d}^{\mathrm{T}}\bar{d} = \|\bar{d}\|_2^2$ and does not, therefore, depend on the dipole orientation. The conductivities, $\bar{\sigma}$, were drawn from the truncated Gaussian distribution $\pi(\bar{\sigma}) \propto \pi_+(\bar{\sigma}) \exp\left(-\frac{1}{2\gamma_{\bar{\sigma}}}(\bar{\sigma} - \bar{\sigma}_*)^{\mathrm{T}}(\bar{\sigma} - \bar{\sigma}_*)\right)$ where $\bar{\sigma}_*$ are the nominal tissue conductivities and $\pi_+(\bar{\sigma}) = 1$ when all element of $\bar{\sigma} > 0$ and equals to zero otherwise.

For the computation of the error statistics, for each geometry $\bar{\lambda}^{(i)}$, a set of M draws were generated from the distributions $\pi(\bar{d})$ and $\pi(\bar{\sigma})$. The samples of the dipole distributions, $\bar{d}$, and the parameter $\bar{\sigma}$ are denoted by

$$\{\bar{d}^{(l)}, \bar{\sigma}^{(l)},\ l = 1, \ldots, M\} \tag{5.41}$$

for each geometry $\bar{\lambda}^{(i)}$. The total number of samples was $N_s = \mathrm{K}M$.

By setting $k = (i-1)\mathrm{K} + l$, the predictions of the accurate and the approximate model were $v^{(k)} = \bar{K}_{\bar{\lambda}^{(i)}}(\bar{\sigma}^{(k)})\bar{d}^{(k)}$ and $v^{(k)} = K_{\lambda_0}(\sigma_0)d^{(k)}$. Samples $d^{(k)}$ were estimated from the linear reduction mapping from geometry $\bar{\lambda}^{(i)}$ to λ_0, $d^{(k)} = P_{\bar{\lambda}^{(i)}}\bar{d}^{(k)}$ (Fig. 5.2).

The samples of the approximation errors $\varepsilon^{(k)}$ were

$$\varepsilon^{(k)} = \bar{K}_{\bar{\lambda}^{(i)}}(\bar{\sigma}^{(k)})\bar{d}^{(k)} - K_{\lambda_0}(\sigma_0)d^{(k)} \quad \text{for } k = 1, \ldots, \mathrm{K}M. \tag{5.42}$$

Let us denote ζ the stacked variables $\zeta = \begin{pmatrix} d \\ \varepsilon \end{pmatrix}$. The numerical joint mean and covariance matrix of the approximation error ε and the unknown d is given by

$$\zeta_* = \frac{\sum_{k=1}^{N_s} \zeta^{(k)}}{N_s} \tag{5.43}$$

and

$$\Gamma_\zeta = \frac{1}{N_s - 1} \sum_{k=1}^{N_s} \theta^{(k)} \theta^{(k)^{\mathrm{T}}} \tag{5.44}$$

where $N_s = \mathrm{K}M$, $\zeta^{(k)} = \begin{pmatrix} d^{(k)} \\ \varepsilon^{(k)} \end{pmatrix}$ are the samples and $\theta^{(k)} = \begin{pmatrix} d^{(k)} \\ \varepsilon^{(k)} \end{pmatrix} - \zeta_*$.

The numerical mean is $\zeta_* \approx \begin{pmatrix} d_* \\ \varepsilon_* \end{pmatrix}$ and the covariance $\Gamma_\zeta \approx \begin{pmatrix} \Gamma_d & \Gamma_{d\varepsilon} \\ \Gamma_{\varepsilon d} & \Gamma_\varepsilon \end{pmatrix}$.

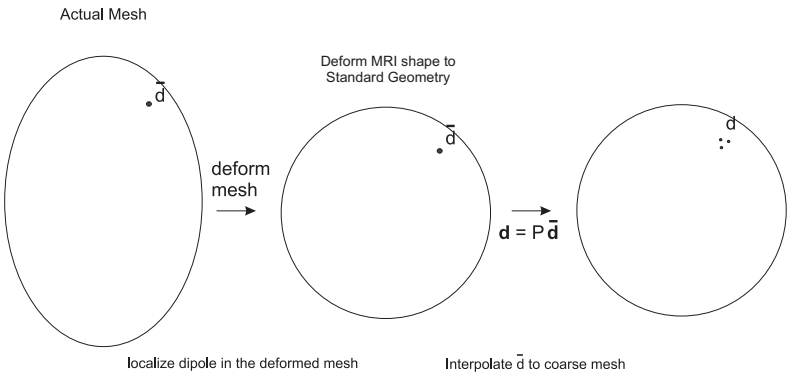

Figure 5.2: Projection of a single dipole to the standard geometry

5.3.3 Different Reconstructions and Quantification of the Accuracy

To test the approximation error approach, a new head geometry that was not included in the set of previous (training) geometries was selected. Then, the boundary data was computed using the accurate head model. With this data, three different reconstructions were computed and compared.

First we estimate the boundary data v_+ by solving the forward problem

$$v_+ = \bar{K}_{\bar{\lambda}_+}(\bar{\sigma}_+)\bar{d}_+ + \xi, \tag{5.45}$$

where $\bar{\lambda}_+$ denotes the accurate geometry with lead field matrix $\bar{K}_{\bar{\lambda}_+}(\bar{\sigma}_+) \in \mathbb{R}^{m \times 2\bar{n}}$, when a sparse dipole vector $\bar{d}_+$ and a noise vector ξ are given.

Afterwards, three different inverse solutions were computed using the estimated data v_+. The first one was computed using a coarsely discretized version of the accurate head model with the correct conductivity distribution. The coarse discretization was used in order to avoid the so-called inverse crime [66]. The second inverse solution was computed using the standard model that consisted of three concentric circles [36] that depicted scalp, skull and brain. The third solution was computed again using the standard model but now accompanied with the statistics that compensated the approximation errors.

The maximum a posteriori (MAP) estimates were used for the evaluation and visualization

of the results. The MAP estimate in the accurate geometry is

$$\hat{d}_{acc} := \min_{d} \|\frac{1}{2}\gamma_{\xi}^{-1}(v_{+} - K_{\lambda_{+}}(\sigma_{+})d)\|_2^2 + \alpha_1 \sum_{i=1}^{n} w_i \|\mathrm{d}_i\|_2, \tag{5.46}$$

where γ_{ξ} is the variance of the measurement noise, $K_{\bar{\lambda}_{+}} \in \mathbb{R}^{m \times 2n}$, $n < \bar{n}$ and $\sigma_{+} = P_{\lambda_{+}}\bar{\sigma}_{+}$ with $P_{\bar{\lambda}_{+}} \in \mathbb{R}^{n \times \bar{n}}$ being a linear interpolation matrix for the fine mesh to the coarse actual mesh.

Subsequently, the MAP estimate in the standard geometry is

$$\hat{d}_{st} := \min_{d} \|\frac{1}{2}\gamma_{\xi}^{-1}(v_{+} - K_{\lambda_0}(\sigma_0)d)\|_2^2 + \alpha_2 \sum_{i=1}^{n_0} w_i \|\mathrm{d}_i\|_2, \tag{5.47}$$

and finally, the third MAP estimate that utilizes the approximation error approach in the standard geometry is

$$\hat{d}_{AEA} := \min_{d} \|L_{\nu}(v - K_{\lambda_0}(\sigma_0)d - \nu_{*|d})\|_2^2 + \alpha_3 \sum_{i=1}^{n_0} w_i \|\mathrm{d}_i\|_2 \tag{5.48}$$

The scaling parameters (α_1, α_2 and α_3) were selected based on visual observations but their values were always lower than the bound defined in section 3.2.3.

5.3.4 Simulation Configuration

In this section, we describe the set-up of the simulations for the evaluation of the performance of the models (5.46), (5.47) and (5.48) when used to reconstruct focal sources.

Head Models for the Error Statistics

For the computation of the approximation error statistics, several accurate head models were needed. Therefore, 32 (training) head geometries were acquired from the OASIS project database [96]. The head geometries were from healthy adults, both men and women.

The analysis was carried out in 2D. First, the traverse (axial) cross sections which correspond to the head area above the eyes were selected (for example see the left image in Fig. 5.3). Each cross section was segmented into three compartments Scalp/Skull/Brain. The scalp was extracted using the FieldTrip toolbox [129]. The skull was segmented using threshold and morphology operators [136] and the brain with the help of the brain masks provided by the OASIS database for each individual adult.

Then, 32 measurement electrodes and an additional fixed ground electrode (above the right-hand-side ear) were equally distributed around the scalp. The corresponding meshes were constructed using comsol64 [53]. The lead field matrices were estimated using the FEM with linear nodal basis functions [182].

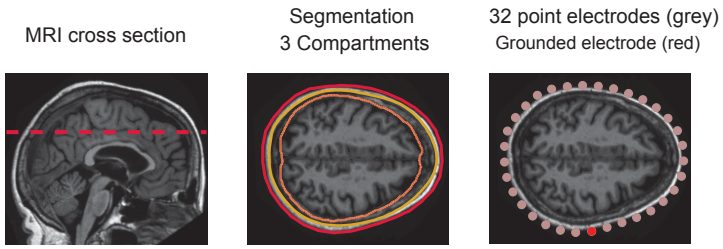

Figure 5.3: Left image: MRI cross section, middle: segmentation into scalp, skull and brain area, right image: 32 point sensors around the 2D domain and a fixed ground point.

Geometries for the Validation

To evaluate the AEA, a new head geometry (the left image in Fig. 5.4) that was not included in the set of the (training) geometries, was used. The mesh of the forward problem was finer than the inverse meshes. For the inverse solutions, we used two different meshes. The mesh in the middle of Fig. 5.4 is a coarse version of the forward mesh. The circular domain ("Standard Model" in Fig. 5.4) was used in the minimization problems (5.47) and (5.48).

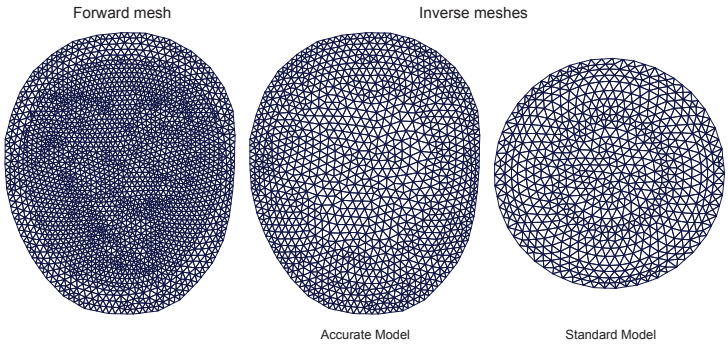

Figure 5.4: The discrete domains used in the forward and inverse problem. (Left image) A fine mesh used to compute the accurate noiseless (forward) measurements. This mesh was constructed based on an MRI cross section. (Middle image) A coarse mesh of the same MRI geometry which was employed in the (accurate model) inversion and (right image) the standard circular mesh employed in the inversion for the standard model and AEA model.

Projection Operator

In this section, we give an explanation how the mapping between the actual geometry and the circular standard model is performed and how the projection operator P in equation (5.33) is constructed.

The selected geometry deformation model (5.34) preserves the angle and relative distance between the center of the domain and the boundary. The construction of the interpolation matrix $P_{\bar{\lambda}}$ in (5.33) was carried out as follows; let $\bar{\mathrm{x}}_i$ be the position vector of the i^{th} node of the FEM mesh of geometry $\bar{\lambda}$. First, we estimate the deformed coordinate $\mathrm{x}_i = T(\bar{\mathrm{x}}_i)$. The estimation is based on $\mathrm{x}_i = r\frac{\bar{\mathrm{x}}_i}{\bar{r}}$, where $\bar{r}$ is the length of the line passes, through point $\bar{\mathrm{x}}_i$ and

connects the center of the domain and the boundary for the MRI geometry, and r is the radius of the standard circular geometry (see for example left and middle image in Fig. 5.5). Subsequently, the FEM element of the standard mesh in which the point x_i is located, is estimated. Once this has been done, we express x_i as a linear combination of the element nodes using barycentric coefficients (l_1, l_2, l_3). We assign the barycentric coefficients in the elements of the i^{th} row of P which correspond to the indices of the nodes of the FEM element where x_i is located (right mesh in Fig. 5.5 shows the element and the nodes of the standard mesh where x_i is located).

Similar deformation scheme has been previously used in [108, 115]. This scheme was found useful also in the test cases studied here. Alternative models for the mapping can be found from image registration literature [49]. However, for small deformation between convex domains we do not expect significant differences between the mapping methods.

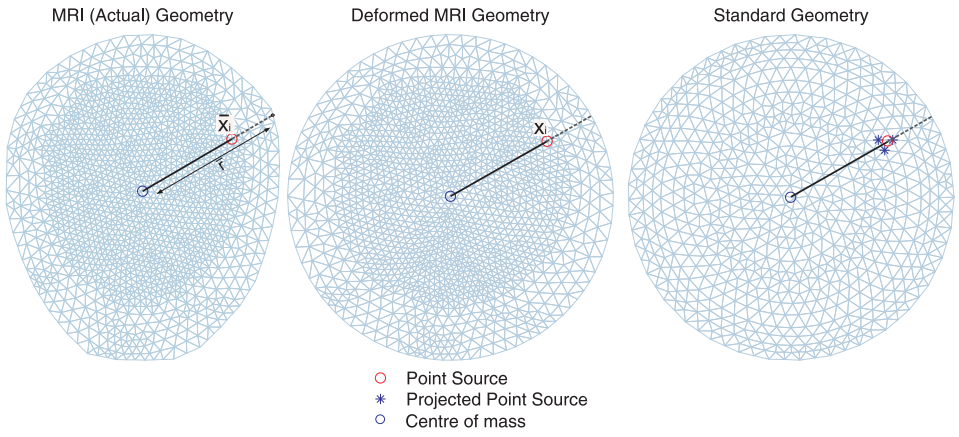

Figure 5.5: First, the deformed coordinates are estimated using a simple radial deformation scheme that keeps the relative distances with respect to the origin. Subsequently, a linear interpolation scheme (barycentric coefficients) is applied for the estimation of the coefficients in the mapping P.

Sources Set-up

The candidate sources were located in the grey matter of the brain (Fig. 5.6) which is in accordance with the fact that the grey matter includes regions of the brain involved in muscle control and sensory perception [122].

The candidate source locations for the accurate model are shown on the left in Fig. 5.6. The candidate source locations of the standard model are the whole brain area, as shown on the right in Fig. 5.6. A single dipole source was generated at a randomly selected candidate source location. The values of the dipole components (in x and y coordinates) were drawn from a Gaussian distribution. The single peak was blurred using a Gaussian [5×5pixel] (where 1 pixel $\approx$ 1mm) low pass filter. Hence, a single source consisted of a small patch with smoothly varying magnitudes and similar orientation. This source resembles a set of pyramidal neurons that form layers with similar orientation. Depending on how many active regions we wanted to

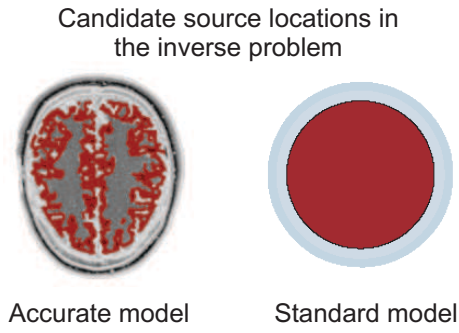

Figure 5.6: Candidate source locations for the accurate model and the standard model.

simulate, we selected the corresponding number of source locations. In the following test cases, we simulated up to three different active regions.

Scaling Parameter and Weighting Factors

The scaling parameters in (5.48), (5.46) and (5.47) were in the range $[0.1\alpha_{max}, 0.001\alpha_{max}]$ where α_{max} is the upper bound which can be derived for each minimization problem according to the analysis in section 3.2.3, and it depends on the lead field matrix, covariance matrix and measurements. For the AEA problem (5.48), the upper bound of this parameter is given in (5.40). The scaling parameters were selected to be in this range in order to relax the strict sparsity and to enable the fast algorithmic convergence.

The scaling parameter of the AEA minimization problem (5.48) was selected to be slightly higher than the parameters used in the other two problems (5.46) and (5.47). Specifically, matrix L_ν in (5.48) tends to spread the solution. Therefore, we ensured that the solution in (5.48) is focal by selecting a slightly higher scaling parameter. The weighting factors w_i were computed according to section 3.3.

5.3.5 Metrics for Evaluation

The validation of the inverse EEG method is a difficult task due to the lack of the "ground truth" and the gap for systematic ways of inspection and supervision of the brain activity and functionality. The most efficient way to test the liability of the proposed method is by reconstructing simulated data $\bar{d} \in \mathbb{R}^{2\bar{n}}$. In this section, we describe the validation metrics used to evaluate the accuracy of the inverse EEG solutions.

We denote $\hat{d} \in \mathbb{R}^{2n_0}$ a solution of the inverse problem and $d = P\bar{d} \in \mathbb{R}^{2n_0}$ the projection of the actual dipole vector to the inverse geometry. We compared the estimated $\hat{d}$ with the projected vector d or the actual dipole $\bar{d}$ by using four different metrics. The first two metrics, the earth's mover distance (EMD) and the nearest source distance (NSD) give a quantitative rendering of how far are the estimated distribution from the actual sources. With the strength difference (SD) we compared the total power difference between the two distributions. The weighted angle difference (WAD) gives information related to the difference in the orientations

of the actual sources and the reconstructed ones.

In particular, for assessing quantitatively the source localization accuracy we used the earth mover's distance (EMD) metric. The EMD has been introduced in computer vision for comparing image [145] and it has been used previously in EEG [42, 91] as it is suitable for comparing signals with possibly non-overlapping support e.g. sparse vectors.

The EMD is defined as the minimum work that must be done to transform one normalized discrete signal into the other, when a metric between the discrete points of the domain is provided. For the EEG inverse solution, we are interested in measuring the weighted distance between the locations of the actual sources and the estimated distribution. The EMD gives these weights which are called flow values and they correspond to the fraction of the estimated dipole strength which is "transported" from location i to j in such way that the work is minimized. The EMD is shown graphically in Fig. 5.7. Given $\hat{d}$ and d, the EMD is estimated according to

$$\begin{aligned} \mathrm{EMD}(\hat{d}, d) &= \min_{\{f_{ij}\}} \sum_{i,j} f_{ij} l_{ij} \\ \text{s.t. } \sum_{i,j} f_{ij} = 1,\ \sum_{j} f_{ij} &\leq \hat{g}_i,\ \sum_{i} f_{ij} \leq g_j \end{aligned} \tag{5.49}$$

where $\hat{g}_i = \frac{\|\hat{\mathrm{d}}_i\|_2}{\sum_{i=1}^{n_0} \|\hat{\mathrm{d}}_i\|_2}$ is normalized vector of the estimated dipole strengths and $g_j = \frac{\|\mathrm{d}_j\|_2}{\sum_{j=1}^{n_0} \|\mathrm{d}_j\|_2}$ the normalized actual strengths, for $i, j = 1, \ldots, n_0$ and f_{ij} the flow. As a metric between the source locations we use the Euclidean distance $l_{ij} = \|\mathrm{x}_i - \mathrm{x}_j\|_2$ where x_i and x_j are the coordinates of the i^{th} and j^{th} nodes of the mesh. The minimization problem (5.49) is computed

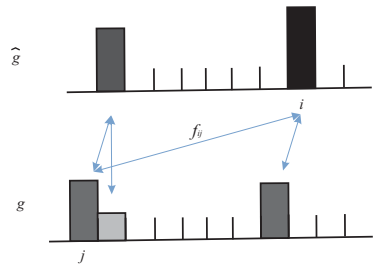

Figure 5.7: The EMD for the EEG problem is the minimum work needed to transform the normalized strength $\hat{g}$ of the estimated distribution to the actual normalized distribution g.

using linear programming solver [11, 135].

The second metric used is called Nearest Source Distance (NSD) and it is given by

$$\mathrm{NSD} = \frac{\sum_i \min\limits_{j=1,\ldots,k} \{l_{ij}\} \|\hat{\mathrm{d}}_i\|_2}{\sum_i \|\hat{\mathrm{d}}_i\|_2}, \tag{5.50}$$

where $\min\limits_{j=1,\ldots,k} \{l_{ij}\}$ is the minimum Euclidean distance between the estimated dipole at location i and a focal source at location x_j with k the total number of actual focal sources.

For instance, in Fig. 5.8, there are two actual sources ($j = 1, 2$) and the estimated distribution

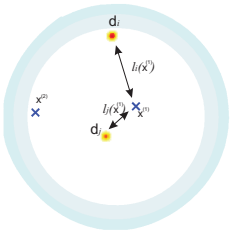

Figure 5.8: NSD is the mean distance between a reconstructed distribution and its nearest actual dipole source.

has two active regions which are close to source $j = 1$. The NSD is the weighted distances between the estimated distribution and the location $\mathrm{x}_{(1)}$.

We used two different metrics for the source localization evaluation because there are cases were the depicted results cannot be explained by the EMD and we needed the complementary NSD validation metric. Specifically, the EMD and NSD metrics are expected to give almost similar results for a single source case. However, for more than one sources, the values of the EMD and NSD may differ from each other. Usually the EMD gets higher values than the NSD. For example, for the case of two equal sources which are far from each other, the reconstruction algorithm may give two sources in the correct locations but with uneven strengths. In this case, the EMD value can be unexpectedly high because a fraction of the more intense source is "transferred" to the less intense source location. On the other hand the NSD value is going to be quite low (for example see test case in Fig. 5.14).

Additionally, to assess the strength difference in Decibel (db) between the simulated vector $\bar{d}$ and the reconstructed $\hat{d}$ we use the strength difference metric

$$\mathrm{SD} = 10 \log_{10} \frac{\|\hat{d}\|_2^2}{\|\bar{d}\|_2^2} \tag{5.51}$$

For the orientation error we estimate the angle between the dipole $\hat{\mathrm{d}}_i$ at location i and the projected dipole d_j weighted by the flow values f_{ij} that were estimated in (5.49) according to

$$\mathrm{WAD} = \sum_{i,j} f_{ij} |\omega_{ij}| \quad \text{where } \omega_{ij} = \cos^{-1} \frac{\hat{\mathrm{d}}_i \cdot \mathrm{d}_\mathrm{j}}{\|\hat{\mathrm{d}}_i\|_2 \|\mathrm{d}_j\|_2}. \tag{5.52}$$

5.4 Results and Discussion

In this section, we study the feasibility of the AEA to reduce the source location errors due to the unknown head shape, different thicknesses of the head layers, coarse discretization of the mesh and conductivity uncertainties. Two different types of test cases were studies. In the first set of test cases, it was studied how AEA could be used to compensate head geometry errors. In the second set of test cases, also conductivity and measurement errors were considered.

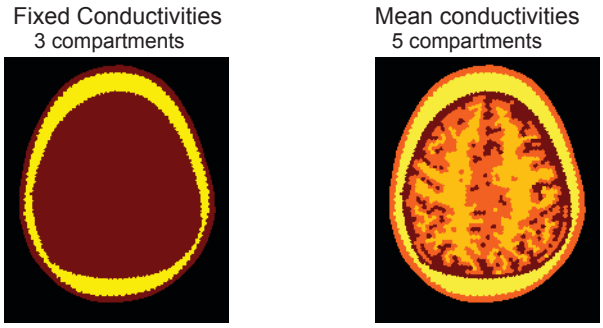

Figure 5.9: Conductivity distribution of the forward models. The left hand side image corresponds to the first cases (unknown geometry) where the conductivities in the three compartments are fixed. The right hand side image has the mean values of the conductivities for the 5 layer model which corresponds to the second case study (Unknown geometry and conductivities).

5.4.1 Case 1: Unknown geometry

In these test cases, only the effects of the unknown geometry were studied. A new head geometry (that was not included in the training geometries) and sparse dipole distributions were selected. The boundary data was computed using the forward model with accurate geometry and three compartments (scalp, skull, brain as shown in the left hand side picture of Fig. 5.9). The conductivities of the different compartments (0.33, 0.016 and 0.33 S/m, respectively) were fixed. The total number of MRI cross sections used for the estimation of the error statistics in (5.42) was $K = 32$[1].

In the following figures, the small images on the left hand side show the actual head geometry and the simulated dipoles. The location of the simulated dipole is marked with a blue circle and the orientation with a small blue line. The remaining images, starting from the left, show the reconstruction solution of (5.46), (5.47) and (5.48) respectively. In particular, in the images titled "Accurate model" we have the results obtained by solving the accurate model (5.46) where the geometry and conductivity distribution are the same as in the forward model but the dimension of the inverse model is lower. The images named "Standard" depict the result obtained from the standard model (5.47), in this case we considered the 3 concentric circles and we did not take into account the AEA statistics. The right hand side images ("AEA") show the AEA results obtained from (5.48). The blue circle shows the correct location of the projected

[1]Appendix D.1 presents reconstruction results when the approximation error statistics were estimated based on different number of MRI geometries.

dipole. The estimated metrics (as defined in section 5.3.5) for each inverse model are shown below the images. In the right hand side of the figures, there is a scale in millimeters in order to give a quantitative estimation how far are located the reconstructed sources from the actual dipole locations. In this study, there was no additive measurement noise.

Single Source

The first set of pictures shows the results in the cases where a single focal region of activity is recovered. We studied the reconstructions for different depths and different locations around the brain: we placed the source deep in the brain (Fig. 5.10) and in the frontal area and back side (Fig. 5.11). In the test case with a deep source, all the models have good performance as shown in Fig. 5.10. With visual inspection of Fig. 5.11, we can see that the AEA model is

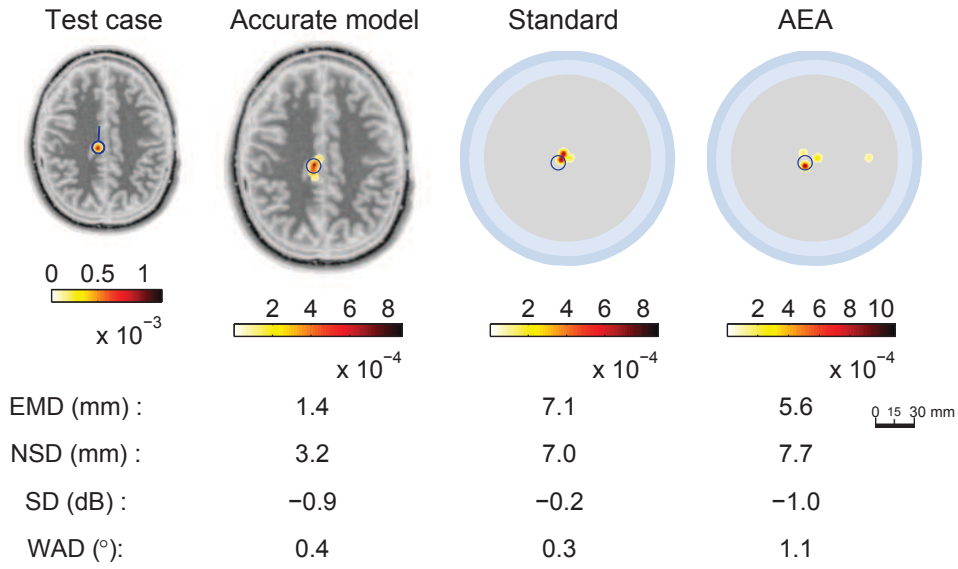

Figure 5.10: A test case of a single deep source reconstruction is examined. The left image shows the actual dipole source and the other three pictures (from left to right) show the reconstructions when: (1) the actual geometry and conductivity distribution, (2) the standard modelling and (3) the AEA model are used.

able to localize a superficial dipole source more accurately than the standard model. This is in agreement with the EMD and NSD metrics. Also, it is worth noting that the differences between the EMD values of the accurate and AEA model are quite moderate.

Moreover, the standard model without using the AEA recovered slightly scattered source distributions which quantitatively are expressed with higher values of the EMD metric. The scattered solutions are partly related to the differences between the forward geometry and the inverse one. The solution would be less scattered if a higher α parameter had been selected. However, the dipole would have been misplaced deeper in the brain. Also, about the standard model without AEA we can say that this model gives better reconstruction when the source is in the back side compared to the case where the source is in the front side. This may be related

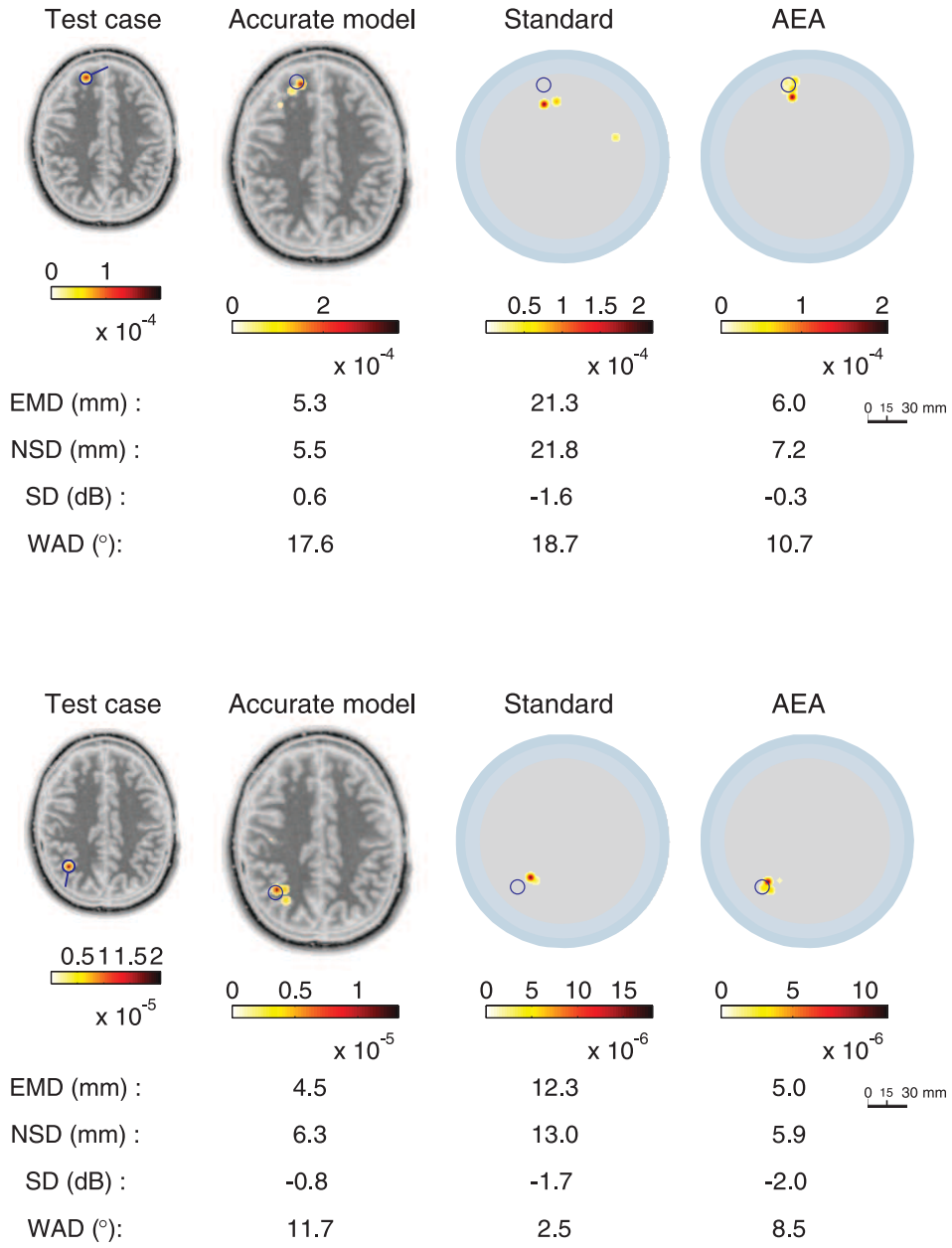

Figure 5.11: Two test case of a single source located in the frontal side and back side. The left image shows the actual dipole source and the other three pictures (from left to right) show the three different reconstructions when: (1) the actual geometry and conductivity distribution are considered, (2) the standard geometry without the AEA statistics and (3) the standard model with the AEA statistics are used. Below the pictures, the estimated metric values are presented for the three different reconstructions.

to the head deformations, i.e. in the forehead area the differences between the MRI geometry and the three concentric circles are more prominent.

The previous results show that the AEA can compensate errors related to the geometry because it gives better accuracy that the standard model. In the superficial source cases, the

AEA is almost as good as the accurate model based on the EMD values. The accurate and the standard model perform better when the source is deep in the domain. Possibly, the different discretization (between the forward and the inverse model) close to the boundaries can cause some numerical errors which result in less accurate superficial source reconstructions.

Additionally, we evaluated the overall performance of the three different reconstructions by running 500 simulations of single dipole sources and estimating the EMD and NSD values. In the histograms, Fig. 5.12, the first row shows the EMD distributions for the three reconstructions and the second row shows the NSD distributions. Under the title of each picture, the averages and the standard deviations of the EMD and NSD are presented. The EMD and NSD statistics indicate that the AEA model works better than the standard model and that the AEA and accurate model have quite similar performance.

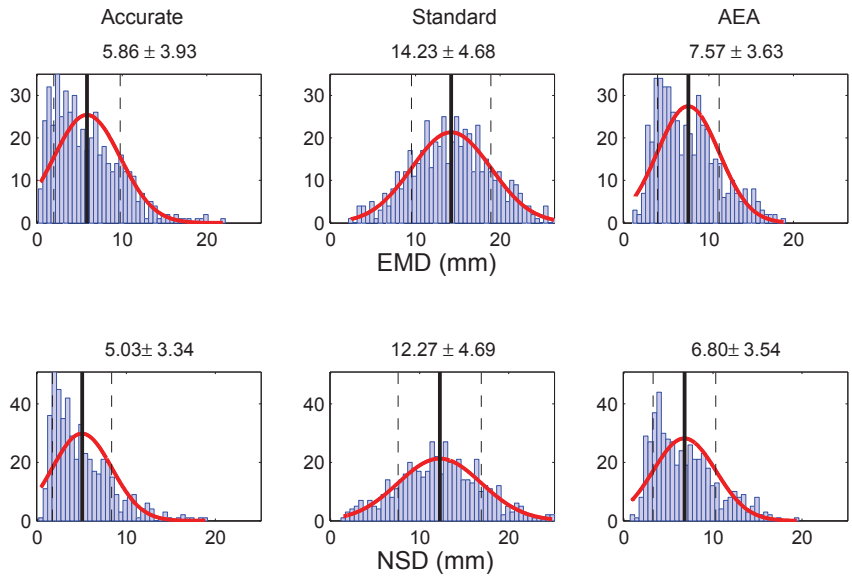

Figure 5.12: Statistics of the EMD and NSD for single dipole reconstructions using the accurate, standard and AEA model. The statistics were estimated based on the reconstructions of 500 different simulated single sources. Above each image, the average and the standard deviation of the corresponding metrics are given.

Furthermore, Fig. 5.13 illustrates how the three different reconstructions depend on the depth of the source by depicting the average EMD with respect to depth. For the accurate model the lowest average EMD values correspond to deep dipole locations while the highest errors are for dipoles near the boundaries (see leftmost image in Fig. 5.13). The EMD value is pretty constant with respect to depth for the standard model (middle picture Fig. 5.13) even though its performance is worse compared to the accurate model. The AEA model shows almost similar performance both for deep and superficial source reconstructions.

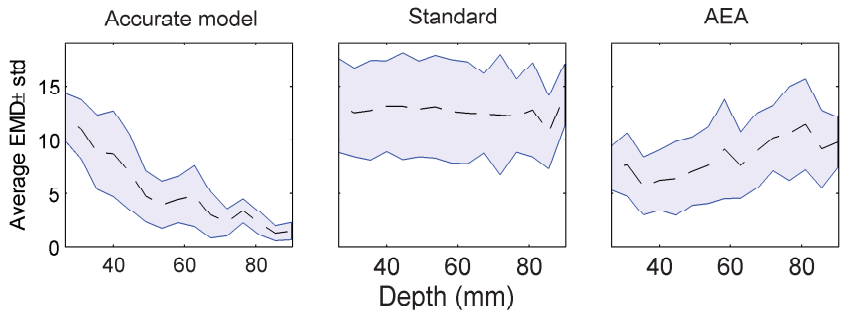

Figure 5.13: Average and standard deviations of the EMD with respect to the depth of a single focal source are presented. The EMD values decrease when the source is deep in the domain for the accurate model. The overall performance of the AEA model is better than the conventional (standard) model both for deep and shallow sources.

Two Sources

Next, we simulated two sources with equal strength and randomly chosen orientations. In Fig. 5.14 and Fig. 5.15 we show two cases. In the first case, the sources are close to each other and in the second case the sources are far from each other. It seems that two sources are not always found when they are close to each other: for example, the accurate model finds one broad source in the middle and another smaller on in the wrong brain hemisphere, the same happens with the standard model, but the AEA on the other hand finds both sources relatively accurately. When the sources are far apart, all the models have some difficulties: the accurate model reconstructs several additional small sources; standard model finds two sources which however have very uneven intensities; and AEA finds two slightly spread sources. The EMD values are higher than in the single dipole cases. Based on these figures and the metric values, the AEA model gives better results than the standard model.

Furthermore, the values of the EMD and NSD metrics are notably different for the standard model. For instance, in the middle image of Fig. 5.14, the EMD is pretty high compared to the respective NSD value. In this case, the standard model finds two sources that are visually quite close to the correct locations but still the EMD value is very high because of the wrong intensities. In other words, EMD does not only depend on the accuracy of the locations of the sources but also on the accuracy of their strengths. One the other hand, the NSD value is lower because it is a weighted average of the distances between the reconstructed dipoles and the closest actual dipoles. Here, it should also be noted that the EMD numbers may contain small numerical errors due to the projections from the accurate domain to the circular domain.

We assessed the feasibility of the models to reconstruct two sources with equal strengths by performing 500 reconstructions. The histograms in Fig. 5.16 shows the overall performance of the three models. AEA model performs better than the standard model and pretty similar to the accurate model. Additionally, we compare the average EMD values as a function of the distance between the two sources (see Fig. 5.17). The average value of the EMD is almost the same for the AEA and accurate model regardless how far the two sources are from each other

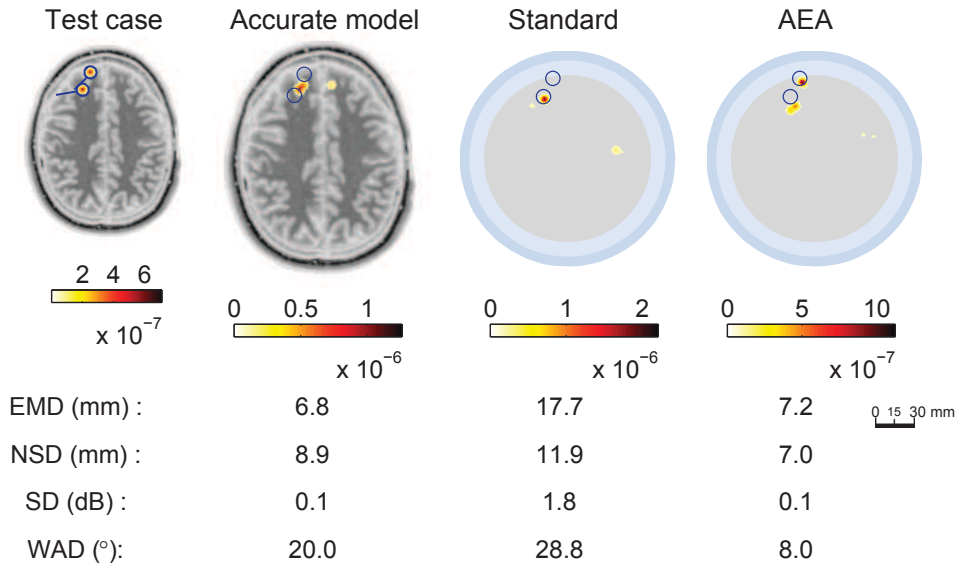

Figure 5.14: A test case with two sources close to each other. The left image shows the actual dipole source and the other three pictures (from left to right) show the three different reconstructions using the different models. Below the pictures, the estimated metric values are presented for the three different reconstructions. The AEA model manages to recover two separated sources.

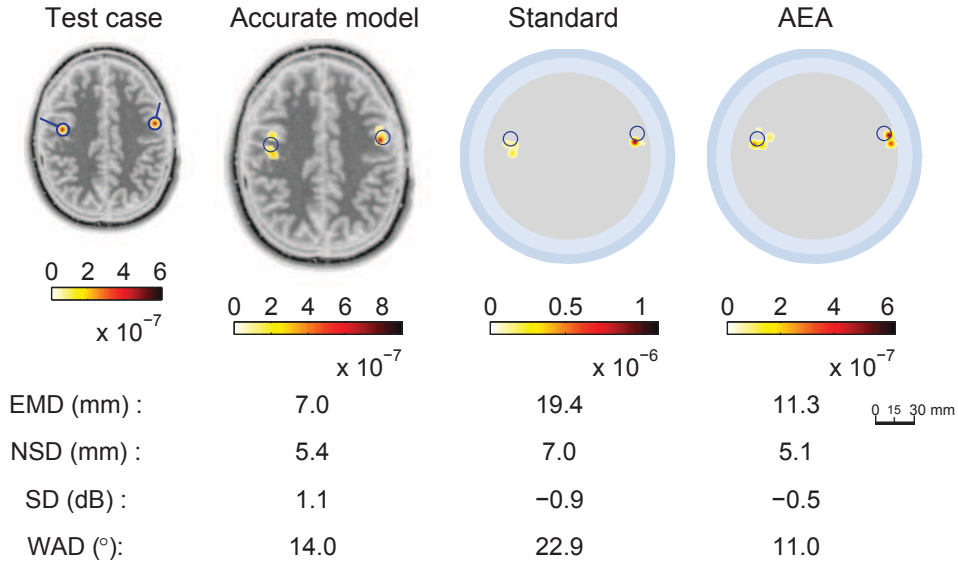

Figure 5.15: A test case with two sources symmetrically placed in the two sides of the head. The reconstruction results are good both for the accurate and the AEA model.

(right hand side Fig. 5.17). The poorest performance is shown in the middle image especially when the source are far apart from each other. Probably, the standard model (5.47) cannot retrieve two locations or the strength of the dipoles is dramatically uneven.

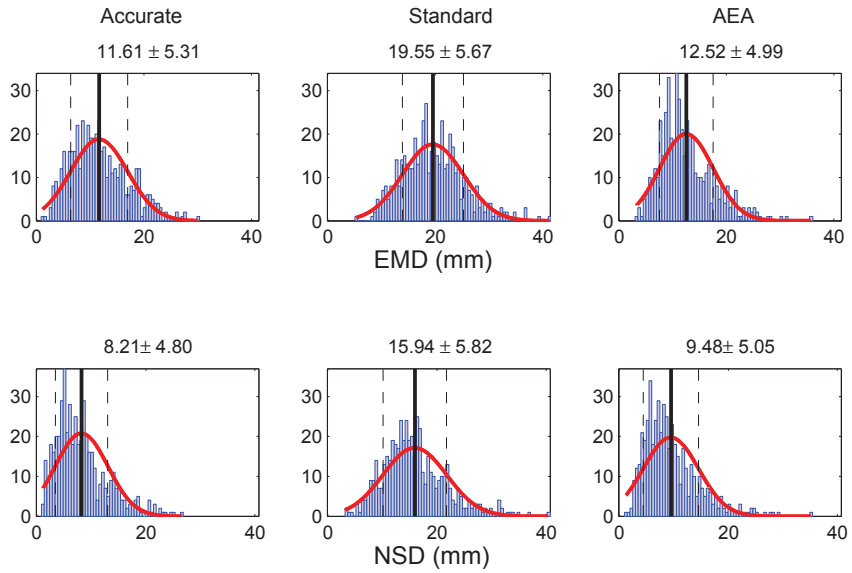

Figure 5.16: EMD and NSD statistics for 500 reconstructions for the case where two focal sources are reconstructed. Also a Gaussian curve is fitted to examine how close is the histogram of the metrics to the normal distribution.

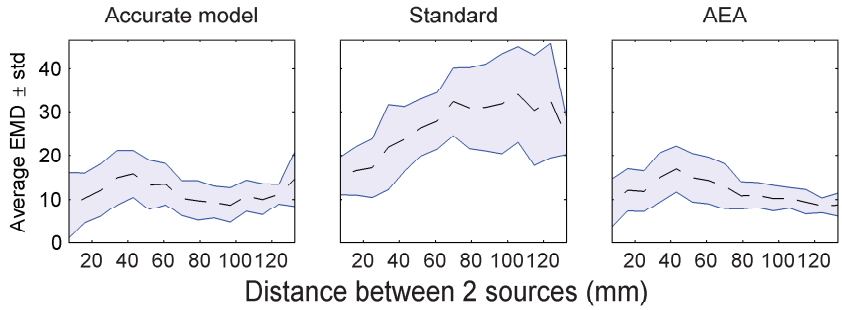

Figure 5.17: Average EMD and standard deviation with respect to the distance between two sources which have equal strength.

Three Sources

In the following cases, we tested the potential of the models to recover three regions of activity. The simulated sources had equal strengths and randomly chosen orientations. In the following figures, we present two test cases. In the first case, we have three sources which are clearly separated from each other (Fig. 5.18). The reconstruction results show that the accurate model can localize the sources, but there are also some artefact, the standard model retrieves three regions of activity but the intensities are uneven and the two out of three sources are misplaced. The AEA model localizes quite accurately the two of the three focal sources and recovers also the third source but with lower intensity.

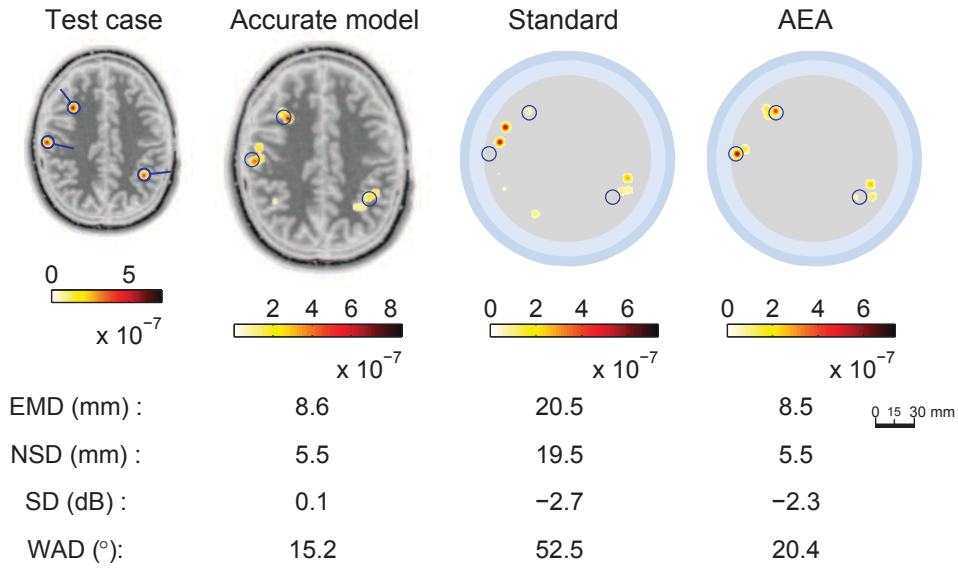

Figure 5.18: A test case where three sources are placed close to the surface. The AEA results are comparable to those obtained from the accurate model.

For the second test case, there is one deep source and two sources near the boundaries. From the results in Fig. 5.19 we can say that the accurate model detects the three regions of activity even though the result is a bit scattered. The standard model reconstructs two regions, one closer to the boundary and the other between the deep and the superficial source.

The AEA model gives a slightly scattered source reconstruction but it is able to localize all the three regions of activity (even though the intensities are uneven). There is an extra peak in the right hand side of the circular domain. The EMD values are lower for the AEA model than the standard model since the reconstructed peaks are closer to the actual dipole locations despite the extra peak.

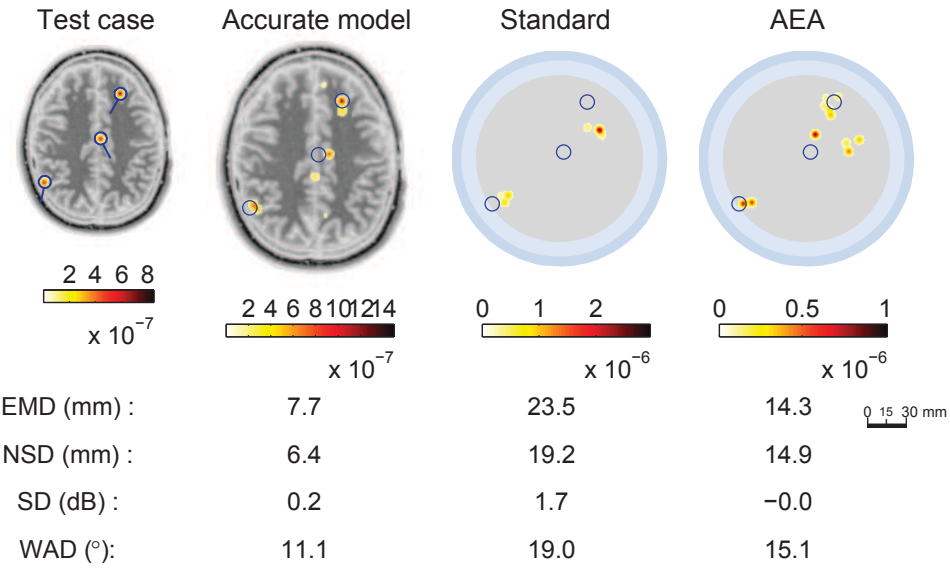

Figure 5.19: A test case with two sources near the surface and one deep in the domain. The metrics and the images designate the AEA model with the error statistics is superior over the standard modeling.

For 500 reconstruction, we estimated the statistics of the EMD and NSD. The values of the metrics are higher than in the previous test cases and consequently the reconstruction errors increase for the three dipole case compared to the two sources case (Fig. 5.20). The average and standard deviation of EMD are comparable for the AEA and accurate model. In Fig. 5.21, the

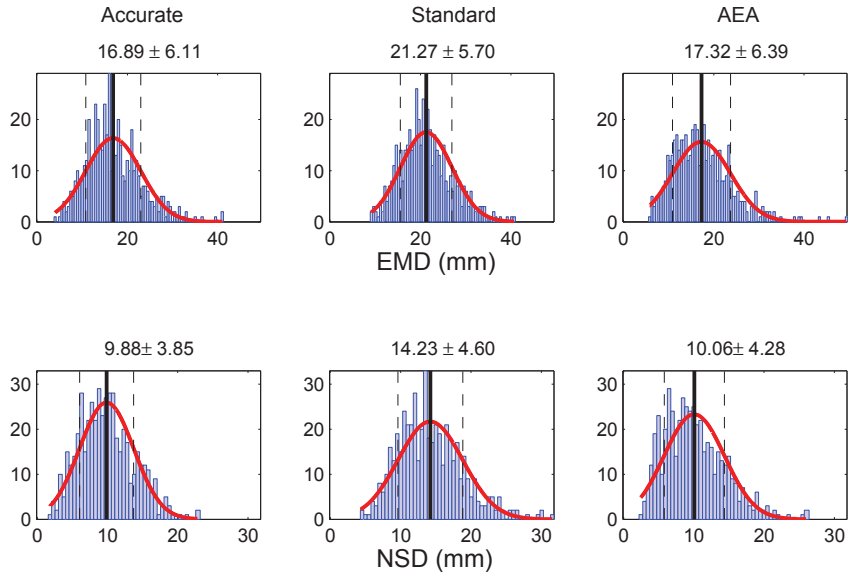

Figure 5.20: Histograms of the EMD and NSD for the three source case. The average and the standard deviation of the metrics were estimated based on 500 different realizations.

average and standard deviation of the EMD with respect to the triangular area that connects the three sources is presented. Sources which are close to each other or collinear have small

surface area. In Fig. 5.21, the AEA model gives average EMD values between $10 - 18$ mm and the result seems that slightly improves for sources which are far apart from each other. It should

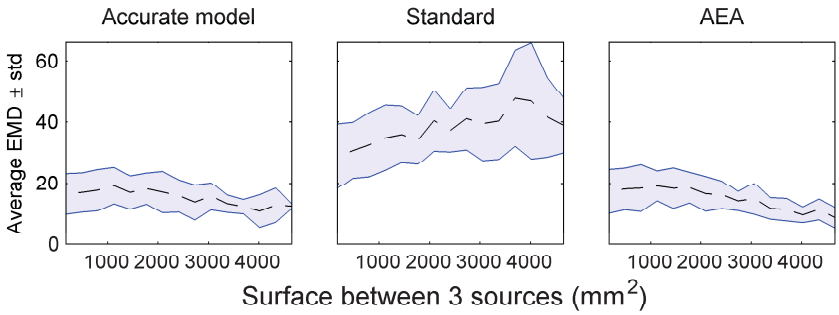

Figure 5.21: Average EMD values with respect to the area designated by the three focal sources.

be noted that recovering more than two focal points is a challenging task because the difficulty of the problem increases. Also, the evaluation of the results is challenging because the EMD and NSD may not always be appropriate criteria for good performance. This is because these metrics can have high values even when the sources are correctly localized if the reconstructed intensities are incorrect.

5.4.2 Case 2: Noise, unknown geometry and conductivity

In these test cases, we assess the use of AEA when the head geometry and the precise tissue conductivities are unknown and the boundary measurements contain noise. The forward boundary data was now computed using the five compartment head model (scalp, skull, CSF, GM and WM as shown in the second picture of Figure 5.9). The conductivities of the tissues were drawn from Gaussian distributions: the mean values were the nominal conductivity values (0.33, 0.016, 1.76, 0.14, 0.33 S/m, respectively) and the standard deviations were 1% of the nominal values. Finally, additive measurement Gaussian noise was simulated and the signal to noise ratio (SNR) was 40dB and 20dB, that corresponds to noise level: 1% and 10% of the standard deviation of the measurements.

In the "accurate" inverse solution, the accurate geometry and precise conductivity values were known. In the "standard" and "AEA" models, the head consists of three circles (scalp, skull, brain) and the conductivity values are fixed to their nominal values (0.33, 0.016 and 0.33 S/m, respectively).

Single Source

In these test cases, we deal with errors caused by the additive noise, the unknown geometry and conductivity distribution. For the single source case, in the following two figures we show the results for a deep and superficial source reconstruction. These cases correspond to the same noiseless cases as in Fig. 5.11 and Fig. 5.10.

In these tests, we generated 30 different noise vectors and we performed 30 reconstructions using the noisy boundary data. Figure 5.22 and Fig. 5.23 show the average of the 30 reconstructions. The average and the standard deviation of the estimated metrics are listed below the figures. For the low noise case (40dB), we noticed that the values of the metrics increase when compared to the noiseless case (Fig. 5.11) and the results deteriorate except for the standard ("without AEA") model whose performance is largely unchanged. For the standard model this is possibly because the reconstruction artefact caused by the modelling errors (geometry and conductivity) are much higher than the ones caused by the simulated noise.

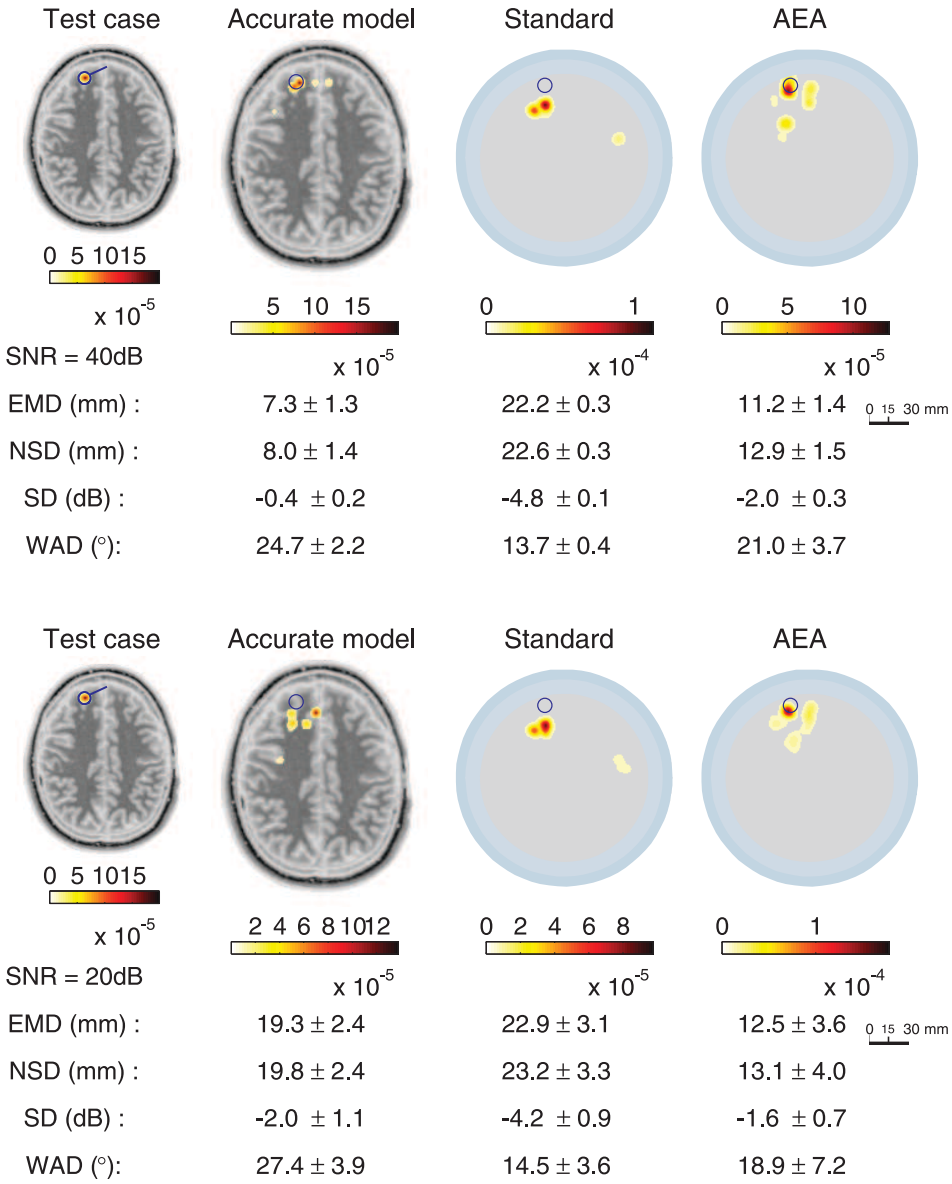

Figure 5.22: One test case with a single superficial source is shown on the left. The dipole location is the same as (frontal source) Fig. 5.11. However, here five compartment forward model was used and the conductivity distribution was considered uncertain. The reconstruction results are averages of 30 different realization of noisy measurement (in dB) and the averages and standard deviations of the EMD, NSD, SD, and WAD are shown below the reconstructions.

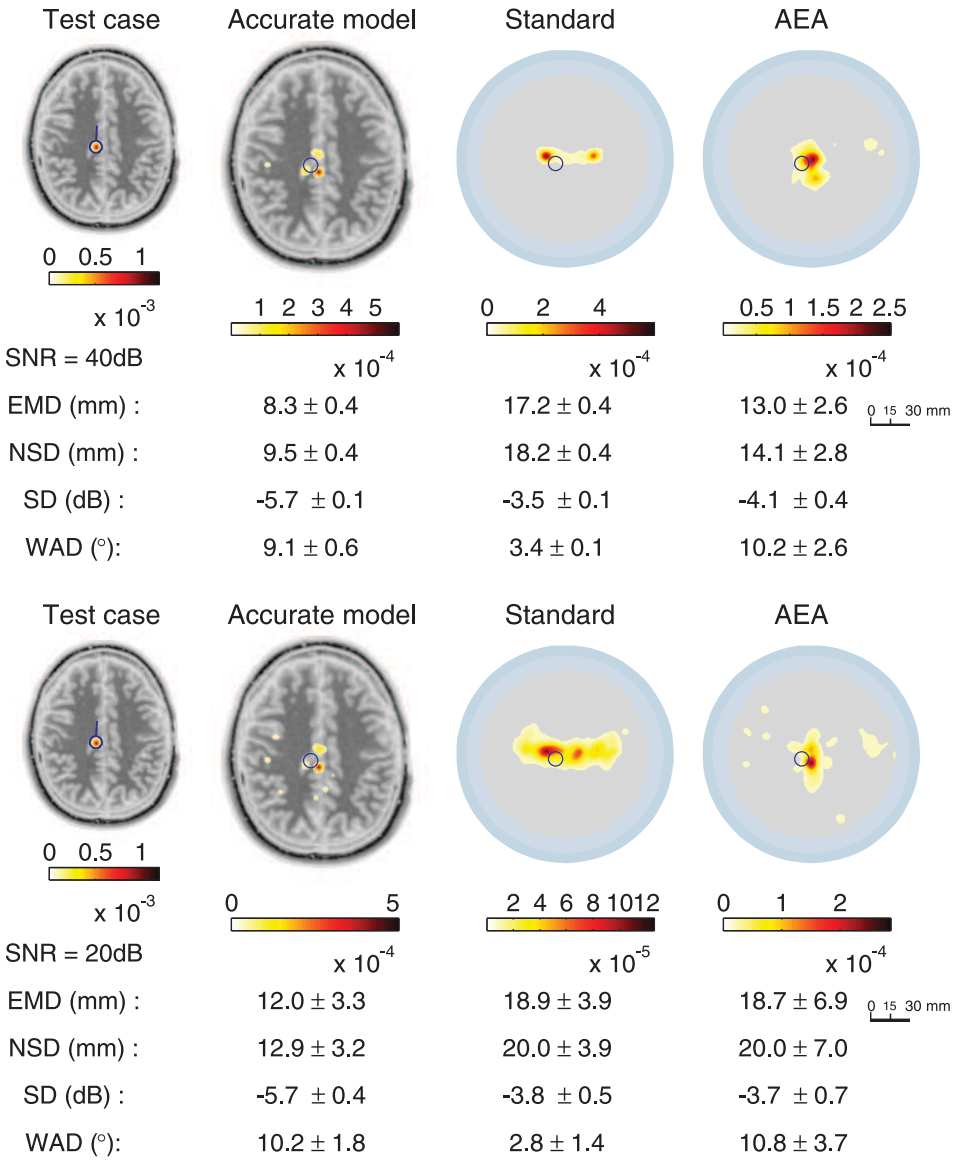

Figure 5.23: A test case with a deep source is shown on the left. The simulation setting were as explained in Fig 5.22. The reconstruction solutions with the three models are presented in the rest of the pictures for two different levels of noise.

Similar conclusions can be drawn from Fig. 5.24. Figure 5.24 shows histograms of the EMD evaluated on 500 simulated single sources at both 40dB and 20dB SNR. The EMD values in Fig. 5.24 indicate that when the SNR decreases from 40dB to 20dB, the performance of the AEA and accurate models becomes closer to the standard model. For the AEA model, we can say that when the level of the additive noise is higher than the level of approximation error i.e. in the covariance $\Gamma_{\nu|d} = \Gamma_{\xi} + \Gamma_{\varepsilon|d}$, the noise part Γ_{ξ} is dominating over the $\Gamma_{\varepsilon|d}$ then we expect that the result becomes closer to the standard model solution. For additive errors, in general, it is required $\|\xi_*\|_2^2 + \text{trace}(\Gamma_{\xi}) \leq 4(\|\varepsilon_{*|d}\|_2^2 + \text{trace}(\Gamma_{\varepsilon|d}))$ to ensure that the the modelling errors dominate the measurement noise [68].

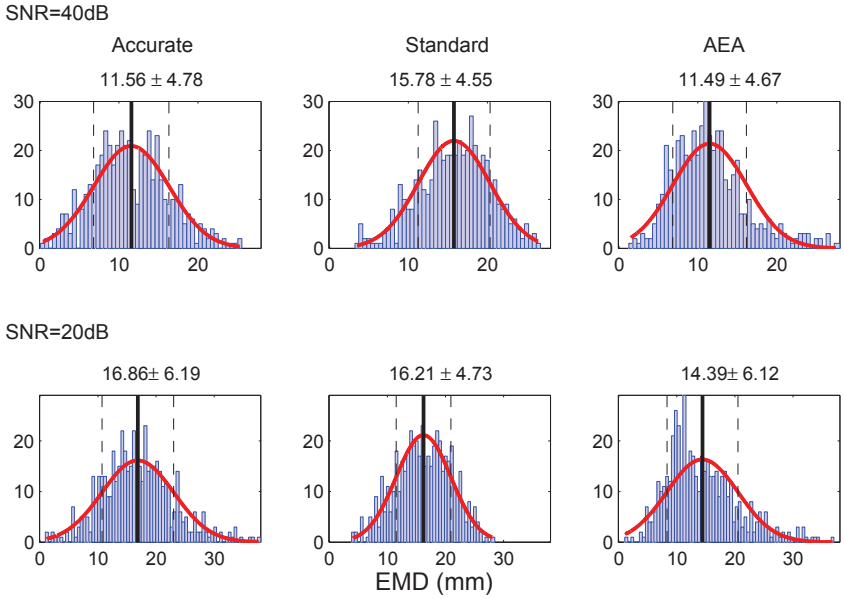

Figure 5.24: Histograms with the EMD values for 500 different single source reconstructions. Above the histograms are shown the average and standard deviation of the EMD for each of the three models.

Two Sources

The two source reconstruction results are presented in Fig. 5.25. The actual sources have equal strengths and different orientations. The test case corresponds to the noiseless case shown in Fig. 5.15. It can be seen that all the models have some problems reconstructing the two sources. However, the AEA model can reconstruct pretty well the two sources.

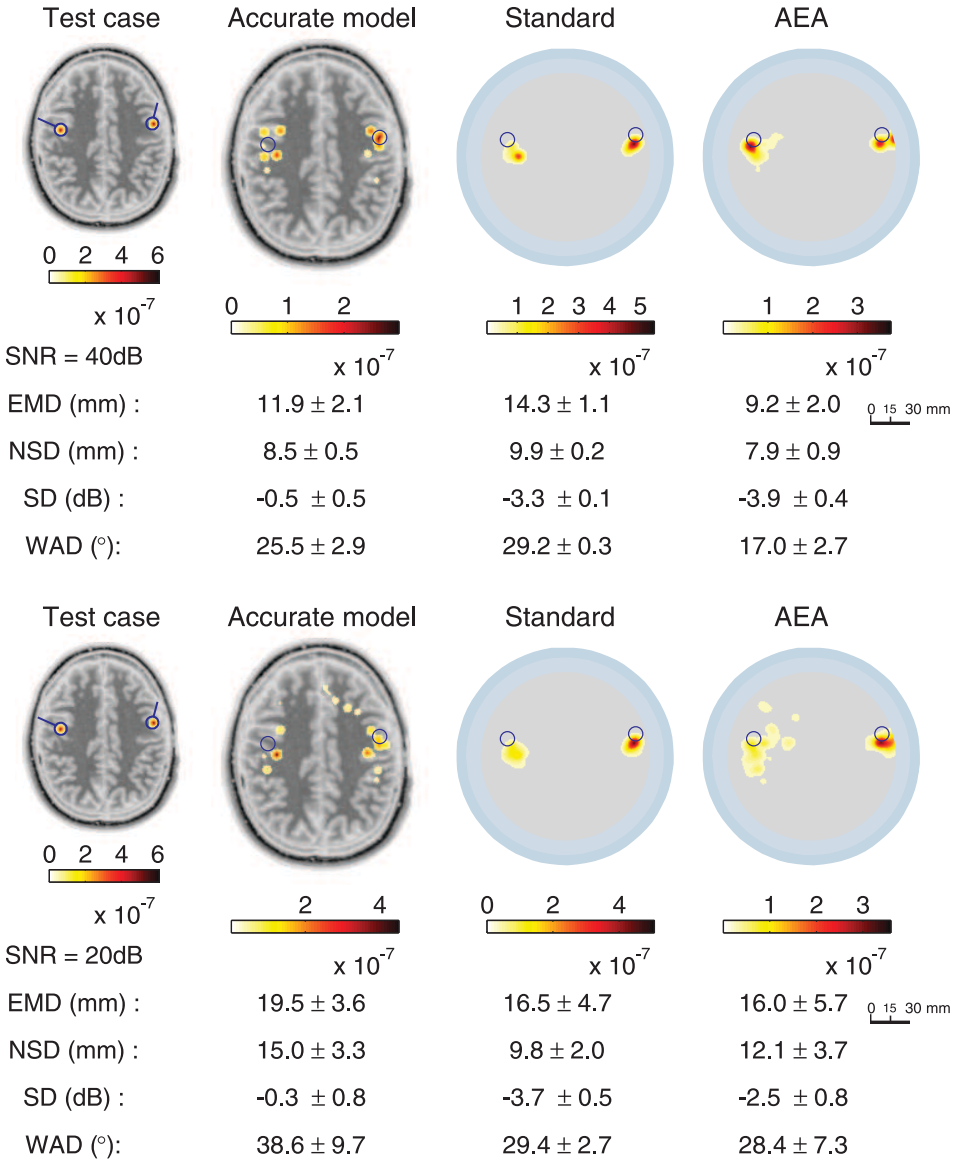

Figure 5.25: Reconstruction of two superficial sources far apart from each other in the presence of measurement noise when the forward model consists of 5 compartments and the conductivity in each tissue is perturbed.

Three Sources

One test case with three equal sources was selected, the same as in Fig. 5.19. It is interesting to observe that the AEA model results are very good and less scattered than the results of the other two models even for the case where the noise level is 20dB.

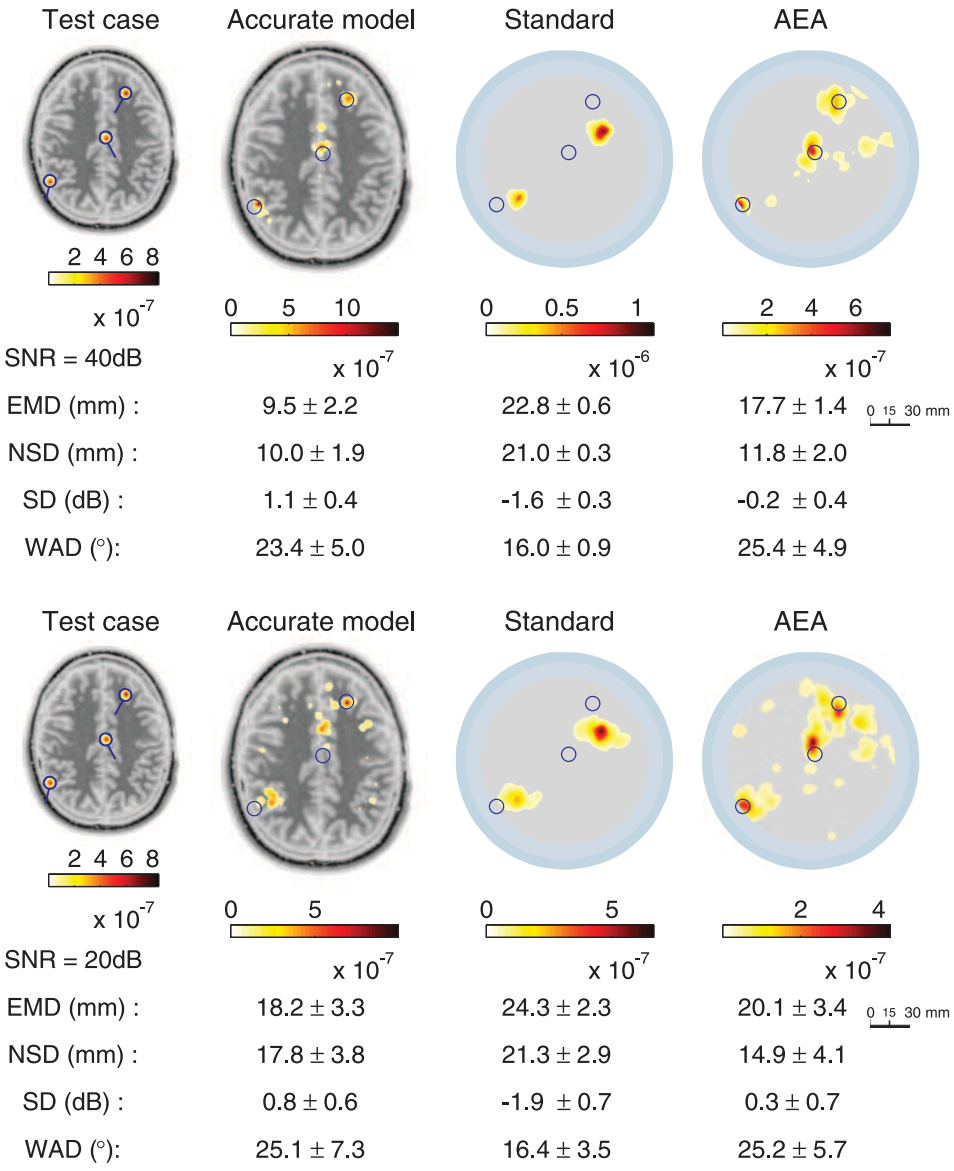

Figure 5.26: A test case with three focal sources and SNR =40dB and 20dB. The dipole location is the same as in Fig. 5.19. But here the five compartment forward model was used and the conductivity distribution was perturbed from the nominal values. The reconstruction results are averages of 30 different realization of noisy measurement and the averages and standard deviations of the corresponding metrics are shown below the reconstructions.

We summarize the EMD statistics estimated from the reconstruction of 500 dipole distributions using the three models. The results are shown in Table 5.1 with the corresponding forward model used for the measurements, number of sources and SNR level. For all the cases the accurate model and AEA reached the same level of EMD values. It can be seen that the EMD values are lower for the noiseless 3 compartment cases (case 1: unknown geometry), and that the increase of noise (lower SNR) in the 5 compartment cases (case 2:unknown geometry and conductivities) gives higher EMD values.

Table 5.1: To evaluate the accuracy of the different solutions, 500 dipole distributions were simulated. Here are the averages and the standard deviations of the corresponding EMD-values when the different inverse models were used.

Forward model	Number of sources	SNR (dB)	EMD (mm) Accurate model	Standard model	AEA model
3 compartments	1	∞	5.9 ± 3.9	14.2 ± 4.6	7.6 ± 3.7
3 compartments	2	∞	11.6 ± 5.3	19.6 ± 5.6	12.5 ± 5.0
3 compartments	3	∞	16.9 ± 6.1	21.3 ± 5.7	17.3 ± 6.4
5 compartments	1	40	11.6 ± 4.8	15.8 ± 4.5	11.5 ± 4.7
5 compartments	1	20	16.9 ± 6.2	16.2 ± 4.7	14.4 ± 6.1
5 compartments	2	40	17.1 ± 6.0	23.1 ± 7.1	17.8 ± 5.9
5 compartments	2	20	20.3 ± 5.9	23.5 ± 7.2	20.5 ± 6.5
5 compartments	3	40	19.5 ± 5.3	23.2 ± 7.0	19.2 ± 5.0
5 compartments	3	20	23.3 ± 5.3	26.9 ± 7.0	22.6 ± 5.4

It is worth noting that the quality of the reconstruction depends on the approximation error statistics, i.e. how similar the test geometry is to the set of the (training) geometries used for the estimation of the approximation error statistics. An example, where different test geometries were used, is shown in Appendix D.2.

5.5 Summary

In this chapter we studied the reconstruction of one, two and three foci of brain activity. We showed that the AEA can be used to cope with uncertainties related to the head geometry, tissue conductivities and noisy measurements. AEA model proved to be feasible regardless of the number of focal sources and the source locations; in particular, the AEA results for superficial sources were far better than the results with the standard model. Surprisingly, in some cases the AEA also worked better than the accurate model in which the geometry and conductivity uncertainties were known. Therefore we can conclude that with AEA model it is not always necessary to know the exact head geometry nor the accurate tissue conductivities.

Chapter 6

Future work and Conclusions

The study and analysis of techniques for the reconstruction of dipole source distributions and electric fields inside the brain were the major objectives of this thesis. The results demonstrated the feasibility of these techniques to localize the brain activity.

This chapter gives the suggestions for the future work. The chapter is divided into two main sections. Section 6.1 concerns the future aspects in vector field tomography (VFT) and section 6.2, the improvement of the focal source estimation. Moreover, we describe the basic concepts how VFT could be used in trans-cranial direct simulation and how the Bayesian approximation error approach (AEA) could enhance EEG cortical imaging.

6.1 Vector Field Tomography in Brain Electric Field Imaging

In this thesis, it was shown that the line integral equations penalized with prior information can be efficiently used for the reconstruction of electric fields generated by dipole sources inside the brain. The proposed approach was tested with a simple circular head model in 2D and in the future work more realistic models will be used.

Electric Fields of Dipole Sources

The future aspects of the electric field reconstruction using VFT are the followings: 3D modelling, numerical approximation of the line integrals and experimental studies using real data. More precisely, electric fields are inherently three dimensional, therefore the reconstruction of electric fields produced by intracellular dipole sources will be carried out in 3D. Also more realistic head model will be used.

In some cases, the linear approximation of the line integrals and the corresponding electric field may not be accurate enough. Therefore, it is justified to study other line integral approximations. Another possibility is to utilize approximation error statistics to compensate the associated numerical errors. Finally, the utilization of real data is in our prospective plans.

Electric Fields due to Trans-cranial Currents

Another interesting bioelectric application in which the VFT could be used is the brain stimulation with an external source such as the trans-cranial direct current stimulation (tDCS). The tDCS is a non invasive excitatory technique applied to the brain by injecting weak currents through planar electrodes. This technique can be used for example in therapeutical rehabilitation after a stroke or other neuropathologies [117]. We propose the utilization of the VFT approach for the reconstruction of the electric field produced by these external stimulation. In the following paragraphs, we describe the tDCS problem and illustrate how the VFT could be used.

In particular, the inverse problem in tDCS can be defined as the recovery of the electric field induced by external (applicable) source. The VFT could be used for the computation of the direction of the electric field. The knowledge of the electric field is important for verifying that the selected electrode locations are such that correct brain areas will be excited and the treatment will be effective.

In mathematical terms, the volume conduction problem posed in tDCS can be described by the quasi-static Maxwell equations, which lead to the Laplace equation [141] and algebraically it can be expressed by

$$Au = v, \tag{6.1}$$

where A is the FEM matrix (2.11) estimated in section 2.4, $u(\mathrm{x})$ the potential inside the head volume denoted by Ω and v the electrodes excitatory voltages. The continuous electric field is given by $\mathrm{e}(\mathrm{x}) = -\nabla u(\mathrm{x})$ and the electric field is associated with the current source according to $\mathrm{j}(\mathrm{x}) = \sigma \mathrm{e}(\mathrm{x})$ where σ is the tissue conductivities.

The electric field produced by the tDCS can be estimated employing VFT. The linear system (4.26) can be used in the inversion which has the advantage over matrix A that the exact knowledge of the tissue conductivities is not required.

Another possible extension is the application of the AEA to directly estimate the source j when the tissue conductivities are unknown. Specifically, similar to (4.26), we can have

$$Dv = \mathrm{S}^{\|} e. \tag{6.2}$$

Moreover, $j = \Sigma e$ where is the matrix representation of the continues relationship $\mathrm{j}(\mathrm{x}) = \sigma \mathrm{e}(\mathrm{x})$. Matrix Σ is a diagonal matrix with the conductivity values at the discrete nodes. The observation model for the tDCs with respect to the source distribution in VFT can be defined as

$$Dv = \mathrm{S}^{\|}\Sigma^{-1} j + \xi, \tag{6.3}$$

where ξ is the noise vector. Similarly as in section 5.2, a simplified computational model (homogeneous/isotropic domain) with an additional error term can be used

$$Dv = \mathrm{S}^{\|} j + \varepsilon + \xi, \tag{6.4}$$

where the approximation error is $\varepsilon = \mathrm{S}^{\|}\Sigma^{-1}j - \mathrm{S}^{\|}j$ and ξ additive noise. This approach requires a set of training models in which the electrical properties of the tissues and the geometries are accurately known for the approximation error statistics.

6.2 Brain Source Imaging with EEG

Two approaches for the recovery of focal source distributions inside the brain were described in chapters 3 and 5. For the reconstruction of focal sources the dipole strength prior, also called $L_{1,2}$ norm, was used. For the solution of the problem a solver based on truncated Newton interior point method (TNIPM) employing logarithmic barrier of the $L_{1,2}$ norm was utilized. In future, the TNIPM can be used with mixed priors that incorporate structural and physiological information related to the neurophysiological information, for instance the connectivity between different brain regions or a mixed regularizer that combines relative smoothness and sparsity as in [42]. Moreover, the suggested solver can be used in other applications related to vector parametrization problems (flow fields) or in problems related to compressed sensing and color (rgb) imaging.

Compensation of Modelling Errors

The study presented in chapter 5 acts as the proof of concept for applying AEA in EEG imaging and further work is required to make AEA applicable in practice. For example, the approach needs to be tested in 3D, more precise computational model for the training set geometries needs to be applied for a more precise estimation for the approximation error statistics and finally the approach needs to be validated with real data.

In particular, for the improvement of the method we propose the following possible future tasks.

- The statistics of the approximation errors (5.42) can be computed using more accurate training geometries where the gray and white matter anisotropy are considered [179, 181].
- The corresponding lead field matrices can be constructed using different basis functions than the linear ones which could describe the conductivity "jump" between the tissue boundaries basis more accurately [180]. One possibility is to use the discontinues Galerkin method [18].
- For the standard model (geometry), a more realistic head model than the concentric circle model could be used to improve the identification of active regions. For example, an elliptic geometry with distinctive brain regions could enhance the result.
- Supplementary MEG data which has the advantage that it is insensitive to head inhomogeneities could be included in the modeling [122]. Since the brain activity propagates with respect to time, also the application of temporal constraints in order to improve reconstruction accuracy could be studied as was suggested in [131].

All in all, it can be said that AEA will become important in EEG source imaging in the future. This is because it can be used to take into account many different uncertainties in the experimental setup. Even when highly accurate head models are used there may be significant uncertainties related to the electrode positions and the electrode-skin contact which can also be integrated in the approximation error statistics.

Skull related Uncertainties in Cortical Imaging

The AEA can be used for many different applications. In the field of brain imaging using EEG, one of them could be EEG cortical imaging in which the uncertainties related to the skull thickness and conductivity could be taken into account.

Cortical imaging (also called high resolution EEG [122]) is defined as the reconstruction of the potential distribution on the cortical surface (dura) from potential measurements on the scalp [124]. Cortical imaging can be very beneficial as a diagnostic tool because it can improve the spatial resolution that is deteriorated due to the skull inhomogeneities. Moreover, it can potentially reduce the need of diagnostic surgery in which electrodes are implanted on the brain surface for better monitoring of the cortical activity. The cortical imaging differs from the source imaging in the sense that we are interested in the estimation of the potential distribution on the dura instead of the actual neural sources. Compared to the EEG source imaging, cortical imaging is slightly easier problem as we do not need to deal the dipole source modelling, possible singularities and the high dimensionality of the source imaging problem.

However, for the accurate estimation of the cortical potential, precise knowledge of the electrical properties and the shape of the skull are required for the computational model. Instead of an accurate model, the statistic of the modelling errors can be incorporated into a less accurate model in a similar fashion as in the EEG source imaging.

In particular, if the computational model is described by $v = A_0 u_{cort} + \varepsilon + \xi$ where v are the potentials around the electrodes, u_{cort} the potentials along the cortical surface, A_0 is a standard modeling matrix given in [126], ξ the measurement noise and ε the modeling error then by following the steps described in section 5.2, the cortical potentials could be estimated using the AEA. Of course, an appropriate prior model needs to be considered. In Fig. 6.1 and 6.2, preliminary results of cortical potential estimation are presented. In the right images of Fig. 6.1 and Fig. 6.2, we can see the cortical potentials estimated using three different models. Specifically, the estimated cortical potentials using a computational model where the correct thickness of the skull is known is depicted with the black line, the result of the standard model without AEA is with the green line and the AEA model is in blue. For the standard model, the skull thickness was constant. It can be seen that the AEA gives better results than the standard modelling. For the cases in which the exact skull shape cannot be extracted then the AEA approach seems to be the best alternative.

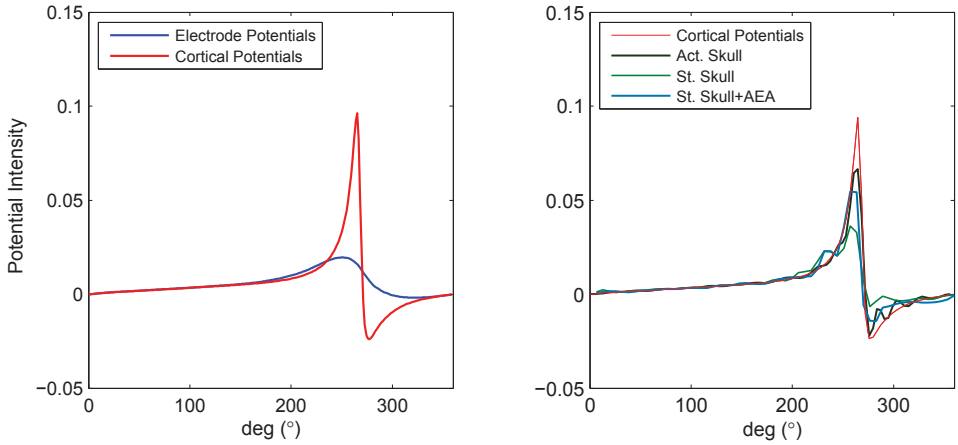

Figure 6.1: Potentials evoked by a tangential superficial source. (Left Image) Potentials on the electrodes (in blue) and on the cortical surface (in red). (Right Image) Estimated cortical potentials when (a) the thickness of the skull is known (black line), (b) standard circular skull is used (green line) and (c) standard circular skull with AEA is used (blue line).

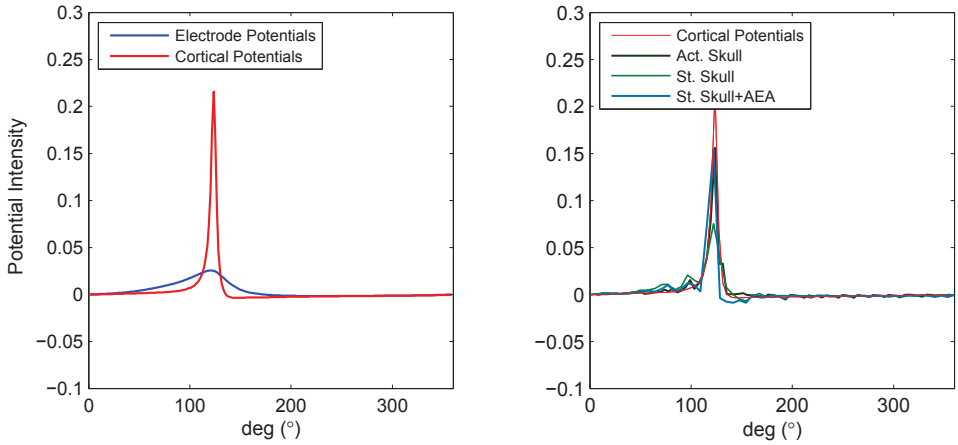

Figure 6.2: Potentials evoked by a radial superficial source. (Left Image) Potentials on the electrodes (in blue) and on the cortical surface (in red). (Right Image) Estimated cortical potentials when (a) the thickness of the skull is known (black line), (b) standard circular skull is used (green line) and (c) standard circular skull with AEA is used (blue line).

6.3 Conclusions

In this thesis, three different mathematical approaches were developed and presented for the accurate estimation of focal brain activity using EEG measurements. The proposed approaches were tested and found feasible using simulated test cases.

In chapter 3, we developed and analyzed an algorithm for the recovery of sparse dipole sources. It was showed that the solution employing the dipole strength penalty term (called the $L_{1,2}$ norm) is superior over other common priors for focal source recovery. The proposed algorithm for the solution of the inverse problem was based on the truncated Newton interior point method with a logarithmic barrier function. In addition, we used Bayesian analysis to derive the depth weights in the prior that were used to reduce the tendency of the solver to favor superficial sources. It is worth noting that until now, there has not been a rigorous presentation of how to derive these weights; previously, the weights have always been considered as ad-hoc choices.

In chapter 4, we proposed a method of recovering the electric field produced by dipole sources using vector field tomography. The electric field was reconstructed using a set of line integrals. We showed that, even though the absolute values of the reconstructed electric field were not always exact, the pattern of the field identified the correct location of the activity which in most cases is the paramount consideration. The benefit of this approach is that there is no need to use a mathematical model for the sources.

The most significant shortcoming of most EEG inverse methods is that an accurate head model (geometry and tissue conductivities) is required for each individual in order to get a reliable solution. The procedure to extract these features is time consuming, expensive, requires special expertise and in many cases is not even possible. Therefore, approaches that do not require exact knowledge of these features would be extremely valuable. In this thesis, we suggest and evaluate an approach that fills these requirements.

In chapter 5, we showed that exact knowledge of the head geometry and tissue conductivities are not always necessary. These head features can be taken into account statistically by using the approximation error approach. We demonstrated that a coarse model, the three concentric circle model, accompanied with the approximation error statistics is able to give results comparable to those obtained with an accurate head model. This means that it is possible to get accurate EEG imaging results for every patient without having detailed knowledge of their head features; it is enough to know the statistical variations in these features.

Bibliography

[1] S. Ahlfors, R. Ilmoniemi, and M. Hämäläinen. Estimates of visually evoked cortical currents. *Electroencephalography and Clinical Neurophysiology*, 82:225–236, 1992.

[2] F. Alizadeh and D. Goldfarb. Second-order cone programming. *Mathematical Programming*, 95:3–51, 2001.

[3] G. B. Arfken and H. J. Weber. *Mathematical Methods for Physicists*. Elsevier Academic Press, 6th edition, 2005.

[4] S. R. Arridge, J. P. Kaipio, V. Kolehmainen, M. Schweiger, E. Somersalo, T. Tarvainen, and M. Vauhkonen. Approximation errors and model reduction with an application in optical diffusion tomography. *Inverse Problems*, 22:175–195, 2006.

[5] J. P. Ary, S. A. Klein, and D. H. Fender. Location of sources of evoked scalp potentials: corrections for skull and scalp thickness. *IEEE Transa*, 28(6):447–452, 1981.

[6] K.A. Awada, D.R. Jackson, Stephen B. Baumann, J.T. Williams, D.R. Wilton, P.W. Fink, and B.R. Prasky. Effect of conductivity uncertainties and modeling errors on EEG source localization using a 2-D model. *IEEE Transactions on Biomedical Engineering*, 45(9):1135–1145, 1998.

[7] S. Baillet, J. J. Riera, G. Marin, J. F. Mangin, J. Aubert, and L. Garnero. Evaluation of inverse methods and head models for EEG source localization using a human skull phantom. *Physics in Medicine and Biology*, 46:77–96, 2001.

[8] M. A. Bezuglova, E. Y. Derevtsov, and S. B. Sorokin. The reconstruction of a vector field by finite difference methods. *Journal of Inverse and Ill-Posed Problems*, 10(2):123–154, 2002.

[9] H. Bhatia, G. Norgard, V. Pascucci, and P.-T. Bremer. The Helmholtz-Hodge Decomposition - A Survey. *IEEE Transactions on Visualization and Computer Graphics*, 19:1386–1404, 2013.

[10] S. P. Boyd, N. l. Parikh, E. Chu, B. Peleato, and J. Eckstein. Distributed Optimization and Statistical Learning via the Alternating Direction Method of Multipliers. *Found. Trends Mach. Learn.*, 3(1):1–122, January 2011.

[11] S. P. Boyd and L. Vandenberghe. *Convex Optimization*. Cambridge University Press, 2004.

[12] H. Braun and A. Hauck. Tomographic reconstruction of vector fields. *IEEE Transactions on Signal Processing*, 39:464–471, 1991.

[13] Romain Brette and Alain Destexhe, editors. *Handbook of Neural Activity Measurements*. Cambridge University, 2012.

[14] J. D. Bronzino, editor. *Biomedical Engineering Fundamentals*. Richard C. Dorf-University of California, Davis. Joseph D. Bronzino, 3rd edition, 2006.

[15] Helmut Buchner, Gunter Knoll, Manfred Fuchs, Adrian Riencker, Rainer Beckmann, Michael Wagner, Jiri Silny, and Jrg Pesch. Inverse localization of electric dipole current sources in finite element models of the human head. *Electroencephalography and Clinical Neurophysiology*, 102:267–278, 1997.

[16] M. Burger, H. Dirks, and J. Müller. *Inverse Problems in Imaging*. Rad. Ser. Comp. App., 2013.

[17] P. G. Ciarlet. *The finite element method for elliptic problems*. Society for Industrial and Applied Mathematics, 2002.

[18] B. Cockburn, G. E. Karniadakis, and C.-W. Shu. The Development of Discontinuous Galerkin Methods. In Bernardo Cockburn, GeorgeE. Karniadakis, and Chi-Wang Shu, editors, *Discontinuous Galerkin Methods*, volume 11 of *Lecture Notes in Computational Science and Engineering*, pages 3–50. Springer Berlin Heidelberg, 2000.

[19] C. D. Correa and K-Liu Ma. A Comparison of Gradient Estimation Methods for Volume Rendering on Unstructured Meshes. *IEEE Transactions on Visualization and Computer Graphics*, 17:305–319, 2011.

[20] B. N. Cuffin. Effects of local variations in skull and scalp thickness on EEG's and MEG's. *IEEE Transaction on Biomedical Engineering*, 40(1):42–48, 1993.

[21] B. Neil Cuffin. Effects of head shape on EEGs and MEGs. *IEEE Transactions on Biomedical Engineering*, 37:44–52, 1990.

[22] A. M. Dale and M. I. Sereno. Improved Localization of Cortical Activity by Combining EEG and MEG with MRI Cortical Surface Reconstruction: A Linear Approach. *Journal of Cognitive Neuroscience*, 5:162–176, 1993.

[23] R. Grave de Peralta-Menendez and S. L. Gonzalez-Andino. A critical analysis of linear inverse solutions to the neuroelectromagnetic inverse problem. *IEEE Transactions on Biomedical Engineering*, 45(4):440–448, 1998.

[24] M. Defrise and G. T. Gullberg. 3D reconstruction of tensors and vector. Technical report, Lawrence Berkeley National Laboratory, 2005.

[25] L. Desbat and A. Wernsdorfer. Direct algebraic reconstruction and optimal sampling in vector field tomography. *IEEE Transactions on Signal Processing*, 43(8):1798 –1808, Aug. 1995.

[26] L. Ding and B. He. Sparse source imaging in electroencephalography with accurate field modeling. *Human Brain Mapping*, 29(9):1053–1067, 2008.

[27] L. Ding and H. Yuan. Inverse source imaging methods in recovering distributed brain sources. *Biomedical Engineering Letters*, 2(1):2–7, 2012.

[28] M. Fuchs, J. Kastner, M. Wagner, S. Hawes, and J. S. Ebersole. A standardized boundary element method volume conductor model. *Clinical Neurophysiology*, 113:702–712, 2002.

[29] Manfred Fuchs, Michael Wagner, and Hans-Aloys Wischmann. Linear and Nonlinear Current Density Reconstructions. *Journal of Clinical Neurophysiology*, 16:267–295, 1999.

[30] I. M. Gelfand and S. V. Fomin. *Calculus of Variations (Dover Books on Mathematics)*. Dover Publications, 2000.

[31] N. G. Gencer and S. J. Williamson. Differential characterization of neural sources with the bimodal truncated SVD pseudo-inverse for EEG and MEG measurements. In *Biomedical Engineering*, 1998.

[32] D. B. Geselowitz. On bioelectric potentials in an inhomogeneous volume conductor. *Biophysical Journal*, 7(1):1–1, 1967.

[33] M. S. Gockenbach. *Understanding and implementing the finite element method*. SIAM: Society for Industrial and Applied Mathematics, 2006.

[34] I. F. Gorodnitsky and B. D. Rao. Sparse signal reconstruction from limited data using FOCUSS: a re-weighted minimum norm algorithm. *IEEE Transactions on Signal Processing*, 45:600–616, 1997.

[35] Irina F. Gorodnitsky, John S. George, and Bhaskar D. Rao. Neuromagnetic source imaging with FOCUSS: a recursive weighted minimum norm algorithm. *Electroencephalography and Clinical Neurophysiology*, 95:231–251, 1995.

[36] R. Grech, T. Cassar, J. Muscat, K. Camilleri, S. Fabri, M. Zervakis, P. Xanthopoulos, V. Sakkalis, and B. Vanrumste. Review on solving the inverse problem in EEG source analysis. *Journal of neuroengineering and rehabilitation*, 5(1):25, 2008.

[37] J. Hadamard. *Lectures on Cauchy's problem in linear partial differential equations*. Dover Publications, 1923,New York.

[38] H. Hallez, B. Vanrumste, R. Grech, J. Muscat, W. De Clercq, A. Vergult, Y. D'Asseler, K. P. Camilleri, S. G. Fabri, S. Van Huffel, and I. Lemahieu. Review on solving the forward problem in EEG source analysis. *Journal of Neuroengineering and Rehabilitation*, 4, 2007.

[39] M. S. Hämäläinen and R. J. Ilmoniemi. Interpreting magnetic fields of the brain: minimum norm estimates. *Medical and Biological Engineering and Computing*, 32:35–42, 1994.

[40] P. C. Hansen. *Rank-deficient and Discrete Ill-posed Problems: Numerical Aspects of Linear Inversion*. Society for Industrial and Applied Mathematics, Philadelphia, PA, USA, 1998.

[41] S. Haufe, V. V. Nikulin, A. Ziehe, K.-R Müller, and G. Nolte. Estimating vector fields using sparse basis field expansions. *Neural Information Processing Systems*, pages 617–624, 2008.

[42] S. Haufe, V. V. Nikulin, A. Ziehe, K.-R. Müller., J.ller, and G. Nolte. Combining sparsity and rotational invariance in EEG/MEG source reconstruction. *NeuroImage*, 42(2):726–738, 2008.

[43] M. T. Heath. *Scientific computing: an introductory survey*. 2002.

[44] J. Heino, E. Somersalo, and J. P. Kaipio. Compensation for geometric mismodelling by anisotropies in optical tomography. *Optics Express*, 13(1):296–308, 2005.

[45] Jenni Heino and Erkki Somersalo. A modelling error approach for the estimation of optical absorption in the presence of anisotropies. *Phys. Med. Biol.*, 49(20):4785–4798, 2004.

[46] J. Heiskala, V. Kolehmainen, T. Tarvainen, J. P. Kaipio, and S. R. Arridge. Approximation error method can reduce artifacts due to scalp blood flow in optical brain activation imaging. *Journal of Biomedical Optics*, 17(9):096012–1–096012–7, 2012.

[47] S. Helgason. *The Radon transform (Progress in Mathematics)*, volume 5. Birkhauser, 2nd edition, 1999.

[48] H. M. Hertz. Kerr effect tomography for nonintrusive spatially resolved measurements of asymmetric electric field distributions. *Applied Optics*, 25(6):914–921, 1986.

[49] D. L. Hill, P. G. Batchelor, M. Holden, and Hawkes D. J. Medical image reg. *Physics in Medicine and Biology*, 46(3):R1–R45, 2001.

[50] Haitham Hindi. A tutorial on convex optimization II: duality and interior point methods. In *American Control Conference*, 2006.

[51] Y. Hoshi. Functional near-infrared optical imaging: Utility and limitations in human brain mapping. *Psychophysiology*, 40:511–520, 2003.

[52] http://cvxr.com/cvx/.

[53] http://www.comsol.com/livelink-for matlab.

[54] M.-Xiong Huang, A. M. Dale, T. Song, E. Halgren, D. L. Harrington, I. Podgorny, J. M. Canive, S. Lewis, and R. R. Lee. Vector-based spatialtemporal minimum L1-norm solution for MEG. *Neuroimage*, 31:1025–1037, 2006.

[55] G. Huiskamp, M. Vroeijenstijn, R. Van Dijk, G. Wieneke, and A. C. van Huffelen. The need for correct realistic geometry in the inverse EEG problem. *IEEE Transaction on Biomedical Engineering*, 46(11):1281–1287, 1999.

[56] J. M. J. Huttunen and J. P. Kaipio. Approximation error analysis in nonlinear state estimation with an application to state-space identification. *Inverse Problems*, 23:2141–2157, 2007.

[57] J. M. J. Huttunen and J. P. Kaipio. Model reduction in state identification problems with an application to determination of thermal parameters. *Applied Numerical Mathematics*, 59:877–890, 2009.

[58] A. A. Ioannides, J. P. R. Bolton, and C. J. S. Clarke. Continuous probabilistic solutions to the biomagnetic inverse problem. *Inverse Problems*, 6:523–542, 1990.

[59] I. Javanovic. *Inverse Problems in Acoustic Tomography: Theory and Applications*. PhD thesis, EPFL, 2008.

[60] Johnson. Measurements and reconstruction of three-dimensional fluid flow. United States Patent, 1979.

[61] C. R. Johnson. Computational and numerical methods for bioelectric field problems. In *Critical Reviews in BioMedical Engineering*, pages 162–180. CRC Press, Boca Ratan, 1997.

[62] C. R. Johnson, R. S. MacLeod, and M. A. Matheson. Computational medicine: Bioelectric field problems. *Computer (IEEE Computer Society press)*, 26(10):59–67, 1993.

[63] D. H. Johnson. Scanning our past - origins of the equivalent circuit concept: The voltage-source equivalent. *Proceedings of the IEEE*, 91(4), 2003.

[64] S. A. Johnson, J. F. Greenleaf, W.A. Samayoa, F.A. Duck, and J. Sjostrand. Reconstruction of three-dimensional velocity fields and other parameters by acoustic ray tracing. In *1975 Ultrasonics Symposium*, pages 46–51, 1975.

[65] I. Jovanovia, L. Sbaiz, and M. Vetterli. Acoustic tomography for scalar and vector fields: Theory and application to temperature and wind estimation. *Journal of Atmospheric and Oceanic Technology*, 8 2009.

[66] J. P. Kaipio and E. Somersalo. *Statistical and Computational Inverse Problems*. Applied Mathematical Series. Springer, 2004.

[67] J. P. Kaipio and E. Somersalo. Statistical inverse problems: Discretization, model reduction and inverse crimes. *Journal of Computational and Applied Mathematics*, 198(2):493–504, 2007.

[68] J.P. Kaipio and V. Kolehmainen. Approximate marginalization over modeling errors and uncertainties in inverse problems. In P. Damien, N. Polson, and D. Stephens, editors, *Bayesian Theory and Applications*. Oxford University Press, 2013.

[69] S.-J. Kim, K. Koh, M. Lustig, S. Boyd, and D. Gorinevsky. An Interior-Point Method for Large-Scale L1-Regularized Least Squares. *IEEE Journal of Selected Topics in Signal Processing*, 1(1):606–617, 2007.

[70] Wilhelm Emil Kincses, Christoph Braun, Stefan Kaiser, Wolfgang Grodd, Hermann Ackermann, and Klaus Mathiak. Reconstruction of extended cortical sources for EEG and MEG based on a Monte-Carlo-Markov-chain estimator. *Human Brain Mapping*, 18:100–110, 2003.

[71] A. Kirsch. *An introduction to the mathematical theory of inverse problems*. Springer-Verlag New York., NY, USA, 1996.

[72] K. Koh, S.-J. Kim, and S. Boyd. An Interior-Point Method for Large-Scale L1-Regularized Logistic Regression. *Journal of Machine Learning Research*, 2007.

[73] Th. Kohler, M. Wagner, M. Fuchs, H.-A. Wischmann, R. Drenckhahn, and A. Theissen. Depth normalization in meg/eeg current density imaging. In *Engineering in Medicine and Biology Society, 1996. Bridging Disciplines for Biomedicine. Proceedings of the 18th Annual International Conference of the IEEE*, volume 2, pages 812–813 vol.2, Oct 1996.

[74] V. Kolehmainen, S. R. Arridge, J. P. Kaipio, M. Schweiger, E. Somersalo, T. Tarvainen, and M. Vauhkonen. Approximation errors and model reduction in optical tomography. In *Int. Conf. IEEE Eng. Med. Biol. Soc.*, pages 2659–2662, 2006.

[75] V. Kolehmainen, M. Schweiger, I.Nissilä, Tanja Tarvainen, S. R. Arridge, and J. P. Kaipio. Approximation errors and model reduction in three-dimensional diffuse optical tomography. *Journal of the Optical Society of America A.*, 26, 2009.

[76] M. I. Kramar. *A feasibility study about the use of vector tomography for the reconstruction of the coronal magnetic field.* PhD thesis, University of Gottingen, 2005.

[77] S. J. Lade, D. Paganin, and M. J. Morgan. 3-D Vector tomography of Doppler-transformed fields by filtered-backprojection. *Optics Communications*, 253(4-6):382–391, September 2005.

[78] M. M. Lavrentiev, A. V. Avdeev, and V. I. Priimenko. *Inverse Problems Of Mathematical Physics*. Walter De Gruyter, Sep 2003.

[79] C. Ha Lee, A. Varshney, and D. W. Jacobs. Mesh saliency. *ACM Transactions on Graphics*, 24:659–666 (https://www.ceremade.dauphine.fr/ peyre/matlab/fast–marching/content.html), 2005.

[80] A. Lehikoinen, J. M. J. Huttunen, S. Finsterle, M. B. Kowalsky, and J. P. Kaipio. Dynamic inversion for hydrological process monitoring with electrical resistance tomography under model uncertainties. *Water Resour. Res.*, 46(4):W04513, 2010.

[81] Y. Lemoigne, A. Caner, and G. Rahal. *Physics for Medical Imaging Applications*. Springer, 2007.

[82] S. Li. *Fast Algorthms for Sparse matrix inverse computation*. PhD thesis, The institute for Computational and Mathematical Engineering and the Committe on Graduate Studies of Standord University, 2009.

[83] F.-H. Lin, J. W. Belliveau, A. M. Dale, and M. S. Hämäläinen. Distributed current estimates using cortical orientation constraints. *Human Brain Mapping*, 27:1–13, 2006.

[84] A. Lipponen, A. Seppänen, and J. P. Kaipio. Reduced-order estimation of nonstationary flows with electrical impedance tomography. *Inverse Problems*, 26:074010, 2010.

[85] A. Lipponen, A. Seppänen, and J. P. Kaipio. Nonstationary approximation error approach to imaging of three-dimensional pipe flow: experimental evaluation. *Measurement Science and Technology.*, 22(10):104013 (13 pp), 2011.

[86] G. R. Liu and S. S. Quek. *Finite element method : a practical course*. Butterworth-Heinemann, 2003.

[87] H. Liu, X. Gao, P. H. Schimpf, F. Yang, and S. Gao. A recursive algorithm for the three-dimensional imaging of brain electric activity: shrinking LORETA-FOCUSS. *IEEE Transactions on Biomedical Engineering*, 51:1794–1802, 2004.

[88] H. Liu and P. H. Schimpf. Efficient localization of synchronous EEG source activities using a modified RAP-MUSIC algorithm. *IEEE Transactions on Biomedical Engineering*, 53:652–661, 2006.

[89] M. S. Lobo, L. Vandenberghe, S. Boyd, and H. Lebret. Applications of Second-Order Cone Programming. *Linear Algebra and Its Applications*, 284:193–228, 1998.

[90] L. Lovstakken, S. Bjaerum, D. Martens, and H. Torp. Blood flow imaging - a new real-time, flow imaging technique. *IEEE Transactions on Ultrasonics, Ferroelectrics and Frequency Control*, 53(2):289–299, 2006.

[91] F. Lucka, S. Pursiainen, M. Burger, and C. H. Wolters. Hierarchical Bayesian inference for the EEG inverse problem using realistic FE head models: Depth localization and source separation for focal primary currents. *NeuroImage*, 61(4):1364–1382, 2012.

[92] B. Lütkenhöner. Dipole source localization by means of maximum likelihood estimation. I. Theory and simulations. *Electroencephalography and Clinical Neurophysiology*, 106:314–321, 1998.

[93] D. J. C. Mackay. Bayesian Interpolation. *Neural Computation*, 4:415–447, 1992.

[94] D. M. Malioutov, M. Çetin, and Alan S. Willsky. A sparse signal reconstruction perspective for source localization with sensor arrays. *IEEE Transactions on Signal Processing*, 53:3010–3022, 2005.

[95] J. Malmivuo and R. Plonsey. *Bioelectromagnetism : Principles and Applications of Bioelectric and Biomagnetic Fields*. Oxford University Press, USA, 1st edition, 1995.

[96] D. S. Marcus, T. H. Wang, J. Parker, J. G. Csernansky, J. C. Morris, and R. L. Buckner. Open access series of imaging studies (OASIS): cross-sectional MRI data in young, middle aged, nondemented, and demented older adults. *Journal of Cognitive Neuroscience*, 19(9):1498–1507, 2007. URL: http://www.oasis-brains.org.

[97] K. Matsuura and Y. Okabe. Selective minimum-norm solution of the biomagnetic inverse problem. *IEEE Transaction on Biomedical Engineering*, 42(6):608–615, 1995.

[98] K. Matsuura and Y. Okabe. Lp-normalized minimum-L1-norm solution of the biomagnetic inverse problem. In *Annual International Conference of the IEEE Engineering in Medicine and Biology Society, Proceedings in Medicine and Biology Society*, volume 5, pages 2254–2255, 1996.

[99] W. H. Meijs, O. W. Weier, M. J. Petes, and A. Van Oostrom. On the Numerical Accuracy of the Boundary Element Method. *IEEE Transactions on Biomedical Engineering*, 36(10):1038–1049, 1989.

[100] C. D. Meyer. *Matrix Analysis and Applied Linear Algebra*. Siam: Society of Industrial and Applied Mathematics, 2000.

[101] C. M. Michel, R. Grave de Peralta, S. Gonzalez Andino, L. Spinelli, O. Blanke, T. Landis, and M. Seeck. Spatiotemporal EEG Analysis and Distributed Source Estimation in Presurgical Epilepsy Evaluation. *Journal of Clinical Neurophysiology*, 16:239–266, 1999.

[102] C. M. Michel, M. M. Murray, G. Lantz, S. Gonzalez, L. Spinelli, and R. Grave De Peralta. EEG source imaging. *Clin Neurophysiol*, 115(10):2195–2222, 2004.

[103] P. M. Morse and H. Feshbach. *Methods of Theoretical Physics*. York: McGraw-Hill, 1953.

[104] J. C. Mosher and R. M. Leahy. Source localization using recursively applied and projected (RAP) MUSIC. *IEEE Transactions on Signal Processing*, 47:332–340, 1999.

[105] J. C. Mosher, P. S. Lewis, and R. m. Leahy. Multiple dipole modeling and localization from spatio-temporal MEG data. *IEEE Transactions on Biomedical Engineering*, 39:541–557, 1992.

[106] John C. Mosher, Richard M. Leahy, and Paul S. Lewis. EEG and MEG: forward solutions for inverse methods. *IEEE Transactions on Biomedical Engineering*, 46:245–259, 1999.

[107] M. Mozumder, T. Tarvainen, S. R. Arridge, J. Kaipio, and V. Kolehmainen. Compensation of optode sensitivity and position errors in diffuse optical tomography using the approximation error approach. *Biomedical Optics Express*, 4(10):2015–2031, Oct 2013.

[108] M. Mozumder, T. Tarvainen, J. P. Kaipio, S. R. Arridge, and V. Kolehmainen. Compensation of modeling errors due to unknown domain boundary in diffuse optical tomography. *Journal of the Optical Society of America A.*, 31(8):1847–1855, Aug 2014.

[109] J. C. Munck, B. W. van Dijk, and H. Spekreijse. Mathematical dipoles are adequate to describe realistic generators of human brain activity. *IEEE Transactions on Biomedical Engineering*, 35(11):960–966, 1988.

[110] S. Murakami. Contributions of principal neocortical neurons to magnetoencephalography and electroencephalography signals. *Journal of Physiology-london*, 575:925–936, 2006.

[111] F. Natterer. *The mathematics of computerized tomography.* Society for Industrial and Applied Mathematics, Philadelphia, PA, USA, 2001.

[112] A. Nissinen. *Modelling Errors in Electrical Impedance Tomography.* PhD thesis, Publications of the University of Eastern Finland Dissertations in Forestry and Natural Sciences, 2011.

[113] A. Nissinen, L .M. Heikkinen, and J. P. Kaipio. The bayesian approximation error approach for electrical impedance tomographyexperimental results. *Measurement Science & Technology*, 19, 2008.

[114] A. Nissinen, L. M. Heikkinen, V. Kolehmainen, and J. P. Kaipio. Compensation of errors due to discretization, domain truncation and unknown contact impedances in electrical impedance tomography. *Measurement Science and Technology*, 20, 2009.

[115] A. Nissinen, V. Kolehmainen, and J. P. Kaipio. Reconstruction of domain boundary and conductivity in electrical impedance tomography using the approximation error approach. *International Journal for Uncertainty Quantification*, 1(3):203–222, 2011.

[116] A. Nissinen, V. Kolehmainen, and J.P. Kaipio. Compensation of modelling errors due to unknown domain boundary in electrical impedance tomography. *IEEE Transactions on Medical Imaging*, 30(2):231–242, 2011.

[117] M. A. Nitsche, L. G. Cohen, E. M. Wassermann, A. Priori, N. Lang, A. Antal, W. Paulus, F. Hummel, P. S. Boggio, F. Fregni, and A. Pascual-Leone. Transcranial direct current stimulation: State of the art 2008. *Brain Stimulation*, 1:206–223, 2008.

[118] G. Nolte and G. Dassios. Analytic expansion of the EEG lead field for realistic volume conductors. *Physics in Medicine and Biology*, 50:3807–3823, 2005.

[119] S. J. Norton. Tomographic reconstruction of 2D vector fields: Application to flow imaging. *Geophysical Journal International*, 97(1):161 – 168, 1988.

[120] S. J. Norton. Unique tomographic reconstruction of vector fields using boundary data. *IEEE Transactions on Image Processing*, 1:406–412, 1992.

[121] A. Nummenmaa, T. Auranen, M. S. Hämäläinen, L. P. Jäskeläinen, J. Lampinen, M. Sams, and A. Vehtari. Hierarchical Bayesian estimates of distributed MEG sources: Theoretical aspects and comparison of variational and MCMC methods. *Neuroimage*, 35:669–685, 2007.

[122] P. L. Nunez and R. Srinivasan. *Electric Fields of the Brain: The Neurophysics of EEG*. Oxford University Press, 2006.

[123] International Federation of Clinical Neurophysiology: www.ifcn.info/.

[124] J. O. Ollikainen. *Modelling and Computational Aspects in EEG Inverse Problems*. PhD thesis, Kuopion yliopisto (university of Kuopio), 2001.

[125] J. O. Ollikainen, M. Vauhkonen, P. A. Karjalainen, and J. P Kaipio. Effects of local skull inhomogeneities on EEG source estimation. *Medical Engineering & Physics*, 21:143–154, 1999.

[126] J. O. Ollikainen, M. Vaukhonen, P. A. Karjalainen, and J. P. Kaipio. A new computational approach for cortical imaging. *IEEE Transactions on Medical Imaging*, 20(4):325–332, 2001.

[127] P. J. Olver. *Introduction to Partial Differential Equations*. Springer, 2014.

[128] Thom Oostendorp and Adriaan van Oosterom. The potential distribution generated by surface electrodes in inhomogeneous volume conductors of arbitrary shape. *IEEE Transactions on Biomedical Engineering*, 38:409–417, 1991.

[129] R. Oostenveld, P. Fries, E. Maris, and J.-M. Schoffelen. FieldTrip: Open source software for advanced analysis of MEG, EEG and invasive electrophysiological data. *Computational intelligence and Neuroscience*, page 156869, 2011. URL: http://fieldtrip.fcdonders.nl/.

[130] N. F. Osman and J. L. Prince. Reconstruction of Vector Fields in Bounded Domain Vector Tomography. In *International Conference on Image Processing*, pages 476–479, 1997.

[131] W. Ou, M. S. Hämäläinen, and P. Golland. A distributed spatio-temporal EEG/MEG inverse solver. *Neuroimage*, 44:932–946, 2009.

[132] A. Papoulis and S. U. Pillai. *Probability, Random Variables, and Stochastic Processes, Fourth Edition*. McGraw-Hill Europe, 2002.

[133] R. D. Pascual-Marqui. Standardized low resolution brain electromagnetic tomography (sLORETA): technical report. *Mathods and finding in exprerimental and clinical pharmacology*, 24 Suppl, D:5-12, 2002.

[134] Roberto D. Pascual-Marqui, Dietrich Lehmann, Thomas Koenig, Kieko Kochi, Marco C. G. Merlo, Daniel Hell, and Martha Koukkou. Low resolution brain electromagnetic tomography (LORETA) functional imaging in acute, neuroleptic-naive, first-episode, productive schizophrenia. *Psychiatry Research-neuroimaging*, 90:169–179, 1999.

[135] O. Pele and M. Werman. Fast and robust earth mover's distances. In *Proceeding of the IEEE International Conference on Computer Vision*, pages 460–467, 2009.

[136] M. Petrou and P. Bosdogianni. *Image processing - the fundamentals*. John Wiley & Sons, 1999.

[137] M. Petrou and A. Giannakidis. Full tomographic reconstruction of 2D vector fields using discrete integral data. *The Computer Journal*, 53(9), 2010. doi: 10.1093/comjnl/bxq058.

[138] A. Polonsky and M. Zibulevsky. MEG/EEG Source Localization Using Spatio-temporal Spars Representations. In *Independent Component Analysis and Blind Spare Representations*. Springer Berlin / Heidelberg, 2004.

[139] J. L. Prince. Tomographic reconstruction of 3D vector fields using inner product probes. *IEEE Transactions on Image Processing*, 3(2):216–219, 1994.

[140] R. R. Ramirez, D. Wipf, and S. Baillet. Neuroelectromagnetic Source Imaging of Brain Dynamics. In Wanpracha Chaovalitwongse, Panos M. Pardalos, and Petros Xanthopoulos, editors, *Computational Neuroscience*, Springer Optimization and Its Applications, pages 127–155. Springer New York, 2010.

[141] S. M. Rampersad, A. M. Janssen, F. Lucka, U. Aydin, B. Lanfer, Seok L., C. H. Wolters, D. F. Stegeman, and T. F. Oostendorp. Simulating Transcranial Direct Current Stimulation With a Detailed Anisotropic Human Head Model. *IEEE Transactions on Neural Systems and Rehabilitation Engineering*, 22(3):441–452, 2014.

[142] A. Rodriguez-Rivera, B. V. Baryshnikov, B. D. Van Veen, and R. T. Wakai. MEG and EEG source localization in beamspace. *IEEE Transactions on Biomedical Engineering*, 53(3):430–441, 2006.

[143] B. Roth, M. Balish, A. Gorbach, and S. Sato. How well does a three-sphere model predict positions of dipoles in a realistically shaped head? *Electroenceph. Clin. Neurophysiology*, 87(4):175–184, 1993.

[144] D. Rouseff, K. B. Winters, and T. E. Ewart. Reconstruction of Oceanic Microstructure by Tomography: A Numerical Feasibility Study. *Journal of Geophysical Research*, (96:C5):8823–8833, 1991.

[145] Y. Rubner, C. Tomasi, and L. J. Guibas. The Earth Mover's Distance as a Metric for Image Retrieval. *International Journal of Computer Vision*, 40(2):99–121, 2000.

[146] J. Sarvas. Basic mathematical and electromagnetic concepts of the bio-magnetic inverse problems. *Physics in Medicine and Biology*, 32(1):11–22, 1987.

[147] P. W. Schaefer, P. E. Grant, and R. G. Gonzalez. Diffusion-weighted MR Imaging of the Brain. *Radiology*, 217(2):331–345, 2000. PMID: 11058626.

[148] G. Schalk and J. Mellinger. *A Practical Guide to Brain-Computer Interfacing with BCI2000*. Springer Publishing Company, Incorporated, 1st edition, 2010.

[149] M. Scherg, T. Bast, and P. Berg. Multiple Source Analysis of Interictal Spikes: Goals, Requirements, and Clinical Value. *Journal of Clinical Neurophysiology*, 16:214–224, 1999.

[150] M. Scherg and D. Von Cramon. Evoked dipole source potentials of the human auditory cortex. *Electroencephalography and Clinical Neurophysiology/Evoked Potentials Section*, 65(5):344–360, 1986.

[151] M. Scherg and J. S. Ebersole. Models of brain sources. *Brain Topography*, 5:419–423, 1993.

[152] P. H. Schimpf, C. Ramon, and J. Haueisen. Dipole models for the EEG and MEG. *IEEE Transactions on Biomedical Engineering*, 49(5):409–418, 2002.

[153] T. Schuster. The 3D Doppler transform: elementary properties and computation of reconstruction kernels. *Inverse Problems*, 16(3):701–722, 2000.

[154] T. Schuster. Defect correction in vector field tomography: detecting the potential part of a field using BEM and implementation of the method. *Inverse Problems*, 21(1):75–91, 2005.

[155] T. Schuster. 20 years of imaging in vector field tomography: A review. In A. K. Louis (Eds.) Y. Censor, M. Jiang, editor, *Mathematical Methods in Biomedical Imaging and Intensity-Modulated Radiation Therapy (IMRT)*, volume 7 of *Publications of the Scuola Normale Superiore, (CRM)*. Birkhäuser, 2008.

[156] A. Schwarz. Three Dimensional Reconstruction of Temperature and Velocity Fields in a Furnace. *Particle and Particle Systems Characterization*, 12(2):75–80, 1995.

[157] J. R. Shewchuk. An introduction to the conjugate gradient method without the agonizing pain. Technical report, Pittsburgh, PA, USA, 1994.

[158] S. D. Shorvon, E. Perucca, and Jr. J. Engel, editors. *The Treatment of Epilepsy.* John Wiley & Sons, 2009.

[159] G. Shou, L. Xia, M. Jiang, F. Liu, and S. Crozier. Forward and inverse solutions of electrocardiography problem using an adaptive BEM method. In *Proceedings of the 4th international conference on Functional imaging and modeling of the heart*, FIMH'07, pages 290–299, 2007.

[160] P. J. Slomka and R. P. Baum. Multimodality image registration with software: state-of-the-art. *European Journal of Nuclear Medicine and Molecular Imaging*, 36:44–55, 2009.

[161] G. Sparr and K. Strahlen. Vector field tomography, an overview. Center for Nathematical Sciences, Lund Institute of Technology, SE-221 00 Lund, Sweden, 1998. tech. report.

[162] N. Srinivasan. Cognitive neuroscience of creativity: EEG based approaches. *Methods*, 42(1):109–116, 2007.

[163] T. Tarvainen, V. Kolehmainen, J. P. Kaipio, and S. R. Arridge. Corrections to linear methods for diffuse optical tomography using approximation error modelling. *Biomedical Optics Express*, 1(1):209–222, 2010.

[164] T. Tarvainen, V. Kolehmainen, A. Pulkkinen, M. Vauhkonen, M. Schweiger, S. R. Arridge, and J. P. Kaipio. An approximation error approach for compensating for modelling errors between the radiative transfer equation and the diffusion approximation in diffuse optical tomography. *Inverse Problems*, 26(1):015005, 2010.

[165] R. Tomioka and M. Sugiyama. Dual Augmented Lagrangian Method for Efficient Sparse Reconstruction. *IEEE Signal Processing Letters*, 16(12):1067–1070, 2009.

[166] G. J. Tortora and B. H. Derrickson. *Principles of anatomy and physiology.* Wiley, 2009.

[167] K. Uutela, M. Hämäläinen, and R. Salmelin. Global optimization in the localization of neuromagnetic sources. *IEEE Transaction on Biomedical Engineering*, 45(6):716–723, 1998.

[168] K. Uutela, M. Hämäläinen, and E. Somersalo. Visualization of Magnetoencephalographic Data Using Minimum Current Estimates. *NeuroImage*, 10(2):173–180, 1999.

[169] S. P. van den Broek, F. Reinders, M. Donderwinkel, and M. J. Peters. Volume conduction effects in EEG and MEG. *Electroenceph. Clin. Neurophysiol.*, 106(6):522–534, 1998.

[170] B. Vanrumste, G. Van Hoey, R. Van de Walle, M. D'Hav, I. Lemahieu, and P. Boon. Dipole location errors in electroencephalogram source analysis due to volume conductor model errors. *Medical & Biological Engineering & Computing*, 38(5):528–534, 2000.

[171] P. J. Vauhkonen. Second order and infinite elements in three dimensional electrical impedance tomography (report). Technical report, Kuopio (University of Kuopio), 1999.

[172] B. D. Van Veen, W. van Drongelen, M. Yuchtman, and A. Suzuki. Localization of brain electrical activity via linearly constrained minimum variance spatial filtering. *IEEE Transaction on Biomedical Engineering*, 44(9):867–880, 1997.

[173] N. von Ellenrieder, C. H. Muravchik, and A. Nehorai. Effects of geometric head model perturbations on the EEG forward and inverse problems. *IEEE Transactions on Biomedical Engineering*, 53(3):421–429, 2006.

[174] D. F. Wang, R. M. Kirby, and C. R. Johnson. Resolution Strategies for the Finite-Element-Based Solution of the ECG Inverse Problem. 57(2):220–237, 2010.

[175] J. Z. Wang, S. J. Williamson, and L. Kaufman. Magnetic source images determined by a lead-field analysis: the unique minimum-norm least-squares estimation. *IEEE Transactions on Biomedical Engineering*, 39(7):665–675, 1992.

[176] A. Wernsdorfer. Complete reconstruction of three–dimensional vector fields. *Proceedings - ECAPT 93*, Karlsruhe, 1993.

[177] D. Wipf and S. Nagarajan. A unified Bayesian framework for MEG/EEG source imaging. *Neuroimage*, 44(3):947–966, 2009.

[178] D. P. Wipf and B. D. Rao. An Empirical Bayesian Strategy for Solving the Simultaneous Sparse Approximation Problem. *IEEE Transactions on Signal Processing*, 55(7):3704–3716, 2007.

[179] C. H. Wolters. *Influence of Tissue Conductivity Inhomogeneity and Anisotrophy on EEG/MEG based Source Localization in the Human Brain.* PhD thesis, University of Leipzig, 2003.

[180] C. H. Wolters, A. Anwander, G. Berti, and U. Hartmann. Geometry-Adapted Hexahedral Meshes Improve Accuracy of Finite-Element-Method-Based EEG Source Analysis. *IEEE Transactions on Biomedical Engineering*, 54(8):1446–1453, 2007.

[181] C. H. Wolters, A. Anwander, X. Tricoche, D. Weinstein, M. A. Koch, and R. S. MacLeod. Influence of tissue conductivity anisotropy on EEG/MEG field and return current computation in a realistic head model: A simulation and visualization study using high-resolution finite element modeling. *NeuroImage*, 30(3):813–826, 2006.

[182] C. H. Wolters, L. Grasedyck, and W. Hackbusch. Efficient computation of lead field bases and influence matrix for the FEM-based EEG and MEG inverse problem. *Inverse Problems*, 20(4):1099–1116, 2004.

[183] D. Yao. Electric potential produced by a dipole in a homogeneous conducting sphere. *IEEE Transactions on Biomedical Engineering*, 47(7):964–966, 2000.

[184] B. Yvert, O. Bertrand, M. Thvenet, J. F. Echallier, and J. Pernier. A systematic evaluation of the spherical model accuracy in EEG dipole localization. *Electroenceph. Clin. Neurophysiol.*, 102(5):452–459, 1997.

[185] Z. Zhang. A fast method to compute surface potentials generated by dipoles within multilayer anisotropic spheres. *Physics in Medicine and Biology*, 40(3):335–349, 1995.

[186] D. G. Zill and Wright W. S. *Differential Equations with Boundary–Value Problems*. Cengage Learning, 8th edition, 1997.

Appendix A

Theoretical Aspects and Numerical Solution of the EEG Source Imaging

A.1 Maxwell Equations and Derivation of the EEG Source Problem

The derivation of the EEG source imaging problem is based on the macroscopic Maxwell equations inside a domain Ω where $\mathrm{x} \in \Omega \subset \mathbb{R}^3$ and for $t \in \mathbb{R}^+$ [3]. In particular, the Maxwell equations are

$$\nabla \times \mathrm{e}(\mathrm{x}, t) = -\frac{\partial \mathrm{B}(\mathrm{x}, t)}{\partial t}, \tag{A.1a}$$

$$\nabla \times \mathrm{H}(\mathrm{x}, t) = \mathrm{j}(\mathrm{x}, t) + \frac{\partial \mathrm{D}(\mathrm{x}, t)}{\partial t}, \tag{A.1b}$$

$$\nabla \cdot \mathrm{D}(\mathrm{x}, t) = \rho(\mathrm{x}, t), \tag{A.1c}$$

$$\nabla \cdot \mathrm{B}(\mathrm{x}, t) = 0. \tag{A.1d}$$

where $\mathrm{e}(\mathrm{x}, t)$ is the electric field, $\mathrm{B}(\mathrm{x}, t)$ the magnetic field, $\mathrm{H}(\mathrm{x}, t)$ the magnetic field intensity and $\mathrm{D}(\mathrm{x}, t)$ the electric displacement field. Additionally, $\mathrm{j}(\mathrm{x}, t)$ is the electric current density, $\rho(\mathrm{x}, t)$ is the electric charge density. Considering linear and isotropic medium, the following equations hold, i.e.

$$\mathrm{D}(\mathrm{x}, t) = \epsilon(\mathrm{x})\mathrm{e}(\mathrm{x}, t) \tag{A.2a}$$

$$\mathrm{B}(\mathrm{x}, t) = \mu(\mathrm{x})\mathrm{H}(\mathrm{x}, t) \tag{A.2b}$$

$$\tag{A.2c}$$

where $\epsilon(\mathrm{x})$ is the dielectric permittivity and $\mu(\mathrm{x})$ the magnetic permittivity. Furthermore, for the electric current density in the EEG problem we have that

$$\mathrm{j}(\mathrm{x}, t) = \mathrm{j}^p(\mathrm{x}, t) + \sigma(\mathrm{x})\mathrm{e}(\mathrm{x}, t), \tag{A.3}$$

where $\sigma(\mathrm{x})$ is the electric conductivity within the domain, $\mathrm{j}^p(\mathrm{x})$ is the primary neural activity and $\sigma(\mathrm{x})\mathrm{e}(\mathrm{x})$ the induced secondary currents. Here, we need to mention that there are cases where the medium is considered anisotropic and the conductivity is a tensor instead of a scalar function [181] however, in this work we consider only isotropic media.

In EEG problem, the electric neural activity is a time-harmonic signal. In this case, the time-harmonic version of the Maxwell equation (A.1a)-(A.1d) is considered, i.e.

$$\nabla \times \mathrm{e}(\mathrm{x}) = -i\omega \mathrm{B}(\mathrm{x}), \tag{A.4a}$$

$$\nabla \times \mathrm{H}(\mathrm{x}) = \mathrm{j}(\mathrm{x}) + i\omega \mathrm{D}(\mathrm{x}), \tag{A.4b}$$

$$\nabla \cdot \mathrm{D}(\mathrm{x}) = \rho(\mathrm{x}), \tag{A.4c}$$

$$\nabla \cdot \mathrm{B}(\mathrm{x}) = 0, \tag{A.4d}$$

where ω is the angular frequency and i is the imaginary unit. Neural signals recorded using EEG are in very low frequencies (below several kHz) and therefore the quasi-static approximation of the problem is justified [32, 62, 63]. Term $\mathrm{i}\omega\mathrm{B}(\mathrm{x})$ can be neglected and (A.4a) becomes

$$\nabla \times \mathrm{e}(\mathrm{x}) = 0. \tag{A.5}$$

This implies that

$$\mathrm{e}(\mathrm{x}) = -\nabla u(\mathrm{x}), \tag{A.6}$$

where $u(\mathrm{x})$ is an electric scalar potential function.

Using (A.2a) and (A.3) in (A.4b), we get

$$\nabla \times \mathrm{H}(\mathrm{x}) = \mathrm{j}^p + \sigma \mathrm{e}(\mathrm{x}) + i\omega\epsilon \mathrm{e}(\mathrm{x}). \tag{A.7}$$

By taking the divergent $\nabla\cdot$ in both side of the previous equation, we have

$$0 = \nabla \cdot \mathrm{j}^p + \nabla \cdot (\sigma + i\omega\epsilon)\mathrm{e}(\mathrm{x}). \tag{A.8}$$

The capacitance effects are negligible ($\sigma \gg \omega\epsilon$) which results in

$$\nabla \cdot \sigma \mathrm{e}(\mathrm{x}) = -\nabla \cdot \mathrm{j}^p \tag{A.9}$$

or equivalently

$$\nabla \cdot \sigma \nabla u(\mathrm{x}) = \nabla \cdot \mathrm{j}^p. \tag{A.10}$$

A.2 Existence and Uniqueness

In this section, we show that the solution of a Poisson equation with the Neumann boundary condition has a unique solution up to an additive constant and thus an extra constraint is needed to specify this additive constant [127, 103].

In a bounded domain $\Omega \subset \mathbb{R}^3$ with $\mathrm{x} \in \Omega$, the Poisson equation with Neumann condition on the boundary $\partial\Omega$ is given by

$$\nabla \cdot \sigma \nabla u(\mathrm{x}) = \rho(\mathrm{x}) \quad \text{in } \Omega \tag{A.11a}$$

$$\sigma \nabla u(\mathrm{x}) \cdot \hat{n} = 0 \quad \text{on } \partial\Omega, \tag{A.11b}$$

where $\hat{n}$ denotes the outward pointing normal vector on $\partial\Omega$, $\sigma > 0$ defines the properties of the medium (conductivity) and $\rho(\mathrm{x})$ is the source term.

If $\rho(\mathrm{x})$ is continuous and differentiable and $u(\mathrm{x})$ is a solution of (A.11a), then space U is defined to be the set of all real valued function u with the property that u and its first and second derivatives are continuous in $\bar{\Omega} = \Omega + \partial\Omega$. For the existence of a solution, we begin with the assumption that there is a solution $u \in U$ which satisfies (A.11a) and (A.11b). By integrating both sides of (A.11a) and applying the divergence theorem [3], we have that

$$\int_{\mathrm{x}\in\Omega} \rho \, d\mathrm{x} = -\int_{s\in\partial\Omega} \sigma \nabla u \cdot \hat{n} \, ds = 0. \tag{A.12}$$

This is the necessary condition for the existence of a solution u [127]. The complete proof for the existence of a solution relies on the Fredholm Alternative theorem which it is out of the scope of the current paragraph however further details can be found in [127].

The next step is to check if (A.11a) and (A.11b) ensure a unique solution. Uniqueness is ensured if the operator $\nabla \cdot \sigma \nabla$ is positive definite (Ch.10, Theorem 10.20 [127]). We can write that $\nabla \cdot \sigma \nabla$ is positive definite iff

$$\langle u; \nabla \cdot \sigma \nabla u \rangle \quad > 0 \quad \text{for all } u \neq 0 \tag{A.13}$$

$$\langle u; \nabla \cdot \sigma \nabla u \rangle \quad = \quad 0 \;\Rightarrow\; u = 0, \tag{A.14}$$

where $\langle ; \rangle$ denotes the L^2 scalar product[3].

From Green's theorem, we have that

$$\int_{\mathrm{x}\in\Omega} (u \nabla \cdot \sigma \nabla u) \, d\mathrm{x} = -\int_{s\in\partial\Omega} u(\sigma \nabla u) \cdot \hat{n} \, ds + \int_{\mathrm{x}\in\Omega} \sigma (\nabla u)^2 \, d\mathrm{x} = \int_{\Omega} \sigma (\nabla u)^2 \, d\mathrm{x} \geq 0 \tag{A.15}$$

because $\sigma > 0$ is strictly positive. Thus, condition (A.13) is satisfied. However, every constant $u = c$ satisfies condition (A.14). In addition, any constant c satisfies also the homogeneous Neumann boundary condition. So, the solution is no unique because one can add in any constant c to solution u without affecting neither the equations (A.11a), (A.12) nor the boundary conditions (A.11b). Therefore, Poisson boundary value problem with homogeneous Neumann condition does not have a unique solution. Instead, we have a family of solutions which differ by a constant. For uniqueness, an additional condition should be considered. Frequently, it is

used a similar condition as condition (A.12) [33], i.e.

$$\int_{\mathrm{x}\in\Omega} u \, d\mathrm{x} = 0. \tag{A.16}$$

For $u = u + c$, condition (A.16) gives $c = 0$. Alternatively a value for c can be specified (for example in EEG forward problem usually a reference electrode is set).

A.3 Weak Formulation

A sufficiently smooth function u which satisfies (A.11a), (A.11b) and (A.16) is known as a classical solution to the Poisson problem with homogeneous Neumann boundary condition. In general cases of non-smooth domains or discontinues source functions $\rho(\mathrm{x})$, function $u(\mathrm{x})$ may not be smooth enough to be regarded a classical solution. An alternative description to the Poisson boundary value problem is through its weak form where the differentiability requirements imposed on the classical solution can be relaxed [33].

For the weak form, the solutions space of u is

$$U = \{u \in H^1(\Omega),\ \mathrm{x} = (x, y) \in \Omega \mid \sigma \nabla u(\mathrm{x}) \cdot \hat{n} = 0 \ \text{ on } \partial\Omega\}, \tag{A.17}$$

where $H^1(\Omega) = \{u(\mathrm{x}) : \Omega \to \mathbb{R} \mid \int_\Omega u^2 \ d\mathrm{x}, \int_\Omega u_x^2 \ d\mathrm{x}, \int_\Omega u_y^2 \ d\mathrm{x} \geq 0\}$ and u does not need to be twice differentiable. Moreover, as we shall see in the next equations it is only necessary for $\rho(\mathrm{x})$ to be integrable.

If we assume that $u(\mathrm{x})$ satisfies (A.11a) and (A.11b) and $u \in U$ then,

$$\nabla \cdot (\sigma \nabla u)\, g = \rho\, g \quad \text{for all } g \in G, \tag{A.18}$$

where g is a test function defined in space G. By integrating (A.18) and using the Green's identity with homogeneous Neumann condition, we obtain

$$\int_\Omega \sigma \nabla u \cdot \nabla\, g \, d\mathrm{x} = \int_\Omega \rho\, g \, d\mathrm{x} \quad \text{for all} \quad g \in G. \tag{A.19}$$

The weak formulation of (A.11) is to find $u \in U$ such as to satisfy

$$\int_\Omega \sigma \nabla u \cdot \nabla g \, d\mathrm{x} = \int_\Omega \rho\, g \, d\mathrm{x} \quad \text{for all} \quad g \in G. \tag{A.20}$$

Or alternatively,

$$\text{find } u \in U \text{ so that } a(u, g) = f(g) \,\forall\, g \in G. \tag{A.21}$$

where $a(u, g) = \int_\Omega \sigma \nabla u \cdot \nabla g \, d\mathrm{x}$ is the bilinear functional $a : U \times G \to \mathbb{R}$ and $f(g) = \int_\Omega \rho\, g \, d\mathrm{x}$ is the right hand side linear functional $f : G \to \mathbb{R}$.

The solution of (A.11) is also a solution of (A.20), however if u is a solution of (A.20), this does not automatically imply that u is also solution of $(A.11)$. Using calculus of variation [33],

we can show that the solution of the the weak formulation is also solution of the problem (A.11). The proof is omitted but details can be found in [127].

A.4 Galerkin Method

For the numerical solution of the forward problem we reformulate problem (A.11) into the weak form (eq. A.20) and function g is chosen from a suitable space of test functions G.

In particular, the problem is solved in a discrete space $U_n \subset U$ where the space $G = U$[33] and thus, the discrete version of (A.21) is

$$\text{find}\, u_h \in U_n \text{ so that } a(u_h, g_n) = f(g_n) \,\forall\, g_n \in U_n. \tag{A.22}$$

Let $\phi_1, \phi_2, \ldots \phi_N$ be basis functions of U_n, then we can find $u_h \in U_n$ such that

$$a(u_h, \phi_j) = f(\phi_j) \text{ for } j = 1, \ldots, N \tag{A.23}$$

and where $u_h = \sum_{i=1}^{N} \phi_i u_i$.
So,

$$a(\sum_{i=1}^{N} \phi_i u_i, \phi_j) = f(\phi_j) \text{ for } j = 1, \ldots, N. \tag{A.24}$$

A.5 FEM Implementation details

The coefficient of the matrix A in (2.11) can be expressed as the sum of the integrals over the elements Ω_l of the domain $\Omega = \cup_{l=1}^{L} \Omega_l$ where L is the number of the elements of the FE-mesh. A coefficient a_{ij} becomes

$$\begin{aligned} a_{ij} &= \sum_{l=1}^{L} \int_{\Omega_l} \sigma \nabla \phi_i(\mathrm{x}) \cdot \nabla \phi_j(\mathrm{x})\, d\mathrm{x} \\ &= \int_{\cup \Omega_l} \sigma \nabla \phi_i(\mathrm{x}) \cdot \nabla \phi_j(\mathrm{x})\, d\mathrm{x} \quad \text{(i.e if } i \text{ and } j \text{ Nodes} \in \Omega_l\text{)}. \end{aligned} \tag{A.25}$$

For the estimation of the coefficients (A.25) we used one-to-one mapping $\mathrm{x} = F(\hat{\mathrm{x}})$ that maps Ω_l on Ω_{ref} [171] (see Fig. A.1). Thus, we have that

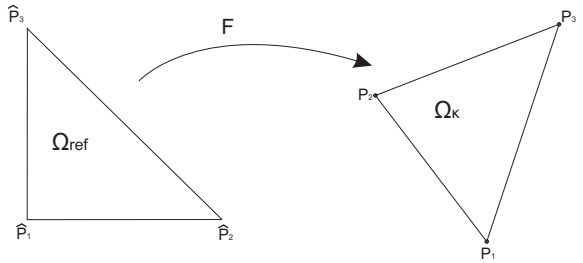

Figure A.1: Mapping F: from element Ω_{ref} to a reference element Ω_l.

$$\int_{\Omega_k} \sigma \nabla \phi_i(\mathrm{x}) \cdot \nabla \phi_j(\mathrm{x})\, d\mathrm{x} = \int_{\Omega_{ref}} \sigma \nabla \phi_i(F(\hat{\mathrm{x}})) \cdot \nabla \phi_j(F(\hat{\mathrm{x}}))| \det \mathrm{J}_F|\, d\mathrm{x}, \tag{A.26}$$

where $\det \mathrm{J}_F$ is the determinant of the Jacobian of F.

The gradients of (A.26) are estimated using the derivative chain rule i.e. $\nabla \phi_i(\hat{\mathrm{x}}) = \mathrm{J}_F^{\mathrm{T}} \nabla \phi_i(\mathrm{x})$ [171]) and thus

$$\nabla \phi_i(\mathrm{x}) = (\mathrm{J}_F^{\mathrm{T}})^{-1} \mathrm{L}_i \tag{A.27}$$

where $\mathrm{L}_i = \nabla \phi_i(\hat{\mathbf{x}})$.

We re-write (A.26) by substituting (A.27)

$$\int_{\Omega_{ref}} \sigma \left[(\mathrm{J}_F^{T^{-1}} \mathrm{L}_i)^{\mathrm{T}} (\mathrm{J}_F^{T^{-1}} \mathrm{L}_j) \right] |\det J_F|\, d\hat{\mathrm{x}}. \tag{A.28}$$

Numerical Estimation of the FEM Integral

The integral (A.28) is estimated using the three points Gaussian Quadrature approximation [43]. The integral (A.28) becomes

$$\int_{\Omega_{ref}} \sigma h_{ij}(\hat{\mathrm{x}})\, d\hat{\mathrm{x}} \approx \frac{1}{6} \left[\sigma_{\hat{\mathrm{x}}_1^m} h_{ij}(\hat{\mathrm{x}}_1^m) + \sigma_{\hat{\mathrm{x}}_2^m} h_{ij}(\hat{\mathrm{x}}_2^m) + \sigma_{\hat{\mathrm{x}}_3^m} h_{ij}(\hat{\mathrm{x}}_3^m) \right], \tag{A.29}$$

where $h_{ij}(\hat{\mathrm{x}}) = (\mathrm{J}_F^{T^{-1}} \mathrm{L}_i)^{\mathrm{T}} (\mathrm{J}_F^{T^{-1}} \mathrm{L}_j) |\det J_F|$, $\hat{\mathrm{x}}_u^m$ are, for $u = 1, 2, 3$, the midpoints of the edges of Ω_{ref} and $\sigma_{\hat{\mathrm{x}}_u^m}$ the corresponding conductivities.

The conductivity at these points is estimated as a linear combination of the conductivities at the nodes i.e. $\sigma_{\hat{\mathrm{x}}_u^m} = \sum_{l=1}^{3} \beta_l \sigma_l$, where σ_l are the conductivities at the corners of the triangle.

Iso-Parametric Mapping

In the FEM implementation, we use an iso-parametric mapping F [171] i.e.

$$\mathrm{x} = \sum_{i=1}^{N_{\Omega_i}} \phi_i(\hat{\mathrm{x}}) \mathrm{x}_i \tag{A.30}$$

where x_i are the coordinates at nodes of the element. For triangle elements, N_{Ω_i} is either 3 or 6 for the linear or quadratic basis function case respectively.

For 2D meshes, the Jacobian of the mapping F is given by

$$\mathrm{J}_F = \left[\frac{\partial \sum_{i=1}^{N_{\Omega_i}} \phi_i(\hat{\mathrm{x}})}{\partial \hat{x}} \mathrm{x}_i \quad \frac{\partial \sum_{i=1}^{N_{\Omega_i}} \phi_i(\hat{\mathrm{x}})}{\partial \hat{y}} \mathrm{x}_i \right]^{\mathrm{T}}. \tag{A.31}$$

where the position vector is $\hat{\mathrm{x}} = (\hat{x}, \hat{y})^{\mathrm{T}}$.

Linear Basis

The linear basis functions for a triangular mesh are

$$\begin{bmatrix}\phi_1(\hat{\mathrm{x}})\\ \phi_2(\hat{\mathrm{x}})\\ \phi_3(\hat{\mathrm{x}})\end{bmatrix} = \begin{bmatrix}1-\hat{x}-\hat{y}\\ \hat{x}\\ \hat{y}\end{bmatrix}. \tag{A.32}$$

We can simultaneous estimate the integrands of (A.28) for the three basis functions and get a 3×3 symmetric matrix.
In particular, if we set $\mathrm{L} = \begin{bmatrix}\mathrm{L}_1 & \mathrm{L}_2 & \mathrm{L}_3\end{bmatrix} = \begin{bmatrix}\nabla\phi_1(\hat{\mathrm{x}}) & \nabla\phi_2(\hat{\mathrm{x}}) & \nabla\phi_3(\hat{\mathrm{x}})\end{bmatrix}$ then

$$\mathrm{L} = \begin{bmatrix}-1 & 1 & 0\\ -1 & 0 & 1\end{bmatrix} \tag{A.33}$$

and the Jacobian (A.31) for the linear case is

$$\mathrm{J}_F = \begin{bmatrix}\mathrm{x}_2-\mathrm{x}_1 & \mathrm{x}_3-\mathrm{x}_1\end{bmatrix}^{\mathrm{T}}. \tag{A.34}$$

Moreover, it can be easily shown that the Jacobian is equal to $\mathrm{J}_F^{\mathrm{T}} = \mathrm{LP}$ where $\mathrm{P} = \begin{bmatrix}\mathrm{x}_1 & \mathrm{x}_2 & \mathrm{x}_3\end{bmatrix}^{\mathrm{T}}$.

Hence, we obtain a 3×3 matrix with the coefficients h_{ij} of (A.28)

$$\mathrm{H} = \left[(\mathrm{J}_F^{T^{-1}}\mathrm{L})^{\mathrm{T}}(\mathrm{J}_F^{T^{-1}}\mathrm{L})\right] \, |\det J_F|. \tag{A.35}$$

Appendix B

Theorems and proofs used in VFT

B.1 Helmholtz Decomposition Theorem

The Helmholtz decomposition is a fundamental theorem of the vector calculus analysis [3, 103]. This theorem states that any vector f which is twice continuously differentiable and which, with its divergence and curl, vanishes faster than $1/r^2$ at infinity (e.g. Schwartz vectorial functions [161]), can be expressed uniquely as the sum of a gradient and a curl as follows

$$\mathrm{f} = \mathrm{f}_I + \mathrm{f}_S \Rightarrow \tag{B.1}$$

$$\mathrm{f} = -\nabla u_0 + \nabla \times \mathrm{a}. \tag{B.2}$$

The scalar function u_0 is the scalar potential and $\mathrm{a} = (a_x, a_y, a_z)$ is the vector potential which should satisfy $\nabla \cdot \mathrm{a} = 0$.

Since, $\nabla \times \mathrm{f}_I = \nabla \times (\nabla u_0) = 0$, component f_I is called irrotational or curl-free while f_S is the solenoidal or divergence-free component as it satisfies $\nabla \mathrm{f}_S = \nabla \cdot (\nabla \times \mathrm{a}) = 0$.

In the 2D, the decomposition equation becomes

$$\mathrm{f} = -\nabla u_0 + \nabla \times a_z(x, y)\hat{z}, \tag{B.3}$$

where $\hat{z}$ is the unit vector normal to the xy plane.

B.2 Fourier Slice Theorem

The Fourier(central) slice theorem (FST) states that the 2D Fourier transform (FT) of scalar function $f(x, y)$ along a line with inclination angle ϕ is equal to the 1D FT of its longitudinal line integral $I(\phi, p)$ along the same line. In particular, the line integral of $f(x, y)$ is

$$I(\phi, p) = \int_{-\infty}^{+\infty} \int_{-\infty}^{+\infty} f(x, y)\delta(x \cos\phi + y \sin\phi - p)dxdy. \tag{B.4}$$

The Fourier transform of $I(\phi, p)$ is

$$\begin{aligned}\tilde{I}(k,\phi) = \int_{-\infty}^{+\infty}\int_{-\infty}^{+\infty}\int_{-\infty}^{+\infty} f(x,y)\delta(x\cos\phi + y\sin\phi - p)e^{-i\kappa p}\, dxdydp = \\ \int_{-\infty}^{+\infty}\int_{-\infty}^{+\infty} f(x,y)e^{-i\kappa(x\cos\phi + y\sin\phi)}\, dxdy = \tilde{f}(k\cos\phi, k\sin\phi).\end{aligned} \tag{B.5}$$

The FST in conjunction with many algorithms (e.g. filtered back-projection) gave rise to the

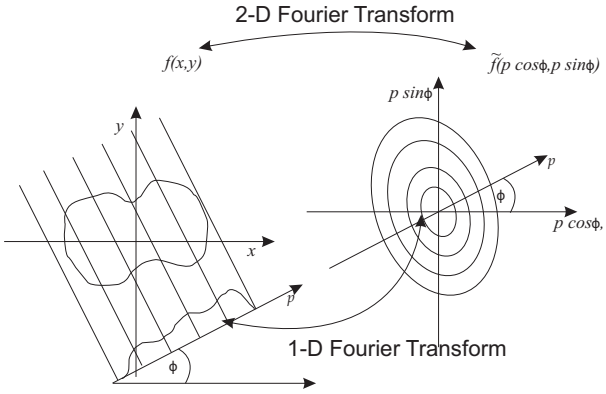

Figure B.1: Central Slice Theorem

development of accurate and robust imaging results (e.g. Computed Tomography (CT) image reconstruction) [111].

B.3 Vectorial Ray Transform

In a bounded 3D domain Ω,the longitudinal ray transform is expressed as

$$\begin{aligned} I_L^{\parallel}(\phi,\theta,p) &= \int_{L(\phi,\theta,p)} \mathrm{f}\cdot\hat{s}_{\phi,\theta}\; d\ell \\ &= \int_{L(\phi,\theta,\rho)} f_x(x,y,z)\cos\phi\sin\theta\; d\ell \\ &+ \int_{L(\phi,\theta,\rho)} f_y(x,y,z)\sin\phi\sin\theta\; d\ell \\ &+ \int_{L(\phi,\theta,p)} f_z(x,y,z)\cos\theta\; d\ell, \end{aligned} \tag{B.6}$$

where f_x, f_y and f_z are the components of vector f, ϕ and θ define the direction of the $\hat{s}_{\phi,\theta}$ unit vector along line $L(\theta,\phi,\mathrm{p})$ as shown in Fig. B.2. Point p gives the intersection coordinates of the line with the plane which passes through the origin and it is orthogonal to $\hat{s}_{\phi,\theta}$. Consequently,

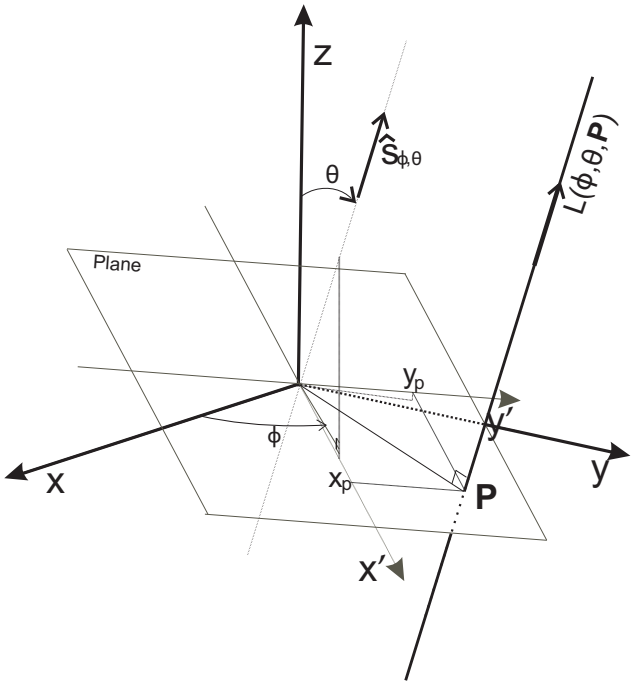

Figure B.2: Londitudinal ray transform in 3D.

the line integral (B.6) can be written as a volume integral using Dirac delta functions. Thus,

$$\begin{aligned} I_L^{\parallel}(\phi,\theta,p) &= \int\int\int_V f_x(x,y,z)\cos\phi\sin\theta\delta_{x_p}\delta_{y_p}\ dxdydz \\ &+ \int\int\int_\Omega f_y(x,y,z)\sin\phi\sin\theta\delta_{x_p}\delta_{y_p}\ dxdydz \\ &+ \int\int\int_\Omega f_z(x,y,z)\cos\theta\delta_{x_p}\delta_{y_p}\ dxdydz, \end{aligned} \tag{B.7}$$

where $\delta_{y_p} = \delta(x\sin\phi - y\cos\phi - y_p)$ and $\delta_{x_p} = \delta(-x\cos\phi\cos\theta - y\sin\phi\cos\theta + z\sin\theta - x_p)$ where (x_p, y_p) are shown in (Fig. B.2).

B.4 Reconstruction of the Solenoidal Component of a Vector Field

In this section, we show that the CST can be used for the reconstruction of the solenoidal part of the field from longitudinal line integrals assuming homogeneous boundary condition [119, 120]. Particularly, the Fourier Transform (FT) of (B.6) $I_L^{\parallel}(\phi,\theta,\mathrm{p}=\{x_p,y_p\})$ is

$$\widetilde{I}_{\phi,\theta}(\kappa_1,\kappa_2) = \int\int I_L^{\parallel}(\phi,\theta,x_p,y_p)e^{-i(\kappa_1 x_p+\kappa_2 y_p)}\ dx_p dy_p, \tag{B.8}$$

where $i = \sqrt{-1}$. So, from (B.8) we obtain

$$\widetilde{I}_{\phi,\theta}(\kappa_1, \kappa_2) = \cos\phi \sin\theta \widetilde{f}_x(\nu, v, w) + \sin\phi \sin\theta \widetilde{F}_y(\nu, v, w) + \cos\theta \widetilde{f}_z(\nu, v, w) \tag{B.9}$$

where $\widetilde{f}_x$, $\widetilde{f}_y$ and $\widetilde{f}_z$ are the FT of f_x, f_y and f_z respectively and $\nu = \kappa_1 \sin\phi - \kappa_2 \cos\phi \cos\theta$, $v = -\kappa_1 \cos\phi - \kappa_2 \sin\phi \cos\theta$ and $w = \kappa_2 \sin\theta$.

Applying the Helmholtz decomposition (eq. B.2) we have

$$\begin{aligned} f_x(x, y, z) &= \frac{\partial a_z}{\partial y} - \frac{\partial a_y}{\partial z} - \frac{\partial u_0}{\partial x} \\ f_y(x, y, z) &= -\frac{\partial a_z}{\partial x} + \frac{\partial a_x}{\partial z} - \frac{\partial u_0}{\partial y} \\ f_z(x, y, z) &= \frac{\partial a_y}{\partial x} - \frac{\partial a_x}{\partial y} - \frac{\partial u_0}{\partial z}. \end{aligned} \tag{B.10}$$

For vanishing boundary values the FT yields to

$$\begin{aligned} \widetilde{f}_x(\nu, v, w) &= iv\widetilde{a}_z(\nu, v, w) - iw\widetilde{a}_y(\nu, v, w) - i\nu\widetilde{u}_0(\nu, v, w) \\ \widetilde{f}_y(\nu, v, w) &= iw\widetilde{a}_x(\nu, v, w) - i\nu\widetilde{a}_z(\nu, v, w) - iv\widetilde{u}_0(\nu, v, w) \\ \widetilde{f}_z(\nu, v, w) &= i\nu\widetilde{a}_y(\nu, v, w) - iv\widetilde{a}_x(\nu, v, w) - iw\widetilde{u}_0(\nu, v, w). \end{aligned} \tag{B.11}$$

Therefore, from (B.9) and (B.11) we have

$$\begin{aligned} \widetilde{I}_{\phi,\theta}(\kappa_1, \kappa_2) =& i(\kappa_1 \cos\phi \cos\theta + \kappa_2 \sin\phi)\widetilde{a}_x \\ &+ i(\kappa_1 \sin\phi \cos\theta - \kappa_2 \cos\phi)\widetilde{a}_y - i\kappa_1 \sin\theta \widetilde{a}_z \end{aligned} \tag{B.12}$$

In two dimensional cases, $\theta = \pi/2$, $\kappa = \kappa_1$ and $\kappa_2 = 0$

$$\widetilde{I}_{\phi}(\kappa) = -i\kappa\widetilde{a}_z(\kappa\cos\phi, \kappa\sin\phi). \tag{B.13}$$

B.5 Discrete Laplace Operator

In our implementations we employ the symmetric/normalized discrete Laplace operator B which is given by

$$B = \mathrm{I}^{2N\times 2N} - \mathrm{diag}(H)^{-1/2} H \mathrm{diag}(H)^{-1/2}, \tag{B.14}$$

where $\mathrm{I}^{2N\times 2N}$ is the identity matrix and the elements of matrix H are for $i \neq j$ we have that $H_{ij} = -\frac{1}{h_{ij}}$ if nodes i and j are connected with a vertex, otherwise $H_{ij} = 0$, and the diagonal element equal to $H_{ii} = -\sum_j H_{ij}$ where h_{ij} is the distance between the nodes j and j.

Appendix C

Interior Point Solver

C.1 Interior Point Method with Logarithmic Barrier

Here we show that for increasing values of t, the solution of the interior point function with s logarithmic barrier converges to the optimal value of the primal constrained problem (C.1), and that for any given positive t, this solution cannot be more than n/t suboptimal, where n is the number of constraints [11]. Additionally, we define the dual problem and we show that duality problem gives lower bounds to the optimal value of the primal problem. The analysis is based on [11, 50].

Convergence of the Interior Point Solution

Lemma 1. *Suppose we have the convex constrained problem (Primal Problem)*

$$\begin{aligned} p^* &= \min_{(d,u)\in C} f(d,r) \\ \textit{subject to } & \ r_i \geq f_i(d), \ \ i = 1 \cdots n \end{aligned} \tag{C.1}$$

where $f : D \to \mathbb{R}$, p^* is the optimal value and f is differentiable.
We define a feasible set C as $C = \{(d,r) \in D : r_i - f_i(d) > 0 \ i = 1, \ldots, n\}$ and the associated centering problem

$$f_t(d,r) = f(d,r) - 1/t \sum_{i=1}^{n} \log\left(r_i - f_i(d)\right) \tag{C.2}$$

we show that, if $(d_t^*, r_t^*) \in C$ is a minimizer of (C.2) for given $t > 0$, then

$$0 \leq f(d_t^*, r_t^*) - p^* \leq n/t \tag{C.3}$$

and

$$\lim_{t\to\infty} f(d_t^*, r_t^*) = p^* \tag{C.4}$$

where n is then number of constrains in (C.1).

Proof. Let assume that $(d_t^*, r_t^*) \in C$ is a minimizer of (C.2) for $t > 0$. So, for the minimizer

(d_t^*, r_t^*) we have that the optimality condition

$$\nabla_{(d_t,r_t)} f_t(d_t^*, r_t^*) - \sum_{i=1}^{n} \frac{1}{t(r_i^* - f_i(d_t^*))} \nabla_{(d,r)}[r_i^* - f_i(d_t^*)] = 0 \tag{C.5}$$

In addition, (d_t^*, r_t^*) minimizes the Lagrangian of (C.1) given by

$$L(d, r, \nu) = f(d, r) + \sum_{i=1}^{n} \nu_i (r_i - f_i(d)) \tag{C.6}$$

when $\nu_i^* = \frac{1}{t(r_i^* - f_i(d_t^*))}$.

In particular, the gradient of the Lagrangian at (d_t^*, r_t^*) is

$$\nabla_{(d_t,r_t)} L(d_t^*, r_t^*, \nu) = \nabla_{(d_t,r_t)} f(d_t^*, r_t^*) - \sum_{i=1}^{n} \nu_i [r_i^* - f_i(d_t^*)]. \tag{C.7}$$

From (C.5) and (C.7) we obtain that

$$\nabla_{(d_t,r_t)} L(d_t^*, r_t^*, \nu^*) = 0 \quad \text{when } \nu_i^* = \frac{1}{t(r_i^* - f_i(d_t^*))} \text{ for } i = 1, \ldots, n. \tag{C.8}$$

Additionally, the optimal value p^* is related with the Lagrangian according to

$$\begin{aligned} p^* &\geq \min_{(d,r)\in C} L(d, r, \nu) \\ &= \min_{(d,r)\in C} f(d, r) - \sum_{i=1}^{n} \nu_i (r_i - f_i(d)) \\ &= f(d_t^*, r_t^*) - \sum_{i=1}^{n} \nu_i^* (r_i^* - f_i(d_t^*)) \\ &= f(d_t^*, r_t^*) - \sum_{i=1}^{n} \frac{1}{t(r_i^* - f_i(d_t^*))} (r_i^* - f_i(d_t^*)) \\ &= f(d_t^*, r_t^*) - n/t. \end{aligned} \tag{C.9}$$

Thus,

$$f(d_t{}^*, r_t{}^*) - p^* \leq n/t. \tag{C.10}$$

As p^* is the optimal value of (C.1), we have that $p^* \leq f(d_t^*, r_t^*)$. So, we proved equation (C.3) which ensures that for any given $t > 0$, the minimizer of (C.2) is no more than n/t suboptimal.

Moreover, from (C.3) we can deduce directly condition (C.4) i.e. $p^* = \lim_{t\to\infty} f(d_t^*, u_t^*)$, which confirms that for large values of t, (d_t^*, r_t^*) is the minimizer of problem (C.1).

Dual Problem and Duality Gap

A dual problem of (C.1) is defined as the minimization of Lagrangian (C.6) over $(d, r) \in D$

$$\tilde{g}(\nu) = \inf_{(d,r)\in D} L(d, r, \nu) \tag{C.11}$$

where ν should be dual feasible point in order $\tilde{g}(\nu) > -\infty$.

From (C.8) we have that every point (d_t^*, u_t^*) which minimizes the objective (C.2) yields to a dual feasible point ν^* and consequently we have that $p^* \geq \tilde{g}(\nu^*)$.

In particular, we define the duality gap between (C.1) and (C.11) as

$$\eta = f(d, r) - \tilde{g}(\nu). \tag{C.12}$$

For the minimizer (d_t^*, r_t^*) of (C.2) and ν^* a dual feasible point we have that

$$\eta = f(d_t^*, r_t^*) - \tilde{g}(\nu^*) = f(d_t^*, r_t^*) - L(d_t^*, r_t^*, \nu^*) = n/t. \tag{C.13}$$

From (C.11) and (C.9)

$$f(d_t^*, r_t^*) = n/t + \tilde{g}(\nu^*) \quad \text{and} \quad f(d_t^*, r_t^*) - p^* \leq n/t \;\Rightarrow p^* \geq \tilde{g}(\nu^*) \tag{C.14}$$

which shows that the dual problem gives lower bounds on the optimal value of the primal problem. Finally, we define the relative duality gap, which we use in our implementation, as

$$\eta_{rel} = \frac{f(d_t^*, r_t^*) - \tilde{g}(\nu^*)}{\tilde{g}(\nu^*)} \geq \frac{f(d_t^*, r_t^*) - p^*}{p^*}. \tag{C.15}$$

C.1.1 Sub-Differential

The sub-differential concept generalizes the derivative to functions which are not differentiable. In particular, a vector $\mathrm{z} \in \mathbb{R}^k$ is defined as the sub-gradient of a function $f : \mathbb{R}^k \to \mathbb{R}$, at $\mathrm{x} \in \mathbb{R}^k$ if for all $\mathrm{y} \in \mathbb{R}^k$

$$f(\mathrm{y}) \geq f(\mathrm{x}) + \mathrm{z}^{\mathrm{T}}(\mathrm{y} - \mathrm{x}). \tag{C.16}$$

Function f is called sub-differentiable at x if there is at least one sub-gradient at x. The set of sub-gradients of f at x is called the sub-differential of f at x, and is denoted by $\partial f(\mathrm{x})$. For example, consider $f(x) = |x|$ which is not differentiable at 0. For $x < 0$, the sub-differential is unique: $\partial f(x) = \{-1\}$. Similarly, for $x > 0$, $\partial f(x) = \{1\}$. At $x = 0$, the sub-differential is defined by the inequality $|y| \geq zy$, which is satisfied if $z \in [-1, 1]$ and therefore $\partial f(0) = [-1, 1]$.

C.2 Preconditioned Conjugate Gradient (PCG)

C.2.1 Newton system

For the minimization of the associated centering problem (3.13) we seek a zero of the gradient $\nabla\Phi_t(p) = 0$, where $p = [d^{\mathrm{T}}, r^{\mathrm{T}}]^{\mathrm{T}}$. The gradient of Φ_t can be approximated by the truncated Taylor expansion [43].

$$\nabla\Phi_t(p + \Delta p) \simeq \nabla\Phi_t(p) + H_{\Phi_t}(p)\Delta p, \tag{C.17}$$

where $\Delta p = [\Delta d^{\mathrm{T}}, \Delta r^{\mathrm{T}}]^{\mathrm{T}}$ the search direction in column form. The new point $p := p + \Delta p$ leads to an optimal estimation if $\nabla\Phi_t(p + \Delta p) \simeq 0$.

So, we want to estimate a new p such as

$$H_{\Phi_t}(p)\Delta p = -\nabla\Phi_t(p). \tag{C.18}$$

This is called Newton'z system (C.18) and Δp is the Newton's step. This system can be solved efficiently using iterative methods (e.g Steepest Descent Method, Conjugate Gradient etc. [43]). Far from the actual solution, the Newton step Δp gives an unreliable estimate. Usually, a parameter s can be estimated along Δp using line search scheme in order to ensure that the new point approximates the solution. The update rule is then

$$p := p + s\Delta p. \tag{C.19}$$

When $s \simeq 1$, from (C.17) and (C.18) we deduce that the new point is near the solution as $\nabla\Phi_t(p + s\Delta p) \simeq 0$.

C.2.2 Gradient and Hessian of Newton System

In this section, we give the explicit formulae for the gradient and the Hessian of Φ_t (3.13) for the 2D case problem where vector $d = [d_x^{\mathrm{T}}, d_y^{\mathrm{T}}]^{\mathrm{T}}$, similar expressions can be derived for the 3D case.

We set $\nabla\Phi_t(p) = g(p)$ where $g(p) = [g_x^{\mathrm{T}}, g_y^{\mathrm{T}}, g_r^{\mathrm{T}}]^{\mathrm{T}} \in \mathbb{R}^{3n}$ and $p = [d_x^{\mathrm{T}}, d_y^{\mathrm{T}}, r^{\mathrm{T}}]^{\mathrm{T}} \in \mathbb{R}^{3n}$.

The gradients with respect to x, y and r are given analytically

$$g_x = \nabla_x\Phi_t(d_x, d_y, r) = 2tK_x^{\mathrm{T}}(Kd - v) + \begin{bmatrix} \frac{2d_x^{(1)}}{r^{(1)2} - d_x^{(1)2} - d_y^{(1)2}} \\ \vdots \\ \frac{2d_x^{(n)}}{r^{(n)2} - d_x^{(n)2} - d_y^{(n)2}} \end{bmatrix} \in \mathbb{R}^n. \tag{C.20}$$

Similar expression we obtain for the y component g_y. Also, we have

$$g_r = \alpha t \mathbf{1} - \begin{bmatrix} \frac{r^{(1)2}}{r^{(1)2}-d_x^{(1)2}-d_y^{(1)2}} \\ \vdots \\ \frac{r^{(n)2}}{r^{(n)2}-d_x^{(n)2}-d_y^{(n)2}} \end{bmatrix} \in \mathbb{R}^n \tag{C.21}$$

where $\mathbf{1} \in \mathbb{R}^n$ is a unit vector and $K = [K_x, K_y]$ is the lead field matrix.

The Hessian matrix is given by

$$H(p) = \begin{bmatrix} 2tK_x^{\mathrm{T}}K_x + H_{11} & 2tK_x^{\mathrm{T}}K_y + H_{12} & H_{13} \\ 2tK_y^{\mathrm{T}}K_x + H_{12} & 2tK_y^{\mathrm{T}}K_y + H_{22} & H_{23} \\ H_{13} & H_{23} & H_{33} \end{bmatrix} \in \mathbb{R}^{3n\times 3n} \tag{C.22}$$

where the elements of H are diagonal matrix given by

$$\begin{aligned}
H_{11} =& \text{diag}\left(2\frac{r^{(1)2}+d_x^{(1)2}-d_y^{(1)2}}{(r^{(1)2}-d_x^{(1)2}-d_y^{(1)2})^2}, \ldots, 2\frac{r^{(n)2}+d_x^{(n)2}-d_y^{(n)2}}{(r^{(n)2}-d_x^{(n)2}-d_y^{(n)2})^2}\right) \\
H_{22} =& \text{diag}\left(2\frac{r^{(1)2}+d_y^{(1)2}-d_x^{(1)2}}{(r^{(1)2}-d_x^{(1)2}-d_y^{(1)2})^2}, \ldots, 2\frac{r^{(n)2}+d_y^{(n)2}-d_x^{(n)2}}{(r^{(n)2}-d_x^{(n)2}-d_y^{(n)2})^2}\right) \\
H_{12} =& \text{diag}\left(4\frac{d_y^{(1)}d_x^{(1)}}{(r^{(1)2}-d_x^{(1)2}-d_y^{(1)2})^2}, \ldots, 4\frac{d_y^{(n)}d_x^{(n)}}{(r^{(n)2}-d_x^{(n)2}-d_y^{(n)2})^2}\right) \\
H_{13} =& -\text{diag}\left(4\frac{r^{(1)}d_x^{(1)}}{(r^{(1)2}-d_x^{(1)2}-d_y^{(1)2})^2}, \ldots, 4\frac{r^{(n)}d_x^{(n)}}{(r^{(n)2}-d_x^{(n)2}-d_y^{(n)2})^2}\right) \\
H_{23} =& -\text{diag}\left(4\frac{r^{(1)}d_y^{(1)}}{(r^{(1)2}-d_x^{(1)2}-d_y^{(1)2})^2}, \ldots, 4\frac{r^{(n)}d_y^{(n)}}{(r^{(n)2}-d_x^{(n)2}-d_y^{(n)2})^2}\right) \\
H_{33} =& \text{diag}\left(2\frac{r^{(1)2}+d_x^{(1)2}+d_y^{(1)2}}{(r^{(1)2}-d_x^{(1)2}-d_y^{(1)2})^2}, \ldots, 2\frac{r^{(n)2}+d_x^{(n)2}+d_y^{(n)2}}{(r^{(n)2}-d_x^{(n)2}-d_y^{(n)2})^2}\right).
\end{aligned} \tag{C.23}$$

C.2.3 PCG Algorithm

The algorithmic steps of PCG for the estimation of the search direction Δp by solving system (C.18) [43, 157]. From (C.18) we set $x = \Delta p$, $H(p) = H$ and $\nabla\Phi_t(p) = g$. PCG algorithm solves the system $Hx = -g$ with pre-conditioner P as follows:

Algorithm 5 Preconditioned Conjugate Gradient

Initialization: $k = 0$, residual $a_0 = g + Hx_0$, direction of PCG $\Delta x_0 = P^{-1}a_0$
Stopping criteria: convergence tolerance ϵ_{PCG} or maximum number of iterations N_{PCG}
Pre-conditioner: P
Repeat for $k = 1, 2, \ldots$ until convergence:

1. $\alpha_k = \frac{a_k^T P^{-1} a_k}{\Delta x_k^T H \Delta x_k}$
2. $x_{k+1} = x_k + \alpha_k \Delta x_k$
3. $a_{k+1} = x_k - \alpha_k H \Delta x_k$
4. $\beta_{k+1} = \frac{a_{k+1}^T P^{-1} a_{k+1}}{a_k^T P^{-1} a_k}$
5. $\Delta x_{k+1} = P^{-1} a_{k+1} + \beta_{k+1} \Delta x_k$
6. **Quit** if $k + 1 = N_{\text{PCG}}$ or $\|a_{k+1}\|_2 / \|g\|_2 \leq \epsilon_{\text{PCG}}$

At each iteration k of the PCG we need to apply two vector matrix multiplications, i.e. $H\Delta x_k$ and $P^{-1}a_{k+1}$. Step $P^{-1}a_{k+1}$ even though it adds an extra matrix-vector multiplication can accelerate the conjugate gradient method. By transforming the linear system into $P^{-1}Hx_k = -P^{-1}g$, the transformed matrices may have better eigenvalue clustering and lower condition number and thus the algorithm can converge more quickly than the original one [157]. The algorithm terminates when the norm of the residual falls below a small fraction of the initial residual $\|g\|_2$.

In the current implementation, the pre-conditioner P is an approximation of the Hessian, keeping the diagonal elements of the lead field matrix K and the Hessian matrices (C.23) i.e. $P = 2t\text{diag}(K^{\text{T}}K) + \nabla^2\Phi_t(p)$.

C.2.4 t Update Rule explanation

In the t-update rule (3.41), line search threshold s_{min} determines if the values of t will increase or not in each outer loop. As we explain here, we select a value for the threshold s_{min} in order to ensure that the value of t is updated when the new estimated solution (d, r) approximates the minimizer $(d^*(t), r^*(t))$ of Φ_t (3.13).

In particular, let assume that the line search step $s \simeq 1$ in (Alg. 2). This implies that the search direction $[\Delta d^{\text{T}}, \Delta r^{\text{T}}]^{\text{T}}$ estimated from the Newton system (3.14) gives a new point $[d^{\text{T}}, r^{\text{T}}]^{\text{T}} + s[\Delta d^{\text{T}}, \Delta r^{\text{T}}]^{\text{T}}$ which nearly minimizes (3.13) as for the new value $\nabla\Phi_t \simeq 0$. On the other hand, when $s \ll 1$, the new estimation is not close to the minimizer of Φ_t (3.13).

Hence, we select the threshold $s_{\min}$ in (3.41) to be close to 1. With this selection when the line search gives a value approximately 1, we know that the estimated solution approximates the actual minimizer and thus the value of t is updated. Otherwise, when $s < s_{min}$ the algorithms continues with constant t until the solution is nearly optimal.

Moreover the choice of the update rule for the branch of (3.41) where $s \geq s_{\min}$ can be

explained as follows. We showed that the optimum (d^*, r^*) of Φ_t (3.13) gives no more than n/t suboptimal estimates (*lemma* 1, appendix C.1) which means that the function $f(d)$ in (3.9) satisfies $f(d^*) - p^* \leq n/t$ where p^* is the optimal value of problem (3.9). In addition, we have $f(d) - p^* \leq \eta$ because $p^* \geq \tilde{g}(\nu)$ (3.21) and $\eta = f(d) - \tilde{g}(\nu)$ is the duality gap.When $s \simeq 1$, then the value d approximates the minimizer d^*. Therefore, the previous two inequalities give that $t \leq n/\eta$ which is the update rule for t when s is greater that $s_{\min}$.

C.3 Levenberg Marquardt (LMA) Algorithm

In this paragraph, we give the steps of the LMA algorithm used for the estimation of the Gaussian prior variances [43].

Algorithm 6 Estimate Variances γ_d of the Gaussian prior

Initialization: Set $\gamma_d^{(i)} = 1/\gamma_{\text{ML}}^{(i)}$ and estimate $G(\gamma_d)$ (3.56) and the Jacobian of G, J.
Set the parameters: $\kappa = 10^{-6} \max\{\text{diag}(J^{\text{T}}J)\}$, $\lambda = 2$ and maximum number of iterations N_{max}.
Repeat:

1. Estimate Jacobian $J = \nabla G(\gamma_d)$.
2. Approximate Hessian $H \approx (J^{\text{T}}J + \kappa I^{kn \times kn})$.
3. Solve $\Delta\gamma_d = -(H^{\text{T}})^{-1}J^{\text{T}}$.
4. Perform Line Search (Alg. 2): estimate s along $\Delta\gamma_d$
   - If $s > 0.5$
     Update $\gamma_d := \gamma_d + s\Delta\gamma_d$ and $G_{\text{new}}(\gamma_d) := G(\gamma_d + s\Delta\gamma_d)$
     $\kappa := \kappa/\lambda$
   - Else $\kappa := \lambda\kappa$ and go to step 2.
5. **Quit** if $G_{\text{new}} < \epsilon_{\text{tol}}^{(1)}$ and $\|s\Delta\gamma_d\|_2 < \epsilon_{\text{tol}}^{(2)}\|\gamma_d\|_2$ or exceed $N_{\max}$.

Appendix D

Further Results using Bayesian Approximation Error Approach

This chapter is complementary to chapter 5 and its aims are (i) to present some further test cases examined during the investigation of the application of the Bayesian approximation error approach in the EEG source imaging problem, (ii) to show some extra results which were not of primal importance but may be of interest to some readers.

D.1 AEA Results when Different Numbers of training Geometries for the Error Statistics

It is well known that the number of MRI geometries can affect the accuracy of the Bayesian approximation error solution. For instance, by using only few geometries, the computed covariance matric may not efficiently describe the variation within individuals. On the other hand, the estimation of the error statistics using too many geometries is not very practical. In this section, we examined how the reconstruction results were affected when the statistics of the approximation errors were computed using different number of MRI geometries. To evaluate how the number of geometries influences the performance, we reconstructed dipole distributions using potential data obtained solving the three compartment forward problem with constant nominal conductivity in each compartment (skull/skull/brain). For the inverse solution, the three compartment circular domain was used. The approximation error covariance matrix was estimated using 5, 15 and 32 MRI cross sections. The results in Fig. D.1 and Fig. D.2 suggest that when the number of MRI geometries is 32, the reconstruction results improve. More precisely, we can expect that when the EMD number is low and approximates the EMD value of the accurate model, additional geometries cannot improve the EMD number of the AEA model. By comparing the EMD values of these results with the EMD of the accurate MRI model (which was equal to EMD=7.2 for the case of Fig. D.1 and EMD=5.31 for the case in Fig. D.2) we can say that the 32 geometries seems to be good in describing the geometrical variation of the MRI cross sections. Thus, this is the number that was used for the estimation of the error statistics

in the test cases presented in chapter 5.

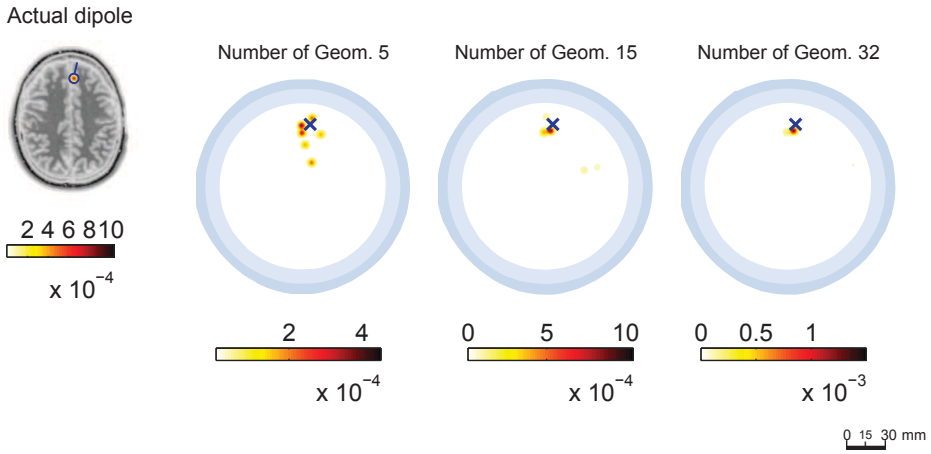

EMD (mm) :	10.6	9.75	7.62
NSD (mm) :	12.5	10.4	7.5
SD (dB) :	0.389	0.335	0.366
WAD (°):	10.1	5.11	2.89

Figure D.1: Single source reconstructions using different number of training geometries in the approximation error statistics.

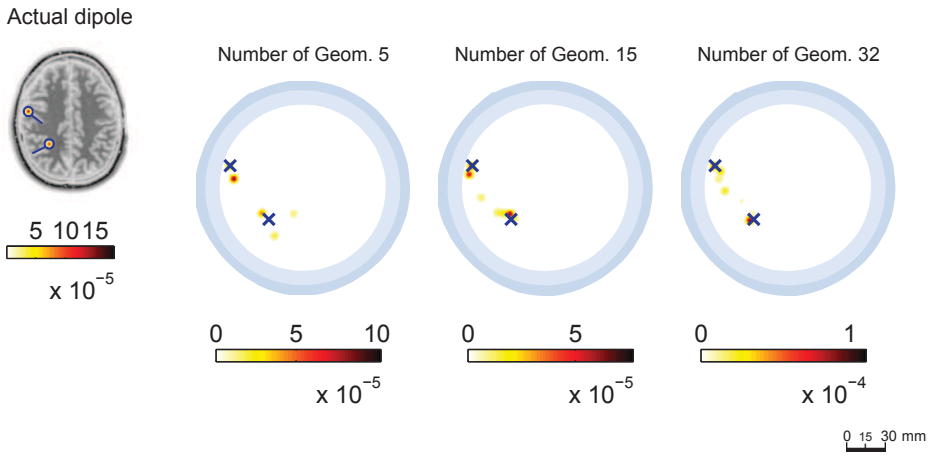

EMD (mm) :	10.7	6.97	5.81
NSD (mm) :	8.97	6.71	6.01
SD (dB) :	−3.26	−1.59	−1.44
WAD (°):	23.5	17.4	11.8

Figure D.2: Two source reconstructions using different number of training geometries in the approximation error statistics.

D.2 Reconstructions using two Different Forward Geometries

In this section, our intention was to compare the performance of the Bayesian AEA to localize correctly sources for two different individuals i.e. two persons with different head geometries when the electric activity inside the brain is in the same area.

In the following figures, the reconstruction results obtained using two forward models (which correspond to two individuals) when a source is located approximately in the same place in both geometries. According to the metrics, the overall results are better for the individual with geometry A (test case A) compared to the individual with geometry B (test case B). For the standard model (without AEA) this is possible because the difference between the circular domain and the MRI are smaller for the geometry A compared to geometry B. Also, the AEA performs better for the test case A which could be explained as follows: The set of the geometries used for the computation of the error statistics share more similarities with geometry A than with geometry B. In other words, the statistics "support" better the features (shape/conductivities) of geometry A.

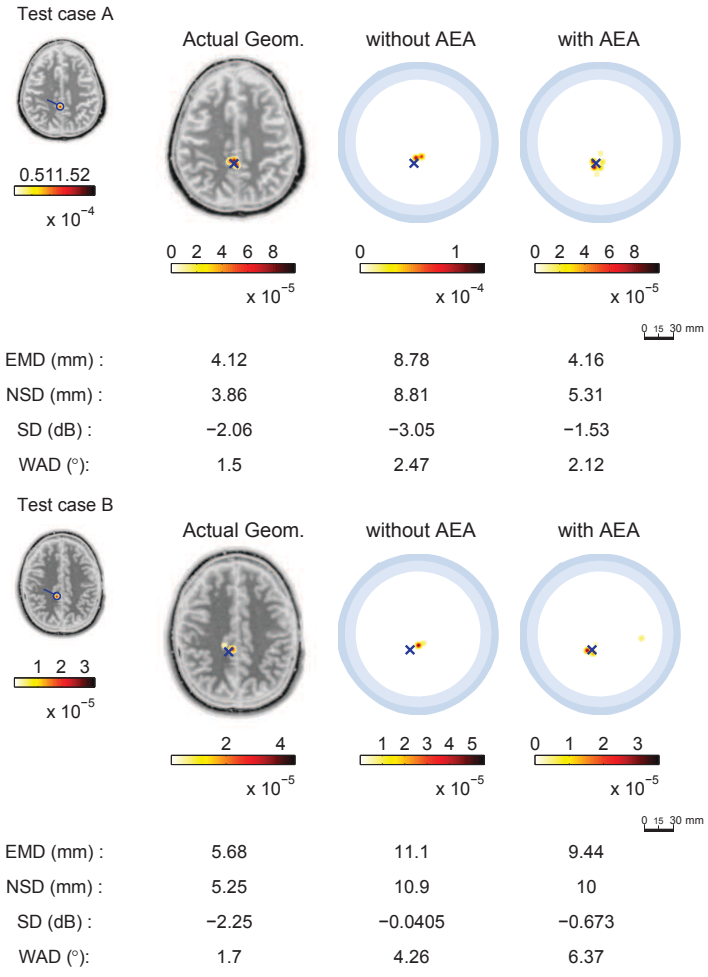

Figure D.3: A test case with a deep source when two different forward models were used.

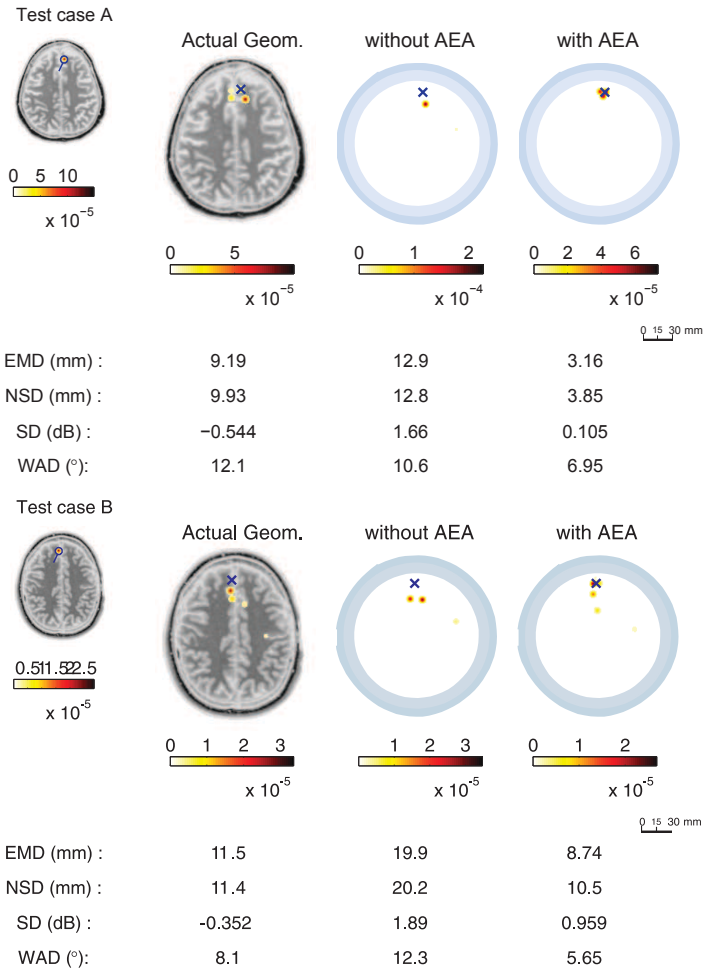

Figure D.4: Superficial source reconstructions in geometry A and B.

D.3 Further Results

D.3.1 Histograms of WAD and SD

For the EEG source imaging problem, we are usually interested in source localization errors and for this purpose, EMD and NSD are more suitable than the SD and WAD metrics. However, in order to have a better understanding of the overall performance of the different solvers we decided to include here the corresponding histograms of SD and WAD metrics for the one, two and three sources case, studied in section 5.4.1. In those cases, the forward and inverse model were consisted of three compartments and there was no additive noise. In most cases, also SD and WAD metrics verify that the AEA model works better than the standard model (without AEA).

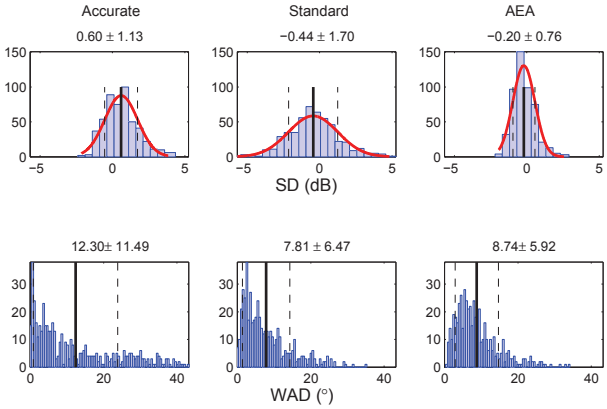

Figure D.5: Single source: Histograms of SD and WAD for 500 simulations of a single dipole. Values closer to zero for the SD figures and smaller values for the WAD indicate better result.

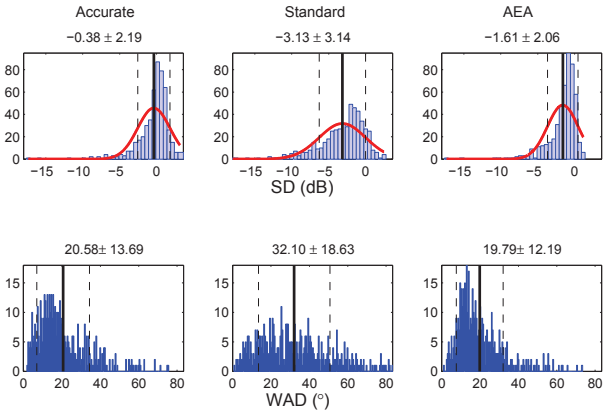

Figure D.6: Two sources: Histograms of SD and WAD for 500 simulations of two dipoles with equal strength.

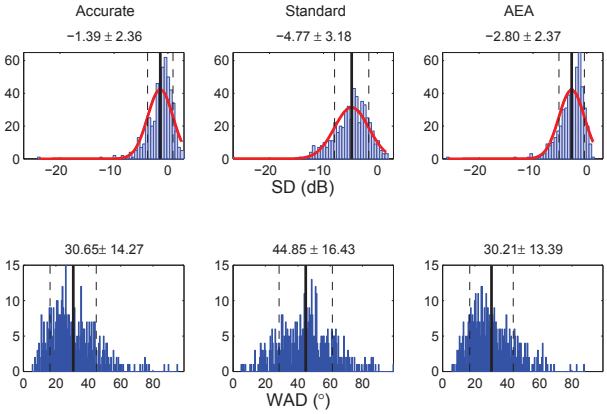

Figure D.7: Three sources: Histograms of SD and WAD for 500 simulations of three simulated dipoles.

D.3.2 Effect of the Orientation of the Dipole

In this section, we study the effect of the source orientation to the reconstruction result. We simulate a single dipole with different direction and constant strength (Fig. D.8). From the graphs, we see that there is periodicity in the values of the metrics as a function of the orientation. The values of the EMD and NSD seem to be relatively stable with respect to the orientation. However, the WAD metric is affected by the orientation of the simulated dipole. The strength difference SD has the greatest fluctuation in the standard model.

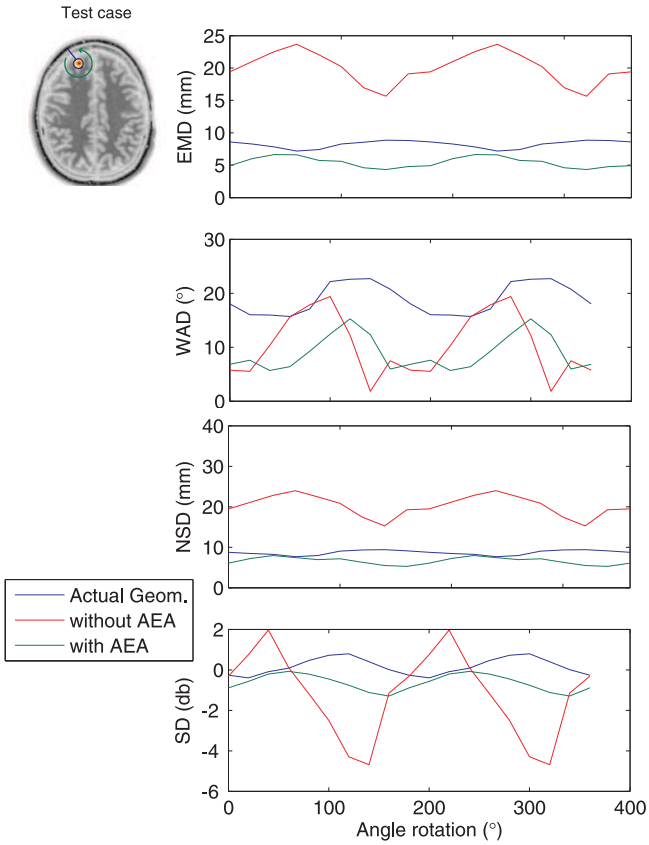

Figure D.8: EMD, WAD, NSD and SD for different dipole orientations. The dipole was rotated anti-clockwise from the shown orientation.